UNIVERSITAT DE BARCELONA

Hybrid bio-robotics: from the nanoscale to the macroscale

Rafael Mestre Castillo

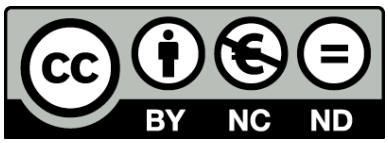

UNIVERSITAT DE BARCELONA

Doctoral Thesis

Hybrid bio-robotics: from the nanoscale to the macroscale

Rafael Mestre Castillo

Hybrid bio-robotics: from the nanoscale to the macroscale

Memòria presentat per optar al grau de doctor per la Universitat de Barcelona

Programa de doctorat en Nanociències

Autor: **Rafael Mestre Castillo**

Director: **Prof. Dr. Samuel Sánchez Ordóñez**

Tutor: **Prof. Dr. Ignacio Pagonabarraga Mora**

UNIVERSITAT DE BARCELONA

The research described in this thesis was carried out in the group 'Smart nano-bio-devices' at the Institute for Bioengineering of Catalonia (IBEC), in Barcelona, Spain, and received funding from "la Caixa" Foundation through IBEC International PhD Programme "la Caixa" Severo Ochoa fellowships (LCF/BQ/SO16/52270018).

Contents

List of Figures

List of Tables

Abstract

Hybrid bio-robotics is a discipline that aims at integrating biological entities with synthetic materials to incorporate features from biological systems that have been optimized through millions of years of evolution and are difficult to replicate in current robotic systems. We can find examples of this integration at the nanoscale, in the field of catalytic nano- and micromotors, which are particles able to self-propel due to catalytic reactions happening in their surface. By using enzymes, these nanomotors can achieve motion in a biocompatible manner, finding their main applications in active drug delivery. At the microscale, we can find single-cell bio-swimmers that use the motion capabilities of organisms like bacteria or spermatozoa to transport microparticles or microtubes for targeted therapeutics or bio-film removal. At the macroscale, cardiac or skeletal muscle tissue are used to power small robotic devices that can perform simple actions like crawling, swimming, or gripping, due to the contractions of the muscle cells.

This dissertation covers several aspects of these kinds of devices from the nanoscale to the macroscale, focusing on enzymatically propelled nano- and micromotors and skeletal muscle tissue bioactuators and bio-robots. On the field of enzymatic nanomotors, there is a need for a better description of their dynamics that, consequently, might help understand their motion mechanisms. Here, we focus on several examples of nano- and micromotors that show complex dynamics and we propose different strategies to analyze their motion. We develop a theoretical framework for the particular case of enzymatic motors with exponentially decreasing speed, which break the assumptions of constant speed of current methods of analysis, and need different strategies to characterize their motion. Finally, we consider the case of enzymatic nanomotors moving in complex biological matrices, such as hyaluronic acid, and we study their interactions and the effects of the catalytic reaction using dynamic light scattering, showing that nanomotors with negative surface charge and urease-powered motion present enhanced parameters of diffusion in hyaluronic acid.

Moving towards muscle-based robotics, we investigate the application of 3D bioprinting for the bioengineering of skeletal muscle tissue. We demonstrate that this technique can yield well-aligned and functional muscle fibers that can be stimulated with electric pulses. Moreover, we develop and apply a novel co-axial approach to obtain thin and individual muscle fibers that resemble the bundle-like organization of native skeletal muscle tissue. We further exploit the versatility of this technique to print several types of materials in the same process and we fabricate bio-actuators based on skeletal muscle tissue with two soft posts. Due to the deflection of these cantilevers when the tissue contracts upon stimulation, we can measure the generated forces, therefore obtaining a force measurement platform that could be useful for muscle development studies or drug testing. With these applications in mind, we study the adaptability of muscle tissue after applying various exercise protocols based on different stimulation frequencies and different post stiffness, finding an increase of the force generation, especially at medium frequencies, that resembles the response of native tissue. Moreover, we adapt the force measurement platform to be used with human-derived myoblasts and we bioengineer two models of young and aged muscle tissue that could be used for drug testing purposes. As a proof of concept, we analyze the effects of a cosmetic peptide ingredient under development, focusing on the kinematics of high stimulation contractions.

Finally, we present the fabrication of a muscle-based bio-robot able to swim by inertial strokes in a liquid interface and a nanocomposite-laden bio-robot that can crawl on a surface. The first bio-robot is thoroughly characterized through mechanical simulations, allowing us to optimize the skeleton, based on a serpentine or spring-like structure. Moreover, we compare the motion of symmetric and asymmetric designs, demonstrating that, although symmetric bio-robots can achieve some motion due to spontaneous symmetry breaking during its self-assembly, asymmetric bio-robots are faster and more consistent in their directionality. The nanocomposite-laden crawling bio-robot consisted of embedded piezoelectric boron nitride nanotubes that improved the differentiation of the muscle tissue due to a feedback loop of piezoelectric effect activated by the same spontaneous contractions of the tissue. We find that bio-robots with those nanocomposites achieve faster motion and stronger force outputs, demonstrating the beneficial effects in their differentiation.

This research presented in this thesis contributes to the development of the field of bio-hybrid robotic devices. On enzymatically propelled nano- and micromotors, the novel theoretical framework and the results regarding the interaction of nanomotors with complex media might offer useful fundamental knowledge for future biomedical applications of these systems. The bioengineering approaches developed to fabricate murine- or human-based bio-actuators might find applications in drug screening or to model heterogeneous muscle diseases in biomedicine using the patient's own cells. Finally, the fabrication of bio-hybrid swimmers and nanocomposite crawlers will help understand and improve the swimming motion of these devices, as well as pave the way towards the use of nanocomposite to enhance the performance of future actuators.

Resumen

La bio-robótica híbrida es una disciplina cuyo objetivo es la integración de entidades biológicas con materiales sintéticos para superar los desafíos existentes en el campo de la robótica blanda, incorporando características de los sistemas biológicos que han sido optimizadas durante millones de años de evolución natural y no son fáciles de reproducir artificialmente. Podemos encontrar ejemplos de este tipo de integración en la nanoescala, en el campo de nano- y micromotores catalíticos, que son partículas capaces de auto-propulsarse gracias a reacciones enzimáticas que ocurren en su superficie. Usando enzimas, estos nanomotores pueden generar movimiento activo de forma biocompatible, encontrando posibles aplicaciones en los campos de administración y liberación específica de fármacos. En la microescala, encontramos bio-nadadores formados por microrganismos que utilizan las capacidades de generar movimiento de bacterias o espermatozoides para transportar micropartículas para administración de fármacos o eliminación de biopelículas bacterianas. A escala macrométrica, células musculares cardíacas o esqueléticas se han usado para actuar pequeños dispositivos robóticos que pueden realizar acciones simples como arrastrarse por una superficie, nadar o agarrar objetos, gracias a las contracciones del tejido.

Esta tesis cubre varios aspectos de este tipo de dispositivos desde la nanoescala a la macroescala, enfocándose en nano- y micromotores propulsados enzimáticamente, así como bio-actuadores y bio-robots basados en tejidos muscular esquelético. En el campo de nanomotores enzimáticos, existe la necesidad de encontrar mejores modelos que puedan describir la dinámica de su movimiento para llegar a entender sus mecanismos de propulsión subyacentes. Aquí, nos enfocamos en diversos ejemplos de nano- y micromotores que muestran dinámicas de movimiento complejas y proponemos diferentes estrategias que se pueden utilizar para analizar y caracterizar este movimiento. Desarrollamos un marco teórico para el caso particular de motores enzimáticos que poseen una velocidad que decae exponencialmente, algo que rompe las suposiciones de las teorías existentes actualmente para estudiar su dinámica. Finalmente, consideramos el caso de nanomotores enzimáticos que se mueven en matrices biológicas complejas como ácido hialurónico y estudiamos sus interacciones, así como los efectos de la reacción catalítica usando la técnica de "dynamic light scattering" (dispersión de luz dinámica), mostrando que los nanomotores con carga superficial negativa y movimiento producido por la enzima ureasa muestran mejores parámetros de difusión en ácido hialurónico.

Moviéndonos hacia robots basados en células musculares, investigamos la aplicación de la técnica de bioimpresión en 3D para la biofabricación de músculo esquelético. Demostramos que esta técnica puede producir fibras musculares funcionales y bien alineadas que puede ser estimuladas y contraerse con pulsos eléctricos. Además, desarrollamos y ponemos en práctica un nuevo método basado en bioimpresión coaxial para producir fibras finas e individuales, que muestran más parecido con la organización en forma de fascículos del músculo esquelético. Investigamos la versatilidad de esta técnica para imprimir varios tipos de materiales en el mismo proceso y fabricamos bio-actuadores basados en músculo esquelético y dos postes de material blando. Debido al movimiento de estos postes por las contracciones musculares podemos adquirir medidas de la fuerza ejercida, obteniendo una plataforma de medición de fuerzas que podría ser de utilidad para estudios sobre el desarrollo del músculo o para testeo de fármacos. Con estas aplicaciones en mente, estudiamos la adaptación del tejido

muscular después de aplicar diferentes protocolos de entrenamiento basados en distintas frecuencias de estimulación y diferente dureza de los postes, encontrando un aumento en la fuerza generada, especialmente para frecuencias medias, similar a la respuesta del tejido muscular nativo. Asimismo, adaptamos la plataforma de medida de fuerzas para usarse con mioblastos derivados de humanos y biofabricamos dos modelos de músculo humano joven y envejecido que podría usarse para aplicaciones de testeo de fármacos. Como prueba de concepto, analizamos los efectos de un ingrediente cosmético en desarrollo, enfocándonos en la dinámica de las contracciones a alta frecuencia.

Finalmente, presentamos la fabricación de un bio-robot basado en músculo esquelético capaz de nadar en la superficie de un líquido y un bio-robot con nanocompuestos incrustados que puede arrastrarse por una superficie sólida. El primer de ellos es caracterizado minuciosamente a través de simulaciones mecánicas, permitiéndonos optimizar su esqueleto, basado en una estructura tipo serpentina o muelle. Además, comparamos el movimiento de diseños simétricos y asimétricos, demostrando que, aunque bio-robots simétricos pueden llegar a generar movimiento debido a una rotura espontánea de la simetría durante su autoensamblaje, los bio-robots asimétricos son mucho más rápidos y consistentes. El segundo bio-robot contiene nanotubos piezoeléctricos incrustados en su tejido, los cuales ayudan en la diferenciación del músculo debido a una retroalimentación basada en su efecto piezoeléctrico y activada por las contracciones espontáneas del tejido. Mostramos que estos bio-robots puede generar un movimiento más rápido y una mayor producción de fuerza, demostrando los efectos beneficiales en la diferenciación del tejido.

Para concluir, estos resultados ofrecen varias ventajas en el campo de los bio-robots híbridos. Sobre nano- y micromotores propulsados enzimáticamente, el marco teórico desarrollado y los resultados obtenidos sobre su interacción con fluidos complejos podría proporcionar conocimiento fundamental y útil para próximas aplicaciones biomédicas. Los métodos de bioingeniería desarrollados para la fabricación de músculo esquelético en forma de bio-actuadores con células de ratón o humanas podrían encontrar aplicaciones en detección y testeo de drogas o para modelar enfermedades musculares usando las células de los propios pacientes. Finalmente, la fabricación de los bio-robots capaces de nadar o con nanocompuestos ayudará a entender y mejorar el movimiento de natación de estos robots, así como allanar el camino para el uso de nanocompuestos como método de mejorar la actuación de futuros actuadores híbridos.

I

Introduction

I

Biomimetics

Biomimetics has always fascinated human beings, driving scientific knowledge and technological development to its utmost limits. We can find one of the first exponents of this enthusiasm in the works of Leonardo da Vinci, who observed the dynamics and the anatomy of flying birds and mammals, and composed designs of flying machines, resembling the structure of animal's wings that, unfortunately, never succeeding at flying (Figure 1.1A). Several centuries of scientific and technical development, closely following nature's steps, brought us to transform da Vinci's dream of flying into a reality. Nonetheless, Leonardo's interests would go much further. Fascinated by the anatomy of human beings, he designed and possibly constructed the first human automaton in 1495, the so-called Leonardo's humanoid robot, as his writings in his *Codex Atlanticus* reflect[1]. This robot, dressed in a suit of armor, contained clock-work systems, sets of pulleys and various mechanisms and gears and could perform actions like sitting up, wave its arms, open its jaw, move its head and even produce sounds thanks to automated drums (Figure 1.1B). The awe that this sort of machine could have produced 500 years ago is hard to imagine when we still find ourselves astonished by the degree of sophistication and understanding of anatomy, biomechanics and motion dynamics of his design.

Half a millennium later, we still use the prescient view of Leonardo da Vinci and look at nature to imitate features from biological systems that have been optimized for thousands and millions of years. From the adhesion of frogs and geckos[2] or the structural coloration of butterflies[3] to the nanostructuring of stronger and tougher materials that mimic spider webs[4] or the design of sustainable buildings that resemble termite mounds[5], biomimetics has found applications in virtually all fields of scientific research and technology. Leonardo's robot was just one of the first examples of human biomimicry that have resulted in better prostheses and orthoses for impaired people[6], as well as humanoid robots that replicate human expressions and facial features, imitate the range of movements of muscles and articulations or sense and respond to complex stimuli[7, 8]. However, these developments are still lagging far behind nature in terms of efficiency, robustness, control, energy storage and power-to-weight ratio, among many other characteristics[9].

Bio-hybrid robotics has emerged as a field that attempts to overcome these difficulties by integrating biological entities with synthetic materials, taking advantage of the best features of both types of systems in a synergistic manner[10]. Developments in bio-hybrid devices span all lengths scales,

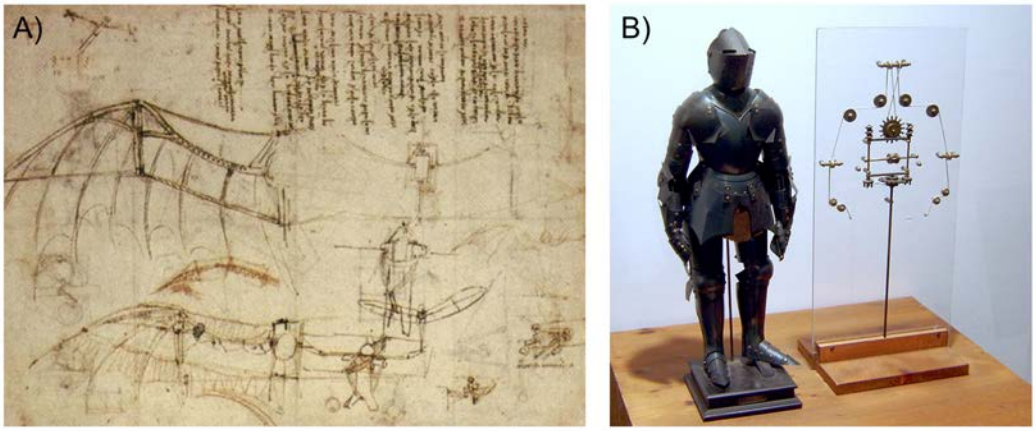

Figure 1.1: Biomimetic lessons from Leonardo da Vinci. A) Da Vinci's designs of a flying machine based upon the structure of bat's wings. Source: drawingsofleonardo.org. B) Leonardo's automaton, from a model at display in Berlin in 2005. On the right, the inner workings are recreated. Source: Wikipedia.org (author: Erik Möller).

from the nanoscale to the macroscale. At the nanoscale, fundamental research in active matter and molecular biotechnology has led to the fabrication of bio-hybrid self-propelled nanoparticles powered by enzymatic reactions[11]. These type of devices have offered benefits in the creation of smart drug delivery systems that can diffuse more efficiently and use biocompatible reactions as their power source. At the microscale, the use of biomolecules can be substituted by whole cells, such as bacteria or spermatozoa, to fabricate bio-hybrid micro-swimmers that utilize the complex and efficient propelling mechanisms of single cells to carry microparticles or microtubes, with applications in biofilm removal, drug delivery, cell manipulation or assisted reproduction[12]. Multiple cells in the form of tissues can also be applied for bio-hybrid robotic systems. In this case, muscle tissue, either skeletal or cardiac, is the choice par excellence in the field, as the contraction capabilities of this tissue can be used to power bio-robots or bio-actuators, biomimicking the structure and organization of the musculoskeletal system. Moreover, current developments aim at integrating several kinds of cells to create multi-cellular engineered living systems with complex and novel functionalities embedded in their design[13].

Bio-hybrid research is continuously increasing (Figure 1.2). A bibliometric search shows that number of publications related to this kind of research has been increasing since 2005, with more than 25% of them being published between 2016 and today (Figure 1.2A). While most of these publications are of the article type, there have been an important number reviews dealing with the topic and even some patents (Figure 1.2B). This search also demonstrates the large multidisciplinarity of this kind of research, with most of the contributions coming from engineering, cell biology, material science, chemistry, instrumentation, molecular biology or physics, while computer science and robotics occupy only the 10^{th} and 11^{th} positions, respectively (Figure 1.2C). Given the wide range of research fields and applicability, there is a need to find proper divisions and categories that can unify the nomenclature and the language used to describe these devices. Recent reviews in the literature have suggested approaches such as the macro-categorization in i) application-oriented non-scalable devices, and ii) general-purpose scalable devices[10]. While the first category refers to a top-down approach, in which artificial technologies are built around an already optimized biological entity, such as bacteria-based micro-swimmers, the second category covers bottom-up strategies in which biological components, like single cells, are bioengineered together to form general-purpose large-scale

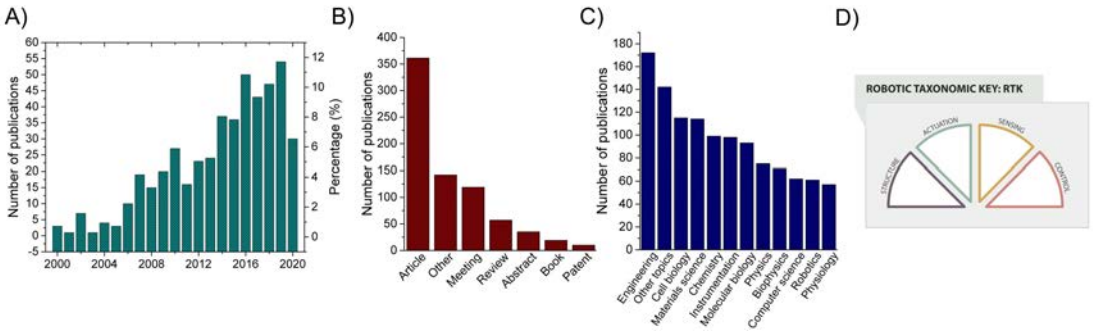

Figure 1.2: Status of bio-hybrid research in the literature, as of June, 2020. A) Number of papers and percentage published between 2000 and June, 2020 on bio-hybrid robots. The analysis was performed in the Web of Science database searching for the following keywords in their title or abstract: "bio-hybrid actuator*", "biohybrid actuator*", "cell-based actuator*", "bacteria robot*", "muscle bioactuator*", "muscle-based bioactuator*", "muscle-based bio-actuator*", "bio-actuator*", "bioactuator*", "biohybrid robot*", "bio-hybrid robot*", "hybrid bio-robot*", "hybrid biorobot*", "bio-bot*", "bio-hybrid device*", "biohybrid device*", "bio-hybrid system*", "biohybrid system*". B) Number of publications on bio-hybrid robots according to their type (note: several publications could have duplicate types). The search was performed using the same keywords. C) Number of publications on bio-hybrid robots according to their field. The search was performed using the same keywords. C) Robotic taxonomic key categorization, which divides bio-hybrid actuators into four main elements. Adapted with permission from [14].

bio-robots, such as muscle-powered devices. Other approaches for categorizing existing bio-hybrid systems is the so-called robotic taxonomic key (RTK)[14]. The RTK divides each system into four key elements: i) structure, ii) actuation, iii) sensing, and iv) control (Figure 1.2C). Each of these elements can be either organic, hybrid or synthetic, and the final result offers a visual and convenient method for categorizing bio-hybrid robots. While both of these types of categorizations are valid, there is still lack of consensus in the literature regarding the proper nomenclature, or even what can be considered a bio-hybrid device. This introduction, however, does not aim at classifying the devices reported in the literature, but rather reviewing the type of biological integration at different length scales from a simpler point of view: from biomolecules at the nano- and microscale, single cells at the microscale, to eventually multi-cellular tissues at the macroscale.

Hybrid machines at the nanoscale

At the nanoscale, hybrid machines can be found in self-propelled nanoparticles that move by enhanced diffusion. These particles, also called nanomotors or nanoswimmers, found their earliest inspiration in the active transport in cells conducted by molecular motors[15]. Kinesins or myosins, for instance, are superfamilies of proteins known as motor proteins that can be found in eukaryotic cells and can generate forces by the hydrolyzation of adenosine triphosphate (ATP) to form adenosine diphosphate (ADP). Thanks to this, kinesins are able to move along microtubule filaments to support cellular functions and certain myosins are responsible for muscle contraction by sliding in actin filaments. This conversion of chemical energy into mechanical work, highly optimized through natural evolution, gave inspiration for the creation of nano- and micromotors that could move based on the same principles. One of the pioneer works was in 2002 by Whitesides *et al.*, who presented milimiter-sized hemicylindrical plates that could self-propel by the decomposition of hydrogen peroxide by a Pt layer[16]. However, the first example of a motor at the nanoscale based on calalytic reactions was demonstrated in 2004 by Paxton *et al.*, who used bimetallic Pt-Au nano-rods to produce motion thanks to the same decomposition of hydrogen peroxide by Pt[17]. Shortly after, Fournier-Bidoz *et al.* also presented Ni/Au nanomotors based on catalytic reactions, but this time peroxide decomposition was achieve in the Ni part[18]. Since then, nanomotors with a wide variety of sizes and geometries have been demonstrated, for the most part based on chemical reactions catalyzed by different metals, finding their most interesting applications in fundamental physics[19, 20] or environment applications[21, 22].

The first bio-hybrid swimmer based on enzymes was also millimeter-sized. Mano and Heller designed and fabricated a bioelectrochemical system composed of a carbon fiber with two enzymes at each side, glucose oxidase (GOx) and bilirubin oxidase (BOD), which resulted in a net power-generating reaction that could propel the fiber on a water-air interface[23]. Later on, Pantarotto *et al.* fabricated the first nanomotor based on the tandem reaction of GOx and catalase that could move by the catalytic conversion of glucose into D-glucono-1,5-lactone and hydrogen peroxide by GOx and the subsequent decomposition of hydrogen peroxide by catalase[24]. However, several issues affected the motion of these enzyme-based motors, such as movement only taking place at the air-liquid interface in the first case or the need of a continuous flow of pure oxygen to ensure the activity of GOx in the second case. Afterwards, research towards the development of more energy efficient, versatile and biocompatible hybrid nanomachines based on enzymes increased exponentially[11, 25–27].

The combinations of enzymes, geometries, sizes and motion mechanisms are virtually endless[11] (Figure 1.3). Regarding size, smaller hybrid nanomotors based on the half-functionalization of silica

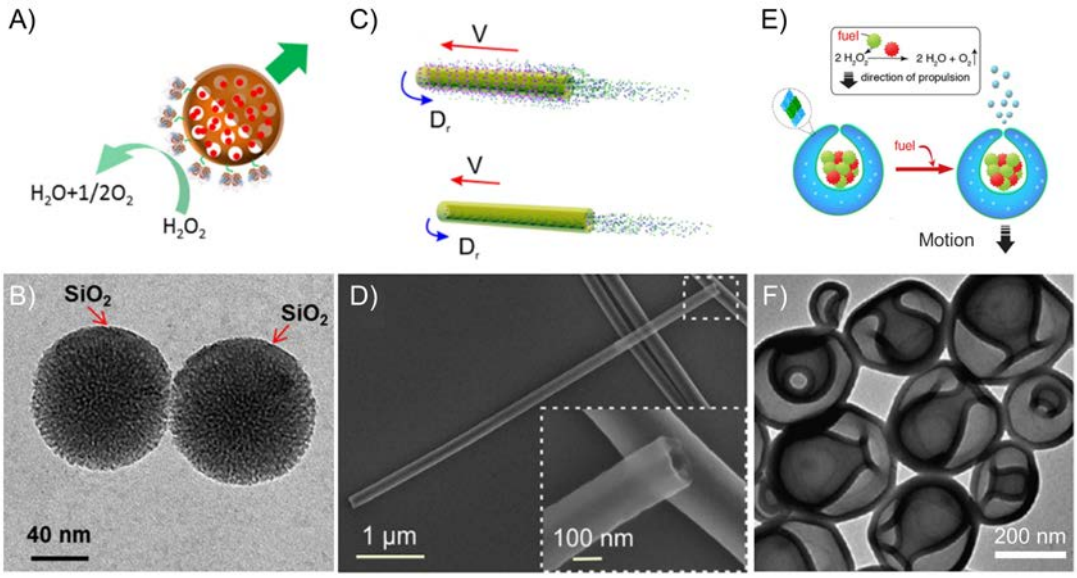

Figure 1.3: Bio-hybrid nanomotors powered by enzymatic reactions. A) Schematic of the structure and working mechanism of a bio-catalytic Janus mesoporous silica nanomotor. Adapted with permission from [28]. B) Transmission electron microscope (TEM) image of the mesoporous silica nanoparticles that compose such motor. Adapted with permission from [28]. C) Schematic representation of the motion of urease-powered nanotubes depending on enzyme localization: inside and outside (up) or only inside (bottom). Adapted with permission from [27]. D) Scanning electron microscope (SEM) image of the silica nanotubes. Adapted with permission from [27]. E) Schematic representation of the structure and working mechanism of a polymeric stomatocyte nanomotor with multiple enzymes encapsulated in its interior and working *via* cascade decomposition of glucose and hydrogen peroxide by GOx and catalase. Adapted with permission from [31]. F) TEM image of a group of polymeric stomatocytes used to fabricate this nanomotor. Adapted with permission from [31].

nanoparticles of 90 nm with catalase (creating the so-called Janus particles) can achieve motion by enhanced diffusion (Figure 1.3A and B)[28], while on the other end, hollow silica microparticles of 2 μm of diameter heterogeneously coated with urease can propel themselves with directionality[29]. Their geometries can range from spherical particles, as in the previous cases, to tubular shapes that can be propelled by bubble generation when their dimensions are micron-sized[26] or bubble-free propulsion if they are nanotubes (Figure 1.3C and D)[27]. A few different kinds of enzymes have also been employed. Ma *et al.* fabricated Janus nanomotors based on silica nanoparticles using three types of enzymes: urease, GOx and catalase[30]. Due to the induced asymmetry of the enzyme functionalization, all types of motors showed enhanced diffusion after the addition of their corresponding fuels, namely urea, glucose and hydrogen peroxide. Later, they proved the controllability of urease-powered nanomotors by the addition of urease inhibitors (Ag^{+} and Hg^{2+}) to stop the motion and dithiothreitol (DTT) to reactivate it by competitive binding[29]. Moreover, the deposition of a thin Fe layer allowed the guidance of these bio-hybrid nanomotors with magnetic fields. Other geometries and materials have also been studied, such as the polymeric stomatocytes by Abdelmohsen *et al.*, who encapsulated catalase and GOx enzymes inside them, achieving motion of these nanomotors while protecting the enzymes from the external influences of the media (Figure 1.3E and F)[31].

Most of the applications of hybrid nano- and micromotors have aimed at the development smart drug delivery systems[32]. For instance, enhanced diffusion of urease-based nanomotors can improve the efficiency of anti-cancer drugs in 2D and 3D cultures of bladder cancer cells by showing an increased internalization when the nanomotors are targeted to a transmembrane protein (Figure 1.4A and B)[33, 34]. Similarly, Ramos-Docampo *et al.* used polystyrene nanomotors functionalized with collagenase to improve the internalization on cell spheroids by the cleavage of collagen by the enzyme (Figure 1.4C)[35]. Moreover, they showed that calcium ions could be used as an activator, displaying

an enhanced internalization only when calcium was present (Figure 1.4D). Recently, GOx-catalase nanomotors triggered by near infrared light (NIR) were shown to improve drug delivery *in vitro* to cancer cells through synergistic photodynamic and starvation therapies[36].

However, before more studies can be carried out *in vivo*, biological barriers such as interstitial flow pressure, phagocytic sequestration or endosomal escape need to be investigated, as they pose challenges for the use of these devices in clinical trials[37]. For this purpose, approaches based on enzyme cascade reactions or compound systems with various functionalizations, such as peptides, antibodies or light-responsive moieties are being developed. For instance, Joseph *et al.* recently showed the fabrication and use of asymmetric polymerosomes with tandem GOx-catalase reactions that could follow gradients of glucose (Figure 1.4E and F). By performing *in vivo* studies, they found an almost 4-fold increase of nanomotor delivery through the blood brain barrier in rats[38]. Other systems based on chemotaxis, cascade reactions, compartmentalization, gatekeepers for *on-demand* release of drugs or particle functionalization with several moieties that fulfill different purposes, are being investigated to safely and efficiently use these devices as drug delivery methods [31, 39–45].

Despite all the advances in drug delivery applications, there is a growing need for a better understanding of the dynamics of this type of nanomotors, their interactions with complex media or their response to certain stimuli. For instance, the effects of salts or other molecules present in physiological fluids are not completely understood, as they could affect the reactions catalyzed by the enzymes, and thus their movement[33, 46]. Their motion in simple Newtonian fluids like water, although necessary to characterize and optimize their performance, is not an appropriate model of an *in vivo*

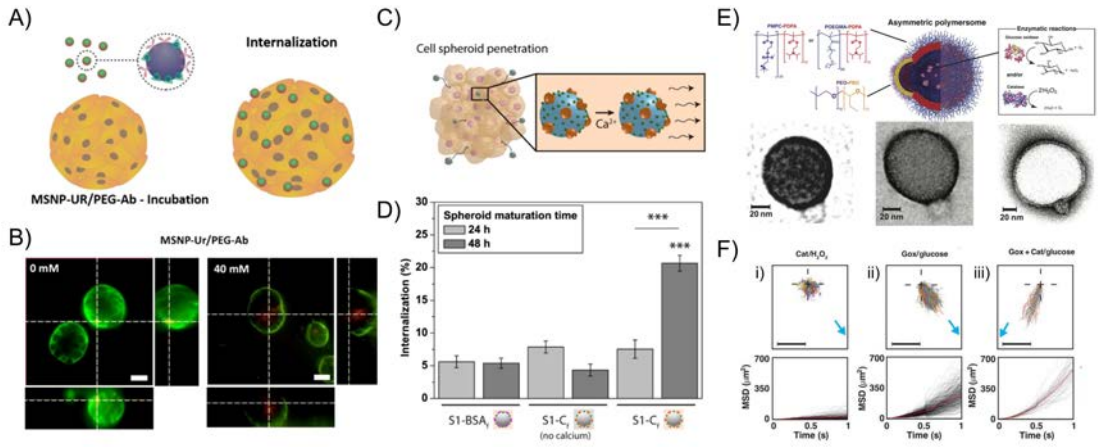

Figure 1.4: Applications of bio-hybrid nanomotors powered by enzymatic reactions. A) Schematic representation of an urease-powered silica nanomotor functionalized with antibodies for enhanced penetration in bladder cancer spheroids. Adapted with permission from [33]. B) Confocal fluorescence images of nanomotors incubated with spheroids at 0 mM and 40 mM of urea (scale bars are 50 μm). Green: targeted antigen (FGFR3); red: nanomotors. Adapted with permission from [33]. C) Schematic representation of the working mechanism of enhanced spheroid penetration of nanomotors by cleavage of collagen with collagenase attached to the surface of the particle and activated upon the presence of calcium ions. Adapted with permission from [38]. D) Percentage of internalization for control particles functionalized with bovine serum albumin (BSA), nanomotors without calcium and nanomotors with calcium after 24 h and 28 h of incubation, measured *via* confocal immunofluorescence. Adapted with permission from [35]. E) Schematic representation of an asymmetric polymerosome nanomotor propelled by the tandem reaction of GOx and catalase. Bottom images show characterizations of the polymerosome imaged under several types of staining targeting different polymers. Adapted with permission from [38]. F) Normalized trajectories and corresponding mean squared displacements (MSDs) of asymmetric polymerosomes (i) loaded with catalase and responding to a gradient of hydrogen peroxide, (ii) loaded with GOx and responding to a gradient of glucose, and (iii) loaded with GOx and catalase responding to a gradient of glucose. Adapted with permission from [38].

environment, since the nanomotors will need to interact with the crowded environment of tissues and cells, affecting their diffusion and biocatalytic reactions. More investigation of the motion of nanomotors in complex environments will be necessary to optimize their fabrication to move efficiently in biological fluids or protect them from adverse effects[47].

Hybrid machines at the microscale

At the microscale, Brownian fluctuations stop playing a fundamental role in motion of hybrid micromachines and viscosity becomes an essential aspect of their movement. As it was described by Purcell in 1977, motion in a fluid at the microscale, or low Reynolds number, is dominated by the viscous properties of the liquid and time-irreversible mechanisms are necessary to achieve net displacements[48]. Enzymatically propelled micromotors can move at this scale, as they have a continuous source of energy coming from bio-catalytic reactions. Although hybrid nanomotors are ideally more useful for drug delivery because of their size, their micron-sized counterparts can still find relevant applications in medical imaging through positron emission tomography (PET) or magnetic resonance imaging (MRI) techniques. For instance, Vilela *et al.* demonstrated that Au-coated micromotors with iodine isotope chemisorbed in the surface of Au could be tracked in a PET scan[49]. Although this micromotor was not propelled by enzymes, this study opened up the possibility of using enzyme-powered micromotors for enhanced detection of their position *in vivo* through computer tomography techniques during targeted drug delivery (Figure 1.5A and B).

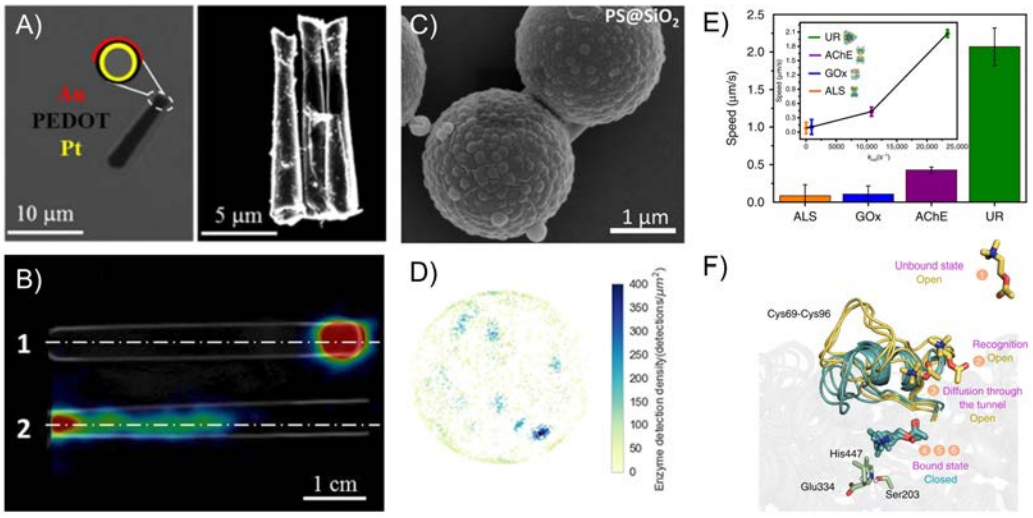

Figure 1.5: Applications of catalytic micromotors. A) Optical microscopy and SEM imaging of Au micromotors for medical imaging. Adapted with permission from [49]. B) Positron emission tomography in combination with computed tomography (PET-CT) image (longitudinal projection) of Au micromotors in two channels without (up) and with (down) their fuel, hydrogen peroxide, showing the enhanced diffusion and tracking of these motors. Adapted with permission from [49]. C) SEM image of silica microparticles used to fabricate urease-powered micromotors. Adapted with permission from [50]. D) 3D reconstruction of enzyme distribution on the surface of silica microparticles detected by stochastically optical reconstruction microscopy (STORM), showing a patchy-like distribution. Adapted with permission from [50]. E) Average speed of bio-hybrid micromotors based on hollow silica microparticles depending on the enzyme used as biocatalytic engine. Inset shows the correlation of the speed with the catalytic rate of the enzyme. Adapted with permission from [51]. F) Representation of the binding mechanism of acetylcholine on acetylcholinesterase *via* molecular dynamics simulations. Adapted with permission from [51].

Besides their applications in bio-medicine, bio-hybrid micromotors are also crucial in fundamental applications trying to decipher their underlying mechanisms of motion, as their bigger size allows them to be characterized more easily. At the nanoscale, enzymatic nanomotors show enhanced diffusion, due to the effect of Brownian fluctuations but, at the microscale, it is possible to achieve directionality and ballistic motion, which can help in the extraction of parameters that characterize their movement[52]. It is generally assumed that an asymmetry in enzyme coverage, in the form of a Janus particle, is necessary for net motion to happen[28, 30, 53]. However, it was demonstrated using micron-sized urease-powered motors that full functionalization of a particle's surface with urease can result in active motion due to inhomogeneous or patchy-like coverage (Figure 1.5C and D)[50]. Motion analysis and optical tweezer measurements revealed that the amount of urease molecules needed to achieve motion displayed a minimum threshold below which only Brownian diffusion was observed. Intrinsic enzymatic properties can also affect the motion of the hybrid micromotors. Arqué *et al.* studied the catalytic rate and conformation changes during catalysis to understand their contribution to active motion through optical recordings and molecular dynamic simulations, using four different enzymes: urease, acetylcholinesterase, GOx, and aldolase[51]. It was found that high catalytic activity was crucial for efficient motion and that conformational dynamics were required for certain bio-catalyses to take place (Figure 1.5E and F). Furthermore, the study of enzyme-powered microparticles in ionic solutions helped determine the role of ionic species and Debye length in motion and to extrapolate these results into nanomotors with numerical simulations[46]. Therefore, enzymatic motors at the microscale pose interesting examples of active matter systems and are relevant tools in fundamental research aiming at understanding their intricate motion mechanisms.

Beyond enzymatic micromotors, we can find at the microscale further examples of biological motility or activity in microorganisms. Some single cells have developed sophisticated mechanisms to achieve motion at low Reynolds number with time-irreversible strokes. For example, bacterial species, such as *E. coli*, *S. marcescens* or magnetotactic bacteria, sperm cells or even strains of protozoa or algae can generate forces for motion thanks to flagella or cilia differently distributed along their bodies[12, 54, 55]. The incorporation of these single-cell organisms by their entrapment in microtubes or their attachment to microparticles leads to the fabrication of bio-hybrid micro-swimmers that use the motion capabilities of these cells for their advantage (Figure 1.6). The use of these organisms also entail other types of benefits, such as their ease of acquisition, their survival under rough environmental conditions, like high temperature or acidic pH, and the requirement of low amount of simple nutrients, like glucose, for their survival[12]. Moreover, secondary control mechanisms, such as magnetotaxis, chemotaxis, galvanotaxis, phototaxis, thermotaxis or aerotaxis can be used to direct the motion of these types of hybrid robots towards specific directions[10, 56]. Different types of applications have been envisioned, ranging from drug delivery systems[55, 57, 58] and fertilization methods[59] to bacteria biofilm removal[60] and micro-scale manipulation[61–63].

The use of spermatozoa can result in interesting applications in artificial fertilization techniques, as well as in fundamental aspects of the motion of this single-cell organisms. For instance, a bio-hybrid sperm-bot was fabricated by Magdanz *et al.* by encapsulating sperm cells in a rolled-up microtube consisting of Ti and iron that could be controlled *via* magnetic fields, offering a promising system for alternative fertilization methods[54]. Likewise, in another publication, sperm cells were trapped into micro-tubes and their motion in simulated viscoelastic oviduct fluid was demonstrated, as well as their guidance using magnetic fields (Figure 1.6A)[59]. Moreover, the heads of dead sperm cells were coated with magnetic nanoparticles and stimulated with rotating magnetic fields, simulating the rotatory motion of the sperm's flagella. The authors studied the propagation of waves of magnetically actuated sperm cells and compared their thrust forces and speed with alive cells, providing insights into the efficient motion of spermatozoa at low Reynolds number[64].

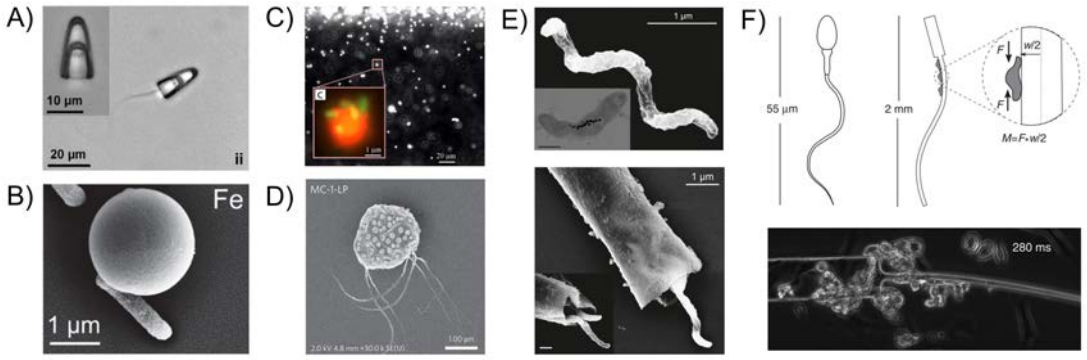

Figure 1.6: Bio-hybrid microrobots based on single cells. A) Optical microscopy image of a sperm-driven microrobot with a streamlined cap design. Adapted with permission from [59]. B) SEM image of a bio-hybrid microrobot based on *E. coli*. The bacterium attaches preferentially to the metallic Fe surface of the micro-particle, deposited by e-beam. Adapted with permission from [65]. C) Fluorescent image of a swarm of bacteria-based microswimmers moving by chemotaxis towards the upper side of the image. Inset shows a fluorescently labeled image of a microswimmer, composed of a polystyrene bead and several *S. marcescens* attached in random positions. Adapted with permission from [66]. D) SEM image of a magneto-aerotactic bacterium loaded with nano-liposomes to target tumor hypoxic regions. Adapted with permission from [67]. E) (Top) SEM image of a non-pathogenic magnetotactic bacterium *Magnetosopirrillum gryphiswalense* (MSR-1), with an inset of TEM image showing the distribution of the internal magnetosome. (Bottom) SEM image of a MSR-1 bacterium captured within a micro-tube, forming a bio-hybrid micromotor. Adapted with permission from [60]. D) Schematic representation of a bio-hybrid swimmer able to move at low Reynolds number due to the contractions of cardiomyocyte cells. A drawing of a real sperm cell (left) is compared with the micro-robot (right), showing the position of attachment of the cardiac cells. On the bottom, an optical microscopy image shows cardiac cells attached to the portion close to the head, where they are able to move the flagellum. Adapted with permission from [68].

Generally, bacterial organisms have been used to propel beads[66, 69, 70], microtubes[60] or even micro-gears to convert their chemical energy into mechanical work[62, 63]. As bacteria is attracted to metal surfaces, the integration of these organisms with metallic microparticles are in general straightforward. Stanton *et al.* demonstrated the fabrication of bio-hybrid Janus micro-swimmers driven by *E. coli*, using e-beam deposition to cover half of the surface of polystyrene microparticles with Ti, Au, Fe or Pt (Figure 1.6B)[65]. Single bacteria readily attached themselves to the metallic surface of the particles and transported them with magnetic field guidance. Later, Singh *et al.* developed an engineered method to improve the adhesion of these cells into microparticles by biotin-streptavidin linkages to create Janus-like hybrid particles, greatly improving the stability of the attachment when compared to Au, Pt or glycol monolayers[71]. The increasing engineering complexity of these bio-hybrid systems has led to the development of multifunctional bacteria-driven microswimmers with embedded magnetic nanoparticles that could deliver an anti-cancer drug to cancerous cells *in vitro* with magnetic guidance, being proposed as the next generation of *in vivo* targeted drug delivery systems[57].

The collective motion of multiple bacteria or bio-hybrid swimmers has also been investigated. Zhuang *et al.* studied the chemotactic drift towards L-serine of thousands of hybrid swimmers driven by multiple bacteria in microfluidic channels (Figure 1.6C)[66]. Likewise, green-fluorescent-protein-(GFP)-expressing *E. coli* were attached to spherical and disk-shaped micro-particles and showed chemotaxis towards L-aspartic acid[72]. Another type of bacteria, *S. typhimurium* was used in a bio-hybrid device to investigate the effects of a chemo-repellent, $NiSO_4$[73]. Other control mechanisms, such as pH-taxis, which could be useful in cancer treatment applications, have also been demonstrated[74]. Likewise, magneto-aerotactic bacteria have already transported drug-loaded liposomes into hypoxic regions of tumors in mice (Figure 1.6D)[67]. All of these examples prove the great versatility of these hybrid bacterial systems thanks to their environmental control methods, the possibility of genetically

modifying them or the encapsulation of drugs, which could be exploited for targeted therapeutics[75]. However, several challenges, such as the toxicity of the bacterial cells, immune responses or the loss of engineered behavior are major concerns to be investigated and that might need response in a one-by-one basis. Nonetheless, several solutions, such as the use of the human microbiota or the tools offered by synthetic biology to delicately engineer bacteria strands, have been proposed[75].

Magnetotactic bacteria are a particular kind of organisms that can achieve high swimming speeds and synthesize a chain of nanoparticles called magnetosomes, made of Fe_3O_4 crystals, that allow them to align to the Earth's magnetic field[76]. Unlike many of the previous cases, which used artificial materials with magnetic properties to guide the direction of the bio-hybrid robot, this type of bacteria can be used as both the propulsion system and steering system, and have been proposed for MRI tracking in drug delivery applications[76]. Other promising applications include biofilm removal, since these colonies are generally difficult to eliminate and resistant to antibiotic treatment, requiring more targeted approaches[60]. On this regard, Stanton *et al.* used magnetotactic bacteria to effectively target and reduce *E. coli* biofilms by releasing an antibiotic triggered by the acidic environment of the biofilm itself (Figure 1.6E)[60].

Flagellar motion cannot only be achieved with organisms that have that kind of power source. With a biomimetic approach, Williams *et al.* fabricated a synthetic flagellar swimmer operating at low Reynolds number[68]. This swimmer was made of polydimethylsiloxane (PDMS) filaments attached to a short, rigid head, resembling a sperm cell (Figure 1.6F). In order to obtain an autonomous power source, they used single cardiomyocytes, the contractile cells that make up heart muscle tissue. By selectively functionalizing different parts of the swimmer, cardiac cells were attached to the region near the head, producing sufficient power strokes that lead to powerful tail thrusts. These contractile cells, which contract spontaneously and synchronize with each other, generated motion of the bio-hybrid swimmer at ~ 10 μm/s.

Motion at the microscale can be difficult to achieve artificially due to the strong influence of viscous forces over inertial forces. However, in bio-hybrid cell-based robots, this issue can be less critical due to the use of the propelling mechanisms of bacteria or sperm cells. In these cases, most of the obstacles reside in their efficient assembly, their precise control and their potential toxicity for *in vivo* applications. The field of enzymatically powered motors at the microscale, on the other hand, faces several challenges regarding the description of their dynamics. Although research in bio-hybrid motors at the nanoscale is primarily focused on biomedical applications and their challenges revolve around their interaction with complex environments, micromotors are still lacking a complete description of their motion mechanisms, despite their relatively easier characterization due to their size. Further research should focus on the generalization of the governing equations to embrace the complex motion that might arise from the increasing number of enzymatic micromotors being developed. Thus, with better tools for a full and precise characterization, their underlying mechanisms could be more easily understood.

Hybrid machines at the macroscale

At the macroscale, ranging from hundred of μm to several cm, the field bio-hybrid robotics has taken advantage of whole tissues to produce fully functional hybrid machines with outstanding characteristics adopted from biological systems. As it was briefly mentioned at the beginning, biomimetics has led to the creation of humanoid robots that can replicate many biological functions and ranges of movement. However, the performance of these machines is still far from the efficiency of natural

systems, despite all the great efforts through biologically inspired engineering[77]. In classic robotics, simple tasks for animals, such as the handling of fragile objects or moving through irregular or unknown terrains, remain difficult to achieve due to the rigidity of the materials used. Especially when these robots need to be used for human interaction or for medical operations, finding soft materials that can be integrated in these systems has become an important area of research[78]. Soft robotics aims at exploiting, in a biomimetic way, the types of structures found in non-skeletal parts of animals or marine organisms, such as the tentacles of squids[79], the muscle tissue of mammals[80] or the trunks of elephants[81].

In particular, the replication of muscles has become one of the most important challenges in soft robotics, as they are a crucial component of the musculoskeletal system that allows animals to move with extreme sensitivity. Material science research has lead to the creation of different types of soft polymers that can be used as actuators that attempt to replicate muscle contraction. Electroactive polymers (EAPs), for instance, are electrically activated soft actuators that could have potential in the development of muscle-like actuators thanks to their capabilities of converting electrical energy into mechanical energy[77, 82]. EAPs can be divided according to their actuation method into ionic EAPs, driven by the mobility of ions, or electronic EAPs, driven by Coulomb interactions or electric fields[82], and many developments have been achieved in both types of actuators[83, 84]. However, several limiting factors, such as their electrochemical performance, the need of pre-stretching or the high voltages typically required for actuation, hinder their universal applicability in soft robots[82–84]. Pneumatically driven actuators, or PAMs, are also among the most highly researched biomimetic actuators. Martinez *et al.* developed robotic tentacles that could grasp objects in different ways using this kind of soft actuators, and even embedded a video camera in them[81]. Fully soft and pneumatically driven robots[85, 86] or their combination with hard parts[87] have also appeared as interesting examples towards applications in search and rescue missions. As classical materials for soft actuators reach their limitations, other types of actuation, such as hydraulic[88] or based on shape-memory alloys[89, 90] are starting to appear. Fully autonomous soft robots, however, are still far from being as efficient as animals, as electronic components or power sources are usually hard and heavy, and stretchable electronics, flexible sensors or complex control systems might be required[91, 92]. Wehner *et al.* presented a fully untethered and autonomous robot made of soft materials, called 'octobot', that could move its tentacles thanks to microfluidic logic based on catalytic decomposition of hydrogen peroxide[79]. Despite its simple mode of actuation (raising and lowering its tentacles), this integrated design with all the necessary components for autonomous actuation might make it the foundation for the next generation of fully soft and autonomous robots.

It is not surprising to think that, due to great limitations of current muscle actuators, bio-hybrid devices have focused on the integration of muscle tissue from different sources into small robotic systems. The majority of bio-hybrid robots in the literature have used muscle from mammalian sources, either cardiac or skeletal. However, contractile cells isolated from insects, although they might be less researched or more difficult to manipulate, provide great advantages[14]. Invertebrate cells, in particular dorsal vessel (DV) tissues, are environmentally robust to extreme temperatures, pH conditions or pressures, metabolically adaptable and relatively autonomous[96]. Akiyama *et al.* fabricated a bio-hybrid robot from extracted DVs from the moth *Thysanoplusia intermixta* that was able to move due to friction differences between contractions and relaxation and achieved speeds of ~ 500 μm/s after the addition of a neuroactive chemical that increased its contraction frequency (Figure 1.7A and B)[93]. Previously, the same group already demonstrated the feasibility of using cultures of insect cells without temperature control that resulted in spontaneously contracting tissue[97] and later presented a long-term and room temperature hybrid bio-actuator from DV of the lepidoptera larva *Ctenoplusia agnata*, using micropillars that could measure their force and kept working at room

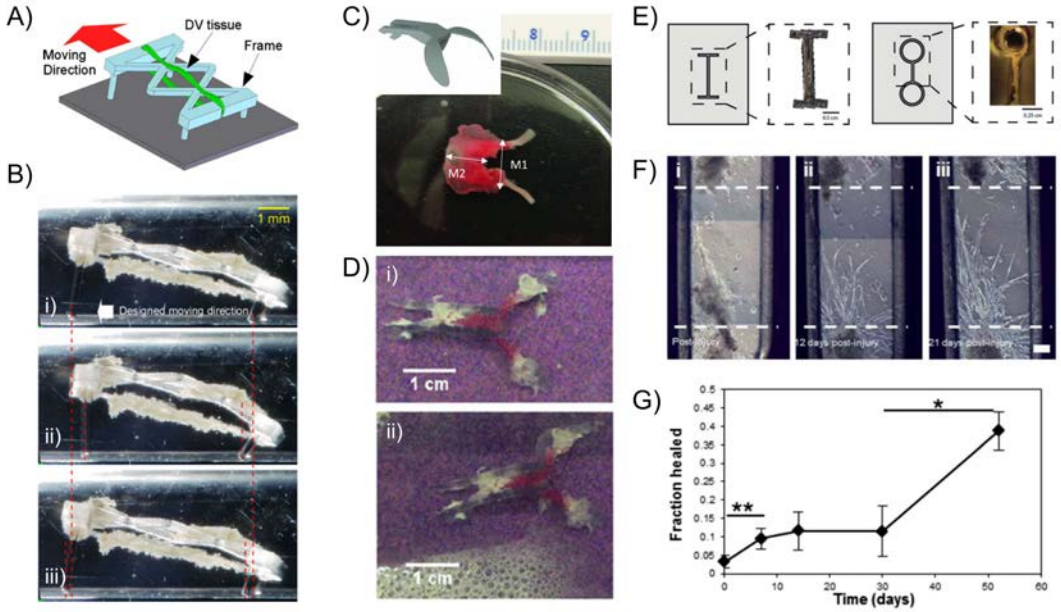

Figure 1.7: Insect-powered bio-hybrid robots. A) Schematic illustration of an insect-muscle-powered robot, based on differential friction during contraction and relaxation. Adapted with permission from [93]. B) Optical microscopy images of such robot (i) before, (ii) during, and (iii) after contraction. Adapted with permission from [93]. C) Bio-hybrid robot based on isolated muscle from the sea slug *Aplysia californica*. Inset shows a rendering 3D image of the robot. Adapted with permission from [94]. D) Images of the bio-hybrid robot (i) before and (ii) two minutes of electrical stimulation. Adapted with permission from [94]. E) Two examples of seeding chambers for the self-assembly of bio-hybrid actuators based on insect muscle. Adapted with permission from [95]. F) Self-healing of the insect tissue at (i) 0, (ii) 12, and (iii) 21 days post injury. Adapted with permission from [95]. G) Fraction of healed tissue over time, showing also the long-term survival capabilities of the bio-robot. Adapted with permission from [95].

temperature for more than 90 days without medium change[98]. The use of chemicals for regulation of contractile response of DV tissue with several neuropeptides was also proved[99] and, recently, Tanaka *et al.* demonstrated the fabrication of a bio-hybrid pump powered by earthworm muscle, chemically modulated by the addition of acetylcholine, although with a slow response time of 42 s[100]. Moreover, Webster *et al.* fabricated a 3D-printed bio-hybrid robot capable of crawling at speeds of $\sim$ 80 μm/s (Figure 1.7C and D)[94]. Isolation, optimization of culture conditions and cryopreservation of embryonic muscle cells from tobacco hornworm *Manduca sexta* larvae was studied by Baryshyah *et al.* (Figure 1.7E), demonstrating the expression of contractile proteins like myosin heavy chain and the presence of sarcomeric structures[96]. This study provided significant advances towards the development of established methods to culture, cryopreservation and differentiation embryonic myoblasts from insects, although there is still need a for scalability of the approaches to achieve extended use of DV tissue in bio-hybrid robotics. Nonetheless, later on, they demonstrated the fabrication of a 3D bio-actuator that could self-repair (Figure 1.7F), survive for months without medium changes (Figure 1.7G) and that was tolerant to different temperature and pH conditions, producing stresses of 2 kPa, which are comparable to those reported for skeletal muscle bio-robots[101].

Early approaches of cardiac-based bio-hybrid devices consisted on polymeric cantilevers that could be deflected by the contractions of seeded cardiomyocyte cells and could also be used to measure their forces[105, 106]. Parallelly, Xi *et al.* and Kim *et al.* reported the fabrication of untethered bio-hybrid robots of 3 legs (Figure 1.8A)[102] and 6 legs (Figure 1.8B)[103], respectively, that could move due to friction differences. The 3-legged bio-robot could achieve speeds of 38 μm/s while the 6-legged bio-robot could move at estimated speeds of 87 μm/s. Likewise, Feinberg *et al.* fabricated and char-

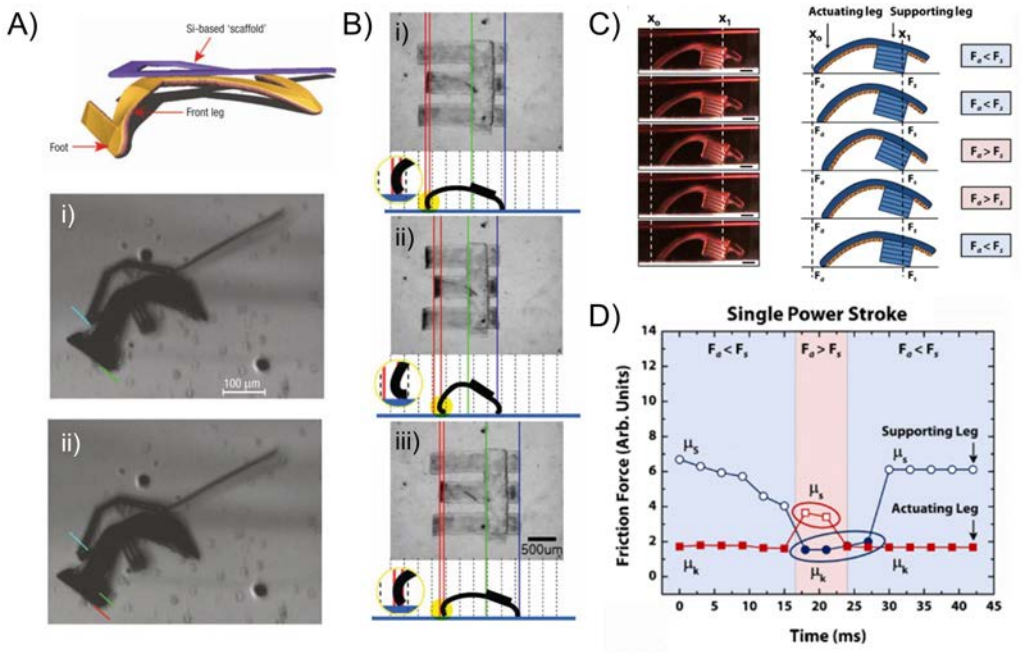

Figure 1.8: Bio-hybrid crawling robots based on cardiac muscle tissue. A) 3D representation of the skeleton of a 3-legged bio-hybrid robot based on cardiomyocytes. The bottom images show optical microscopy snapshots of such device (i) before and (ii) after contraction of the leg. Adapted with permission from [102]. B) Sequential images and motion mechanism of a 6-legged bio-hybrid robot based on cardiomyocytes (i) before, (ii) during, and (iii) after contraction. Adapted with permission from [103]. C) Snapshots and motion mechanism due to friction of a bio-hybrid robot based on a thin film of cardiomyocytes. Adapted with permission from [104]. D) Plot of friction vs force of each one of the legs of the bio-bot (supporting and actuating), indicating that motion happens when the coefficient of static friction (μ_s) of the actuating leg is larger than the coefficient of kinetic friction (μ_k) of the supporting leg. Adapted with permission from [104].

acterized muscular thin films made of PDMS and functionalized with fibronectin for cardiomyocyte attachment[107]. This muscular thin films could adopt engineered 3D conformations like coils or helical shapes and they demonstrated the creation of a walker and a swimmer with the same method.

In the following years, more complex and engineered bio-robots based on cardiac muscle made appearance, although all of them built on the same principle of thin films. In 2012, Chan *et al.* developed a 3D-printed bio-bot, based on a poly(ethylene glycol) diacrylate (PEGDA) skeletons of different designs that could move at speeds of more than 200 μm/s (Figure 1.8C)[104]. Their bio-bot was composed of a hard base and a softer cantilever, seeded with a cardiac cell sheet, that could deflect this thin film and push the bio-bot forward by creating differences in friction during a power stroke (Figure 1.8D). Based on a similar design, Holley *et al.* fabricated cardiac-based swimming bio-robots that could self-stabilize upon external disturbances[108].

Two of the most complex examples of biomimetic and bio-hybrid reverse engineering are the cases of the tissue-engineered medusoid and stingray[109, 110]. To fabricate a reverse-engineered jellyfish, Nawroth *et al.* observed the propulsion and anatomy of jellyfishes and designed their own medusoid, using perfectly located and aligned cardiomyocytes on PDMS thin films that could replicate the stroke kinematics of a jellyfish (Figure 1.9A and B)[109]. By analyzing their motion and dynamics of the surrounding flow fields, they found that their medusoid achieved speeds of ~ 0.5 body lengths per stroke, within the range of actuation of natural jellyfish (Figure 1.9C). Later on, Park *et al.* recreated the body and motion of a stingray, using mold-casted PDMS structure and a microfabricated gold skeleton as flexible and rigid parts of the body (Figure 1.9D), respectively, followed

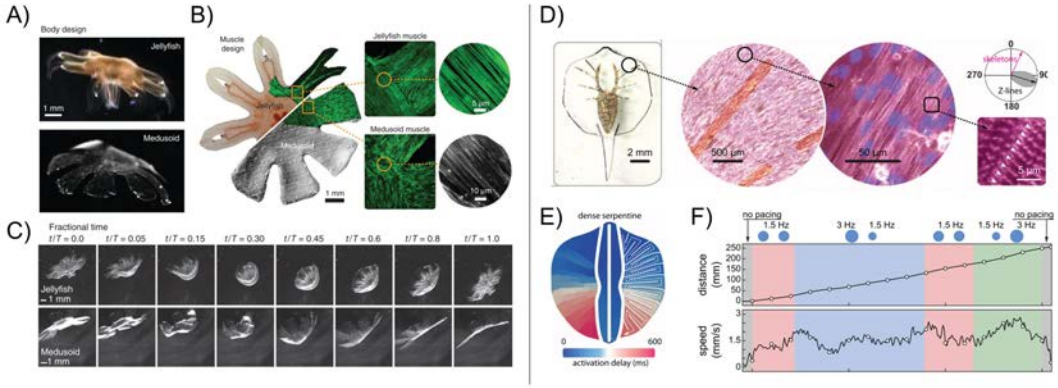

Figure 1.9: Bio-hybrid swimmers based on cardiac muscle tissue. A) Body designs of a jellyfish (top) and a bio-hybrid medusoid (bottom), made of a flexible PDMS thin film with seeded cardiomyocytes. Adapted with permission from [109]. B) Comparison of the muscular structure of a jellyfish and a bio-hybrid medusoid, showing the similarities between their muscle tissues. Adapted with permission from [109]. C) Snapshots corresponding of a time-lapse of a stroke cycle of a jellyfish (top) compared to a bio-hybrid medusoid (bottom) paced at 1 Hz, normalized to the duration of the stroke, T. Adapted with permission from [109]. D) Image of a bio-hybrid stingray made of a mold-casted PDMS structure stabilized with a gold skeleton and cardiomyocytes seeded on top. Right-hand images were immunostained for sarcomeric α-actinin (red) and cell nuclei (blue), revealing its sarcomeric structures. Adapted with permission from [110]. E) A dense serpentine pattern of fibronectin was used to guide the attachment of cardiac cells and engineer a wave propagation pattern that simulated the deflection of a stingray's fins. Adapted with permission from [110]. F) Kinematic analysis of the distance travelled and speed of a bio-hybrid stingray upon different types of optical stimulation. Adapted with permission from [110].

by a serpentine-patterned attachment of cardiomyocytes. This serpentine pattern was a key element to achieve the undulatory motion of a sting-ray fins by delayed propagation of the contraction waves (Figure 1.9E). Moreover, they genetically modified the cardiac cells to respond and contract to blue light on demand, achieving steering and speed control reaching almost 3 mm/s (Figure 1.9F)[110].

Bio-hybrid systems actuated by cardiomyocytes have also been used to measure contractile forces, with possible applications in regenerative medicine and pharmacological testing[105, 111–113]. Lind *et al.* fabricated a completely 3D-printed microphysiological device based on a thin film of seeded rat cardiomyocytes that could measure differences in stresses after the addition of drugs like the L-type calcium channel blocker verapamil and the β-adregenic agonist isoproterenol[114]. Using multi-material 3D printing, they printed on the same process: the base PDMS layer, strain gauge wires made of a thermoplastic polyurethane ink loaded with carbon black nanoparticles (CB:TPU), tissue guiding microfilaments, electrical and contact pads with a polyamide ink filled with Ag nanoparticles (Ag:PA) and finally, PDMS wells and insulation. The deflections of the cardiomyocyte-seeded thin film upon contractions could be measured thanks to the piezoresistive properties of the CB:TPU ink, obtaining direct measurements of the stresses generated.

Skeletal muscle is currently the most used tissue for bio-hybrid engineering due to its controllability and adaptability[10]. Although it is generally weaker than cardiac tissue, skeletal muscle poses several advantages that benefit its use. Unlike cardiomyocytes, skeletal muscle is inherently three-dimensional, making it easier to engineer in different structures, without relying in thin film architectures. Moreover, except during differentiation or myogenesis, spontaneous contractions are scarce and electrical, optical or neural stimulation are needed to activate the tissue, resulting in a higher level of on/off control. Bio-hybrid actuators that biomimic the muscle-tendon unit (MTU) of the musculoskeletal system of mammals have been fabricated as a possible alternative to hard or soft robotic grippers that do not possess the sensitivity and control of native muscle tissue[10]. Hereof, Morimoto

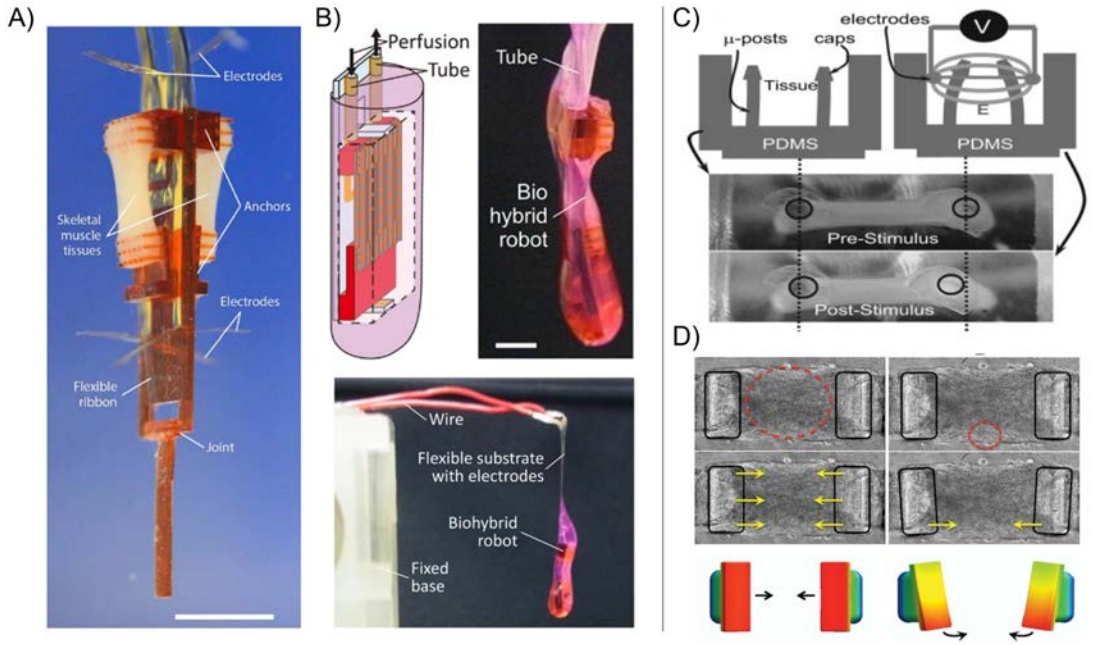

Figure 1.10: Bio-hybrid actuators based on skeletal muscle tissue. A) Image of a bio-hybrid actuator based on an antagonistic pair of skeletal muscle tissues. Scale bar: 5 mm. Adapted with permission from [115]. B) Schematic representation and real images of a bio-hybrid actuator covered with a collagen structure for actuation in air. Perfusion tubes allow the flow of culture media to the muscle tissue. Scale bar: 2 mm. Adapted with permission from [116]. C) Schematic representation of a bio-hybrid actuator based on skeletal muscle tissue used as a drug screening platform. Two PDMS micro-posts are deflected when the tissue is electrically stimulated, allowing to measure its force. Adapted with permission from [117]. D) Optical microscopy images of optogenetic skeletal muscle micro-tissues moving two posts when optical stimulation is applied globally (left) and locally (right). Adapted with permission from [118].

et al. fabricated a bio-hybrid actuator based on an antagonistic pair of skeletal muscle tissues[115]. Their device, which resembled a human finger with extended degrees of motion, could be bent in opposite directions by the selective alternative contraction of the adjacent muscles thanks to external gold electrodes located at a close distance (Figure 1.10A). The skeletal muscle tissues, extracted from neonatal rats, could achieve forces of tens of mN for up to 20 days and they proved the possibility of object manipulation using one or several of these bio-hybrid devices[115]. Recently, the same group presented a similar bio-hybrid actuator that could be operated in air by being encapsulated in a collagen matrix with a perfusion system to maintain the necessary humidity conditions (Figure 1.10B)[116]. Although the range of movement was decreased when compared to the previous version of the bio-actuator, these results entail a step forward towards muscle-based bio-actuators that could potentially replace actuators in soft robots, while enduring changes in environmental conditions.

Simpler bio-actuators based on skeletal muscle tissue can be useful for fundamental research in tissue development, bioengineering of relevant tissue models to study diseases, regenerative medicine or drug screening. Most of these tethered bio-actuators are composed of a set of soft cantilevers surrounded by a tissue ring that can bend them upon induced contractions, and can be used with both cardiac[113, 119] or skeletal muscle tissue[117, 118]. Vandenburgh *et al.* used microposts to measure the force of murine micro-tissues upon the addition of several drugs, such as insulin-like growth factor 1 (IGF-1) and atorvastatin (Figure 1.10C)[117]. Later, Sakar *et al.* employed optogenetically modified skeletal muscle cells to prove the local control of the contractions by applying concentrated light pulses (Figure 1.10D), also with potential applications as a drug screening platform[118]. However, for these biomedical applications, the use of human-derived myoblasts, instead of murine cells, as in the previous cases, is preferred. On this subject, some three-dimensional studies of tissue engi-

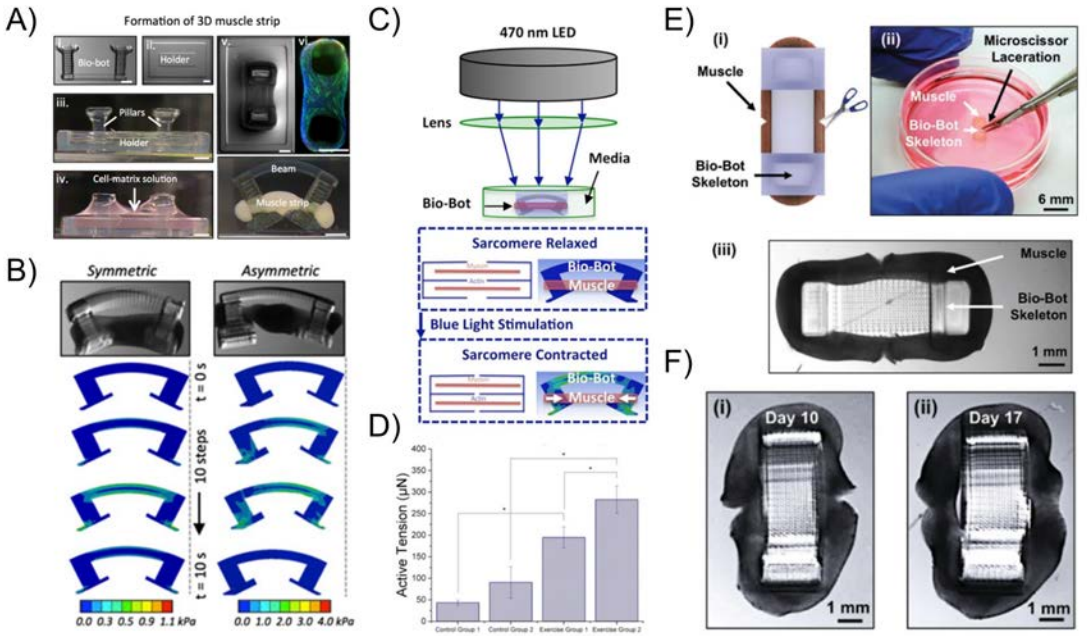

Figure 1.11: Bio-hybrid crawling robots (bio-bots) based on skeletal muscle tissue. A) Images representing the formation of bio-bot. (i) 3D-printed skeleton; (ii) its holder; (iii) side-view of the holder containing the bio-bot skeleton before and (iv) after the addition of the cell-laden hydrogel; (v) after several days the tissue compacts around the posts; (vi) immunostaining image of myosin heavy chain (green) and cell nuclei (blue). Adapted with permission from [123]. B) Comparison of the motion of a bio-bot with a symmetric skeleton and with an asymmetric one *via* finite element analysis (FEA) simulations, showing that only the asymmetric skeleton produces net motion. Adapted with permission from [123]. C) Schematic representation of the optical stimulation apparatus for blue light stimulation of optogenetic bio-bots. Adapted with permission from [101]. D) Active tension achieved by control and optical-mechanical exercising groups, showing the adaptability of the muscle tissue. Adapted with permission from [101]. E) Schematic representation (i) of the mechanical damage *via* laceration performed on the bio-bot's tissue and photographs (ii) showing the manual process and (iii) the final state of the bio-bot. Adapted with permission from [124]. F) After 10 (i) and 17 (ii) days, the muscle tissue has started to recover thanks to the addition of fresh myoblasts in the damaged area. Adapted with permission from [124].

neering of human cells have been performed, focusing on the effects of mechanical stimulation[120], cyclic preconditioning[121] or obtaining clinically relevant responses[122].

Untethered bio-hybrid robots based on skeletal muscle tissue have also received attention in the past years. Cvetkovic *et al.* fabricated a bio-bot using 3D printing techniques and 3D bio-engineering of muscle myoblasts. The bio-bot consisted of two T-shaped legs with a bridge structure joining both parts and could move with a crawling mechanism (Figure 1.11A). They optimized the stiffness of the material and analyzed the passive forces exerted by the tissue during myogenesis. Moreover, they compared the efficiency of symmetric and asymmetric bio-bots, both experimentally and through finite element analysis (FEA) simulations (Figure 1.11B), proving that an asymmetry is needed to produce differential friction coefficients that allowed the bio-bot to move at speeds reaching more than 150 μm/s[123]. Later on, Raman *et al.* used the same system with optogenetically modified cells that allowed them to control the bio-bots with blue light stimulation (Figure 1.11C). Furthermore, they took advantage of the versatility of this stimulation technique and analyzed the effects of short-term optical and mechanical exercising in the bio-bots performance, obtaining significant increments in force generation (Figure 1.11D)[101]. This study was able to prove the feasibility of one of the promised advantages of using skeletal muscle tissue in soft robotics, the adaptation to system requirements that can make the tissue increase or decrease its force output depending on the demands. Other long-sought aspects, such as self-healing, scalability or integration with neurons or

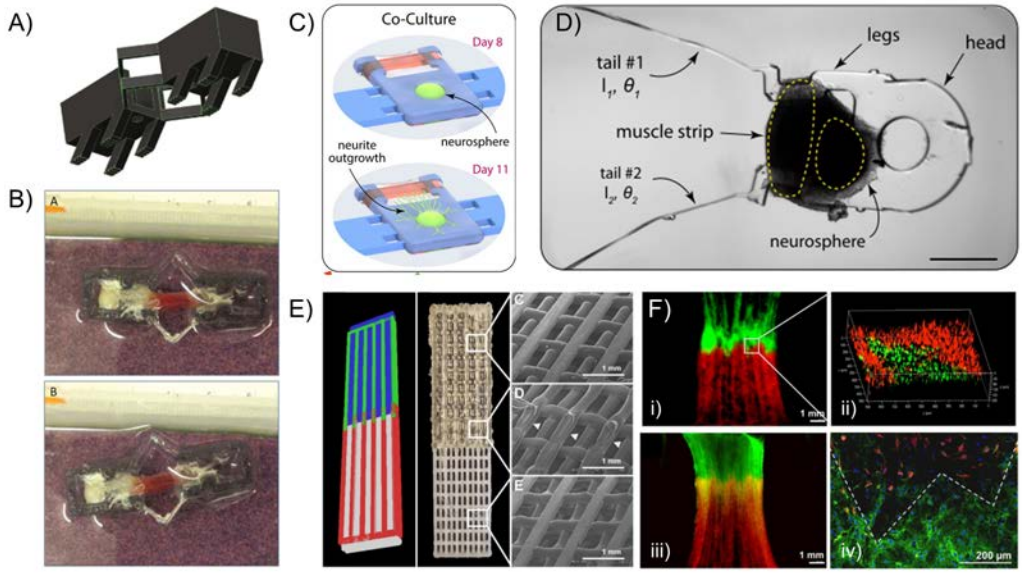

Figure 1.12: Multi-cellular approaches for bio-hybrid robotic systems. A) 3D model of the skeleton of an inchworm-like bio-hybrid robot powered by neuromuscular tissue. Adapted with permission from [128]. B) Characteristic locomotion example of the multi-cellular bio-hybrid robot after electrical/chemical stimulation, showing starting (A) and final (B) positions. Adapted with permission from [128]. C) Schematic representation of the co-culture of neurospheres with skeletal muscle tissue after 8 days of differentiation of the muscle, for the fabrication of a bio-hybrid swimmer. Normally, at day 11, neurite growth can be already observed. Adapted with permission from [129]. D) Optical microscopy image of the bio-hybrid swimmer after release from its anchors, indicating the position of the muscle tissue and the neurospheres, which are activated *via* optical stimulation to induce contractions and swimming motion. Adapted with permission from [129]. E) Schematic representation of the muscle tendon unit (MTU) construct and final aspect under SEM imaging. Green: polyurethane; red: polycaprolactone; blue: C2C12 myoblasts; red: NIH/3T3 fibroblasts. Adapted with permission from [130]. F) Fluorescently labeled MTU constructs after one (i, ii) and seven (iii, iv) days of culture, showing cell-cell interaction and movement. Green: C2C12 myoblasts; red: NIH/3T3 fibroblasts; yellow: interface region. Adapted with permission from [130]

embedded electronics were later proved by the group using the same type of system (Figure 1.11E and F)[124–127].

Most of the control mechanisms of hybrid bio-robots have been based on electrical stimulation, mimicking the effect of neuronal action potentials, or optical stimulation, through the optogenetic modification of cells to depolarize their membranes upon the presence of light. Multi-cellular approaches offer the possibility of stimulation with neurons, although these approaches pose a significant challenge in the fabrication of more complex and controllable bio-hybrid robots. Webster *et al.* employed neuromuscular tissue directly isolated from the sea slug *Aplysia californica* to power an inchworm-inspired bio-hybrid actuator[128]. The addition of carbamylcholine chloride, a drug that activates acetylcholine receptors, was used to induce neural stimulation, resulting in significantly larger muscle tension (Figure 1.12A and B). Recently, Aydin *et al.* presented a bio-hybrid swimmer based on skeletal muscle tissue in co-culture with neurospheres containing motor neurons[129]. The bio-swimmer could form functional neuromuscular junctions (NMJs) and optical stimulation of the neurospheres could, in turn, induce contractions in the muscle tissue (Figure 1.12C and D). Although the bio-hybrid swimmer did not attain very fast speeds compared to other examples in the literature due to the difficulty of motion at low Reynolds number, it represents the first bio-hybrid swimmer based on skeletal muscle in co-culture with motor neurons, which could offer scalability to bio-engineer larger and more efficient multi-cellular robots.

Other multi-cellular approaches have focused on engineering of tendon-like interfaces that better resemble the structure of native musculoskeletal tissue. Promising advances were carried out by Merceron *et al.*, who 3D-bioprinted an MTU made of a stiff part containing fibroblasts and a softer part with skeletal myoblasts (Figure 1.12E and F)[130]. This MTU showed high viability, appropriate tensile properties and expression of relevant genes in the muscle-tendon junction. This 3D-bioprinting approach could be further integrated in previously reported bio-hybrid devices to improve the force transfer efficiency[10]. Not only neurons and fibroblasts are relevant for the reproduction of native muscle. Endothelial cells, that form the vasculature, are also essential for the proper delivery of nutrients, specially in thick tissues. On this regard, 3D bioprinting has emerged as a viable tool for the biofabrication of complex multi-cellular tissue constructs and vascular networks based on sacrificial polymers that could give rise to the next generation of multi-cellular bio-hybrid robots[13, 131–136].

Bio-hybrid robotics powered by muscle cells is a very heterogeneous field with a wide range of possibilities, especially when multi-cellular approaches are starting to be investigated. Nevertheless, there is a lack of consensus in the community about the language and nomenclature of these systems[14], but also most of the reported bio-hybrid devices are rarely taken a step forward, particularly towards biomedical applications such as drug testing or muscle tissue modeling, where they might find their most straightforward adoption before they can be applied in full robotic systems. The rise of more scalable techniques, such as 3D bioprinting, could be a solution to some of the challenges, like reproducibility or a smooth multi-material integration, that might hinder their applications in biomedical research. Drug screening platforms, skeletal muscle or cardiac disease modeling could take advantage of a large part of the research carried out in bio-hybrid actuators and robotics, but communication between very multidisciplinary fields like soft robotics, tissue engineering, biomedicine or nanotechnology will be necessary to obtain more meaningful research.

Objectives

According to the presented scientific literature, the objectives of this thesis were set in order to tackle the key aspects and needs of the community, and are defined as follows:

(i) To study the motion of enzymatic nano- and micromotors with complex dynamics and in complex media, and improve their analysis, considering the limits and assumptions of current methods.

(ii) To evaluate the use of 3D bioprinting as a convenient tool to 3D bioengineer functional skeletal muscle tissue that resembles the native organization of this tissue, improving scalability and versatility of current fabrication approaches.

(iii) To fabricate 3D-printed bio-actuators based on skeletal muscle tissue that could be used as force measurement platforms and drug screening platforms and prove their feasibility with proof-of-concept studies related to tissue adaptability or drug testing.

(iv) To fabricate a fully functional untethered bio-robot based on skeletal muscle tissue that can compete with state-of-the-art examples.

(v) To investigate the addition of nanocomposites into bioengineered muscle tissue to enhance the performance of bio-robots.

In order to fulfill these objectives, this dissertation covers several aspects of bio-hybrid robots from the nanoscale to the macroscale. Firstly, in Chapter II, I investigate the motion of self-propelled particles at the nano- and microscale under complex motion dynamics. Due to the challenge of understanding of their underlying motion mechanisms, researchers on nano- and micromotors are in need of robust analysis tools and methods that allow them to study and compare their efficiency and dynamics. Therefore, in this chapter, I cover four case studies of both synthetic and bio-hybrid nano- and micromotors, analyze their motion and propose different approaches to tackle the complexity, either by a generalization of the typically used equations, the development of new descriptive formulas or by their motion in complex media using uncommon experimental techniques while considering their limitations.

Chapter III moves into hybrid bio-robots of larger length scales, from micrometers to millimeters. Here, I study and optimize the bioengineering of three-dimensional skeletal muscle tissue using 3D bioprinting for bio-hybrid robotic applications at the micro- and macroscale. I investigate the fabrication of functional and morphologically relevant skeletal muscle tissue, with particular emphasis in the material properties. Later, I present a novel and universal system based on co-axial 3D bioprinting for the fabrication of individual and controlled micro-tissues of skeletal muscle that resemble the bundle-like organization of native tissue, and could solve current challenges, like the limited diffusion of nutrients and oxygen in engineered muscle.

In Chapter IV, after mastering the fabrication technique, I demonstrate the versatility of the 3D bioprinting to fabricate tethered bio-hybrid actuators that can be used as force measurement and drug testing platforms. The first part deals with a multi-material fabrication approach to simultaneously, and in a single-step process, fabricate bio-hybrid actuators based on skeletal muscle tissue in a fast, versatile and of high-throughput manner. In the second part, the bio-actuator platform is optimized for the use with human-derived myoblasts, towards the development of relevant tissue models of young and aged human muscle. With this platform, I study the force generation and contraction kinetics of these two types of models and perform a proof-of-concept study of the effects of a cosmetic drug in development.

Finally, Chapter V culminates by merging all the previously acquired knowledge in the fabrication of biological actuators to create a bio-hybrid swimmer and a nanocomposite bio-hybrid crawler with enhanced efficiency due to the piezoelectric effect of embedded nanotubes. The first swimmer represents the fastest skeletal-muscle-based bio-hybrid swimmer up to date and one of the fastest ones considering cardiac-based robots. The second bio-robot paves the way towards the use of nanocomposites to enhance the performance of these actuators by successfully integrating piezoelectric nanotubes in the muscle tissue.

References

[1] M. E. Moran, *The da Vinci robot,* Journal of Endourology **20**, 986 (2006).

[2] B. Bhushan, *Biomimetics: Lessons from Nature - an overview,* Philosophical Transactions of the Royal Society A: Mathematical, Physical and Engineering Sciences **367**, 1445 (2009).

[3] S. L. Burg and A. J. Parnell, *Self-assembling structural colour in nature,* Journal of Physics Condensed Matter **30** (2018), 10.1088/1361-648X/aadc95.

[4] V. Gabara, *High-Performance Fibers,* in *Ullmann's Encyclopedia of Industrial Chemistry*

(Wiley-VCH Verlag GmbH & Co. KGaA, Weinheim, Germany, 2016) pp. 1–22.

[5] Biomimicry Institute, *The Biomimicry Institute - Examples of nature-inspired sustainable design,* (2019).

[6] M. Cianchetti, C. Laschi, A. Menciassi, and P. Dario, *Biomedical applications of soft robotics,* Nature Reviews Materials **3**, 143 (2018).

[7] J. Markoff, *Modest Debut of Atlas May Foreshadow Age of 'Robo Sapiens',* (2013).

[8] M. Greshko, *Meet Sophia, the Robot That Looks Almost Human,* (2019).

[9] L. Ricotti and A. Menciassi, *Bio-hybrid muscle cell-based actuators,* Biomedical Microdevices **14**, 987 (2012).

[10] L. Ricotti, B. Trimmer, A. W. Feinberg, R. Raman, K. K. Parker, R. Bashir, M. Sitti, S. Martel, P. Dario, and A. Menciassi, *Biohybrid actuators for robotics: A review of devices actuated by living cells,* Science Robotics **2**, eaaq0495 (2017).

[11] T. Patiño, X. Arqué, R. Mestre, L. Palacios, and S. Sánchez, *Fundamental Aspects of Enzyme-Powered Micro- and Nanoswimmers,* Accounts of Chemical Research **51**, 2662 (2018).

[12] R. W. Carlsen and M. Sitti, *Bio-hybrid cell-based actuators for microsystems,* Small **10**, 3831 (2014).

[13] R. D. Kamm, R. Bashir, N. Arora, R. D. Dar, M. U. Gillette, L. G. Griffith, M. L. Kemp, K. Kinlaw, M. Levin, A. C. Martin, T. C. McDevitt, R. M. Nerem, M. J. Powers, T. A. Saif, J. Sharpe, S. Takayama, S. Takeuchi, R. Weiss, K. Ye, H. G. Yevick, and M. H. Zaman, *Perspective: The promise of multi-cellular engineered living systems,* APL Bioengineering **2**, 040901 (2018).

[14] V. A. Webster-Wood, O. Akkus, U. A. Gurkan, H. J. Chiel, and R. D. Quinn, *Organismal engineering: Toward a robotic taxonomic key for devices using organic materials,* Science Robotics **2**, eaap9281 (2017).

[15] H. Hess and V. Vogel, *Molecular shuttles based on motor proteins: Active transport in synthetic environments,* Reviews in Molecular Biotechnology **82**, 67 (2001).

[16] R. F. Ismagilov, A. Schwartz, N. Bowden, and G. M. Whitesides, *Autonomous movement and self-assembly,* Angewandte Chemie - International Edition **41**, 652 (2002).

[17] W. F. Paxton, K. C. Kistler, C. C. Olmeda, A. Sen, S. K. St. Angelo, Y. Cao, T. E. Mallouk, P. E. Lammert, and V. H. Crespi, *Catalytic nanomotors: Autonomous movement of striped nanorods,* Journal of the American Chemical Society **126**, 13424 (2004).

[18] S. Fournier-Bidoz, A. C. Arsenault, I. Manners, and G. A. Ozin, *Synthetic self-propelled nanorotors,* Chemical Communications , 441 (2005).

[19] J. Katuri, X. Ma, M. M. Stanton, and S. Sánchez, *Designing micro-and nanoswimmers for specific applications,* Accounts of Chemical Research **50**, 2 (2017).

[20] P. Romanczuk, M. Bär, W. Ebeling, B. Lindner, and L. Schimansky-Geier, *Active Brownian particles: From individual to collective stochastic dynamics,* European Physical Journal: Special Topics **202**, 1 (2012).

[21] D. Vilela, A. C. Hortelao, R. Balderas-Xicohténcatl, M. Hirscher, K. Hahn, X. Ma, and S. Sánchez, *Facile fabrication of mesoporous silica micro-jets with multi-functionalities,* Nanoscale **9**, 13990 (2017).

[22] J. Parmar, D. Vilela, K. Villa, J. Wang, and S. Sánchez, *Micro- and Nanomotors as Active Environmental Microcleaners and Sensors,* Journal of the American Chemical Society **140**, 9317 (2018).

[23] N. Mano and A. Heller, *Bioelectrochemical propulsion,* Journal of the American Chemical Society **127**, 11574 (2005).

[24] D. Pantarotto, W. R. Browne, and B. L. Feringa, *Autonomous propulsion of carbon nanotubes powered by a multienzyme ensemble,* Chemical Communications , 1533 (2008).

[25] Y. Wang, R. M. Hernandez, D. J. Bartlett, J. M. Bingham, T. R. Kline, A. Sen, and T. E. Mallouk, *Bipolar electrochemical mechanism for the propulsion of catalytic nanomotors in hydrogen peroxide solutions,* Langmuir **22**, 10451 (2006).

[26] S. Sanchez, A. A. Solovev, Y. Mei, and O. G. Schmidt, *Dynamics of Biocatalytic Microengines Mediated by Variable Friction Control,* Journal of the American Chemical Society **132**, 13144 (2010).

[27] X. Ma, A. C. Hortelao, A. Miguel-López, and S. Sánchez, *Bubble-Free Propulsion of Ultrasmall Tubular Nanojets Powered by Biocatalytic Reactions,* Journal of the American Chemical Society **138**, 13782 (2016).

[28] X. Ma and S. Sánchez, *Bio-catalytic mesoporous Janus nano-motors powered by catalase enzyme,* Tetrahedron **73**, 4883 (2017).

[29] X. Ma, X. Wang, K. Hahn, and S. Sánchez, *Motion Control of Urea-Powered Biocompatible Hollow Microcapsules,* ACS Nano **10**, 3597 (2016).

[30] X. Ma, A. Jannasch, U.-R. Albrecht, K. Hahn, A. Miguel-López, E. Schäffer, and S. Sánchez, *Enzyme-Powered Hollow Mesoporous Janus Nanomotors,* Nano Letters **15**, 7043 (2015).

[31] L. K. E. A. Abdelmohsen, M. Nijemeisland, G. M. Pawar, G.-J. A. Janssen, R. J. M. Nolte, J. C. M. van Hest, and D. A. Wilson, *Dynamic Loading and Unloading of Proteins in Polymeric Stomatocytes: Formation of an Enzyme-Loaded Supramolecular Nanomotor,* ACS Nano **10**, 2652 (2016).

[32] J. Wang and W. Gao, *Nano/microscale motors: Biomedical opportunities and challenges,* ACS Nano **6**, 5745 (2012).

[33] A. C. Hortelao, R. Carrascosa, N. Murillo-Cremaes, T. Patino, S. Sánchez, A. C. Hortelão, R. Carrascosa, N. Murillo-Cremaes, T. Patiño, and S. Sánchez, *Targeting 3D Bladder Cancer Spheroids with Urease-Powered Nanomotors,* ACS Nano **13**, 429 (2019).

[34] A. C. Hortelão, T. Patiño, A. Perez-Jiménez, À. Blanco, and S. Sánchez, *Enzyme-Powered Nanobots Enhance Anticancer Drug Delivery,* Advanced Functional Materials **28**, 1705086 (2018).

[35] M. A. Ramos-Docampo, M. Fernández-Medina, E. Taipaleenmäki, O. Hovorka, V. Salgueiriño, and B. Städler, *Microswimmers with Heat Delivery Capacity for 3D Cell Spheroid Penetration,* ACS Nano **13**, 12192 (2019).

[36] Y. You, D. Xu, X. Pan, and X. Ma, *Self-propelled enzymatic nanomotors for enhancing synergetic photodynamic and starvation therapy by self-accelerated cascade reactions,* Applied Materials Today **16**, 508 (2019).

[37] E. Blanco, H. Shen, and M. Ferrari, *Principles of nanoparticle design for overcoming biological barriers to drug delivery,* Nature Biotechnology **33**, 941 (2015).

[38] A. Joseph, C. Contini, D. Cecchin, S. Nyberg, L. Ruiz-Perez, J. Gaitzsch, G. Fullstone, X. Tian, J. Azizi, J. Preston, G. Volpe, and G. Battaglia, *Chemotactic synthetic vesicles: Design and applications in blood-brain barrier crossing,* Science Advances **3**, e1700362 (2017).

[39] X. Zhao, H. Palacci, V. Yadav, M. M. Spiering, M. K. Gilson, P. J. Butler, H. Hess, S. J. Benkovic, and A. Sen, *Substrate-driven chemotactic assembly in an enzyme cascade,* Nature Chemistry **10**, 311 (2018).

[40] F. Peng, Y. Tu, A. Adhikari, J. C. Hintzen, D. W. Löwik, and D. A. Wilson, *A peptide functionalized nanomotor as an efficient cell penetrating tool,* Chemical Communications **53**, 1088 (2017).

[41] M. Nijemeisland, L. K. E. A. Abdelmohsen, W. T. S. Huck, D. A. Wilson, and J. C. M. van Hest, *A Compartmentalized Out-of-Equilibrium Enzymatic Reaction Network for Sustained Autonomous Movement,* ACS Central Science **2**, 843 (2016).

[42] Y. Wang, Y. Cui, Y. Zhao, B. He, X. Shi, D. Di, Q. Zhang, and S. Wang, *Fluorescent carbon dot-gated multifunctional mesoporous silica nanocarriers for redox/enzyme dual-responsive targeted and controlled drug delivery and real-time bioimaging,* European Journal of Pharmaceutics and Biopharmaceutics **117**, 105 (2017).

[43] Y. Wu, X. Lin, Z. Wu, H. Möhwald, and Q. He, *Self-propelled polymer multilayer janus capsules for effective drug delivery and light-triggered release,* ACS Applied Materials and Interfaces **6**, 10476 (2014).

[44] P. S. Schattling, M. A. Ramos-Docampo, V. Salgueiriño, and B. Städler, *Double-Fueled Janus Swimmers with Magnetotactic Behavior,* ACS Nano **11**, 3973 (2017).

[45] A. Llopis-Lorente, A. Garciá-Fernández, N. Murillo-Cremaes, A. C. Hortelaõ, T. Patinõ, R. Villalonga, F. Sancenón, R. Martínez-Máñez, and S. Sánchez, *Enzyme-powered gated mesoporous silica nanomotors for on-command intracellular payload delivery,* ACS Nano **13**, 12171 (2019).

[46] M. De Corato, X. Arqué, T. Patiño, M. Arroyo, S. Sánchez, and I. Pagonabarraga, *Self-Propulsion of Active Colloids via Ion Release: Theory and Experiments,* Physical Review Letters **124**, 108001 (2020).

[47] S. Palagi, D. Walker, T. Qiu, and P. Fischer, *Microbiorobotics: Biologically Inspired Microscale Robotic Systems*, 2nd ed. (Elsevier Inc., 2017) pp. 133–162.

[48] E. M. Purcell, *Life at low Reynolds number,* American Journal of Physics **45**, 3 (1977).

[49] D. Vilela, U. Cossío, J. Parmar, A. M. Martínez-Villacorta, V. Gómez-Vallejo, J. Llop, and S. Sánchez, *Medical Imaging for the Tracking of Micromotors,* ACS Nano **12**, 1220 (2018).

[50] T. Patiño, N. Feiner-Gracia, X. Arqué, A. Miguel-López, A. Jannasch, T. Stumpp, E. Schäffer, L. Albertazzi, and S. Sánchez, *Influence of Enzyme Quantity and Distribution on the Self-Propulsion of Non-Janus Urease-Powered Micromotors,* Journal of the American Chemical Society **140**, 7896 (2018).

[51] X. Arqué, A. Romero-Rivera, F. Feixas, T. Patiño, S. Osuna, and S. Sánchez, *Intrinsic enzymatic properties modulate the self-propulsion of micromotors,* Nature Communications **10**, 2826 (2019).

[52] J. R. Howse, R. A. L. Jones, A. J. Ryan, T. Gough, R. Vafabakhsh, and R. Golestanian, *Self-Motile Colloidal Particles: From Directed Propulsion to Random Walk,* Physical Review Letters **99**, 048102 (2007), arXiv:0706.4406 .

[53] R. Golestanian, T. B. Liverpool, and A. Ajdari, *Designing phoretic micro- and nano-swimmers,* New Journal of Physics **9**, 126 (2007), arXiv:0701168 [cond-mat] .

[54] V. Magdanz, S. Sanchez, and O. G. Schmidt, *Development of a sperm-flagella driven micro-bio-robot,* Advanced Materials **25**, 6581 (2013).

[55] O. Yasa, P. Erkoc, Y. Alapan, and M. Sitti, *Microalga-Powered Microswimmers toward Active Cargo Delivery,* Advanced Materials **30**, 1 (2018).

[56] S. Martel, *Bacterial microsystems and microrobots,* Biomedical Microdevices **14**, 1033 (2012).

[57] B. W. Park, J. Zhuang, O. Yasa, and M. Sitti, *Multifunctional Bacteria-Driven Microswimmers for Targeted Active Drug Delivery,* ACS Nano **11**, 8910 (2017).

[58] H. Xu, M. Medina-Sánchez, V. Magdanz, L. Schwarz, F. Hebenstreit, and O. G. Schmidt, *Sperm-Hybrid Micromotor for Targeted Drug Delivery,* ACS Nano **12**, 327 (2018).

[59] F. Striggow, M. Medina-Sánchez, G. K. Auernhammer, V. Magdanz, B. M. Friedrich, and O. G. Schmidt, *Sperm-Driven Micromotors Moving in Oviduct Fluid and Viscoelastic Media,* Small **16**, 2000213 (2020).

[60] M. M. Stanton, B. W. Park, D. Vilela, K. Bente, D. Faivre, M. Sitti, and S. Sánchez, *Magnetotactic Bacteria Powered Biohybrids Target E. coli Biofilms,* ACS Nano **11**, 9968 (2017).

[61] S. Martel, C. C. Tremblay, S. Ngakeng, and G. Langlois, *Controlled manipulation and actuation of micro-objects with magnetotactic bacteria,* Applied Physics Letters **89**, 14 (2006).

[62] L. Angelani, R. Di Leonardo, and G. Ruocco, *Self-starting micromotors in a bacterial bath,* Physical Review Letters **102**, 2 (2009), arXiv:0812.2375 .

[63] R. Di Leonardo, L. Angelani, D. Dell'Arciprete, G. Ruocco, V. Iebba, S. Schippa, M. P. Conte, F. Mecarini, F. De Angelis, and E. Di Fabrizio, *Bacterial ratchet motors,* Proceedings of the National Academy of Sciences of the United States of America **107**, 9541 (2010), arXiv:0910.2899 .

[64] I. S. Khalil, V. Magdanz, J. Simmchen, A. Klingner, and S. Misra, *Resemblance between motile and magnetically actuated sperm cells,* Applied Physics Letters **116**, 1 (2020).

[65] M. M. Stanton, J. Simmchen, X. Ma, A. Miguel-López, and S. Sánchez, *Biohybrid Janus Motors Driven by Escherichia coli,* Advanced Materials Interfaces **3** (2016), 10.1002/admi.201500505.

[66] J. Zhuang and M. Sitti, *Chemotaxis of bio-hybrid multiple bacteria-driven microswimmers,* Scientific Reports **6**, 1 (2016).

I

[67] O. Felfoul, M. Mohammadi, S. Taherkhani, D. De Lanauze, Y. Zhong Xu, D. Loghin, S. Essa, S. Jancik, D. Houle, M. Lafleur, L. Gaboury, M. Tabrizian, N. Kaou, M. Atkin, T. Vuong, G. Batist, N. Beauchemin, D. Radzioch, and S. Martel, *Magneto-aerotactic bacteria deliver drug-containing nanoliposomes to tumour hypoxic regions,* Nature Nanotechnology **11**, 941 (2016).

[68] B. J. Williams, S. V. Anand, J. Rajagopalan, and M. T. A. Saif, *A self-propelled biohybrid swimmer at low Reynolds number,* Nature Communications **5**, 3081 (2014).

[69] D. Kim, A. Liu, E. Diller, and M. Sitti, *Chemotactic steering of bacteria propelled microbeads,* Biomedical Microdevices **14**, 1009 (2012).

[70] M. R. Edwards, R. Wright Carlsen, and M. Sitti, *Near and far-wall effects on the three-dimensional motion of bacteria-driven microbeads,* Applied Physics Letters **102**, 10 (2013).

[71] A. V. Singh and M. Sitti, *Bacteria-Driven Particles: Patterned and Specific Attachment of Bacteria on Biohybrid Bacteria-Driven Microswimmers (Adv. Healthcare Mater. 18/2016),* Advanced Healthcare Materials **5**, 2306 (2016).

[72] A. Sahari, M. A. Traore, B. E. Scharf, and B. Behkam, *Directed transport of bacteria-based drug delivery vehicles: bacterial chemotaxis dominates particle shape,* Biomedical Microdevices **16**, 717 (2014).

[73] D. Park, S. J. Park, S. Cho, Y. Lee, Y. K. Lee, J. J. Min, B. J. Park, S. Y. Ko, J. O. Park, and S. Park, *Motility analysis of bacteria-based microrobot (bacteriobot) using chemical gradient microchamber,* Biotechnology and Bioengineering **111**, 134 (2014).

[74] J. Zhuang, R. W. Carlsen, and M. Sitti, *PH-taxis of biohybrid microsystems,* Scientific Reports **5**, 1 (2015).

[75] Z. Hosseinidoust, B. Mostaghaci, O. Yasa, B. W. Park, A. V. Singh, and M. Sitti, *Bioengineered and biohybrid bacteria-based systems for drug delivery,* Advanced Drug Delivery Reviews **106**, 27 (2016).

[76] S. Martel, M. Mohammadi, O. Felfoul, Zhao Lu, and P. Pouponneau, *Flagellated magnetotactic bacteria as controlled MRI-trackable propulsion and steering systems for medical nanorobots operating in the human microvasculature,* International Journal of Robotics Research **28**, 571 (2009).

[77] T. Patino, R. Mestre, and S. Sánchez, *Miniaturized soft bio-hybrid robotics: A step forward into healthcare applications,* Lab on a Chip **16**, 3626 (2016).

[78] F. Ilievski, A. D. Mazzeo, R. F. Shepherd, X. Chen, and G. M. Whitesides, *Soft robotics for chemists,* Angewandte Chemie - International Edition **50**, 1890 (2011).

[79] M. Wehner, R. L. Truby, D. J. Fitzgerald, B. Mosadegh, G. M. Whitesides, J. A. Lewis, and R. J. Wood, *An integrated design and fabrication strategy for entirely soft, autonomous robots,* Nature **536**, 451 (2016).

[80] C. P. Chou and B. Hannaford, *Measurement and modeling of McKibben pneumatic artificial muscles,* IEEE Transactions on Robotics and Automation **12**, 90 (1996).

[81] R. V. Martinez, J. L. Branch, C. R. Fish, L. Jin, R. F. Shepherd, R. M. D. Nunes, Z. Suo, and G. M. Whitesides, *Robotic tentacles with three-dimensional mobility based on flexible elastomers,* Advanced Materials **25**, 205 (2013).

[82] L. J. Romasanta, M. A. Lopez-Manchado, and R. Verdejo, *Increasing the performance of dielectric elastomer actuators: A review from the materials perspective,* Progress in Polymer Science **51**, 188 (2015).

[83] M. Duduta, R. J. Wood, and D. R. Clarke, *Multilayer Dielectric Elastomers for Fast, Programmable Actuation without Prestretch,* Advanced Materials **28**, 8058 (2016).

[84] H. S. Wang, J. Cho, D. S. Song, J. H. Jang, J. Y. Jho, and J. H. Park, *High-Performance Electroactive Polymer Actuators Based on Ultrathick Ionic Polymer-Metal Composites with Nanodispersed Metal Electrodes,* ACS Applied Materials and Interfaces **9**, 21998 (2017).

[85] R. F. Shepherd, F. Ilievski, W. Choi, S. A. Morin, A. A. Stokes, A. D. Mazzeo, X. Chen, M. Wang, and G. M. Whitesides, *Multigait soft robot,* Proceedings of the National Academy of Sciences of the United States of America **108**, 20400 (2011), arXiv:84855503964 .

[86] M. T. Tolley, R. F. Shepherd, B. Mosadegh, K. C. Galloway, M. Wehner, M. Karpelson, R. J. Wood, and G. M. Whitesides, *A Resilient, Untethered Soft Robot,* Soft Robotics **1**, 213 (2014).

[87] A. A. Stokes, R. F. Shepherd, S. A. Morin, F. Ilievski, and G. M. Whitesides, *A Hybrid Combining Hard and Soft Robots,* Soft Robotics **1**, 70 (2014).

[88] M. Meller, B. Kogan, M. Bryant, and E. Garcia, *Model-based feedforward and cascade control of hydraulic McKibben muscles,* Sensors and Actuators A **275**, 88 (2018).

[89] J. K. Paik, E. Hawkes, and R. J. Wood, *A novel low-profile shape memory alloy torsional actuator,* Smart Materials and Structures **19**, 125014 (2010).

[90] S. Seok, C. D. Onal, K. J. Cho, R. J. Wood, D. Rus, and S. Kim, *Meshworm: A peristaltic soft robot with antagonistic nickel titanium coil actuators,* IEEE/ASME Transactions on Mechatronics **18**, 1485 (2013).

[91] D. Rus and M. T. Tolley, *Design, fabrication and control of soft robots,* Nature **521**, 467 (2015).

[92] J. Walker, T. Zidek, C. Harbel, S. Yoon, F. S. Strickland, S. Kumar, and M. Shin, *Soft robotics: A review of recent developments of pneumatic soft actuators,* Actuators **9**, 3 (2020).

[93] Y. Akiyama, K. Odaira, K. Sakiyama, T. Hoshino, K. Iwabuchi, and K. Morishima, *Rapidly-moving insect muscle-powered microrobot and its chemical acceleration,* Biomedical Microdevices **14**, 979 (2012).

[94] V. A. Webster, K. J. Chapin, E. L. Hawley, J. M. Patel, O. Akkus, H. J. Chiel, and R. D. Quinn, *Aplysia californica as a novel source of material for biohybrid robots and organic machines,* in *Lepora N., Mura A., Mangan M., Verschure P., Desmulliez M., Prescott T. (eds) Biomimetic and Biohybrid Systems. Living Machines 2016. Lecture Notes in Computer Science*, Vol. 9793 (Springer, Cham, 2016) pp. 365–374.

[95] A. L. Baryshyan, L. J. Domigan, B. Hunt, B. A. Trimmer, and D. L. Kaplan, *Self-assembled insect muscle bioactuators with long term function under a range of environmental conditions,* RSC Advances **4**, 39962 (2014).

[96] A. L. Baryshyan, W. Woods, B. A. Trimmer, and D. L. Kaplan, *Isolation and maintenance-free culture of contractile myotubes from Manduca sexta embryos,* PLoS ONE 7, e31598 (2012).

[97] Y. Akiyama, K. Iwabuchi, Y. Furukawa, and K. Morishima, *Culture of insect cells contracting spontaneously; research moving toward an environmentally robust hybrid robotic system,* Journal of Biotechnology **133**, 261 (2008).

I

[98] Y. Akiyama, K. Iwabuchi, Y. Furukawa, and K. Morishima, *Long-term and room temperature operable bioactuator powered by insect dorsal vessel tissue,* Lab on a Chip **9**, 140 (2009).

[99] Y. Akiyama, K. Iwabuchi, Y. Furukawa, and K. Morishima, *Biological contractile regulation of micropillar actuator driven by insect dorsal vessel tissue,* in *2008 2nd IEEE RAS & EMBS International Conference on Biomedical Robotics and Biomechatronics, Scottsdale, AZ* (2008) pp. 501–505.

[100] Y. Tanaka, S. ichi Funano, Y. Noguchi, Y. Yalikun, and N. Kamamichi, *A valve powered by earthworm muscle with both electrical and 100% chemical control,* Scientific Reports **9**, 1 (2019).

[101] R. Raman, C. Cvetkovic, S. G. Uzel, R. J. Platt, P. Sengupta, R. D. Kamm, and R. Bashir, *Optogenetic skeletal muscle-powered adaptive biological machines,* Proceedings of the National Academy of Sciences of the United States of America **113**, 3497 (2016).

[102] J. Xi, J. J. Schmidt, and C. D. Montemagno, *Self-assembled microdevices driven by muscle,* Nature Materials **4**, 180 (2005).

[103] J. Kim, J. Park, S. Yang, J. Baek, B. Kim, S. H. Lee, E. S. Yoon, K. Chun, and S. Park, *Establishment of a fabrication method for a long-term actuated hybrid cell robot,* Lab on a Chip 7, 1504 (2007).

[104] V. Chan, K. Park, M. B. Collens, H. Kong, T. A. Saif, and R. Bashir, *Development of miniaturized walking biological machines.* Scientific Reports **2**, 857 (2012).

[105] J. Park, J. Ryu, S. K. Choi, E. Seo, J. M. Cha, S. Ryu, J. Kim, B. Kim, and S. H. Lee, *Real-time measurement of the contractile forces of self-organized cardiomyocytes on hybrid biopolymer microcantilevers,* Analytical Chemistry 77, 6571 (2005).

[106] J. Park, J. Kim, D. Roh, S. Park, B. Kim, and K. Chun, *Fabrication of complex 3D polymer structures for cell-polymer hybrid systems,* Journal of Micromechanics and Microengineering **16**, 1614 (2006).

[107] A. W. Feinberg, A. Feigel, S. S. Shevkoplyas, S. Sheehy, G. M. Whitesides, and K. K. Parker, *Muscular thin films for building actuators and powering devices,* Science **317**, 1366 (2007).

[108] M. T. Holley, N. Nagarajan, C. Danielson, P. Zorlutuna, and K. Park, *Development and characterization of muscle-based actuators for self-stabilizing swimming biorobots,* Lab on a Chip **16**, 3473 (2016).

[109] J. C. Nawroth, H. Lee, A. W. Feinberg, C. M. Ripplinger, M. L. McCain, A. Grosberg, J. O. Dabiri, and K. K. Parker, *A tissue-engineered jellyfish with biomimetic propulsion,* Nature Biotechnology **30**, 792 (2012).

[110] S. J. Park, M. Gazzola, K. S. Park, S. Park, V. Di Santo, E. L. Blevins, J. U. Lind, P. H. Campbell, S. Dauth, A. K. Capulli, F. S. Pasqualini, S. Ahn, A. Cho, H. Yuan, B. M. Maoz, R. Vijaykumar, J. W. Choi, K. Deisseroth, G. V. Lauder, L. Mahadevan, and K. K. Parker, *Phototactic guidance of a tissue-engineered soft-robotic ray,* Science **353**, 158 (2016).

[111] J. Kim, J. Park, J. Lee, E. Yoon, J. Park, and S. Park, *Biohybrid microsystems actuated by cardiomyocytes: Microcantilever, microrobot, and micropump,* in *2008 IEEE International Conference on Robotics and Automation, Pasadena, CA* (2008) pp. 880–885.

[112] M. B. Knight, N. K. Drew, L. A. McCarthy, and A. Grosberg, *Emergent Global Contractile Force in Cardiac Tissues,* Biophysical Journal **110**, 1615 (2016).

[113] W. R. Legant, A. Pathak, M. T. Yang, V. S. Deshpande, R. M. McMeeking, and C. S. Chen, *Microfabricated tissue gauges to measure and manipulate forces from 3D microtissues,* Proceedings of the National Academy of Sciences of the United States of America **106**, 10097 (2009).

[114] J. U. Lind, T. A. Busbee, A. D. Valentine, F. S. Pasqualini, H. Yuan, M. Yadid, S. J. Park, A. Kotikian, A. P. Nesmith, P. H. Campbell, J. J. Vlassak, J. A. Lewis, and K. K. Parker, *Instrumented cardiac microphysiological devices via multimaterial three-dimensional printing,* Nature Materials **16**, 303 (2017).

[115] Y. Morimoto, H. Onoe, and S. Takeuchi, *Biohybrid robot powered by an antagonistic pair of skeletal muscle tissues,* Science Robotics **3**, eaat4440 (2018).

[116] Y. Morimoto, H. Onoe, and S. Takeuchi, *Biohybrid robot with skeletal muscle tissue covered with a collagen structure for moving in air,* APL Bioengineering **4**, 026101 (2020).

[117] H. Vandenburgh, J. Shansky, F. Benesch-Lee, V. Barbata, J. Reid, L. Thorrez, R. Valentini, and G. Crawford, *Drug-screening platform based on the contractility of tissue-engineered muscle,* Muscle and Nerve **37**, 438 (2008).

[118] M. S. Sakar, D. Neal, T. Boudou, M. A. Borochin, Y. Li, R. Weiss, R. D. Kamm, C. S. Chen, and H. H. Asada, *Formation and optogenetic control of engineered 3D skeletal muscle bioactuators,* Lab on a Chip **12**, 4976 (2012).

[119] T. Boudou, W. R. Legant, A. Mu, M. A. Borochin, N. Thavandiran, M. Radisic, P. W. Zandstra, J. A. Epstein, K. B. Margulies, and C. S. Chen, *A Microfabricated Platform to Measure and Manipulate the Mechanics of Engineered Cardiac Microtissues,* Tissue Engineering Part A **18**, 910 (2012).

[120] C. A. Powell, B. L. Smiley, J. Mills, and H. H. Vandenburgh, *Mechanical stimulation improves tissue-engineered human skeletal muscle,* American Journal of Physiology - Cell Physiology **283**, 1557 (2002).

[121] D. G. Moon, G. Christ, J. D. Stitzel, A. Atala, and J. J. Yoo, *Cyclic mechanical preconditioning improves engineered muscle contraction,* Tissue Engineering - Part A. **14**, 473 (2008).

[122] L. Madden, M. Juhas, W. E. Kraus, G. A. Truskey, and N. Bursac, *Bioengineered human myobundles mimic clinical responses of skeletal muscle to drugs,* eLife **2015**, 4:e04885 (2015).

[123] C. Cvetkovic, R. Raman, V. Chan, B. J. Williams, M. Tolish, P. Bajaj, M. S. Sakar, H. H. Asada, M. T. A. Saif, and R. Bashir, *Three-dimensionally printed biological machines powered by skeletal muscle,* Proceedings of the National Academy of Sciences of the United States of America **111**, 10125 (2014).

[124] R. Raman, L. Grant, Y. Seo, C. Cvetkovic, M. Gapinske, A. Palasz, H. Dabbous, H. Kong, P. P. Pinera, and R. Bashir, *Damage, Healing, and Remodeling in Optogenetic Skeletal Muscle Bioactuators,* Advanced Healthcare Materials **6**, 1700030 (2017).

[125] C. Cvetkovic, M. H. Rich, R. Raman, H. Kong, and R. Bashir, *A 3D-printed platform for modular neuromuscular motor units,* Microsystems & Nanoengineering **3**, 17015 (2017).

I

[126] G. J. Pagan-Diaz, X. Zhang, L. Grant, Y. Kim, O. Aydin, C. Cvetkovic, E. Ko, E. Solomon, J. Hollis, H. Kong, T. Saif, M. Gazzola, and R. Bashir, *Simulation and Fabrication of Stronger, Larger, and Faster Walking Biohybrid Machines,* Advanced Functional Materials **28**, 1801145 (2018).

[127] Y. Kim, G. Pagan-Diaz, L. Gapinske, Y. Kim, J. Suh, E. Solomon, J. F. Harris, S. W. Nam, and R. Bashir, *Integration of Graphene Electrodes with 3D Skeletal Muscle Tissue Models,* Advanced Healthcare Materials **9**, 1901137 (2020).

[128] V. A. Webster, F. R. Young, J. M. Patel, G. N. Scariano, O. Akkus, U. A. Gurkan, H. J. Chiel, and R. D. Quinn, *3D-Printed Biohybrid Robots Powered by Neuromuscular Tissue Circuits from Aplysia californica,* in *Mangan M., Cutkosky M., Mura A., Verschure P., Prescott T., Lepora N. (eds) Biomimetic and Biohybrid Systems. Living Machines 2017. Lecture Notes in Computer Science* (Springer, Cham, 2017) pp. 475–486.

[129] O. Aydin, X. Zhang, S. Nuethong, G. J. Pagan-Diaz, R. Bashir, M. Gazzola, and M. T. A Saif, *Neuromuscular actuation of biohybrid motile bots,* Proceedings of the National Academy of Sciences of the United States of America **116**, 19841 (2019).

[130] T. K. Merceron, M. Burt, Y.-J. Seol, H.-W. Kang, S. J. Lee, J. J. Yoo, and A. Atala, *A 3D bioprinted complex structure for engineering the muscle–tendon unit,* Biofabrication 7, 035003 (2015).

[131] D. B. Kolesky, R. L. Truby, A. S. Gladman, T. A. Busbee, K. A. Homan, and J. A. Lewis, *3D bioprinting of vascularized, heterogeneous cell-laden tissue constructs,* Advanced Materials **26**, 3124 (2014).

[132] P. Datta, B. Ayan, and I. T. Ozbolat, *Bioprinting for vascular and vascularized tissue biofabrication,* Acta Biomaterialia **51**, 1 (2017).

[133] D. B. Kolesky, K. A. Homan, M. A. Skylar-Scott, and J. A. Lewis, *Three-dimensional bioprinting of thick vascularized tissues,* Proceedings of the National Academy of Sciences **113**, 3179 (2016).

[134] H.-W. Kang, S. J. Lee, I. K. Ko, C. Kengla, J. J. Yoo, and A. Atala, *A 3D bioprinting system to produce human-scale tissue constructs with structural integrity,* Nature Biotechnology **34**, 312 (2016).

[135] T. J. Hinton, Q. Jallerat, R. N. Palchesko, J. H. Park, M. S. Grodzicki, H.-J. Shue, M. H. Ramadan, A. R. Hudson, and A. W. Feinberg, *Three-dimensional printing of complex biological structures by freeform reversible embedding of suspended hydrogels,* Science Advances **1**, e1500758 (2015).

[136] W. Wu, A. Deconinck, and J. A. Lewis, *Omnidirectional printing of 3D microvascular networks,* Advanced Materials **23**, H178 (2011).

II

Complex motion dynamics of nano- and micromotors

Section 3.1 of this chapter has been published in *Angew. Chem. Int. Ed. Engl.* **57**(23) (2018): 6838-6842[1]. Sections 3.2, 3.3 and 3.4 are currently being considered for publication.

II

1. Introduction and state of the art

Active matter is the sub-field of physics that deals with the study of large quantities of active agents that consume energy and are out of thermal equilibrium[2]. These active agents are ubiquitous in nature, and we can find them in everyday examples like flocks of birds, schools of fish or herds of people, but they are also present at the nano- and microscale in the cytoskeleton of cells, cellular tissues or bacterial motion. Inspired by these natural systems, self-propelled particles of different sizes and shapes have emerged as a different class of active agents that can move due to the conversion of energy from the environment into kinetic energy [3–5]. This type of systems can be described under the so-called active Brownian particle model, which assumes an underlying Brownian particle with some sort of "internal" activity leading to its motion[2].

Many different types of self-propelled particles, also called micro- and nanomotors or swimmers, have been fabricated over the last fifteen years[6–8]. While some of them have used chemical reactions to acquire the necessary energy for motion, others have used sources like light[9, 10] or ultrasound[11]. Initial examples were based on rod-like structures that could move by the decomposition of hydrogen peroxide (H_2O_2) due to Au and Pt *via* electrokinetic mechanisms[12, 13]. Likewise, other motors based on carbon fibers[14], nanotubes[15] or microtubes[16] were propelled by reactions catalyzed by enzymes. This type of asymmetric swimmers based on nano- or microtubes could mainly move by the production of gas bubbles (O_2 or H_2) inside their cavities in a jet-like fashion[15–19]. Several proof-of-concept applications have been demonstrated with these microjets, like transport of cargo on-chip[20, 21], cleaning of contaminated water[22–25] or biosensing[26]. Nevertheless, the use of hydrogen peroxide as a fuel, which is not biocompatible at high concentrations, might hinder their applications in the biomedical field as means of directed drug delivery to diseased cells and tissues.

Nano- and micromotors based on spherical particles that move by phoretic mechanisms have had a more extensive development over the last years[8, 27–29]. While Pt-based Janus-particles are the most widely used type of self-propelled particles in fundamental studies in the field of active matter, hybrid nano- and micromotors composed of a biological entity, such as an enzyme, and a artificial substrate, like a passive nanoparticle or nanotube, hold promising applications for biomedicine[6]. The use of enzymes, which catalyze reactions inside our cells, might be the solution for biocompatibility problems of using H_2O_2 as fuel, since both the source and the reaction products are available in our bodies. Several types of enzymes, such as catalase[30–33], glucose oxidase[32, 34] (and the tandem of both[15, 35, 36]), horseradish peroxidase[37], trypsin[38], aldolase[39], or acetylcholinesterase[39] have been used to create these types of self-propelled particles. One of the most widely used enzymes is urease, which catalyzes the decomposition of urea[6]. It has been utilized in nanojets[40], Janus particles[32] and fully- or patchy-covered particles of different sizes[33, 39, 41, 42], which can move with significant speeds thanks to its high catalytic rate.

Their underlying motion mechanisms, however, still remain unclear. Bubble propulsion in microjets, for instance, has been experimentally demonstrated[16, 25, 43], but when bubbles are not present, several theoretical frameworks could explain the observed motion. Self-diffusiophoresis[44, 45] or self-electrophoresis[37, 46] are some of the mechanisms that have been studied experimentally for micromotors using metallic catalysts, but their relevance to enzymatically propelled ones still needs to be defined. Recent studies have shed some light into the effect of ionic salts in the medium and their impact on propulsion, suggesting that electrophoretic effects might play a significant role in the overall mechanism[47–49].

The analysis of their motion, however, is independent on the underlying mechanism. Due to the interplay of catalytic activity with Brownian fluctuations, statistical approaches are necessary to extract parameters that can characterize the type of motion[2]. Optical tracking is the most widely used technique, as it allows to visually track the position of the nano- or micromotors in time. Then, the mean squared displacement (MSD) of a single particle or an ensemble of them can be computed and compared with different conditions to differentiate Brownian motion from active Brownian motion[50]. The MSD can be understood as the average area covered by an active or passive particle after a certain time, t, and different shapes of this curve can give information about the dynamics of the motion. Howse *et al.* developed a theoretical framework, resembling the Uhlenbeck-Orstein process for Brownian motion[51], to easily describe the MSD of nano- and micromotors. At very short times compared to the rotational diffusion time of the particle, τ_r, the motion can be considered ballistic or propulsive, and the MSD for a particle in 2D can be approximated by a quadratic equation of the form $\text{MSD}(\Delta t) = 4D_t\Delta t + v^2\Delta t^2$, where D_t is the translational diffusion of the particle, v is the propulsive speed due to the activity and Δt is the elapsed time. At times much longer than τ_r, however, the MSD shows a linear tendency of the form $\text{MSD}(\Delta t) = 4D_e\Delta t$, where D_e is the enhanced diffusion of the particle, larger than D_t.

These equations have become paramount in the literature, although they require certain assumptions, such as the non-suppression of Brownian fluctuations in the form of randomization of the direction and the constant speed of the particle, that ensures the ergodicity of the system. Deviations from these assumptions are not usually considered and different analysis might be necessary to understand their motion and perhaps shed some light into the identification of the underlying mechanisms. For instance, in other sub-fields of active matter that consider subdiffusion in crowded environments, more general views of the MSD are used ($\text{MSD} \sim \Delta t^{\alpha}$), considering scaling exponents that can range from 0 to 1 for sub-diffusive motion and from 1 to 2 for super-diffusive motion[3, 4].

The motion of micro- and nanomotors has been mainly studied in deionized water, only altered by the presence of the fuel. However, more research is being carried out to study their motion in more complex fluids, such as phosphate buffered saline (PBS) to study the effects of salts[41], simulated and real urine[52], cell culture media[52] or viscoelastic media, like mucin gels[53]. These studies provide important insight into their potential real-life applications, besides their fundamental studies from the physics points of view.

In this chapter, we consider four case studies that deviate from the basic assumptions of this common theoretical framework and we investigate its limitations to effectively describe the motion of nano- and micromotors moving under complex dynamics. In Section 3.1, we study the light-propulsion of a carbonaceous nano-bottle motor that shows non-constant speed dynamics with highly propulsive spikes that hinder Brownian motion. In this case, an analysis based on the directionality of their motion and a more general scaling of the MSD is necessary. In Section 3.2, we study mesoporous silica nanorods that can catalyze the decomposition of hydrogen peroxide by two catalysts with different configurations, and that show different populations of nanomotors with completely different dynamics. Sections 3.3 and 3.4 deepen into the study of bio-hybrid micro- and nanomotors based on enzymatic reactions. In the first case, we investigate the outcomes of having a propulsive speed that decays exponentially. We develop the governing equations behind their MSD and we propose analytical approaches to interpret the results in these kinds of systems. In the second case, we examine another technique to investigate their motion, dynamic light scattering (DLS), and how it can be applied for self-propelled particles moving in water and in hyaluronic acid.

2. Objectives

Motion at the nano- and micro-scale can be complex and difficult to describe. Due to the stochastic nature of the processes occurring at the nanoscale, only statistical descriptions and analyses can provide information about the motion mechanisms that underlie in the observed dynamics. This is most clearly seen when the randomization of the direction of motion (due to Brownian effects) renders seemingly different types of motion in individual experiments. In these cases, it is necessary to find statistically relevant analyses to characterize this motion. The analysis of the MSD is the most widely used metric to characterize groups of particles or nanomotors, as it contains averaged information about the net area covered during their movement. However, other metrics, such as the computation of velocity autocorrelation functions, or even other techniques, like DLS, can also provide statistically averaged results that can help understand their dynamics.

Moreover, although the motion of nano- and micromotors and, in particular, hybrid motors powered by enzyme catalysis have been studied extensively in the literature, most of the studies have been based on assumptions of the ergodicity of the system, constant speed, Newtonian liquids and spherical particles with no deviations from the active Brownian particle model. The objectives of this chapter are to study the limits of applicability of the active Brownian motion paradigm and understand the impacts that small deviations from this model have on the analyses performed. For that reason, four different case studies are considered: i) a carbon-based nanobottle propelled by photothermal effect after excitation with near infrared (NIR) light, which shows highly directional motion with non-constant velocity profiles; ii) silica-based nanorods with catalytic sites located at different places of its structure that can lead to two sub-populations of motion dynamics; iii) spherical hybrid self-propelled micromotors that have an exponentially decreasing speed, which can be described analytically; and iv) spherical hybrid self-propelled nanomotors studied by the DLS technique in viscoelastic media, of which they can change the viscoelastic properties due to the catalytic reaction of urease, which acts as a propulsion engine. With these four case studies, we will understand the need of choosing the appropriate set of metrics to study the motion dynamics of different types of motors in order to obtain meaningful, relevant and trustworthy information for the investigation of their underlying mechanisms.

3. Case studies

3.1. Anomalous diffusion of a nanobottle motor

Motion mechanism

In this section, we describe the motion analysis of a carbonaceous nanobottle (CNB) motor that can propel by NIR-light-induced jet propulsion in water. This motion is highly directional, overcoming at times the typical randomization of Brownian motion, and shows velocity profiles that are not continuous, displaying peaks of very fast motion. This type of nanomotor, thus, cannot be characterized by the common metrics used in nano- and micromotors, such as the propulsion speed or enhanced diffusion coefficient extracted from MSD[28]. Therefore, other analyses based on the MSD scaling exponent or their directionality, are more appropriate to characterize its motion.

The CNB motors were fabricated by a soft-template-based polymerization method based on polymerization of ribose on PEO micelles (Figure 2.1A; see Methods section for detailed information). This polymerization creates an open neck that resembles a bottle, as can be observed from

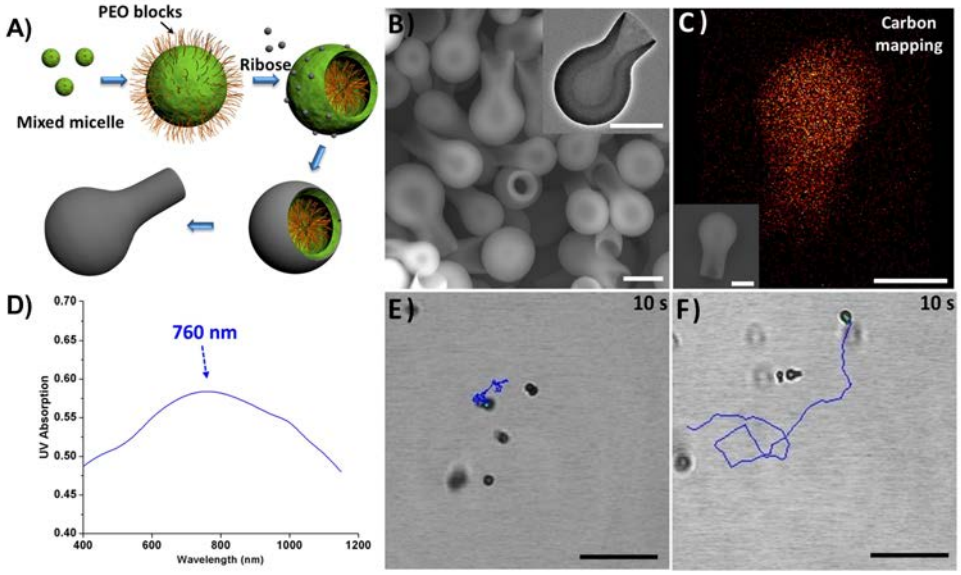

Figure 2.1: Characterization of the as-prepared NIR light-powered carbonaceous nanobottle (CNB) motors. A) Schematic illustration of the preparation of the CNB motors. B) SEM image of the as-prepared CNB motors; The inset is a TEM image of a single CNB motor. Scale bars = 500 nm. C) Elemental mapping of the carbon distribution. The inset is an SEM image of a single CNB motor. Scale bars = 500 nm. D) UV-Vis spectrum of the CNB motors in water. Tracking trajectories of the CNB motors upon illumination by an NIR laser at 0 W/cm^2 (E) and 1.36 W/cm^2 (F). Scale bars = 10 μm. Adapted from [1].

Figure 2.1B in scanning electron microscope (SEM) and transmission electron microscope (TEM) images. The length of CNB motor was approximately 1.5 μm. The inner/external diameters of the spherical part were around 536 nm and 1 μm, respectively. Energy-dispersive X-ray (EDX) mapping of carbon shows that the main component of the CNB motor was carbon (Figure 2.1C). Thanks to this absorption property, the CNB motors could be excited with NIR light to display photothermal effect. After being stimulated with 760 nm wavelength using a two-photon confocal laser scanning microscopy (TP-CLSM), these nanomotors showed a trajectory that greatly differed from Brownian motion in terms of area covered (Figures 2.1E and 2.1F). This trajectory, however, was anomalous and did not follow the typical constant-speed behavior of other nanomotors.

The proposed mechanism of motion was based on the rapid heating of the internal fluid upon exposure to NIR light, which caused propulsion through the ejection of this heated fluid. Figure 2.2 show finite element analysis (FEA) simulations that describe this process. To reduce the computational power needed, the simulations were carried out in a static mode, that is, by assuming the bottle was always at a fixed position. For that reason, these results were only useful for examining the first instant after NIR light was applied, which led to directional movement of the CNB motor. Moreover, since changes in temperature, pressure or fluid velocity happen at the nanosecond scale, these simulations provide a view into the first instants of NIR exposure, which cannot be capture with a microscope. When NIR light is applied, the carbonaceous shell of the CNB motor efficiently absorbs NIR light and generates a local temperature gradient (Figure 2.2A). This temperature gradient rapidly increases the pressure inside the CNB and forces the liquid to be expelled from the bottleneck (Figure 2.2B). Because of the pressure changes, the inner walls of the bottle experience a greater stress than the outer walls, creating a net force in the bottom part of the CNB motor (Figure 2.2C). This net force can produce a very directional motion during the first instants of stimulation, but as the fluid remains heated up, its effect will decrease, creating a velocity profile that is not constant in time. Figure 2.2D displays the z-component of the fluid velocity following the longitudinal profile of the

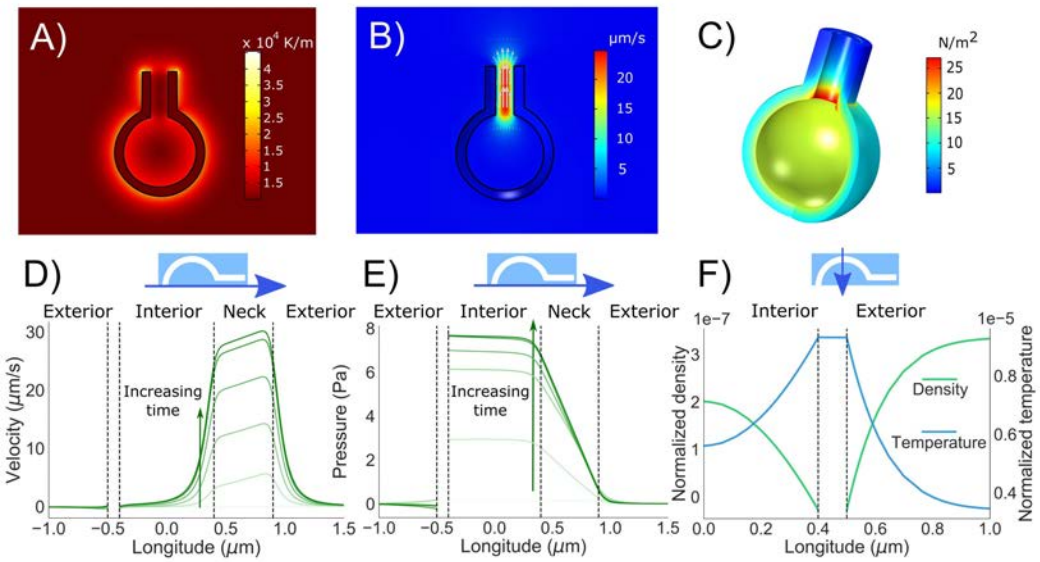

Figure 2.2: FEA simulation of the propulsion mechanism for the NIR-light-powered CNB motor. A) Temperature gradient and B) fluid velocity distribution of the CNB motor at 100 ns. C) Von Mises stress distribution caused by the changes in the pressure of the interior liquid at 100 ns. D) Line profile of the z-component of the fluid velocity in the vertical direction of the CNB motor from 0 ns to 10 ns in intervals of 2 ns. E) Pressure profile in the vertical direction of the CNB motor from 0 ns to 10 ns in intervals of 2 ns. F) Normalized density and temperature distribution in the horizontal direction of the CNB motor at 100 ns. Adapted from [1].

CNB motor during the first seconds of NIR light exposure. The acceleration of the fluid towards the outside, especially in the bottleneck, can be observed. Meanwhile, inside the bottle, the pressure greatly increases in a homogeneous manner due to the decrease in the density at a fixed volume (Figures 2.2E and 2.2F). The pressure changes rapidly and homogeneously within the CNB motor, even though the liquid is being expelled, except in the bottleneck, where it gradually becomes balanced.

Motion dynamics

In order to test this behavior experimentally, NIR light with a power in the range of $0 \sim 2.36$ W/cm^2 was used to illuminate the CNB motor, as regulation of the NIR laser intensity was expected to modulate its speed. The trajectories of the CNB motors under different power intensity were tracked and are shown in Figure 2.3A. The instantaneous velocity of the active CNB motor with respect to the non-active ones indicates a non-continuous mechanism of motion. For the active motion (showing the case of 1.36 W/cm^2 as an example), a high initial peak in the velocity occurs, which corresponds to the moment when most of the liquid is ejected from the interior of the CNB motor (Figure 2.3B), as described in Figure 2.2. After the first significant peak, several secondary peaks (reaching velocities higher than 10 μm/s) are observed, which could be explained by consecutive ejection events caused by the same mechanism. However, one should note that even though the speed decreases after the main peak, the baseline remains two times higher than the instantaneous Brownian speed, indicating an increase in the vibrations of the CNB motor. This instantaneous speed, however, should be carefully considered only for comparative purposes, and not be confused with the actual speed of the particle (especially in the passive case). The instantaneous speed, except in cases with very directional motion, possesses a strong component from Brownian fluctuations of the particle and its actual value depends on the frames per second (FPS) of the microscope. An optical microscope cannot have enough sensitivity to detect the actual Brownian speed, as very complex experimental setups are needed for this purpose[54].

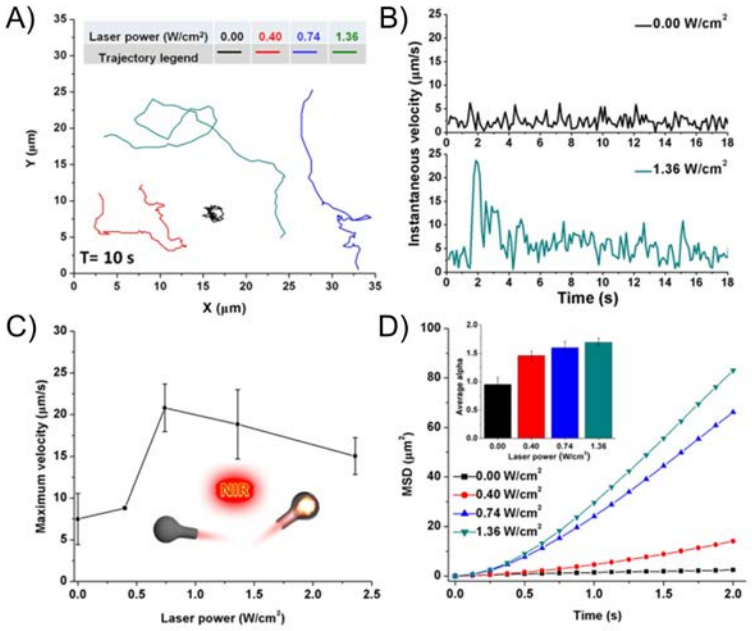

Figure 2.3: Analysis of the dynamics of the CNB motor. A) Trajectories of CNB motors irradiated by different powers of NIR light for 10 s. B) Instantaneous velocity of two CNB motors under irradiation by 0.00 W/cm^2 and 1.36 W/cm^2 NIR light for 18 s. C) Maximum velocity distribution of the CNB motors as a function of the NIR light power. D) Mean square displacement (MSD) and average alpha (α) of the CNB motors for different NIR light powers (inset image). Adapted from [1].

As the velocity of the particle was not constant, we analyzed the maximum velocity reached by the CNB motor as a representative parameter for quantifying the motion (Figure 2.3C). For a low laser power of 0.4 W/cm^2, the maximum velocity was not significantly different from that of Brownian motion (error bars in this case are too small to be seen). At this value, the temperature gradient was not sufficiently high to produce a velocity burst, although the CNB motor still moved with superdiffusive motion. At NIR laser powers higher than 0.74 W/cm^2, the maximum velocity was three-fold larger than that of Brownian motion and seems to become saturated at higher power intensities. Due to the complex propulsion mechanism of the CNB motor with a non-constant velocity, the MSD follows an anomalously trend of the form MSD $\sim \Delta t^{\alpha}$, with an α parameter reaching values of $1.6 \sim 1.7$ (Figure 2.3D inset). The NIR-activated CNB motors covered a wider area than the non-activated CNB motors ($\alpha = 1$), as can be inferred from the MSD. Typically, for nano-sized motors, the superdiffusive regime cannot be observed, and only enhanced diffusion motion can be seen since their rotational diffusion time is very small[28, 41]. In the case of the CNB motor, the superdiffusive regime is visible, which manifests in a significant improvement over constant-velocity nanomotors, as the area covered during motion can be larger. This departure from the common case can be understood through the large velocity bursts that the CNB motor experiences (Figure 2.3B). These strong forces cause Brownian motion to be hindered (and therefore, the theory of active Brownian motion cannot be applied) and lead to very directional superdiffusive movement.

An interesting effect was observed with NIR light powers of 2.36 W/cm^2. The CNB motors exploded, as the heated internal liquid was immediately ejected through the small open neck and the nanostructure could not withstand the internal pressure caused by this heated fluid (Figure 2.4). The instantaneous velocity profile demonstrates that the speed of the CNB motor rapidly increased and snapshots at different time-points showed that the structure was maintained before the explosion. However, after reaching the highest velocity point in this example (after 4.2 s), the bottle was de-

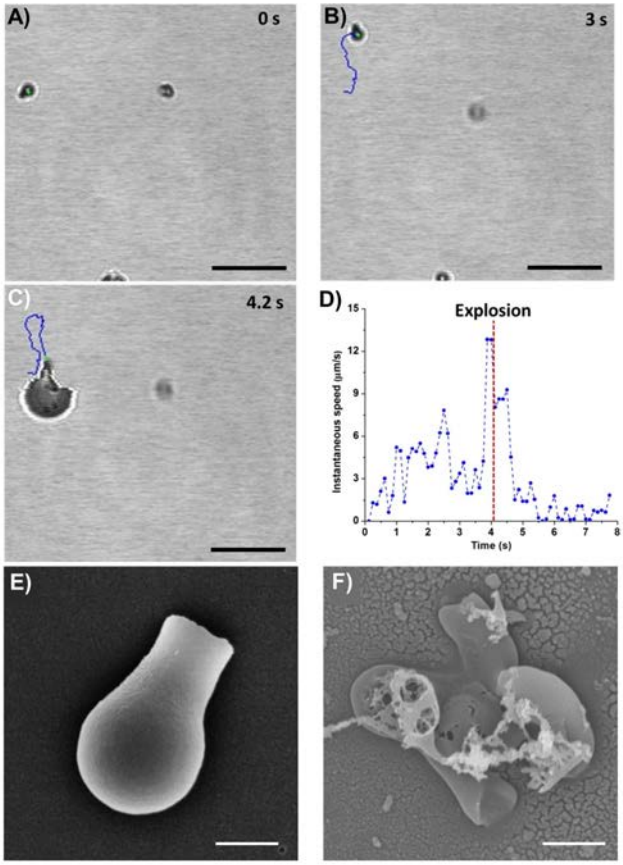

Figure 2.4: Analysis of the explosion even of a CNB motor. A-C) Time-lapsed images of the explosion process of CNB motor upon illumination with 2.36 W/cm^2 NIR light, scale bars = 10 μm. D) Instantaneous speed profile of the previous case. E-F) SEM images of CNB motor before (E) and after (F) explosion; scale bars = 500 nm. Adapted from [1].

stroyed, as the ejection of the heated liquid was not fast enough to balance out the internal pressure. SEM images in Figures 2.4E and 2.4F show the state of the CNB motor before and after the explosion.

The average angular velocity decreased upon increasing the NIR light power (Figure 2.5A), suggesting that high-power NIR light increased the directional motion of the CNB motor. The angular autocorrelation ($\langle \cos \Delta\theta \rangle$) shows that the CNB motors exposed to high-power NIR light (0.74 W/cm^2 and 1.36 W/cm^2) experienced directional motion with similar autocorrelation functions (Figure 2.5B). For a low laser power of 0.4 W/cm^2, autocorrelation was still observed but to a lesser extent, which could be related to the fact that these CNB motors do not show initial velocity bursts, as discussed in Figure 2.3B.

The speed of the CNB motor could be easily regulated by tuning the power of the NIR laser. The "on/off" motion of the CNB motor could be controlled by the "open/closed" states of the NIR light source (Figure 2.6). When the NIR laser was applied, consecutive pairs of off/on motion were tracked and analyzed (Figure 2.6A). In the absence of NIR illumination, the CNB motor showed Brownian motion. Upon irradiation by a 1.36 W/cm^2 NIR laser for 11.2 s, directional movement was immediately observed. Once the NIR laser was switched off at $t = 22.4$ s, the CNB motor rapidly decelerated, and its motion completely came back to Brownian motion. As expected from Figure 2.6B, the instantaneous velocity showed velocity bursts upon illumination with the NIR laser. Moreover, the instantaneous angular velocity decreased when the NIR laser was applied, indicating

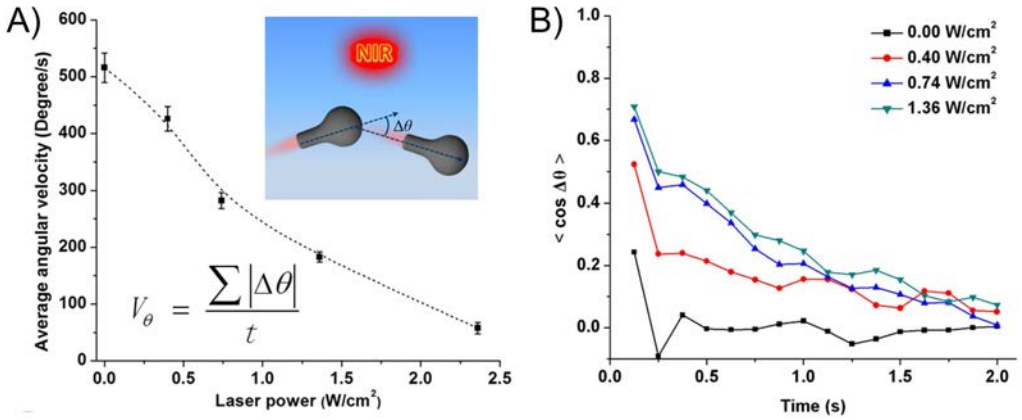

Figure 2.5: Directionality analysis of the CNB motor during NIR-light-powered propulsion. A) Average angular velocity of a CNB motor as a function of the NIR light power. The inset image is a schematic illustration of the swing-type motion of the CNB motor. B) Angular autocorrelation ($< \cos \Delta\theta >$) of the CNB motors. Adapted from [1].

a linear movement pattern. The MSD and $\langle \cos \Delta\theta \rangle$ of the CNB motor changed upon NIR light illumination in comparison with those under no irradiation. The behavior of the MSD changed from linear to a power law with an exponent of $\alpha = 1.6$ (Figure 2.6C), as also shown in Figure 2.3D. In addition, $\langle \cos \Delta\theta \rangle$ showed a decrease in the directional motion when the laser was shut off (Figure 2.6D).

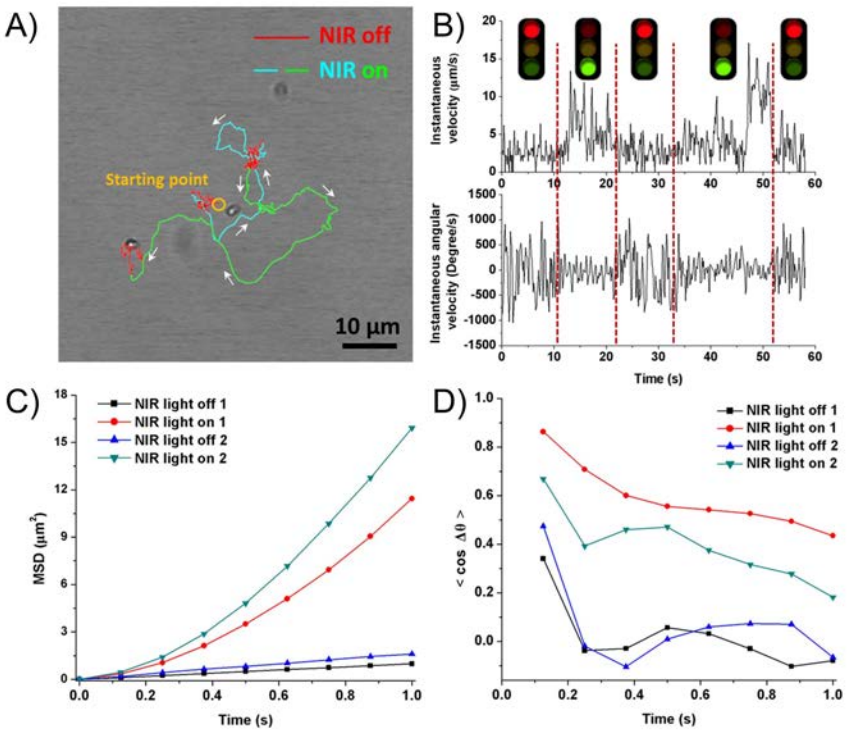

Figure 2.6: Analysis of the "on/off" motion of the CNB motor. A) Time-lapse images of the motion of a CNB motor regulated by switching a 1.36 W/cm^2 NIR light on and off over 58 s. B) Instantaneous velocity and instantaneous angular velocity of the CNB motor. C) MSD variation and D) $\langle \cos |\Delta\theta| \rangle$ variation during the on/off motion process. Adapted from [1].

3.2. Nanomotors based on mesoporous silica nanorods

Fabrication and characterization

This section deals with the motion analysis of non-spherical silica-based micromotors, self-propelled by inorganic catalytic reactions. Particularly, these motors are based on mesoporous silica nanorods (MSNRs), synthesized by a sol-gel method that uses Pluronic P123 as surfactant and yields nanorods with straight and cylindrical mesopores, longitudinally along their main axis. These nanorods are coupled with one or more metallic components that can catalyze reactions and become nanomotors in three different manners: i) nanorods sputtered with Pt to achieve an asymmetric coating over its surface (MSNR-Pt); ii) nanorods with Fe_2O_3 nanoparticles embedded inside their mesopores (MSNR-Fe); and iii) a combination of both, namely nanorods with Pt sputtered on their surface and Fe nanoparticles inside their pores (MSNR-Pt-Fe). Pt is one of the most widely used metals to catalyze the decomposition of H_2O_2 and generate motion of nano- and micro-structures, generally needing an asymmetric covering. Sputtering Pt ions over MSNRs induces such an asymmetric covering in half the surface that should generate some sort of motion, according to previous reports[7]. However, due to the elongated geometry of the MSNRs, it seems unlikely that such a lateral covering would induce an efficient directional motion; most likely, it would enhance the diffusivity of the nanorods, their active fluctuations and therefore the area covered. In order to improve the directionality, Fe_2O_3 nanoparticles were synthesized within the mesopores, similar to a previously reported strategy where enzymes were added inside micro-rods to achieve directional motion[40]. The reduction of Fe^{3+} to Fe^{2+} and the oxidation of Fe^{2+} to Fe^{3+} in a Fenton reaction could also generate motion. Finally, the combination of both species could yield an even more efficient and directional motion mechanism.

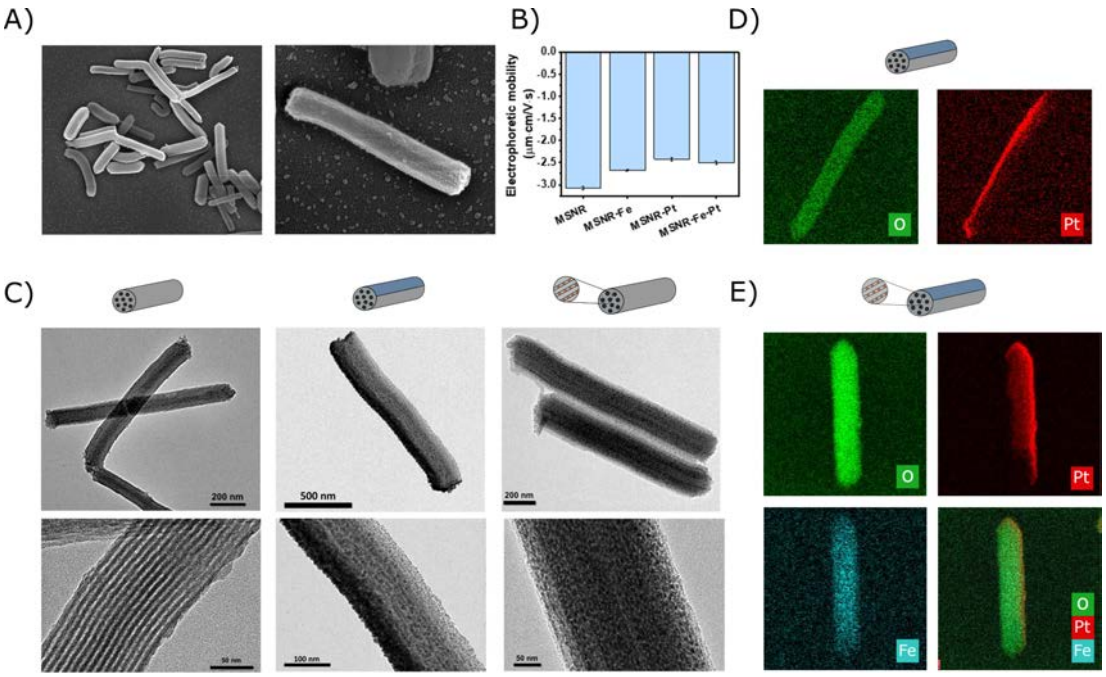

Figure 2.7: Characterization of the MSNRs motors under SEM, TEM, DLS and EDX. A) SEM images of MSNRs. B) Electrophoretic mobility of different types of MSRNs motors. C) TEM imaging of MSNRs, MSNRs sputtered with Pt (MSNRs-Pt) and MSNRs with Fe_2O_3 nanoparticles inside its mesopores (MSNRs-Fe). D) EDX mapping of MSNRs-Pt and E) MSNRs sputtered with Pt and Fe_2O_3 nanoparticles in its mesopores (MSNRs-Pt-Fe).

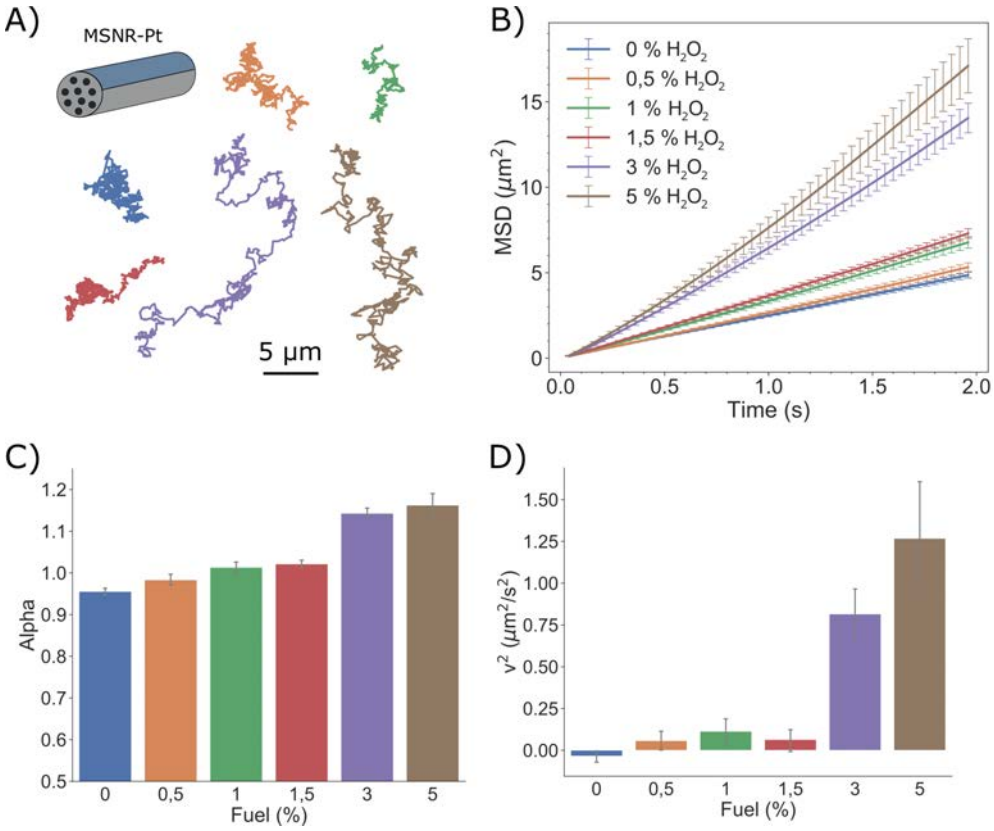

Figure 2.8: Analysis of motion of MSNR-Pt. A) Representative trajectories of the motors under different fuel concentrations and B) their corresponding MSDs. C) Performing a logarithmic fitting reveals increasing exponent α with fuel concentration indicating the presence of superdiffusive regime. D) Performing a quadratic fitting instead allows extracting the squared speed of the motors, showing only a modest positive value for higher fuel concentrations.

The three types of motors were characterized by SEM, TEM, DLS and EDX spectroscopy mapping (Figure 2.7). Figure 2.7A shows SEM images of the MSNRs, with an average length of 1.4 μm and diameter of around 200-300 nm. The electrophoretic mobility of Figure 2.7B shows that, as expected, the MSNRs had a negatively charged surface, as well as the three types of nanomotors considered, demonstrating that the addition of the metallic components did not alter the surface charge. Figure 2.7C shows TEM images of MSNRs (left), MSNR-Pt (center) and MSNR-Fe (right). The longitudinal mesopores of MSNRs, measuring about 8 nm, are clearly visible under high magnification. For MSNR-Pt, the half-coverage of Pt can be also observed, displaying a darker contrast where in the Pt sputtered region. Finally, in MSNR-Fe the mesopores are not visible, but a speckle-like pattern of darker spots can be attributed to the presence of Fe nanoparticles, as revealed by the EDX mapping presented in Figure 2.7E. Figure 2.7D also shows the distribution of oxygen (indicating the presence of silica) and Pt, clearly revealing its distribution on half of the surface, of MSNR-Pt. Finally, Figure 2.7E also displays the presence of Fe all along the surface of the nanorod, demonstrating the synthesis of Fe_2O_3 nanoparticles inside the MSNRs.

Motion dynamics

Motion of MSNR-Pt under the presence of hydrogen peroxide (H_2O_2) at different volume concentrations is shown in Figure 2.8. Both the representative trajectories and the MSDs clearly show that the area covered by the nanomotors increased with fuel concentration, indicating a catalytically induced motion (Figures 2.8A and 2.8B). For a nanoparticle of a non-spherical shape, such as a

nanorod, the translation and rotational diffusions are coupled with each other in our frame of reference, as the viscous drag forces depend on the orientation of the particle. From the frame of reference of the nanorod these diffusivities can be decoupled from rotations, displaying greater translational diffusion along its main axis. However, as optical microscopy does not allow to precisely identify the orientation of strongly fluctuating nanorods, we cannot study the diffusion along different directions separately and a global approach is needed, considering the MSNRs as point particles that follow the Einstein-Smoluchowski equation of diffusion. Nonetheless, when fuel is added to a cylindrical nanomotor, it is advisable to study its motion dynamics using a more general formula, assuming $\mathrm{MSD}(\Delta t) = D\Delta t^{\alpha}$. This analysis was performed in Figure 2.8C, which shows the result of α after a fitting to the previous equation. All fuel concentrations up to 1.5% show roughly $\alpha = 1$, indicating normal diffusive behavior. However, it is possible that while the MSD remained linear, the diffusions of the MSNR-Pt were enhanced due to the catalytic activity. Only fuels at 3% and 5% showed α values higher than 1, indicating superdiffusive behavior. In general, nano- and micromotors that show superdiffusion follow the well-known equation of the form $\mathrm{MSD}(\Delta t) = 4D_t\Delta t + v^2\Delta t^2$ in 2D, where v is the propulsive speed of the particle and D_t its translational diffusion. Depending on the ratio between these two terms, a fitting of the type Δt^{α} to the MSD will not yield $\alpha = 1$ or $\alpha = 2$, but some value in between, as both the linear and quadratic terms contribute to the curvature. Therefore, if we assume that these MSNR-Pt can achieve a propulsive regime with α between 1 and 2 we can perform a fitting to the quadratic equation and extract the propulsive speed, as reported in Figure 2.8D. In this case, and throughout the section, the square value of the propulsive speed is plotted, as cases with $v = 0$ can yield negative square speeds that have no physical meaning. It can be seen that higher speed concentrations are showing a positive speed, although their values are not high and their variability is large. This difference seems small compared to the very clear differences observed in the representative trajectories of Figure 2.8A and their corresponding MSDs, thus a more in-depth analysis was needed.

Looking at the distribution of α values over the whole population of nanomotors can improve the analysis. Figure 2.9A shows this distribution for a fuel concentration of 5%. We can see that there are two main peaks in the density function, which is indeed confirmed by performing a bimodal model fitting to the histogram. The first peak represents nanomotors that move diffusively, that is, with α very close to 1, but might have an enhanced diffusion thanks to the catalytic activity. The second peak of higher α represents a sub-population of nanomotors that move in a superdiffusive manner and probably with higher directionality. It is clear then, that we cannot treat these two populations with the same statistical approach, as the represent completely different types of motion. This difference might be due to the inhomogeneity of the Pt coating, giving rise to different types of asymmetry in the covering that favor a specific kind of motion. For this reason, we decided to set a threshold of $\alpha = 1.2$ for the statistical treatment of the nanomotors. On the one hand, if $\alpha < 1.2$, a nanomotor was considered as moving diffusively and approximated to $\alpha = 1$ to extract the translational diffusivity. On the other hand, if $\alpha > 1.2$, the nanomotors were assumed to move propulsively and fitted to a quadratic equation to extract their propulsive speed.

Figure 2.9B shows the extracted diffusion coefficient of the sub-population of MSNR-Pt with $\alpha < 1.2$. As expected, even if their motion is diffusive in nature, the diffusivities were actually enhanced with respect to the control case (0% fuel), due to the catalytic reaction of Pt with H_2O_2, reaching up to a 3-fold increase. Performing a quadratic fitting to the MSDs of the highest two concentrations (which clearly show this sub-population division), we can see that the sub-population of motors with $\alpha < 1.2$ do not have propulsive speed, as expected, but those with $\alpha > 1.2$ do show a significant speed. Compared with the results of Figure 2.8D, we can see that the low speed reported in that case was a result of the mixing up of the two sub-populations, further justifying the approach

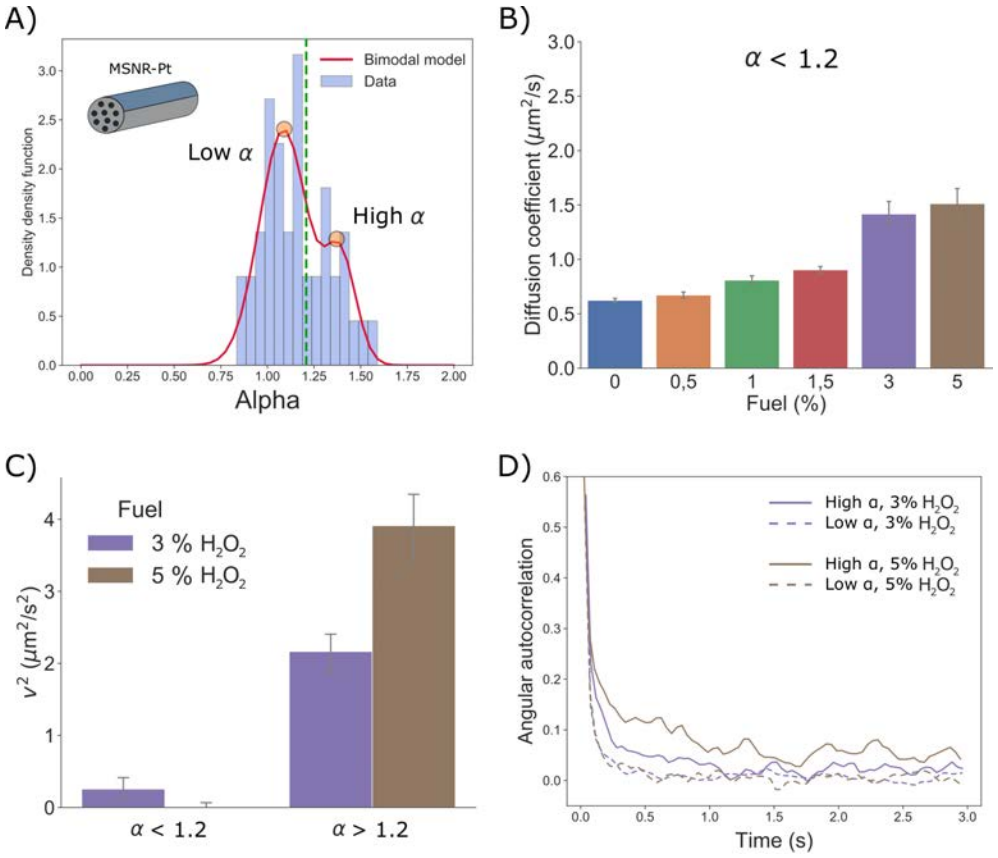

Figure 2.9: Analysis of subpopulations of MSNR-Pt. A) The distribution of MSD exponents (α) for a fuel concentration of 5% revels that there are two subpopulations of motors, some behaving diffusively ($\alpha = 1$) and others superdiffusively ($\alpha > 1$). Green dashed line indicates the threshold. B) Approximating all motors with $\alpha < 1.2$ to a diffusive behavior with $\alpha = 1$ shows that for higher fuel concentrations, there is an enhanced diffusion of the motors. C) If we approximate the MSDs to a quadratic equation reveals that the sub-population of motors behaving superdiffusively have a squared speed roughly four times higher than the one reported in the global analysis. D) The angular autocorrelation functions of both sub-populations for higher fuel concentrations show that the high α sub-population has a higher directionality than the low α one, which shows no correlation.

of separating both sub-populations, as they show different dynamics. Finally, the angular autocorrelation (Figure 2.9D) demonstrates that the high-α sub-population has more directional motion. Dashed lines, corresponding to low-α cases, show no autocorrelation, typical of Brownian fluctuations, while straight lines that correspond to high-α nanomotors display a long-term autocorrelation, specially for the 5% case.

Figure 2.10 shows now the same type of analysis for MSNR-Fe nanomotors. The representative trajectories and the MSDs of Figures 2.10A and 2.10B already indicate modest changes when increasing the concentration of fuel. Indeed, a linear fitting to the MSD shows small increases of the diffusion coefficient compared to the control case (Figure 2.10C). A quadratic fitting of the highest fuels cases also demonstrate the presence of two sub-populations of nanomotors (Figure 2.10D), but the squared speed of the ones with high-α is almost half of the values reported for MSNR-Pt (Figure 2.9D). Therefore, the presence of Fe_2O_3 nanoparticles inside the mesopores seemed to slightly increase the diffusivity of the nanorods, but not in a strong and directional manner as initially hypothesized.

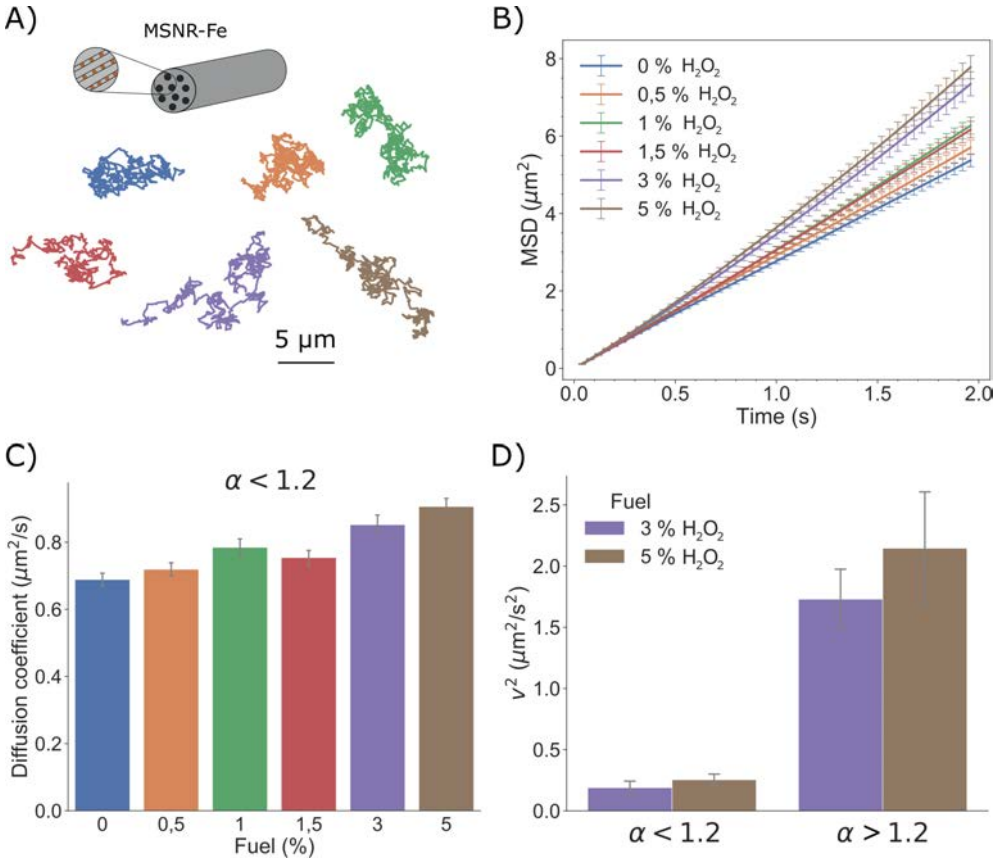

Figure 2.10: Analysis of motion of MSNRs-Fe. A) Representative trajectories of the motors under different fuel concentrations and B) their corresponding MSDs. C) Approximating all motors with $\alpha < 1.2$ to a diffusive behavior with $\alpha = 1$ shows a very modest increase of the diffusion coefficient with fuel concentration. D) Approximating both sub-populations to a quadratic equation shows that only those with $\alpha > 1$ have a small positive speed squared.

The analysis of MSNR-Fe-Pt nanomotors, using a combination of both catalytic mechanisms is presented in Figure 2.11. Figure 2.11A and 2.11B show directional trajectories for all of the fuel concentrations and clear differences in the MSDs, which over the course of 2 s can cover a much wider area than the previous cases. Indeed, the diffusion coefficient of the low-α sub-population and the squared speed of the high-α sub-population display the same trend, with increasing values for higher fuel concentrations, with a significant peak for a fuel concentration of 3%. It is striking that such an increment occured for this concentration and not for the highest one, but some sort of inhibition mechanism related to increased reactivity (as both catalysis, Pt and Fe, are present) could be taking place, as the diffusion for 5% is lower than for 1.5%. In any case, it is clear that motion for 3% of fuel concentration was highly efficient, yielding large speeds for directional motors and a greatly enhanced diffusion for non-directional ones.

Finally, Figure 2.12A and 2.12B compare the best two cases of propulsive motion for MSNR-Pt (with 5% of fuel) and MSNR-Fe-Pt (with 3% of fuel). For low-α sub-populations, there is no speed, as expected, while high-α sub-populations of MSNR-Fe-Pt show a two-fold increase in squared speed compared to MSNR-Pt. We hypothesize that the presence of the Pt half-coverage could yield some directional motors (as discussed in Figure 2.8 and reported in 2.12A), a behavior that becomes heightened by the presence of Fe_2O_3 nanoparticles inside the pores. Fe_2O_3 nanoparticles, by themselves, did not produce highly directional motion (as discussed in Figure 2.10), but the directional symmetry breaking caused by the motion greatly enhanced the speed of the MSNR-Pt-Fe.

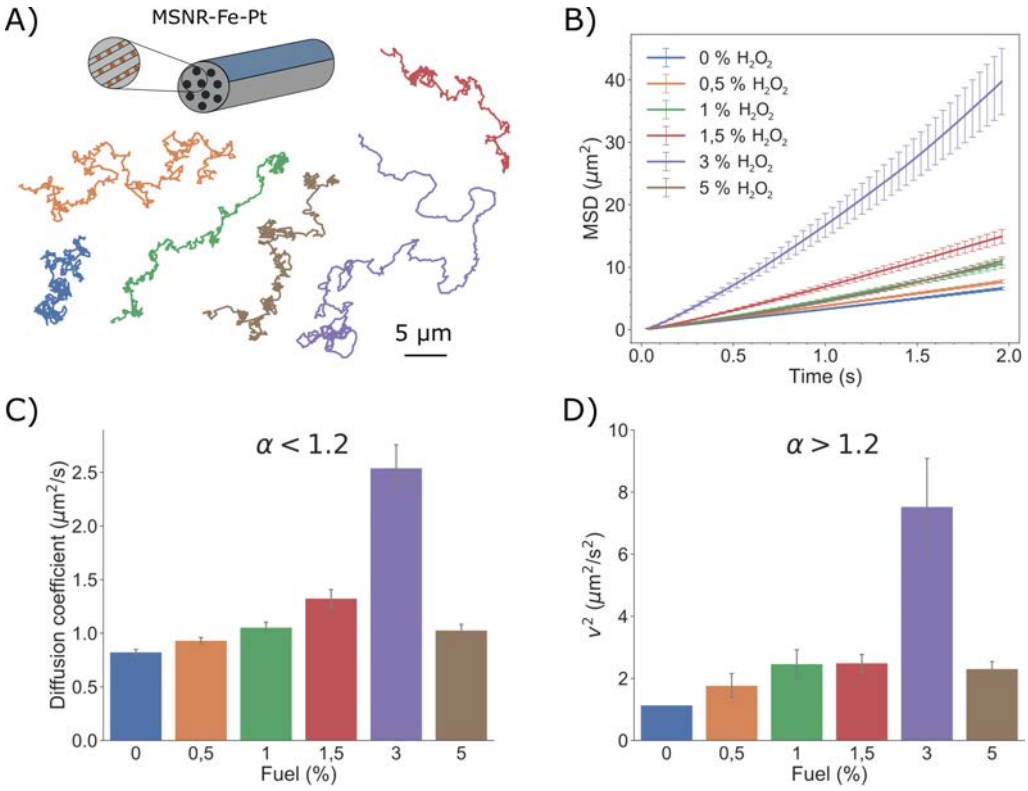

Figure 2.11: Analysis of motion of MSNRs-Fe-Pt. A) Representative trajectories of the motors under different fuel concentrations and B) their corresponding MSDs. C) Approximating the sub-population with $\alpha < 1.2$ to a diffusive behavior with $\alpha = 1$ shows the highest increase of enhanced diffusion coefficient for a concentration of 3%. D) Approximating the sub-population with $\alpha > 1.2$ to a quadratic equation shows the same behavior, with positive squared speeds even for low fuel concentrations (notice that the positive value for 0% corresponds to a single outlier that could be most likely due to statistical fluctuations because of MSD variability).

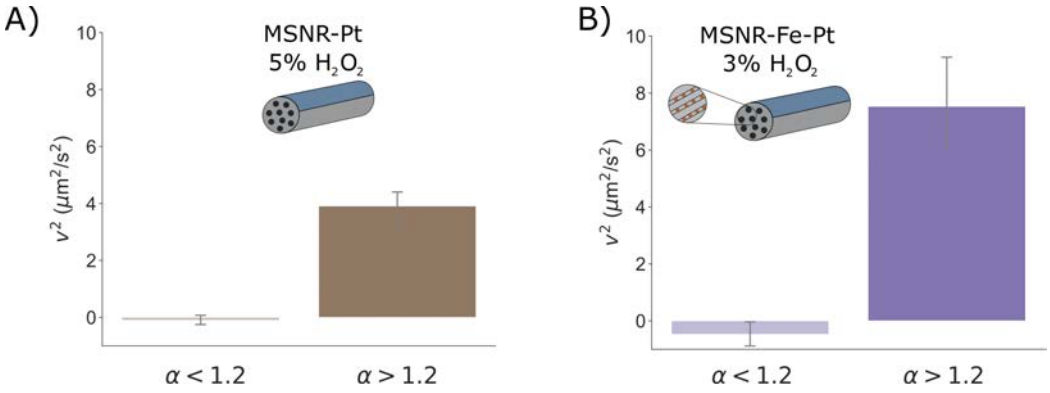

Figure 2.12: Comparison of the best motions of MSNR-Pt and MSNR-Fe-Pt. A) Speed squared of the best concentration of the MSNR-Pt motors (5%) compared with B) the one of MSNR-Fe-Pt (3%), showing that the combination of both metallic materials yields a two-fold increase in speed.

3.3. Enzymatic micromotors with exponentially decaying speed

Active Brownian motion with constant speed

One of the key aspects of the theory of active Brownian motion is the assumption of constant speed. A micro- or nanomotor has an intrinsic power source (as they are self-propelled), which is assumed to be constant in time. If this propulsion comes from a chemical reaction catalyzed by an enzyme or an inorganic metal, such as Pt, this assumption could be correct, as demonstrated by previous works[28]. However, in other realistic cases, there could be several reasons for which this assumption is not necessarily met. Several possibilities could be that the reaction on the surface of the particle is not fast enough to be considered continuous; the shape of the motor is not homogeneous, leading to different velocity profiles at the surface; or the efficiency of the reaction decays over time, also decreasing the speed of the particle.

In this section, we will focus on the last example, which had been previously reported, but never analyzed in depth[55]. For that purpose, we will consider urease-powered micromotors of 1 μm of radius made of hollow silica spheres. The catalytic reaction of urease in the presence of urea releases ammonia, which increases the pH of the solution very rapidly[55]. It has been proposed that self-electro-diffusiophoresis could play a relevant role in the motion mechanism of these motors, and it is therefore heavily influenced by this change of pH[47–49]. This decreases the effective reaction rate of the enzymes, leading to an exponentially decreasing speed that can be analytically described. In order to understand these issues more robust types of analyses are necessary, since in many cases extracting clear and useful metrics is not a trivial task. Here, we will focus particularly on the phenomenon that takes place when ergodicity of the system is broken by an exponentially decaying speed, what parameters can be extracted from the analysis in that case, and what experimental implications it might have, providing some hints on the experimental conditions that need to be met to reach a certain level of accuracy in a non-constant-velocity scenario.

When an active Brownian particle meets the necessary requirements, its motion dynamics can be well characterized by its MSD. The following equation relates the MSD of an active Brownian particle moving in 2D with several parameters of interest, such as the diffusion coefficient, the propulsion speed, or the rotational diffusion time:

$$\mathrm{MSD}(\Delta t) = 4D_t\Delta t + 2v_p^2\tau_r^2\left(\frac{\Delta t}{\tau_r} + e^{-\frac{\Delta t}{\tau_r}} - 1\right), \tag{2.1}$$

where D_t is the diffusion coefficient, v_p is the propulsion speed, τ_r is the rotational diffusion time, defined as the inverse of the rotational diffusion coefficient, and Δt is the elapsed time. This equation hols for any self-propulsive motor of any kind, as long as its speed can be considered constant and is affected by Brownian fluctuations without any hindrance. In layman terms, it simply describes the MSD of a self-propelled particle that re-orients its propulsion direction in a random manner due to fluctuations of the water molecules around it. It is important to notice that this equation holds regardless the size of the particle. However, since the rotational diffusion time, τ_r depends on the radius of the particle, the scaling of the function will be different depending on its size. In practical terms, this means that a big particle, which is not so much affected by Brownian fluctuations, will present a more directional motion, since its directionality will not be disturbed too easily. A small particle, on the other hand, will suffer greatly from randomizations of its position and direction, and its motion will look like classical diffusion.

Normally, two limits of this equation are considered to separately tackle the analysis of these two extreme cases:

$$\text{MSD}(\Delta t) = 4D_e\Delta t \qquad \text{if } \Delta t \gg \tau_r, \tag{2.2a}$$
$$\text{MSD}(\Delta t) = 4D_t\Delta t + v_p^2\Delta t^2 \qquad \text{if } \Delta t \ll \tau_r, \tag{2.2b}$$

where D_e is the enhanced diffusion coefficient that should be larger than D_t, as it encompasses the increased fluctuations caused by the activity of the chemical reaction.

This set of equations are, in most of the cases, a good enough approximation to characterize the motion of these types of particles and compare their efficiency by considering the values of D_e and v_p, for nano- and micromotors, respectively. Nevertheless, there are many hidden assumptions in the application of these equations that might be easily broken without realization. One of these hidden assumptions is ergodicity. An ergodic system in probability theory is such a system for which the time-average and ensemble-average of a particular property are equivalent. For nano- and micromotors, this would mean that it is the same to perform the MSD of a single trajectory by time-averaging or averaging the MSDs of many different particles, as they are statistically indistinguishable. Even more, several trajectories of different particles could simply be concatenated to form a single long trajectory, which is then time-averaged to calculate the MSD, and the results would be equally valid. This ergodicity property is crucial for the field as it gives a lot of experimental flexibility: only a few particles need to be recorded, as long as it is done for a long time; or many particles could be recorded with very short videos. In any of the two cases, if there are enough data points to overcome the tracking errors (strongly dependent on the FPS and the quality of the videos, so there is not a single rule of thumb), reliable results could be obtained.

Speed must be constant to ensure ergodicity. In the case of an exponentially decaying speed, not all trajectories can be consider indistinguishable. Moreover, if during the whole duration of a single trajectory the speed has decreased significantly, a time-average of the MSD will yield a result that cannot be studied with Equation 2.1. In this section we will try to find an analytical solution for this problem, a new MSD equation that encompasses this exponentially decaying speed to help analyze these types of experimental cases.

Active Brownian particle model with exponentially decreasing speed

First, we consider an active Brownian particle problem where the speed of the particle decays exponentially, of the form $v_p = v_0 e^{-\beta t}$, following:

$$\begin{aligned}
\dot{x}(t) &= v_0 e^{-\beta t}\cos(\theta(t)) + \sqrt{2D_t}\xi_x(t),\\
\dot{y}(t) &= v_0 e^{-\beta t}\sin(\theta(t)) + \sqrt{2D_t}\xi_y(t),\\
\dot{\theta}(t) &= \sqrt{2D_\theta}\xi_\theta(t),
\end{aligned} \tag{2.3}$$

where x, y are the Cartesian coordinates and θ the polar coordinate, $\dot{x}$, $\dot{y}$, $\dot{\theta}$ are their time derivatives, D_t is the translational diffusion coefficient, D_θ is the rotational diffusion coefficient, v_p is the

propulsive speed of the particle, v_0 is the initial speed of the particle, β is the inverse of a characteristic time that modulates the exponential decrease of the particle speed, and $\xi_i(t)$ are uncorrelated Gaussian white noise functionals with $\langle \xi_i(t) \rangle = 0$ and $\langle \xi_i(t)\xi_j(s) \rangle = \delta_{ij}\delta(t-s)$. In this case, obtaining the MSD is not straightforward because the system is no longer ergodic. Since the speed of the particle is not constant in time, the ensemble-average MSD (EAMSD) and time-average MSD (TAMSD) will not be the same and will strongly depend on the initial speed of the particle, v_0, as well as the total length of the trajectory (since TAMSD averages over the whole trajectory, with a different speed at each point). Moreover, different particles might have completely different speeds at the time of recording, making the calculation of the EAMSD statistically unreliable. Let's now consider the definition of the MSD in two dimensions, starting at a time t_0 with a time step Δt:

$$\mathrm{MSD}(t_0, \Delta t) = \left\langle (x(t_0+\Delta t) - x(t_0))^2 \right\rangle + \left\langle (y(t_0+\Delta t) - y(t_0))^2 \right\rangle . \tag{2.4}$$

It is crucial to notice that $\langle \cdot \rangle$ here represents only the ensemble average of a set of particles with the same characteristics, not the time-average, which will be performed later. It is also important to notice one assumption that will be taken throughout the derivation: all particles are considered to have the same initial velocity, v_0 and the same decay parameter, β. This might not be always the case experimentally, especially if particles are recorded at different moments. For the time being, we will consider that all particles correspond to fresh experiments where we can assume that the initial conditions are equal. The parts inside the squared brackets in the previous equation can be expressed as an integral of the terms of Equation 2.3. For instance:

$$x(t_0+\Delta t) - x(t_0) = \int_{t_0}^{t_0+\Delta t} dt' \Big(v_0 e^{-\beta t'} \cos(\theta(t')) + \sqrt{2D_t}\xi_x(t') \Big). \tag{2.5}$$

By squaring this integral and averaging over the ensemble of particles, we obtain for the x term:

$$\begin{aligned}
\left\langle (x(t_0+\Delta t) - x(t_0))^2 \right\rangle = \int_{t_0}^{t_0+\Delta t}\int_{t_0}^{t_0+\Delta t} dt'ds' \Big\langle \Big(& e^{-\beta(t'+s')} v_0^2 \cos(\theta(t'))\cos(\theta(s')) + \\
& 2D_t \xi_x(t')\xi_x(s') + \\
& \cancelto{0}{e^{-t'\beta} v_0 \cos(\theta(t'))\sqrt{2D_t}\xi_x(s')} + \\
& \cancelto{0}{e^{-s'\beta} v_0 \cos(\theta(s'))\sqrt{2D_t}\xi_x(t')} \Big) \Big\rangle = \\
= \int_{t_0}^{t_0+\Delta t}\int_{t_0}^{t_0+\Delta t} dt'ds' \Big\langle \Big(& e^{-\beta(t'+s')} v_0^2 \cos(\theta(t'))\cos(\theta(s')) + \\
& 2D_t \xi_x(t')\xi_x(s') \Big) \Big\rangle = \\
= \int_{t_0}^{t_0+\Delta t}\int_{t_0}^{t_0+\Delta t} dt'ds' \Big\langle \Big(& e^{-\beta(t'+s')} v_0^2 \cos(\theta(t'))\cos(\theta(s')) \Big) \Big\rangle + \\
& 2D_t \Delta t.
\end{aligned} \tag{2.6}$$

Here, we have removed some terms due to the properties of the Gaussian noise (defined above) when averaging. Therefore, by analogy for the y component, Equation 2.4 yields:

$$\begin{aligned}\text{MSD}(t_0,\Delta t) &= \left\langle (x(t_0+\Delta t)-x(t_0))^2\right\rangle + \left\langle (y(t_0+\Delta t)-y(t_0))^2\right\rangle = \\ &= \int_{t_0}^{t_0+\Delta t}\int_{t_0}^{t_0+\Delta t} dt'ds' < \left(e^{-\beta(t'+s')}v_0^2\cos(\theta(t'))\cos(\theta(s'))\right) > + \\ &+ \int_{t_0}^{t_0+\Delta t}\int_{t_0}^{t_0+\Delta t} dt'ds' < \left(e^{-\beta(t'+s')}v_0^2\sin(\theta(t'))\sin(\theta(s'))\right) > + \\ &+ 4D_t\Delta t.\end{aligned} \tag{2.7}$$

Developing the cosines and sines multiplications into sums of cosines following trigonometric relations, allows us to rewrite Equation 2.7 as:

$$\text{MSD}(t_0,\Delta t) = v_0^2\int_{t_0}^{t_0+\Delta t}\int_{t_0}^{t_0+\Delta t} dt'ds'e^{-\beta(t'+s')} < \cos(\theta(t')-\theta(s')) > +4D_t\Delta t. \tag{2.8}$$

To solve the first term, we need to recall that both angle variables follow a normal distribution, and thus, their difference will also follow a normal distribution. We define the new statistical variable $\eta = \theta(t') - \theta(s')$, which has an average $\eta_0 = 0$, since $\theta(s'=0) - \theta(t'=0) = \theta(0) - \theta(0) = 0$. Therefore, expressing the ensemble average as an integral over all the possible initial states of the system given by the probability density function, we obtain:

$$\begin{aligned}\left\langle\cos(\theta(t')-\theta(s'))\right\rangle &= \int_{-\infty}^{\infty}\cos(\eta)\frac{e^{-\frac{(\eta-\eta_0)^2}{2\langle\eta^2\rangle}}}{\sqrt{2\pi\left\langle\eta^2\right\rangle}} = \\ &= \mathbb{R}\left\{\int_{-\infty}^{\infty}e^{i\eta}\frac{e^{-\frac{(\eta)^2}{2<\eta^2>}}}{\sqrt{2\pi\left\langle\eta^2\right\rangle}}\right\} = e^{\frac{\left\langle\eta^2\right\rangle}{2}}\end{aligned} \tag{2.9}$$

The expression of $\left\langle\eta^2\right\rangle$ still needs to be defined. By using the integration of the angle $\dot{\theta}(t)$ in Equation 2.3, in an analogous manner to the development in Equation 2.5, we obtain:

$$
\begin{aligned}
\langle \eta^2 \rangle &= \langle (\theta(t') - \theta(s'))^2 \rangle = \langle \theta^2(t') + \theta^2(s') - 2\theta(t')\theta(s') \rangle \\
&= 2D_\theta < \int_{t_0}^{t'} \int_{t_0}^{t'} dt'' dt''' \xi_\theta(t'') \xi_\theta(t''') + \int_{t_0}^{s'} \int_{t_0}^{s'} ds'' ds''' \xi_\theta(s'') \xi_\theta(s''') \\
&\quad - 2 \int_{t_0}^{t'} \int_{t_0}^{s'} dt'' ds'' \xi_\theta(t'') \xi_\theta(s'') >= \\
&= 2D_\theta \int_{t_0}^{t'} \int_{t_0}^{t'} dt'' dt''' \delta(t'' - t''') + \int_{t_0}^{s'} \int_{t_0}^{s'} ds'' ds''' \delta(s'' - s''') \\
&\quad - 2 \int_{t_0}^{t'} \int_{t_0}^{s'} dt'' ds'' \delta(t'' - s'') = \\
&= 2D_\theta t' + 2D_\theta s' - 4D_\theta \int_{t_0}^{t'} \int_{t_0}^{s'} dt'' ds'' \delta(t'' - s'').
\end{aligned}
\tag{2.10}
$$

The last term in Equation 2.10 depends on how the times t' and s' are located with respect to each other:

$$
\begin{aligned}
t' > s': \quad \int_{t_0}^{t'} \int_{t_0}^{s'} dt'' ds'' \delta(t'' - s'') &= \int_{t_0}^{s'} ds'' \left[\int_{t_0}^{s''} dt'' \delta(t'' - s'') + \int_{s''}^{t''} dt'' \delta(t'' - s'') \right] = \\
&= \int_{t_0}^{s'} ds''(1 + 0) = s'
\end{aligned}
\tag{2.11}
$$

$$
\begin{aligned}
s' > t': \quad \int_{t_0}^{t'} \int_{t_0}^{s'} dt'' ds'' \delta(t'' - s'') &= \int_{t_0}^{t'} ds'' \left[\int_{t_0}^{t''} dt'' \delta(t'' - s'') + \int_{t''}^{s''} dt'' \delta(t'' - s'') \right] = \\
&= \int_{t_0}^{s'} ds''(1 + 0) = t'.
\end{aligned}
\tag{2.12}
$$

Then, joining the results of the two previous equations:

$$
\begin{aligned}
t' > s': \quad & 2D_\theta t' + 2D_\theta s' - 4D_\theta s' = 2D_\theta(t' - s') > 0 \\
s' > t': \quad & 2D_\theta t' + 2D_\theta s' - 4D_\theta t' = 2D_\theta(s' - t') > 0,
\end{aligned}
\tag{2.13}
$$

we can see that both scenarios yield positive values. Therefore:

$$
< \eta^2 >= 2D_\theta |t' - s'|. \tag{2.14}
$$

Adding these results to Equation 2.8, we have:

$$\begin{aligned}\mathrm{MSD}(t_0,\Delta t) &= v_0^2\int_{t_0}^{t+\Delta t}\int_{t_0}^{t+\Delta t} dt'ds' e^{-\beta(t'+s')}e^{-D_\theta|t'-s'|} + 2D_t\Delta t = \\ &= v_0^2\int_{t_0}^{t+\Delta t} dt'\left[\int_{t_0}^{t'} ds' e^{-\beta(t'+s')-D_\theta(t'-s')} + \int_{t'}^{t+\Delta t} ds' e^{-\beta(t'+s')+D_\theta(t'-s')}\right] + \\ &+ 4D_t\Delta t = \frac{v_0^2 e^{-2\beta t_0}}{D_\theta^2-\beta^2}\left[2e^{-\Delta t(\beta+D_\theta)} - e^{-2\beta\Delta t} - 1 + \frac{D_\theta}{\beta}\left(1-e^{-2\beta\Delta t}\right)\right] + \\ &+ 4D_t\Delta t.\end{aligned} \tag{2.15}$$

By comparing this equation with Equation 2.1, we can see that in this case there is no dependency on the initial time or any other parameters that might be related to initial conditions. In the exponentially decreasing speed case, this dependency is patent in two parameters: the initial time, t_0, and the initial speed at that time, v_0. Due to this dependency on the initial time, it is clear that a time-averaging of this function will yield something different. That is, the EAMSD and TAMSD are not equivalent[1]. Indeed, we have:

$$\begin{aligned}\mathrm{TAMSD}(\Delta t) &= \frac{1}{T-\Delta t}\int_0^{T-\Delta t} dt_0 \mathrm{MSD}(t_0,\Delta t) = \\ &= \frac{v_0^2}{D_\theta^2-\beta^2}\left[2e^{-\Delta t(\beta+D_\theta)} - e^{-2\beta\Delta t} - 1 + \right. \\ &\left. \frac{D_\theta}{\beta}\left(1-e^{-2\beta\Delta t}\right)\right]\frac{1-e^{-2\beta(T-\Delta t)}}{2\beta(T-\Delta t)} + 4D_t\Delta t,\end{aligned} \tag{2.16}$$

where T is the total time the particle was tracked and Δt here represents the time between steps (the inverse of the FPS).

Experimental case

In practice, this equation would be too complex to fit with experimental data, resulting in a dead-end. However, here we propose an approximation of this equation, based on splitting the trajectory in smaller segments, that would allow us to extract the motion parameters, even if the particle loses speed fast. To show this, we present in Figure 2.13 an experimental example of an enzymatically propelled micro-particle of $R = 1\ \mu$m with an exponentially decreasing speed, based on a previous work[55]. In this case, we recorded a 9 min video and split it in a sequence of periods of 30 s where we alternated recording and pausing to re-focus the particle. We refer to each period of recording as T_i as in Figure 2.13A. In Figure 2.13B we show the trajectory of this particle for the first 30 s and the last 30 s of

[1]It is trivial to see how in the general case of Equation 2.1, both types of MSDs are equivalent. Since the TAMSD is defined as a time integral over the initial time, divided by the length of the integration path, as in Equation 2.16, such time-averaging would not produce any change in the MSD formula. The only time dependeny remains on the time step, Δt, which is independent on the initial time.

recording, showing a clear decrease in speed after 500 s, since the trajectory has shrunk. A reduction in the covered area means that the TAMSD will also decrease over time, as represented by the dashed lines in Figure 2.13C, which decrease in each recording step. By fitting each TAMSD (solid lines) and extracting the speed, we can see how it decays exponentially with time (Figure 2.13D) until it reaches a near 0 propulsive speed. This effect is also observed after calculating the instantaneous speed of the particle along each video. We can see how the instantaneous speed also decreases exponentially with time, but it has a plateau different from 0, since the instantaneous speed also considers the effect that arises from Brownian motion.

In order to find a method of analysis that deals with this kind of time-dependent behavior, we can try to expand Equation 2.16 with a Taylor approximation. In that case, we can separate it into three different components: i) a linear term coming from the Brownian fluctuations; ii) an exponential term (between square brackets) that strongly depends on the parameter β and D_θ; and iii) a correction term that depends on β but also on the length of the video, T, termed $C(T, \beta, \Delta t)$. Since β is usually a small parameter (in our experiment $\beta \sim \mathcal{O}(-2)$ s^{-1}) and considering that $\Delta t/\tau_r \sim 0$, we can perform a Taylor expansion on the exponential (propulsive) terms between square brackets, from which we obtain, up to third order:

$$\mathrm{TAMSD}(\Delta t) = \underbrace{4D_t\Delta t}_{\text{linear term}} + \underbrace{v_0^2\left[\Delta t^2 - \frac{1}{3}\left(D_\theta + 3\beta\right)\Delta t^3\right]}_{\text{propulsive term}}\underbrace{C\left(T, \beta, \Delta t\right)}_{\text{correction factor}}, \tag{2.17}$$

where we define the correction factor as:

$$C(T, \beta, \Delta t) = \frac{1}{T - \Delta t}\left(\frac{1 - e^{-2\beta(T-\Delta t)}}{2\beta}\right). \tag{2.18}$$

From this approximation, depending on the characteristics of the system several approaches can be followed. If the parameter β, that characterizes how fast the particle loses speed, is large, meaning that the particle loses speed very fast, the calculation of the TAMSD will be strongly influenced by the correction factor, since the speed of the particle will be very different at the beginning and the end of the trajectory and the values of $\boldsymbol{r}(t)$ would be incorrectly averaged. This undesirable effect could be corrected by recording short videos in which the speed does not change significantly and the TAMSD could be more reliably calculated, as we report in Figure 2.13. However, we want to emphasize here that, even if we divide the whole trajectory into smaller segments, the system remains non-ergodic, and we are simply deciding to approximate it as a ergodic one. Ultimately, how much the TAMSD is affected by the exponentially decaying speed will depend on each specific case, and also on the length of the recorded trajectories, so the effect of the correction factor function should be carefully analyzed.

Therefore, it is important to understand that the deviation from the constant speed case can change the analysis of the MSD to obtain reliable results. In this particular case, it is especially difficult to extract motion parameters in an accurate manner, not only to compare active particle's motion with different fuel concentrations, but also to understand their lifetime and motion mechanisms, and to gain feedback on how to perform the experiments. As a first approach to understand the dynamics of a new kind of active particle, the first recommendation would be to observe their long time

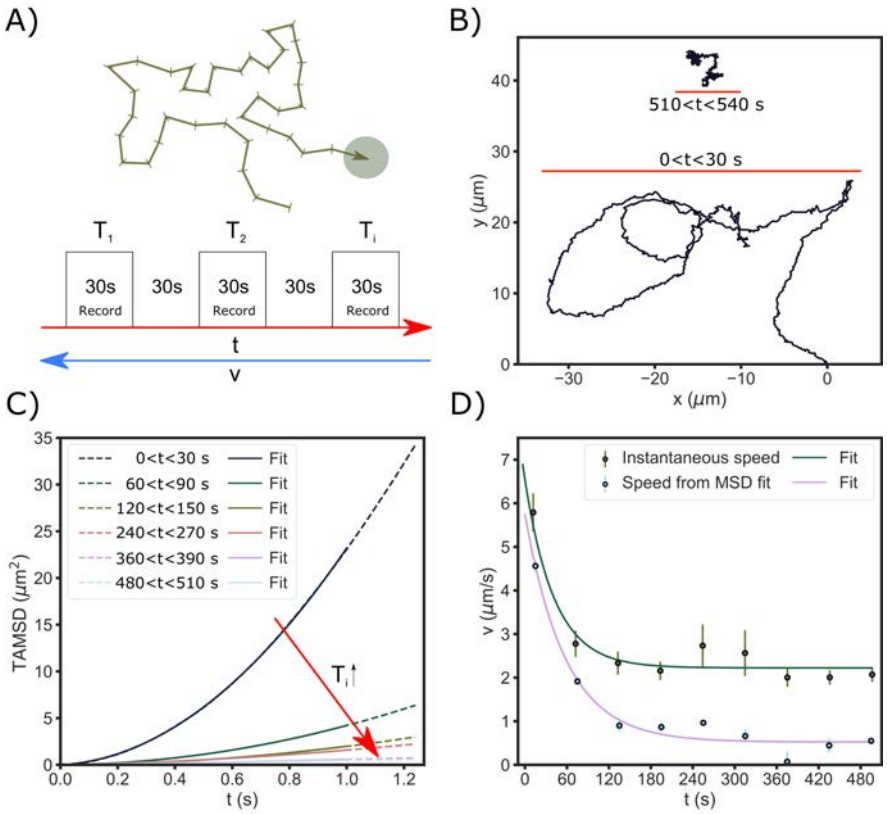

Figure 2.13: Analysis of enzymatically propelled micromotors with decreasing speed. A) Schematic of the time splitting. We record 9 min videos and split it in videos of 30 s. During this time, we alternate 30 s of recording (referred as T_i) and 30 s of stopping. The later T_i, the less propulsive is the particle. B) Trajectory of a R = 1 μm particle recorded for 9 min. Here we present data for T_1 ([0,30) s) and T_9 ([480,510) s). The speed of the particle decreases since the particles travel a bigger distance in the beginning than in the end. C) MSD of the same particle in B), but for different intervals T_i (dashed lines). These MSDs were fitted to a forth-term polynomial only up to 1 s. D) Speed of the same particle as in C). Two different speeds are presented: the propulsive speed taken from the MSD fit in C) and the average of the instantaneous speed for each T_i. In both cases, the speed decreases exponentially.

behavior, extracting the speed profile from short-timed MSDs, as reported in Figure 2.13. In our experimental example, the exponential fitting to the propulsive speed yielded $\beta \sim 0.01$ s^{-1}, and the correction factor (Equation 2.18) plays a significant role on the motion analysis using TAMSD. In this case, plotting this function in terms of different trajectory lengths, T, can help us understand the possibilities and limitations of the analysis.

For that reason, Figure 2.14 shows different scenarios of the correction term for several values of β and trajectory lengths. We can see, for instance, that this function is in general not linear over its time domain, which makes it a complex issue to approximate or simplify the analysis and extraction of parameters. In particular, for a value $\beta = 0.01$ s^{-1} (the order of magnitude of our experimental case), a correction factor of approximately 60% would apply in the initial instants of the TAMSD for a video of 60 s, meaning that the magnitude of the MSD would be 60% smaller than that of a particle moving constantly at the same speed. However, decreasing the length of the trajectory down to 10 s can make this correction decrease to 90%. Nevertheless, although the correction factor is highly non-

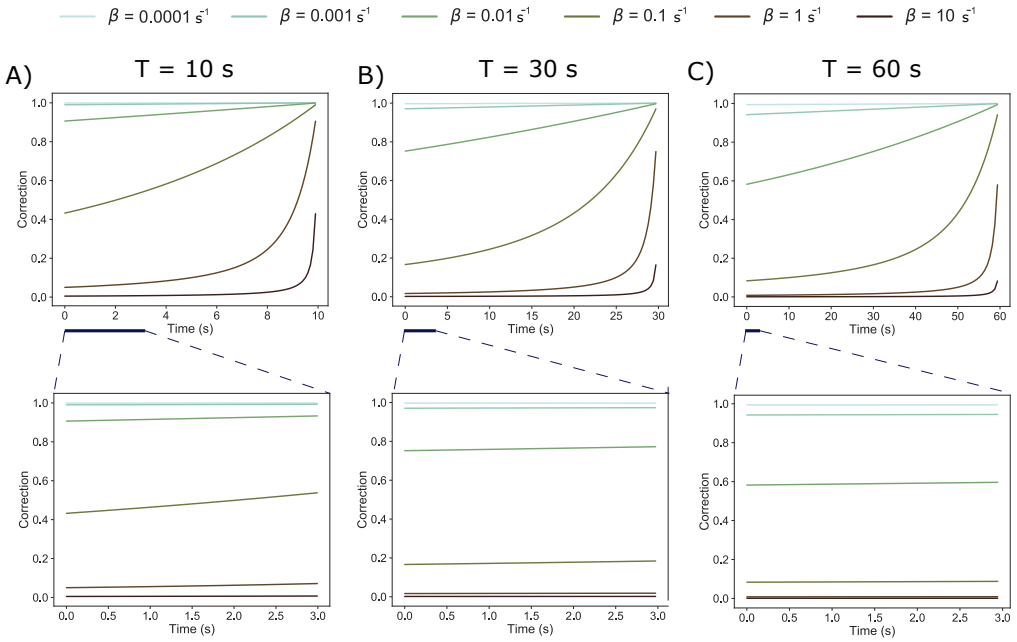

Figure 2.14: Correction factor as a function of time, for three video lengths: A) 10 s; B) 30 s; and C) 60 s. Bottom plots show a close up of the first 3 s of the correction factor, which would apply to a typical MSD, showing how, in general, it can be considered a constant factor.

lineal, we need to remember that only the initial part of the MSD has low variability. Interestingly, this correction factor usually remains constant during the first few seconds of the MSD, which is our region of interest (bottom close-ups of Figure 2.14). This means that, our MSD would thus have the form:

$$\mathrm{TAMSD}(\Delta t) = 4D_t\Delta t + v_0^2\left[\Delta t^2 - \frac{1}{3}\left(D_\theta + 3\beta\right)\Delta t^3\right]C_{T,\beta} \qquad \text{if } 0 < \Delta t \ll 3, \quad (2.19)$$

where $C_{T,\beta}$ represents the correction factor that is constant over that time domain and is defined by the values of T and β. This approximation and the values of the correction factor displayed in Figure 2.14 suggests that a video length as short as possible (or dividing a long one into smaller segments) ensures that the MSD remains "uncorrected" even for particles losing their speed fast. However, if it is too short, the correction factor might not be linear and the extraction of parameters would not be accurate, as for $T = 10$ s in Figure 2.14A. For our experimental case of $\beta = 0.01\ \mathrm{s}^{-1}$ a video length of 30 s was shown to be adequate, as the correction factor remains around 0.75 for 3 s. Therefore, from Equation 2.19, we can see how the actual speed extracted from the MSD would be underestimated by a factor of $\sqrt{0.75} = 0.87$. Indeed, we can see in the first data point of Figure 2.13D that the velocity value extracted from the MSD is slightly underestimated compared to that obtained from the instantaneous speed[2]. It is important to bare in mind that, in any case, we are treating a non-ergodic system as an ergodic one, but we are compiling the non-ergodicity into that constant value that multiplies the non-linear factor of the TAMSD. Therefore, it is theoretically possible to use the TAMSD of a particle that loses speed to extract parameters, as long as the whole function is multiplied by this constant correction factor. However, it is still advisable to perform an ensemble average of

[2]For large particles of $R = 1\ \mu$m with directional motion and high speed, the instantaneous speed can be considered representative. For lower speeds, as previously mentioned, it is not reliable due to the effect of Brownian fluctuations.

several fresh particles, in order to decrease the variability and obtaining useful information about the system's dynamics.

As a general conclusion, we have seen that enzymatically self-propelled particles, which might show an exponentially decreasing speed, are not ergodic systems and need to be carefully analyzed. Time-averaging the MSD of a single trajectory will include points in which the speed was high (at the beginning of the trajectory) and points in which the speed was lower (at the end of the trajectory). This results in an MSD which does not correspond to the classical equations (Equation 2.1), since a correction factor that only affects the propulsive term appears (Equation 2.17). This multiplicative factor depends directly on the length of the trajectory, T, and the parameter that characterizes the decay rate of the speed, β. As it only affects the propulsive part, we can assume that the speed extracted using the classical equations will always be underestimated if the motion dynamics show exponentially decreasing speed. The longer the trajectory, the closer this correction factor becomes to 0, and active motion appears completely suppressed. In that case, the resulting MSD will look like the MSD of a passive Brownian particle, even though the particle was active. Here, we show that this correction factor remains constant during the first few seconds and, since it is common to only consider about 10% of the MSD to reduce variability, we can treat this correction factor as a constant parameter. In this case, it is advisable to consider trajectories of at least 10 s and no more than 30 s, to ensure that the correction applied is not too high. Finding out the β parameter that describes the speed dynamics by recording several consecutive videos of the same particle is also necessary (Figure 2.13) in order to consider the best analysis approach in terms of video length and correction factor. Finally, only fresh particles, with the same assumed initial speed, v_0, should be taken, in order to perform ensemble averaged results.

3.4. Enzymatic nanomotors moving in viscoelastic media

Motivation and basics of DLS

This section aims at analyzing the motion of active particles in simple and complex media by light scattering techniques, namely, DLS. Future biomedical applications towards active drug delivery in tissues or organs will require the active particles to move in the complex media of tissues and travel through the crowded environment of cells if they are endocytosed[52, 56–59]. Although it is known how passive Brownian particles diffuse through different types of medium, and this information is used to characterize the properties of these materials through the technique of microrheology[60], not much is known about the active motion of particles in complex media[57].

Hyaluronic acid (HA) is a polysaccharide that is one of the main constituents of the extracellular matrix of cells and tissues, specially present in joints and synovial fluid[61], where it can reach concentrations of the order of 2 mg/mL, although it can be in much lower concentrations in other fluids, such as the vitreous body of the eye, the lymph fluid or blood serum[62]. Being a relatively simple non-Newtonian fluid, available commercially and well characterized, it is a good choice to start the study of motion in viscoelastic media[58]. Previously, Schamel *et al.* presented a screw-like micromotor that could penetrate HA thanks to a rotational screwing induced by a magnetic field[63]. Later on, they attached urease enzymes on the surface of this micro-screw and added urea to the medium, showing an enhanced penetration in mucin gels[53]. The catalytic reaction of urease with urea, that liberates ammonia molecules, changed the local pH of the gel and decreased the viscosity, helping in the penetration of their device. Urease is one of the most widely used enzymes to power nano- and micromotors[6]. At the microscale, attached to silica microparticles of 1 μm of radius, it has been

shown to produce self-propulsion in water when urea was present[39, 42]. The actual mechanism of motion, based on the catalytic decomposition of urea into ammonia and carbon dioxide, is not completely understood, but it is conventionally assumed to be related to the creation of phoretic flows that can self-propel the particle[6]. It was recently demonstrated that urease-powered micromotors can change the local pH of the medium, making it basic very rapidly, by an *in situ* pH sensing based on DNA nanotechnology[55]. It is known that HA decreases its viscosity at very basic pH due to the breakage of hydrogen bonds[64], which could indicate that urease-powered micromotors should present some enhanced sub-diffusion in this medium due to local pH changes.

DLS is a widely used technology to characterize the size distributions of proteins, nano- and microparticles or even the enhanced diffusion of nanomotors[41, 65]. Moreover, it can be used to characterize the rheological behavior of complex fluids in high frequency ranges that macroscopic rheology might not achieve by analyzing the diffusion of particle tracers inside these media at the microsecond scale[66, 67]. In this section, the motion of urease-powered nanomotors of approximately 400 nm of diameter was studied by using such technique. However, this is a much complex scenario than it might seem. The presence of urea in the medium, necessary fuel for self-propulsion, might change the characteristics of HA. Besides, the charge of the particle might generate different types of attractions or repulsions with the HA chains, as it has already been suggested[59, 68]. Finally, the products of the reaction, that change the pH and introduce more charges in the local environment, might result in complex interactions between all actors involved. For this reason, we systematically characterized the autocorrelation functions of different types of systems, in order to get an understanding of the roles of the charges, the enzymatic reactions or the pH changes, by considering three types of particles (Figure 2.15A and B): i) core-shell particles (CS) of 400 nm of diameter, negatively charged without any surface functionalization; ii) core-shell particles functionalized with amino groups (CS-NH_2) at their surface, having a small positive surface charge; and iii) core-shell particles functionalized with polyethylene glycol (PEG) and urease (CS-PEG-Ur) that can show active motion.

The choice of CS particles of 400 nm of diameter comes from practical aspects: this type of particles, with a mesoporous structure, is ideal for internalization of drugs for drug delivery applications, making them appropriate for this kind of study[41]. Their size is also ideal for this type of applications, as they might need to be internalized by cells. In fact, silica particles of the same size powered by urease have already shown enhanced functionalization in cancer cells, although in 2D cultures in aqueous solutions[52]. During the functionalization with urease, this particles are first functionalized with (3-aminopropyl)triethoxysilane (APTES), leaving amino groups anchored at their surface (see Methods section for more details). The sign of their surface charge is thus modified, from negative values typical of bare silica to positive values (although closer to zero) for amino groups (Figure 2.15B). Using these two types of particles for our study can help us understand the effect of surface charge in their diffusion in HA, when no activity due to urease is present. Finally, the amino groups at the surface of CS-NH_2 particles are used to decorate the surface with PEG and urease through glutaraldehyde linkage. In this case, PEG is added to the surface to avoid aggregation of particles, as short-range interactions between enzymes can easily aggregate CS particles only coated with urease. The PEG groups can help avoid this aggregation, obtaining solutions as monodisperse as possible for a proper DLS analysis. Moreover, besides using these types of particles to differentiate or discriminate between physical forces taking place, the studies were performed in both water and HA, with and without urea at three concentrations: 0 mM, 50 mM and 100 mM, as it has been shown for urease-powered nanomotors of similar size that 100 mM yields the maximum enhanced diffusion[41].

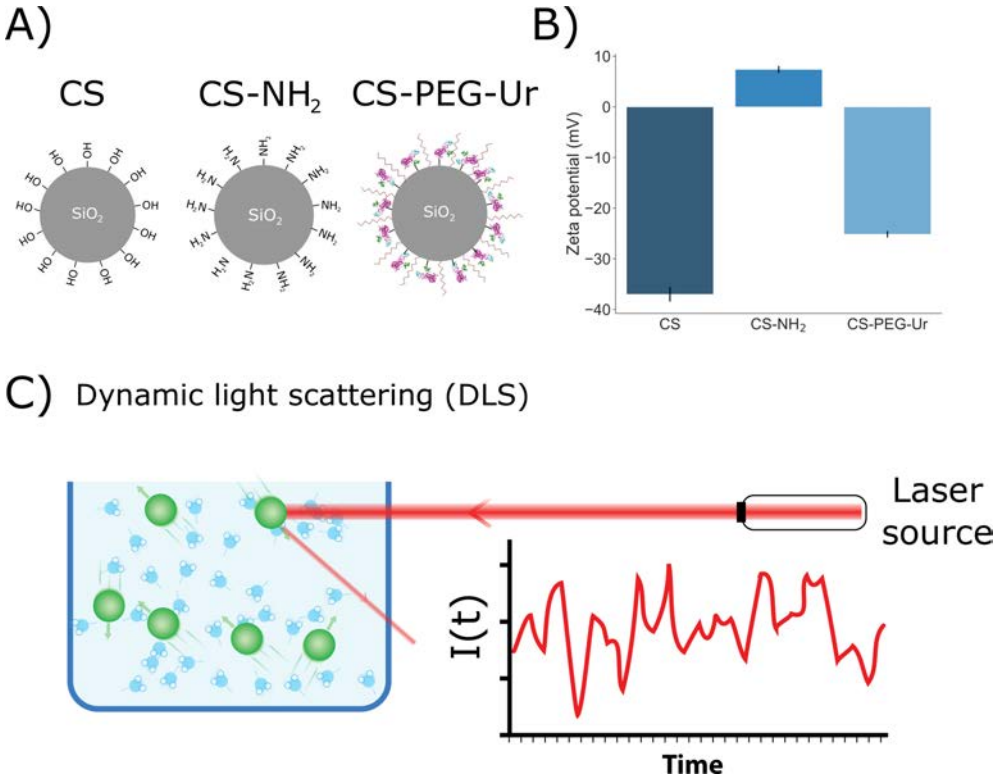

Figure 2.15: Analysis of enzymatic nanomotors with DLS. A) Schematic representation of the three types of particles studied: bare core-shell silica particles (CS), CS particles functionalized with amino groups (CS-NH_2), and CS particles functionalized with urease and PEG (CS-PEG-Ur). B) Zeta-potential of the three types of particles. C) Representation of the working principle of DLS. A laser source illuminates the sample and a detector collects the intensity as a function of time ($I(t)$), which it will autocorrelate to obtain the $g^{(2)}$ function. Source: part C) adapted from wikipedia.org, under CC license (author: Mike Johns).

DLS measures the scattering of light in a sample by applying a laser of a certain wavelength and measuring the intensity with a light detector located at an angle θ from the light path (Figure 2.15C). This intensity, $I(t)$ is auto-correlated and we obtain what is called the normalized second-order intensity autocorrelation function:

$$g^{(2)}(\boldsymbol{q};\tau) = \frac{\langle I(t)I(t+\tau)\rangle}{\langle I\rangle^2}, \tag{2.20}$$

for a specific wave vector $\boldsymbol{q}$, where $\langle I\rangle$ is simply the average intensity or baseline intensity and τ is the lagged time. Notice that, from now on, when taking about lag times related to autocorrelation functions, τ will be used, according to the convention – for the remaining cases, Δt or simply t are reserved. The wave vector depends on the characteristics of the DLS system and the medium and its modulus is:

$$q = |\boldsymbol{q}| = \frac{4\pi n}{\lambda}\sin\left(\frac{\theta}{2}\right), \tag{2.21}$$

where n is the refractive index of the medium, θ is the angle at which the detector is located with respect to the sample cell and λ is the wavelength of the laser used.

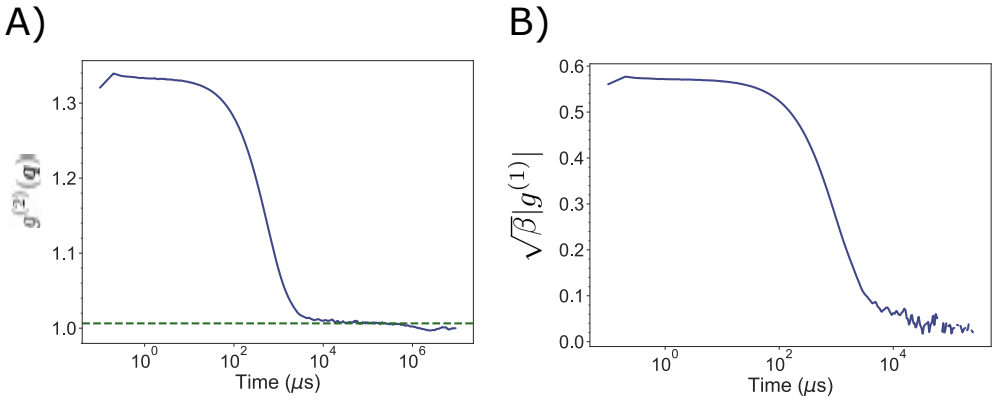

Figure 2.16: Autocorrelation functions extracted from DLS measurements. A) Second-order autocorrelation function ($g^{(2)}(\boldsymbol{q};\tau)$) of an ensemble of CS particles in water. The baseline, B, at long lag times is very close to 1. In order to improve the accuracy of the results, this parameter was found specifically for each autocorrelation function, as indicated by the green dashed line, and the data discarded if $B > 1.05$. B) Modulus of the first-order autocorrelation function ($|g^{(1)}(\boldsymbol{q};\tau)|$) multiplied by the square root of the speckle parameter ($\sqrt{\beta}$). This function shows a typical exponential decay (notice the logarithmic scale in the x-axis).

At very short times, we can expect that the correlation of two intensity measurements remains basically unchanged, since the particles have not had time to change positions and the scattering from the sample is identical. However, after a certain time, all the particles will have moved away, and very little correlation to the initial state of the system will remain. Figure 2.16A shows an example of the second-order autocorrelation function of a monodisperse sample of silica nanoparticles in water. At short lag times τ, the autocorrelation function decreases very slowly. After some time that depends on the size of the particles and therefore their diffusion, the correlation will be lost and the autocorrelation will decrease rapidly to its baseline value 1, since $\langle I(t)I(t+\tau)\rangle \approx \langle I\rangle^2$ for $\tau \to \infty$.

The full description of light scattering is contained in the scattering of the electric field, and all information of interest will be given by the normalized autocorrelation of the electric field[69], also called the normalized first-order autocorrelation function:

$$g^{(1)}(\boldsymbol{q};\tau) = \frac{\langle \boldsymbol{E}(t)\boldsymbol{E}^*(0)\rangle}{\langle |\boldsymbol{E}(t)|^2\rangle}. \tag{2.22}$$

Light detectors measure the intensity $I(t) = \boldsymbol{E}(t)^*\boldsymbol{E}(t)$, and therefore the autocorrelations obtained from the measurements correspond to those of Equation 2.20. The first- and second-order autocorrelation functions can be related to each other thanks to the Siebert relation as:

$$g^{(2)}(\boldsymbol{q};\tau) = B + \beta|g^{(1)}(\boldsymbol{q};\tau)|^2, \tag{2.23}$$

where B is the baseline that normally $B \sim 1$ and β is the speckle factor, related to the reduction of the contrast that depends on the specific conditions of the setup[70]. Figure 2.16B shows the transformation of the second-order autocorrelation function displayed in Figure 2.16A into $\sqrt{\beta}|g^{(1)}|$ by subtracting its baseline to Figure 2.16A and performing a square root (following Equation 2.23).

This first-order autocorrelation function shows a very clean and exponential decay, typical of a monodisperse sample. In fact, if we consider a single type of scatterer or tracer in the medium, in

dilute solutions so that they do not interact with each other, we can write the normalized first-order autocorrelation function as:

$$g^{(1)}(\boldsymbol{q};\tau) = \left\langle e^{i\boldsymbol{q}\cdot\Delta\boldsymbol{r}(\tau)} \right\rangle, \tag{2.24}$$

where $\Delta\boldsymbol{r}(\tau) \equiv \boldsymbol{r}(\tau) - \boldsymbol{r}(0)$ and $\langle\cdot\rangle$ represents the ensemble average over all N particles in a scattering volume V[69]. For this equation to be applicable, the dispersion of particles needs to be dilute enough so that there are no interactions among them, but also of a high enough density so that the number of particles N of the ensemble can provide statistically averaged information in a reliable manner.

Derivation of the MSD from light scattering experiments

We can define the Van Hove function as the probability density of finding a particle i at a vicinity given by $\boldsymbol{R}$ at time t, given that a particle j was in the vicinity of the origin at time $t = 0$ s[71]. In a homogeneous and isotropic system, it is defined as:

$$G(\boldsymbol{R},t) = \frac{1}{N}\left\langle \sum_{i=1}^{N}\sum_{j=1}^{N} \delta(\boldsymbol{R} - [\boldsymbol{r}_i(t) + \boldsymbol{r}_j(0)]) \right\rangle, \tag{2.25}$$

where $\delta(\cdot)$ is the three-dimensional Dirac delta function. This function can be separated into two components, the "self" part when we assume $i = j$ and the "distinct" part when $i \neq j$, which are written as[71]:

$$G_s(\boldsymbol{R},t) = \frac{1}{N}\left\langle \sum_{i=1}^{N} \delta(\boldsymbol{R} - [\boldsymbol{r}_i(t) - \boldsymbol{r}_i(0)]) \right\rangle, \tag{2.26}$$

$$G_d(\boldsymbol{R},t) = \frac{1}{N}\left\langle \sum_{i\neq j}^{N} \delta(\boldsymbol{R} - [\boldsymbol{r}_j(t) - \boldsymbol{r}_i(0)]) \right\rangle. \tag{2.27}$$

The "self" part describes the statistical motion of only the particle i that we are considering, while the "distinct" part considers the motion of the remaining $N-1$ particles. There are more important properties of these functions for light or neutron scattering events that, as they are not crucial for our experiments, can be checked elsewhere[69, 71, 72]. In our case, and in most scattering experiments with DLS, since we will consider dilute suspensions of particles, we will only consider the "self" part of the scattering function, assuming no interactions between them.

It is important to consider the self-intermediate scattering function, which is defined by the spatial Fourier transform of the van Hove function[69, 71], as:

II

$$F_s(\boldsymbol{q};t) = \mathcal{F}\{G_s(\boldsymbol{R},t)\} = \int \mathrm{d}\boldsymbol{R}\, G_s(\boldsymbol{R},t)e^{-i\boldsymbol{q}\cdot\boldsymbol{R}} = \\ = \frac{1}{N}\int \mathrm{d}\boldsymbol{R}\left\langle \sum_{i=1}^{N}\delta(\boldsymbol{R}-[\boldsymbol{r}_i(t)-\boldsymbol{r}_i(0)])\right\rangle e^{-i\boldsymbol{q}\cdot\boldsymbol{R}} = \\ = \left\langle e^{i\boldsymbol{q}\cdot[\boldsymbol{r}_j(t)-\boldsymbol{r}_j(0)]}\right\rangle = \left\langle e^{i\boldsymbol{q}\cdot\Delta\boldsymbol{r}(t)}\right\rangle. \tag{2.28}$$

It can be seen how this transformation yields the same result as Equation 2.24. Therefore, the first order autocorrelation function, that can be obtained from DLS experiments, is indeed the self-intermediate scattering function, evaluated at lag times τ:

$$g^{(1)}(\boldsymbol{q};\tau) = \left\langle e^{i\boldsymbol{q}\cdot\Delta\boldsymbol{r}(\tau)}\right\rangle = F_s(\boldsymbol{q};\tau), \tag{2.29}$$

Therefore, the autocorrelation of intensity scattered by the particles can be related to their displacements $\Delta\boldsymbol{r}(\Delta t)$ through the van Hove density probability function. At this point, it is crucial to know the distribution that the van Hove function follows. The most common approximation is to assume a Gaussian shape. Indeed, for isotropic and homogeneous media, the displacements of a Brownian particle, $\Delta\boldsymbol{r}(\Delta t) = \boldsymbol{r}(t+\Delta t) - \boldsymbol{r}(t)$, after some time Δt, are considered independent and identically distributed. The central limit theorem tells us that the total displacement, $\boldsymbol{R}$, after many individual small increments tending to infinity, will be normally distributed[3, 69], as:

$$G_s(\boldsymbol{R},t) = \frac{2\pi\left\langle\Delta r^2(t)\right\rangle}{d}^{-d/2}\exp\left(\frac{-\boldsymbol{R}^2 d}{2\left\langle\Delta r^2(t)\right\rangle}\right), \tag{2.30}$$

where d is the dimension of space and $\left\langle\Delta r^2(t)\right\rangle = \left\langle[\boldsymbol{r}(t)-\boldsymbol{r}(0)]^2\right\rangle$ is the MSD, which is the variance of this density probability function after applying the operator $\int r^2\,\mathrm{d}\boldsymbol{r}$. If the displacements are independent the variance/MSD increase linearly and we have a diffusive process. This is the case for Brownian particles moving in Newtonian liquids or the enhanced diffusive regime of active Brownian particles. The solution of the Fourier transform of Equation 2.28 for a van Hove function like in Equation 2.30 yields[69]:

$$F_s(\boldsymbol{q};\tau) = \exp\left(\frac{-q^2\left\langle\Delta r^2(\tau)\right\rangle}{2d}\right). \tag{2.31}$$

In our case, $d = 3$, since we are dealing with particles moving in three dimensions. For passive Brownian particles freely diffusing in a Newtonian fluid, it is known that $\left\langle\Delta r^2(\Delta t)\right\rangle = 2dD_t\Delta t$, where D_t is the translational diffusion coefficient. Hence, substituting this into Equation 2.31, we have:

$$F_s(\boldsymbol{q};\tau) = e^{-D_t q^2\tau}. \tag{2.32}$$

Therefore, the self-intermediate scattering function will behave like an exponential function for a monodisperse sample of Brownian particles. This is clear from Figure 2.16B, where we can observe an exponential decay, although with a logarithmic x-scale. It seems obvious now that from the intensity autocorrelation function $g^{(2)}(t)$, it is possible to estimate the ensemble MSD of diffusing particles, and with it their diffusion, by simply finding the self-intermediate scattering function using the Siebert relation of Equation 2.23. In real light scattering measurements, however, there could be some background noise, and the baseline B might not be exactly equal to one. This parameter can be easily calculated for each autocorrelation function by finding the baseline value at long times, when the system has completely decorrelated (as Figure 2.16A indicates with a green dashed lines) . The speckle parameter β, however, is not so easy to find. To make the analysis independent of such parameter, first we can notice that $\beta = g^{(2)}(\boldsymbol{q};0) - B$, since $g^{(1)}(\boldsymbol{q};0) = F_s(\boldsymbol{q};0) = 1$. Knowing this, we can use the intercept of the correlation function at very short times $\tau \to 0$ to normalize self-intermediate scattering function. Subtracting B on both sides of Equation 2.23 and taking logarithms, considering the equality 2.29, yields:

$$\ln\left(g^{(2)}(\boldsymbol{q};\tau) - B\right) = \ln\beta + 2\ln|F_s(\boldsymbol{q};\tau)|, \tag{2.33}$$

and substituting the value of β that we just found:

$$\ln\left(g^{(2)}(\boldsymbol{q};\tau) - B\right) = \ln\left(g^{(2)}(\boldsymbol{q};0) - B\right) + 2\ln|F_s(\boldsymbol{q};\tau)|, \tag{2.34}$$

$$\ln|F_s(\boldsymbol{q};\tau)| = \frac{1}{2}\left[\ln\left(g^{(2)}(\boldsymbol{q};\tau) - B\right) - \ln\left(g^{(2)}(\boldsymbol{q};0) - B\right)\right]. \tag{2.35}$$

Now, remembering the dependence of $F_s(\boldsymbol{q};\tau)$ with the MSD in Equation 2.31, we can write:

$$\left\langle \Delta r^2(\tau)\right\rangle = -\frac{6}{q^2}\ln|F_s(\boldsymbol{q};\tau)| = -\frac{3}{q^2}\left[\ln\left(g^{(2)}(\boldsymbol{q};0) - B\right] - \ln\left(g^{(2)}(\boldsymbol{q};\tau) - B\right)\right]. \tag{2.36}$$

Therefore, the ensemble MSD of a set of particles moving in a fluid can be computed from the second-order intensity autocorrelation function and normalizing with respect to its intercept in the y-axis, $g^{(2)}(\boldsymbol{q};0)$, and its baseline, B. Figure 2.17A shows the calculation of the MSD of CS particles in water, in a log-log scale. It can be seen how there is a constant-slope region for which the MSD scales as MSD $\sim \tau^{\alpha}$ with $\alpha = 1$, for normal diffusion. At very short lag times, the noise due to small variations of the autocorrelation function makes this region unreliable. Although this part of the MSD would give information about very short-time interactions between the particles and the medium, and it could be possible to observe a residual of the inertial motion of the particles, it is unlikely that these effects can be seen for water due to the limitations of the noise and the sensitivity provided by the wavevector $\boldsymbol{q}$. At long lag times, the MSD saturates, but this is due to the decorrelation of the light scattering, not to a real saturation of the MSD, that otherwise would indicate a caging effect. Therefore, the region of intermediate time, close to the decorrelation time or decay constant of the system, provides reliable and useful information about the MSD. The presence of this decay constant is obvious if we express the self-intermediate scattering function as:

$$F_s(\boldsymbol{q};\tau) = e^{-\Gamma\tau}, \tag{2.37}$$

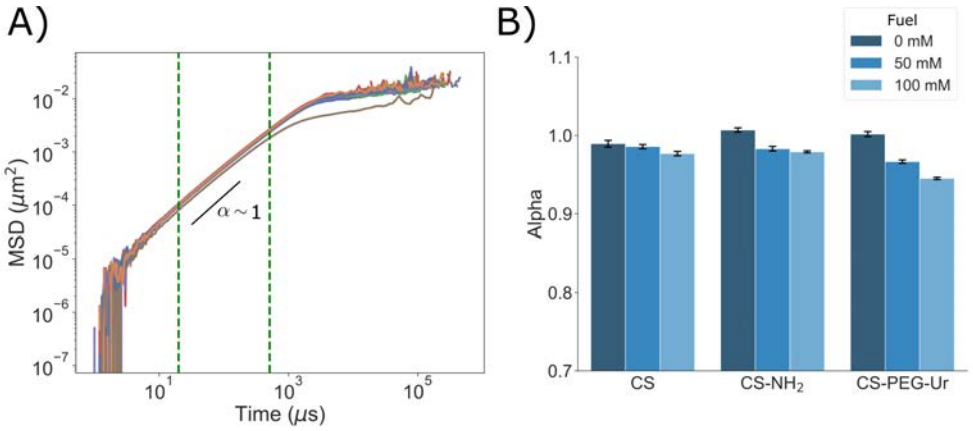

Figure 2.17: Extraction of the MSD and scaling exponent from DLS measurements in water. A) MSD in log-log scale of several sets of CS particles in water. The constant-slope region delimited by the green dashed lines was used to perform the fittings and extract the paramters. B) A fitting in this constant-slope region of the form MSD $\sim \tau^{\alpha}$ results in α exponents very close to 1, as expected for Brownian particles in water, although with small deviations when urea is added.

where Γ would be the decay time and would be defined as $\Gamma = D_t q^2$[73, 74]. Therefore, the value of the wavevector q would allow us to change the region at which we can obtain useful information, if we could modify the scattering angle or the laser wavelength, following Equation 2.21, as some DLS machines can do.

Figure 2.17B shows the α parameter, extracted by a log-log fitting to the stable region of the MSD, for the three kinds of particles, as well as three concentrations of urea. It can be seen how the exponent α remains very close to 1 for all control cases (0 mM urea), although there are some minor deviations. When urea is added these values decrease below 1, reaching down to $\sim$ 0.95 for CS-PEG-Ur with 100 mM of urea. This variation is most likely due to aggregation of particles, that seems to be affected by the presence of urea and cause polydispersity in the samples. The extraction of the diffusion coefficients from these MSDs, assuming a linear tendency, might not be accurate, and it would show contributions from these aggregates.

Aggregation of particles and polydispersity

This analysis can be improved if we assume a certain distribution of sizes or, what is the same, a distribution of decay times, Γ, given by different diffusion coefficients[74]. Then, we could write the self-intermediate scattering function as:

$$F_s(\boldsymbol{q};\tau) = \int_0^{\infty} \mathrm{d}\Gamma H(\Gamma) e^{-\Gamma\tau}, \tag{2.38}$$

where $H(\Gamma)$ is the probability distribution of decay times. Aggregation of particles might give rise to a broadened distribution, due to the increase of hydrodynamic radii, and the MSD will not be a linear function anymore. If we assume only one type of particle with a monomodal peak (instead of several peaks at different radii, that would require a different analysis), we can use the so-called cumulants analysis method, that can relate the self-intermediate scattering function to a Taylor expansion of the form:

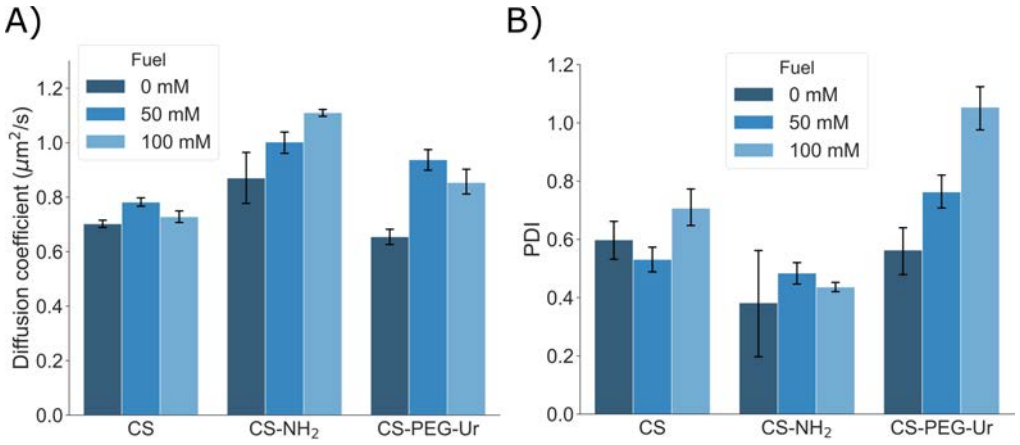

Figure 2.18: Average diffusion coefficient and PDI of all particles at different fuel concentrations. A) Average diffusion coefficient for the three types of particles with different concentrations of urea obtained by the cumulant analysis. B) PDI for the three types of particles with different concentrations of urea obtained by the cumulant analysis.

$$\ln|F_s(\boldsymbol{q};\tau)| = -\bar{\Gamma}\tau + \frac{k_2}{2!}\tau^2 - \frac{k_3}{3!}\tau^3 + \frac{k_4}{4!}\tau^4 + \ldots \tag{2.39}$$

In this equation, $\bar{\Gamma}$ represents the average decay time of the sample, from which we could extract an average diffusion coefficient. The parameters k_2, k_3 and k_4 represent the variance, skewness and kurtosis of the distribution. If such distribution is purely Gaussian, we know that k_3 and k_4 should be equal to zero. This is very unlikely but, in order to avoid overfitting of the data, we will only perform a fitting up to second order. Finally, the polydispersity index (PDI), which gives information about the spread of the distribution, can be computed as PDI $= k_2/\bar{\Gamma}^2$[65].

Figure 2.18 gives the results of these fittings for the three kinds of particles that we are considering and for three fuel concentrations. For bare CS particles, the average diffusion coefficient coincides with values reported in the literature[41], with a small increase when urea is added. However, the diffusion coefficient, according to the Stokes-Einstein theory, for particles of this size should be approximately 1.2 μm^2/s. The deviation from this value can be explained by looking at the PDI (Figure 2.18B), where we can see that the distribution is quite broad for a monodisperse sample[65]. In fact, the changes of diffusion coefficient when urea is added could be simply explained by different polydispersity of the sample. For 50 mM of urea, the PDI decreases, while the diffusion coefficient increases. Urea is a highly polar molecule and CS particles are negatively charged due to surface OH^- groups, which could cause electrostatic interactions and charge screening, affecting the diffusion dynamics.

This dependence between the charge of the particle and their diffusion or PDI is also observed for CS-NH_2 particles. These ones, in fact, show diffusion coefficient values much closer to the theoretical value and we can see that their PDI is smaller than for bare CS, indicating a more monodisperse sample. Although there seems to be broad variations in the aggregation for pure water (0 mM urea), the PDI decreases when urea varies from 50 mM to 100 mM, whereas the diffusion coefficient increases. Nevertheless, the changes in diffusivity could be also explained by surface charge effects. It was suggested that the absolute value of the zeta-potential influences the mobility of nanoparticles by negatively correcting (diminishing) their diffusion[75]. As the charge of bare CS particles (in absolute values) is large, their diffusion could be decreased due to this correction related to the charge. CS-NH_2, however, possess only a small positive charge, and their diffusivity is closer to the theoretical value. The addition of urea could shield the surface charge, or spontaneous dissociation of

urea could introduce more charges in the medium and increase this effect. Therefore, when urea was added, CS-NH_2 particles could decrease their zeta-potential and the correction of their diffusivity could decrease, getting closer to theoretical values.

For the case of CS-PEG-Ur, that catalyzes urea into ammonia and carbon dioxide, generating active motion, we see a clear enhance in the diffusion coefficient. This variation supposes an increase of approximately 43% for 50 mM of urea, which matches previously reported cases in the literature[41]. However, interestingly, we see how their PDI greatly increases to values higher than 1, indicating a very high polydispersity. This increase in polydispersity cannot be taken as aggregation of particles, since in that case the average diffusion coefficient should be lower, not higher. In fact, this increase in PDI indicates the presence of active particles that have enhanced diffusion coefficients (lower apparent hydrodynamic radii), broadening the distribution. This also indicates that not all particles show this great enhanced diffusion and some of them might remain passive. The increase in diffusion coefficient that we can see in Figure 2.18A is most likely underestimated, being much larger for highly diffusive particles.

One small detail might seem striking regarding the motion of the CS-PEG-Ur nanomotors in urea. As we know from the theory of active Brownian particles, the MSD should show a two regions: one propulsive (with quadratic tendency) for $\tau \ll \tau_r$, and one diffusive (with linear tendency) for $\tau \gg \tau_r$, where τ_r is the rotational diffusion time of the particle. For particles of this size, roughly $r = 200$ nm, we would expect a rotational diffusion coefficient of $D_\theta = \frac{K_b T}{8\pi\eta 3} = 23\ \mathrm{s}^{-1}$, where $K_b = 1.38064852 \cdot 10^{23}\ \mathrm{m}^2\ \mathrm{kg}\ \mathrm{s}^{-2}\ \mathrm{K}^{-1}$ is the Boltzmann constant, $T = 298$ K is the temperature and $\eta = 8.9 \cdot 10^{-4}$ Pa·s is the viscosity of water. Given that $\tau_r = 1/D_\theta$, the rotational diffusion time of the particle should be $\tau_r = 0.0435$ s $\approx 44000\ \mu$s. That is, for τ values lower than τ_r, the ballistic regime of the particle should be seen in the MSD, according to the active Brownian particle theory. However, we can see that the scaling factor α of the MSD for the active particles was nearly one (Figure 2.17B), instead of showing a change of regime with a slope going from ~ 2 to ~ 1.

The reason for this comes from the characteristics of the DLS system. For the self-intermediate scattering function $F_s(\boldsymbol{q}, \tau)$ to decay, a particle must move a distance Δr of the order of q^{-1}[69]. On the one hand, if q^{-1} is small compared to the mean path l of the particle, $l \gg q^{-1}$, then the particle will move that distance q^{-1} with a constant and directional propulsive speed v_p. For this kind of motion, it can be proved that $F_s(\boldsymbol{q}, \tau) \sim \exp\left(-\tau^2 q^2 \langle v_p \rangle^2\right)$, assuming isotropically distributed speeds following a Maxwell distribution[69]. On the other hand, when the particle suffers a large number of collisions with the water molecules, decorrelating the direction of its speed, we would have that $l \ll q^{-1}$. In this case, linear trajectories cannot be assumed to compute $F_s(\boldsymbol{q}; \tau)$. A random walker, that is, simple Brownian diffusion, would be more appropriate to describe the motion of these particles under these experimental conditions. This is analogous to the case of an optical microscopy setup and the pixel size. If the minimum spatial resolution of the video cannot discern ballistic trajectories, the motion of the particle will look diffusive, even if it should be ballistic according to the classical limits.

In our current experiments, given the characteristics of the detector, we have $q^{-1} = 3.21 \cdot 10^{-8} = 0.0321\ \mu$m. Knowing that τ_r should be in the range of $\tau_r = 0.0435\ \mathrm{s}^{-1}$, if we assume a speed of the order of $v_p \approx 1\ \mu$m/s, we have that the mean free path $l = v_p \cdot \tau_r = 0.0435\ \mathrm{s}^{-1}$, which is of the same order of magnitude as q^{-1}, and therefore the trajectory cannot be assumed to be ballistic. Even if we go to higher speeds, of $\sim 5\ \mu$m/s, we would have $l = 0.217\ \mu$m, which is only one order of magnitude higher than q^{-1} and might not be considered "much higher" for the effects to be discerned.

These results, therefore, leave room for several possibilities, some of which could have important impacts in the understanding of the motion mechanism of enzymatically propelled nanomotors. One possibility would be, as mentioned, that the propulsive speeds are too small and, therefore, the mean free path is also small compared to the inverse of the wavevector, making it impossible to discriminate the propulsive regime. The second possibility would be that the assumptions of the active Brownian particle theory are not fulfilled for urease-powered nanomotors. The system might not be effectively described as a particle with a self-generated propulsive speed, v_p, that randomizes its direction due to Brownian fluctuations and looks like enhanced diffusion at long times. If no propulsive regime can be observed for particles of this size, the enhanced diffusion mechanism might be related to fluctuations of the particle, instead of a defined speed due to phoretic effects. Perhaps the motion could be effectively described by a propulsive speed, but a local increase of temperature or the appearance of hydrodynamic flows due to the catalytic reaction of the enzyme might decrease its τ_r, modifying the threshold from ballistic to diffusive. Therefore, corrections to the value of τ_r that deviate from the Stokes-Einstein equations might have a significant effect. For instance, it was demonstrated for micron-sized Pt-powered Janus particles that high fuel concentrations can increase the directionality of the movement, hindering Brownian motion and decreasing the rotational time[76].

Hence, with this experimental setup, we are not able to observe the ballistic regime of the particle, even if the time resolution allows us to investigate times $\tau \ll \tau_r$, as the classical theory suggest, either because the minimum observable free path, given by q^{-1}, is not small enough to discern ballistic trajectories of the particle, or because the ballistic regime is not a good approximation of the particle's type of motion. In order to improve these analysis, multi-angle DLS could be performed[77]. In this type of experiment, the detection angle of the DLS is rotated, in order to change the value of q. By performing measurements at different q, one could reach different levels of sensitivity and understand if the motion dynamics can be understood as ballistic trajectories in a fluctuating medium, or are better described in another way. However, in these kinds of experiments, the straightforward relationship between the self-intermediate scattering function and the MSD from Equation 2.31 might not hold anymore. As we will see, the Gaussianity of the van Hove function cannot be ensured for motion dynamics in which $\alpha \neq 1$, such as superdiffusion or subdiffusion. In this case, a different relationship should be found by Fourier transforming the appropriate van Hove function and finding how it relates to its variance, that is, the MSD of the particles following that distribution. A better strategy, however, might be to analyze the motion regimes separately. For short lag times, the particles might be assumed to move ballistically without collisions and the self-intermediate scattering function will be directly correlated to its propulsive speed, instead of its MSD, as it was already mentioned. For longer lag times, the motion will become diffusive again, and the relationship between the self-intermediate scattering function and the MSD will still hold.

Derivation of the MSD for particles in non-Newtonian media

This brings us to the motion in complex fluids, where the central limit theorem, that helped us assume the normality of the van Hove function, does not necessarily apply to the displacement intervals and we cannot ensure a Gaussian distribution whose variance is $\langle \Delta r^2(t) \rangle$. For the case of active particles in 2D, it has actually been proven that the van Hove function behaves like a Gaussian distribution at short times and it rapidly turns into a symmetric two-peaked distribution, but there is no proposed analytic solution for this function[78]. Moreover, it was demonstrated by Zheng *et al.* than Pt-covered Janus particles moving in 2D show non-Gaussian behavior in their position probability distributions, specially for high fuel concentrations, when two symmetric peaks appear, even though their MSD shows the typical quadratic behavior[76]. However, this was only shown for high fuel concentrations, whereas for low concentrations, the distribution function was similar

to a Gaussian distribution, although with some deviations. Demonstrating the shape of van Hove function of active Brownian particles moving in three dimensions is more complex experimentally, as it requires 3D trackings, but it will most likely be non-Gaussian.

For anomalous motion with $\alpha < 1$, such as a particles diffusing in HA, a similar thing happens. The Gaussianity of the van Hove function needs to be demonstrated in order to apply the same treatment as in Equation 2.36 and accurately extract the MSD of particles sub-diffusing in a complex medium. In this case, the position increments $\Delta\boldsymbol{r}(\Delta t) = \boldsymbol{r}(t + \Delta t) - \boldsymbol{r}(t)$ are not independent or identically distributed, as can be assumed from an MSD of the form $\sim \tau^{\alpha}$. This kind of motion can be described by a fractional Brownian motion model (FBM), that includes a power-law memory function on top of the diffusion process[79]. In the FBM, we can just assume a simple law scaling of the form:

$$\left\langle \Delta r^2(t) \right\rangle = 2dK_{\alpha}t^{\alpha}, \tag{2.40}$$

where K_{α} is a generalized diffusion coefficient with dimensions of $\mathrm{m}^2\ \mathrm{s}^{-\alpha}$. At short time intervals, it is expected that the displacements $\Delta\boldsymbol{R}$ will be uncorrelated and dominated by diffusion. At longer times, however, there will be some correlation and they will not be independent. In fact, for superdiffusion ($\alpha > 1$) they will be positively correlated and for subdiffusion ($\alpha < 1$) negatively correlated. However, it can be demonstrated that the position increments $\Delta\boldsymbol{r}(\Delta t) = \boldsymbol{r}(t + \Delta t) - \boldsymbol{r}(t)$ are indeed normally distributed and we have[3, 79]:

$$G_s(\boldsymbol{R}, t) = \left(\frac{d}{2\pi \left\langle \Delta r^2(t) \right\rangle}\right)^{d/2} \exp\left(\frac{-\boldsymbol{R}^2 d}{2\left\langle \Delta r^2(t) \right\rangle}\right) = \left(\frac{1}{4\pi d K_{\alpha} t^{\alpha}}\right)^{d/2} \exp\left(\frac{-\boldsymbol{R}^2}{4K_{\alpha}t^{\alpha}}\right). \tag{2.41}$$

This finding does not necessarily mean that any system with an MSD with a scaling factor $0 < \alpha < 2$ possesses a Gaussian van Hove function, as many different dynamics could yield an MSD of the same characteristics. The intrinsic dynamics of the system, defined by the displacements $\Delta\boldsymbol{r}(\Delta t) = \boldsymbol{r}(t + \Delta t) - \boldsymbol{r}(t)$ after Δt, will determine the probability density function of those displacements. Indeed, if we consider a reflected FBM that tries to model the long-time confinement of particles in complex media, the van Hove function stops being Gaussian for certain times[3]. At short times, the behavior is the same as sub-diffusion, with a MSD scaling with exponent α, and the van Hove function is the one in Equation 2.41. However, at longer times, the MSD starts to saturate, which is a possible effect of being embedded in complex polymeric networks with strong elastic component, and the van Hove function stops being Gaussian. These two FBM models are just dynamic descriptions that can mimic the shape of measurable quantities, such as the MSD, but are not demonstrations of these being the dynamics behind the process. However, it is generally accepted that the FBM is a fair model to describe the sub-diffusive motion of tracers in viscoelastic fluids and, as long as we remain in the region of the MSD where α is constant, we can assume that the van Hove function will be Gaussian[3, 79].

Nevertheless, this might not be always the case. For instance, it has been proven that the van Hove function of tracers in crowded environments shows non-Gaussianity depending on the radii of the crowders and the crowding fraction[80]. By modeling the dynamics of a walker in a porous medium following the continuous time random walk (CTRW) model, consisting on a series of jump-trapping processes, it was also proven that the probability distribution function of positions is not Gaussian.

However, this function still has an analytical form, from which the MSD can be extracted, but the relationship between $F_s(\boldsymbol{q},\tau)$ and $\langle \Delta r^2(\tau)\rangle$ will be different than in Equation 2.31[81]. Moreover, for tracers in an agarose gel, Valentine *et al.* demonstrated by optical tracking that the MSD of these particles saturated at long times, indicating a caging effect, and the van Hove functions deviated from a Gaussian function[82].

All these examples demonstrate that the direct relationship between the self-intermediate scattering function and the MSD should be very carefully considered, since the complex dynamics at interplay in the microscale could yield non-Gaussianity in the van Hove function, usually in the long-time tails. Nevertheless, from these experiments and simulations, it is safe to assume the Gaussianity of the van Hoven function for many polymers, as long as we find ourselves in a region were α is constant[3]. Moreover, in the case of HA, if we consider it a purely viscoelastic medium, we can prove the validity of these approximations by writing the Langevin equations in such medium[3]. The Langevin equations in a simple fluid are:

$$m\dot{v}(t) = -\xi v(t) + f(t), \tag{2.42}$$

where m is tha mass of the particle, $-\xi v(t)$ represents the friction force, with the friction coefficient $\xi = 6\pi\eta r$, and $f(t)$ is a white-noise stochastic force that follows the typical relations $\langle f_i(t)\rangle = 0$ and $\langle f_i(t) f_j(t')\rangle = 2K_bT\xi\delta_{ij}\delta(t-t')$. These equations, in fact, give rise to an MSD of the form:

$$\langle \Delta r^2(t)\rangle = 2dD[t + \tau_p(e^{-t/\tau_p} - 1], \tag{2.43}$$

where τ_p is the relaxation time of the particle, which represents the average time between collisions with medium molecules when the particle can move ballistically driven by inertia. This is also known as the Uhlenbeck-Orstein process and bares similitude to the dynamics of active Brownian particles. However, the correlation time τ_p, which depends on the mass of the particle, is usually < 1 μs, so these ballistic effects cannot usually be observed with DLS, but with very precise optical traps[54]. The Langevin equations can be generalized to take into account more complex dynamics by the addition of a memory kernel, that considers the influence of all the previous states of the system[83]:

$$m\dot{v}(t) = -\int_0^t dt'\xi(t-t')v(t) + f(t), \tag{2.44}$$

For a viscoelastic fluid, we can encode this complexity in a frequency-dependent viscosity $\eta^*(\omega)$. By going into the Fourier domain, we can write the generalized Langevin equations as:

$$-i\omega m\hat{v}(\omega) = -\hat{\xi}(\omega)v(\omega) + \hat{f}(\omega), \tag{2.45}$$

where $\hat{}$ represents Fourier transformed quantities and $\hat{\xi}(\omega) = 6\pi\eta^*(\omega)r$ is now the frequency-dependent friction coefficient. Under the Maxwell model[83], the complex viscosity $\eta^*(\omega)$ of a viscoelastic fluid is related to the complex shear modulus as $G^*(\omega) = -i\omega\eta^*(\omega)$. By the fluctuation-dissipation theorem, the correlation of the random forces are now:

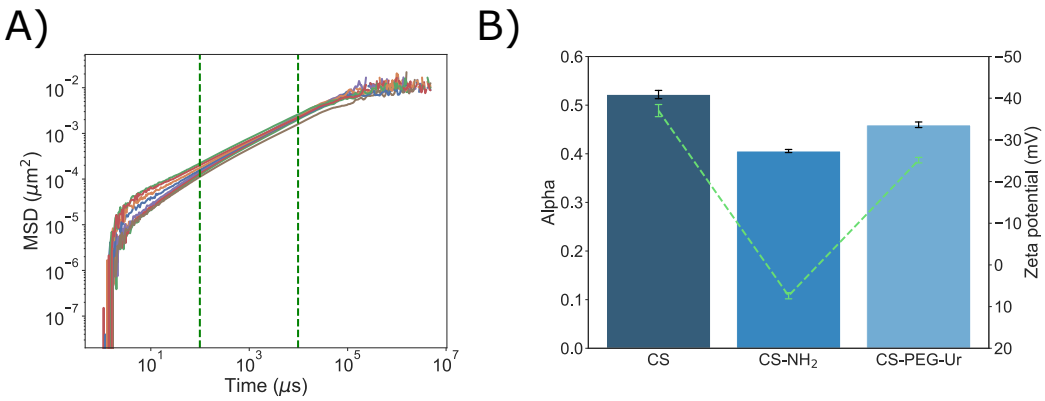

Figure 2.19: Extraction of the MSD from DLS measurements in HA and the correlation between the scaling exponent and the surface charge. A) MSD in log-log scale of several sets of CS particles in HA. We can notice that the constant slope region occurs at longer lag times, compared to the case of water in Figure 2.17, due to the slower diffusion of the particles, taking longer for the system to decorrelate. B) A fitting in this constant-slope region of the form MSD $\sim \tau^{\alpha}$ results in α exponents around ~ 0.5, as expected for sub-diffusion (no urea added). In green, the zeta-potential of the particles, showing the correlation between both values, from Figure 2.15.

$$< \hat{f}_i(\omega)^* \hat{f}_j(\omega') >= 4\pi K_b T \mathbb{R}[\hat{\xi}(\omega)]\delta_{ij}\delta(\omega - \omega'). \tag{2.46}$$

Given this description based on the Maxwell model and the Langevin equations, we can see that the forces are uncorrelated in time[3]. Due to this, we can assume that the displacements $\Delta \boldsymbol{r}(\Delta t) = \boldsymbol{r}(t + \Delta t) - \boldsymbol{r}(t)$ will also be uncorrelated and the van Hove equation corresponds to a Gaussian probability function like in Equation 2.30.

From all these examples, we can assume that the van Hove function of our CS particles subdiffusing in HA will be Gaussian and that the relationship between the MSD and the self-intermediate scattering function established in Equation 2.31 will hold, with an MSD of the form 2.40. Indeed, Figure 2.19 shows an example of $\ln F_s(\boldsymbol{q}; \tau)$ from CS particles in HA, where we can see a central region with a constant growth, as for the case of water. Notice that this region is wider and happens at longer lag times compared to the case presented in Figure 2.17, due to the longer diffusion time of the particles in the complex medium, that takes longer to decorrelate the system. Figure 2.19B shows the extracted exponents for the three cases of particles in HA, without urea, compared with the zeta-potential of the particles, as reported in Figure 2.15. It is interesting to notice the great differences in α between the particles, with CS-NH_2 particles diffusing with slower α than the other two cases. However, we can see a certain correlation with the zeta-potential of the particle. These results indicate that the more positive the particle's charge is, the lower is α. This effect could be a result of interactions between the particles and the polymer chains. As HA is negatively charged[84], it could be that CS-NH_2 particles have constrained subdiffusion due to the attractive electrostatic interactions and spend more time close to polymer chains[68]. Negatively charged particles, especially CS particles, that have the most negative zeta potential, seem to diffusive with the largest exponent α. Similar results were obtained by Xu *et al.* in studies analyzing the diffusion of nanoparticles of different sizes in bovine vitreous *ex vivo*[59]. Polystyrene particles of diameters comparable to the mesh size of the polymer, which possesses negatively charged domains, showed an α exponent that was highly dependent on the surface charge, with positively charged particles (functionalized with NH_2 groups) diffusing with very low α and negatively charged particles (functionalized with COOH groups) diffusing with a much higher α. The authors suggested that anionic particles could diffuse freely in negatively charged vitreous network *via* electrostatic repulsion if their size was small enough to avoid

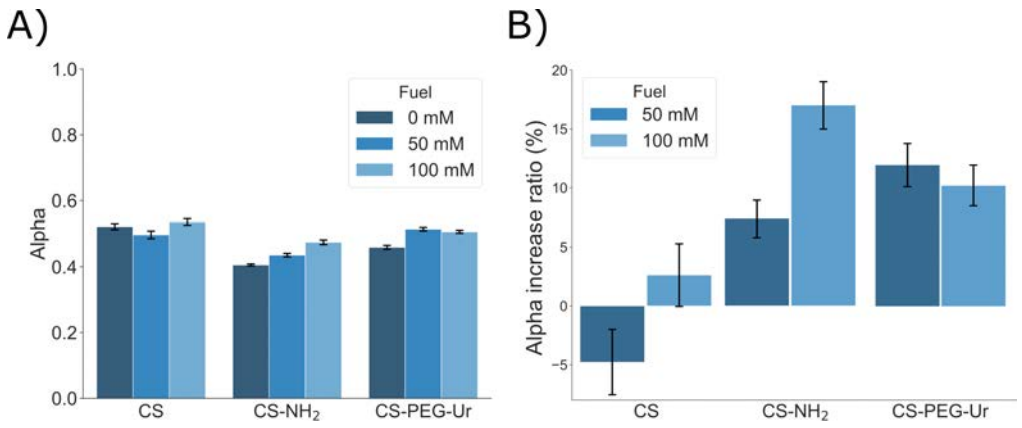

Figure 2.20: Differences in scaling exponent with the addition of urea in HA. A) Exponent α for each particle in HA with different concentrations of urea. B) Porcentual increase of the exponent α for 50 mM and 100 mM with respect to the control at 0 mM.

steric trapping[59], in agreement with our results. Likewise, in another publication, Nance *et al.* suggested that a net negative surface charge might improve the diffusion of nanoparticles in brain tissues due to electrostatic repulsion[85].

It is interesting to investigate how the effect of urea in the medium can change the diffusion dynamics of the three types of particles, in particular of CS-PEG-Ur, whose catalytic activity can change the pH of the medium due to the release of ammonia molecules. Figure 2.20A shows the changes in α when urea is added to the medium. For CS particles, there is barely no change when urea is added, as can be observed by the percent change in Figure 2.20B. CS-NH_2 particles, however, show the biggest increase in their MSD exponent with increasing concentrations of urea, going up to a 17% increase in the best cases. This is most likely due to a shielding effect caused by urea molecules, as previously mentioned. As the charge of CS-NH_2 particles decreases, their interaction with the HA network also decreases, making them diffuse easier. CS-PEG-Ur particles, that catalyze a reaction with urea and produce ammonia, thus changing the pH locally, also experience an increase of about 10% in their α exponent. Compared to the case of CS particles, that also had a negative charge but did not increase its α, this could be attributed to an effect of the enzymatic reaction, making the nanomotors diffuse faster.

Microrheology

DLS of tracer particles in a complex medium is called microrheology, as it allows to extract rheological characterizations of the materials at very high frequencies (very low lag times τ) that might not be accessible by conventional rheology[66]. Continuing the strategy of the generalized Langevin equations, we can understand how the MSD of the particles is related to the complex viscosity of the material and its shear modulus. We can perform an unilateral Laplace transform on the generalized Langevin equation to solve for the velocity spectrum in the Laplace domain given by s:

$$\tilde{v}(s) = \frac{mv(0) + \tilde{f}(s)}{ms + \tilde{\xi}(s)}. \tag{2.47}$$

By computing the velocity autocorrelation function in the Laplace domain and relating it to the

memory function $\tilde{\xi}(s)$, it can be demonstrated that the relationship between the shear modulus of the viscoelastic Maxwell fluid and the MSD of the particles diffusing in it is given by:

$$\tilde{G}(s) = s\tilde{\eta}(s) = \frac{s}{6\pi a}\left[\frac{6K_bT}{s^2\left\langle\Delta\tilde{r}^2(t)\right\rangle} - ms\right], \tag{2.48}$$

where the first term represents the Brownian component from thermal fluctuations and dissipations in the medium and the second term is the inertial term that can be ignored for very low frequencies, which are not accessible with DLS ($ms \rightarrow 0$). Moreover, we can define a generalized diffusion coefficient by:

$$\tilde{D}(s) = \frac{K_bT}{6\pi r s\tilde{\eta}(s)}, \tag{2.49}$$

which is just a generalization of the Stokes-Einstein relationship in the Laplace domain.

In this manner, by extracting the MSD via dynamic light scattering and performing its Laplace transform, we can find the rheological properties of the material, like it shear modulus or its viscosity, as long as certain assumptions are taken, such as the treatment of the fluid as a continuous effective medium or the generalization of Stokes drag for viscous fluids at all s (with no-slip boundary conditions)[83]. However, in order to avoid errors from truncation during Laplace transform of the MSD and to simplify the procedure, Mason *et al.* developed a simplified method by assuming an MSD that follows a local power law[86, 87], which, as far as we have seen in Figure 2.19, is a fair assumption. In this way, we return to the representation in the Fourier domain of Equation 2.48, after ignoring the inertial terms, by:

$$G^*(\omega) = \frac{K_bT}{\pi r i\omega\mathcal{F}_u\{\langle\Delta r^2(t)\rangle\}}, \tag{2.50}$$

where $\mathcal{F}\{\langle\Delta r^2(t)\rangle\}$ is the Fourier transform of the MSD. If we expand this Fourier transform assuming the local power-law behavior, we obtain the approximation:

$$i\omega\mathcal{F}_u\{\langle\Delta r^2(t)\rangle\} \approx \langle\Delta r^2(t)(1/\omega)\rangle\,\Gamma[1+\alpha(\omega)]i^{-\alpha(\omega)}, \tag{2.51}$$

where Γ is the gamma function and $\alpha(\omega)$ is defined as:

$$\alpha(\omega) \equiv \left.\frac{\mathrm{d}\ln < \Delta r^2(t) >}{\mathrm{d}\ln t}\right|_{t=1/\omega}, \tag{2.52}$$

By substituting the expansion of the Fourier transform of the MSD of Equation 2.51 into Equation 2.50 and separating between real and imaginary parts, we obtain:

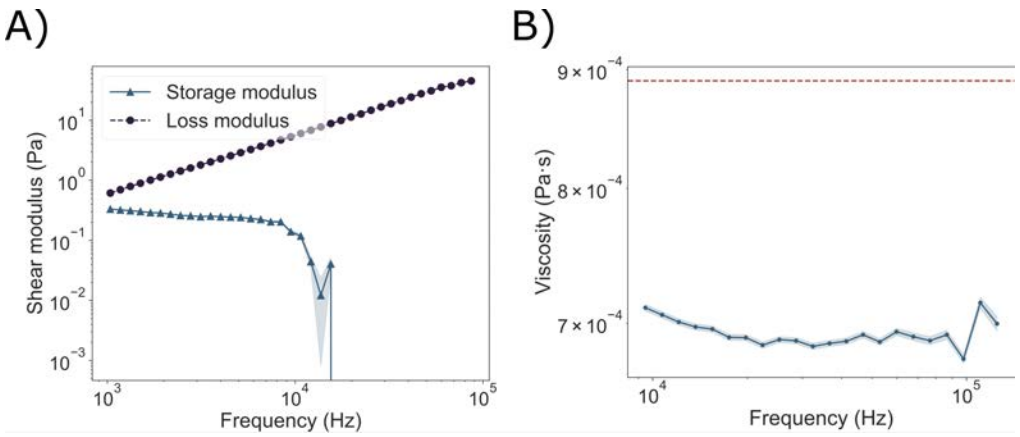

Figure 2.21: Viscoelastic properties of water extracted by DLS. A) Shear modulus of CS particles in water. The loss modulus the expected linear dependency on frequency, while the storage modulus is constant. After a certain frequency, there was not enough sensitivity to compute the loss modulus. B) The apparent viscosity of water is roughly constant accross the frequency range and very close to the expected value of water, indicated by the red dashed line.

$$\begin{aligned} G'(\omega) =& |G^*(\omega)| \cos(\pi\alpha(\omega)/2), \\ G''(\omega) =& |G^*(\omega)| \sin(\pi\alpha(\omega)/2), \end{aligned} \tag{2.53}$$

for the storage and loss modulus, respectively, and where the modulus:

$$|G^*(\omega)| \approx \frac{K_b T}{\pi r \left\langle \Delta r^2(1/\omega) \right\rangle |\Gamma[1+\alpha(\omega)]}. \tag{2.54}$$

Thanks to this description, by obtaining the MSD from the self-intermediate scattering function and evaluating at $\tau = 1/\omega$ we can obtain the shear modulus of the material in the frequency domain. Moreover, as it was mentioned before, by the Maxwell model, we can calculate the complex viscosity of the material as[60]:

$$|\eta^*(\omega)| = \sqrt{\frac{[G'(\omega)]^2 + [G''(\omega)]^2}{\omega^2}}. \tag{2.55}$$

Therefore, light scattering of particles inside a solution can yield a quite complete description of the diffusion of the particles inside the medium, given by the MSD, as well as several properties of the material that can help characterize it, like the frequency-dependent shear modulus or complex viscosity, always taking special care to all the assumptions and approximations taken. For instance, by applying the transformations just described, we can recover the high-frequency rheological properties of water by analyzing the autocorrelation of CS particles, as shown in Figure 2.21. We can see how the loss modulus of water increases linearly with frequency, while the storage modulus remains roughly constant and of a very low value, as it represents the elastic component of water. At high frequencies, however, there is too much error to accurately compute this parameter. These results match with similar characterizations performed in the literature by other techniques[88]. Moreover, the viscosity of water remains basically constant over the frequency range of $10^4 - 10^5$ Hz (Figure 2.21B) with a value similar to the expected one for water at 25 °C ($\eta = 8.9 \cdot 10^{-4}$, red dashed line). These

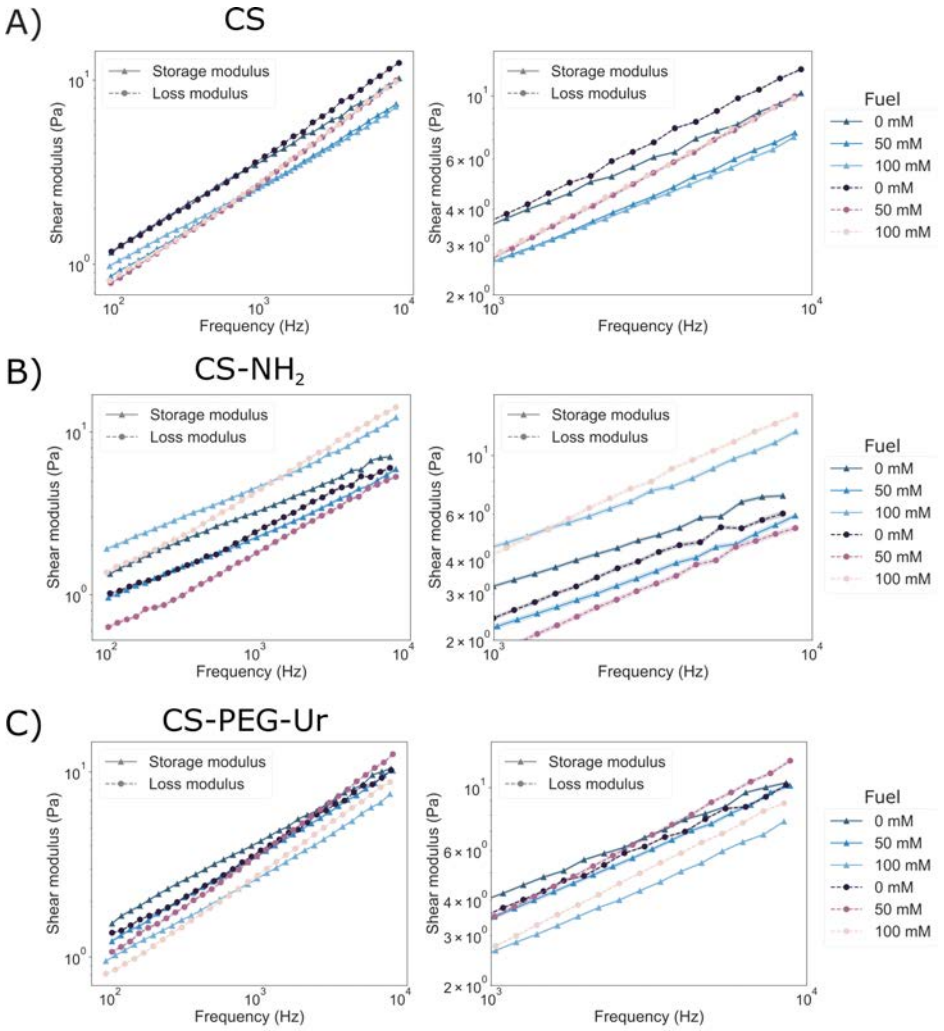

Figure 2.22: Shear modulus of HA for: A) CS particles, B) CS-NH_2, and C) CS-PEG-Ur in HA. On the right side, a zoomed in plot at high frequencies where changes are more easily seen.

small differences could simply be due to computational errors, the presence of surface charges or the aggregation of particles.

For complex fluids like HA, if the particle's diameter is much larger than the average mesh size of the polymer in which it is embedded, such medium could be considered continuous from the particle's point of view, and therefore the rheological parameters obtained from a light scattering technique will be the bulk rheological parameters, which can help expand the knowledge of the material's properties at very high frequencies[84]. However, when the size of the particle is comparable to the mesh size, the interactions with the polymer chains will be more complex, including electrostatic interactions if the particle is charged[59, 85], steric interactions[59], or even contributions from the viscosity of the solvent, as the particle can perform Brownian motion within the pores of the polymer[84]. In this case, the values obtained from Equations 2.54 and 2.55 will not represent the bulk properties, but the microscopic environment felt by the particle. In any case, if our purpose is to understand the interactions and diffusion of active Brownian particles within a viscoelastic fluid like HA, and not to characterize the material itself, this information will be useful.

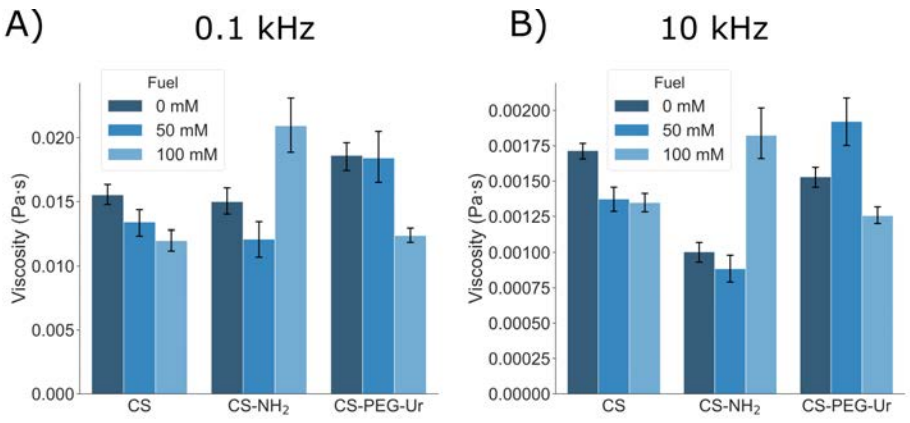

Figure 2.23: Apparent complex viscosity of HA for each type of particle and different fuel concentrations at A) 0.1 kHz, and B) 10 kHz.

Figure 2.22 shows the storage and loss modulus of the three types of particles for the three fuel concentrations. We can notice the difference from the shear response of water, since the storage modulus is also proportional to frequency, due to the elasticity of the material. For CS particles (Figure 2.22A), we see that the presence of urea decreases both the storage and the loss modulus of the material, without changing its frequency response, since the slope is the same. Therefore, the presence of urea decreases the apparent shear modulus, G, of HA, for negatively charged CS particles. For positively charged CS-NH_2 particles (Figure 2.22B) we can see already differences from the control conditions, at 0 mM of urea. For CS-NH_2 particles, the storage modulus is larger than the loss modulus in that frequency range, the opposite behavior than for CS. This means that CS-NH_2 feel the medium as more elastic, which could be related to electrostatic interactions and the fact that CS-NH_2 diffuse with an exponent α that is lower than for CS. The presence of urea, however, induces interesting effects. For 50 mM of urea, both storage and loss moduli decrease their value, but for 100 mM, they increase. For CS-PEG-Ur particles, the presence of urea decreases the apparent storage and loss moduli of the material, proportionally, with the strongest effect seen for 100 mM.

These results can be more easily understood by looking at the viscosity, according to Equation 2.55, focusing on low or high frequencies (Figure 2.23). At low frequencies (long times) we can investigate the long-term behavior of the particles in HA, while at high frequencies, we get a glimpse of the short-term interactions between the polymer chains and the particles. For negatively charged CS, the apparent viscosity of HA decreases for both 0.1 kHz and 10 kHz in a consistent manner, as could already be deduced from Figure 2.23A. The presence of urea, highly polar, could screen the negative charges of HA and make it behave more flexible, as it has already been reported for HA in ionic solutions[84]. Positively charged CS-NH_2 particles, on the other hand, feel the polymer as more viscous, especially for 100 mM of urea. It is interesting to notice that, although the apparent viscosity of the material has increased, the exponent α of CS-NH_2 particles also increased with urea concentration. Lastly, the apparent viscosity of HA for CS-PEG-UR decreases to values comparable to those of CS, but only for 100 mM urea. For 50 mM, it either remains the same (0.1 kHz) or increases (10 kHz).

This interplay of changes is very complex and depends on many parameters and interactions at different time scales. However, some conclusions can be drawn out. The presence of urea helps reducing the apparent viscosity of HA for negatively charged particles (CS) while it increases it for positively charged ones (CS-NH_2), which is an indication of the importance of electrostatic interactions on the diffusion of the particles[68]. As HA possesses carboxylic groups that are negatively

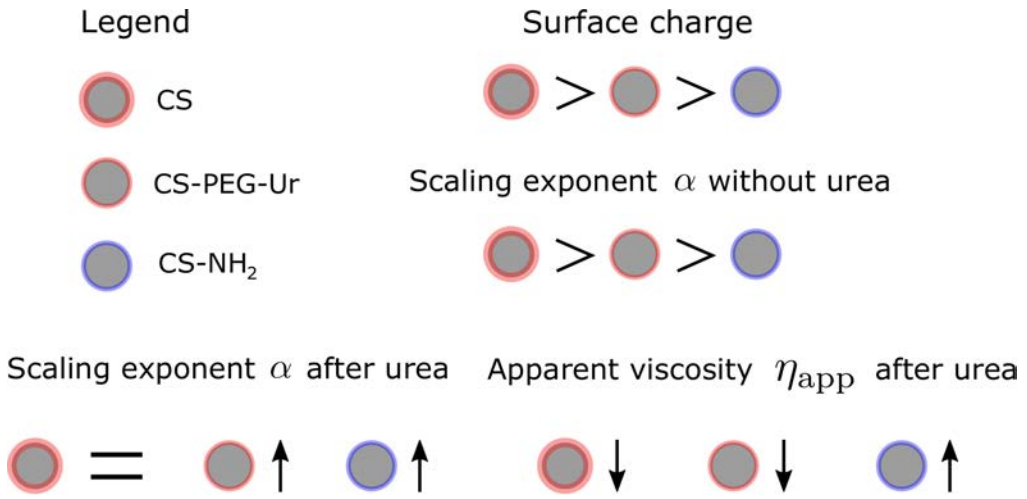

Figure 2.24: Schematic depicting the main findings. Particles with larger net negative surface charge showed higher initial scaling factor α, as electrostatic repulsion avoids trapping effects. When urea was added, both CS-NH_2 and CS-PEG-Ur particles showed an increased α, while CS particles remained the same. The apparent viscosity of the material was also reduced for negatively charged particles, namely CS-PEG-Ur particles and CS particles. Red represents negative charge; blue, positive charge.

charged, the screening effect caused by ionic or polar species can make it a more flexible polymer by assuming a random coil conformation[84, 89]. However, it is important to notice that the exponent α of the MSD, that characterizes the dynamics of subdiffusion, remained the same for CS while it increased for CS-NH_2, making them diffuse more easily. This could be a result of a screening effect of urea on the surface of the particles. Since CS particles had a very high (in negative values) zeta potential, charge shielding by a polar molecule would not produce a significant change in its absolute value. However, for CS-NH_2 that have a small but positive charge, it could cause important changes in the diffusion dynamics of the particles, by bringing it to neutrality, changing their α. CS-PEG-Ur particles also feel a smaller apparent viscosity of the material with higher urea concentration, of the same order of magnitude as CS particles. However, it remains unclear whether this change is a result only of urea, as in the case of CS particles, or the combination of urea and the reaction products from the catalytic process. In any case, the MSD exponent increased by 10% with the addition of fuel to the nanomotors. The combined effects of a reduction of the apparent viscosity and the increase of α results in a faster overall diffusion of the nanomotors. It needs to be considered, however, that despite the increase, the absolute α values achieved by CS-PEG-Ur particles after the addition of urea were the same as for CS particles, since their α for 0 mM urea was already lower (Figure 2.19).

The main findings are summarized in Figure 2.24. As conclusion, we found that negatively charged particles show higher α than positively charged ones, due to electrostatic interaction effects, as previously reported[59, 85]. Moreover, after the addition of urea, both CS-NH_2 and CS-PEG-Ur particles showed an increase in their α exponent, meanwhile CS particles remained roughly the same. The presence of urea in the medium could also improve the diffusion of negatively charged particles by decreasing the apparent viscosity of the material, while for positively charged particles, the apparent viscosity increases. Hence, in order to achieve enhanced subdiffusion of particles within HA, negatively charged particles are more appropriate. Moreover, the catalytic reaction of urease in the surface of CS-PEG-Ur seems to have positive effects by modifying the diffusion dynamics and increasing α by 10%, while decreasing the viscosity. Therefore, nanomotors can subdiffuse faster in HA matrices thanks to the catalytic reaction and these results indicate that modulation of the surface charge, making it more negative, might enhance these effects.

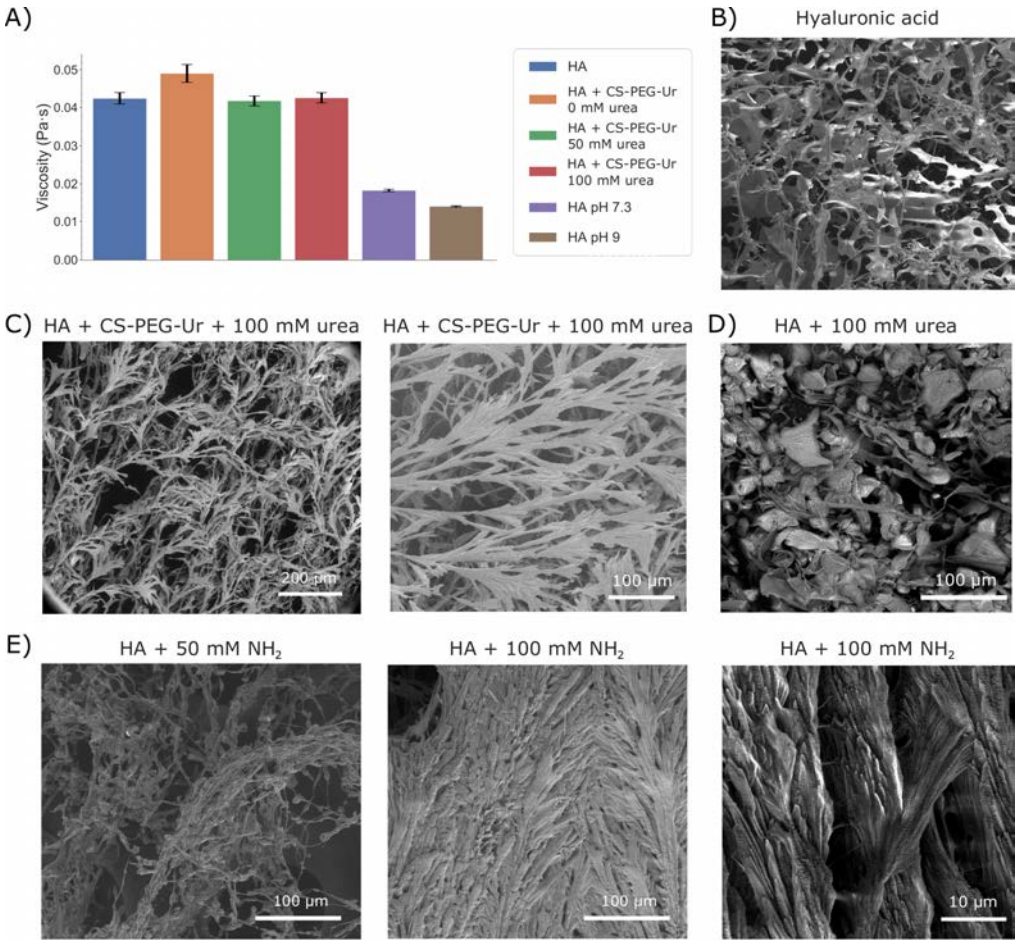

Figure 2.25: Bulk viscosity of HA in different conditions and corresponding SEM images. A) Bulk viscosity of HA in different conditions at 1 Hz, measured with a rheometer. B) SEM image of the structure of unmodified HA. C) SEM images of the structure of HA after the addition of CS-PEG-Ur nanomotors with 100 mM for 2 h. D) SEM image of the structure of HA with 100 mM of urea. E) SEM images of the structure of HA with 50 mM and 100 mM NH_2.

Macroscopic and microscopic effects or nanomotors in HA

We might wonder what is the macroscopic effect of the catalytic reaction in all these changes. Figure 2.25A shows the viscosity of HA at 1 Hz, from macro-rheological characterization, in different conditions: in physiological conditions, where its pH is 6, at pH 7.4 and at pH 9, as well as embedded with CS-PEG-Ur particles with no urea and CS-PEG-Ur with 100 mM of urea. We can clearly see that the viscosity of HA decreases with basic pH, as already known[64]. When the material is embedded with CS particles, its bulk viscosity increases, as expected. However, when 100 mM of urea is added and the sample is left to react for 2 h, the bulk viscosity of the material decreases, but it reaches the same values of HA at normal conditions. Therefore, the macroscopic viscosity of HA embedded with CS-PEG-Ur particles remains unchanged when the reaction takes place, despite creating changes in the diffusion of the particles at the microscopic level.

The changes produced by urea and the release of NH_2 were observable by SEM imaging. Figure 2.25B shows the structure of HA acid and Figure 2.25C, on the other hand, shows the effect of adding CS-PEG-Ur nanomotors with 100 mM of urea for 2 h, where the structure of HA has been abruptly modified. A different change is observed by the addition of just 100 mM urea, without nanomotors (Figure 2.25D). However, this variation in the internal structure seems different to that induced by

the catalytic reaction, in Figure 2.25C. In order to ensure that the change in Figure 2.25C is produced by the release of ammonia, Figure 2.25E shows the structure of HA with two different concentrations of NH_2, 50 mM and 100 mM. With 50 mM, there is not much variation from the natural structure of HA. However, with 100 mM, the configuration of the polymer chains are the same as with active nanomotors, hence confirming the effects of the products of the catalytic reactions.

4. Conclusions

In this chapter, we have studied the dynamics of different types of micro- and nanomotors, paying special attention to the deviations from the classic theories of motion. These theories are independent of the mechanism of motion, but they rely on certain assumptions that are not always fulfilled, such as the ergodicity of the system, the presence of a constant speed or the non-disturbance of the underlying Brownian motion. In this case, the MSD of the particles can be simply divided into a propulsive region (at short times) and a diffusive region (at long times). However, deviations from these assumptions can give rise to complex dynamics that need more exhaustive analytical approaches.

First, we revised the anomalous motion of a carbonaceous nanobottle that could move by illumination with NIR light. The strong initial burst of speed violated the assumption of constant velocity and our analyses showed that the MSD was better described as scaling with a non-specified parameter α. Moreover, the speed autocorrelation was another useful metric to characterize the directionality of the motion and distinguish on/off cases. Finite element analysis simulations were consistent with the hypothesis of liquid expulsion through the nanobottle neck upon heating of the carbon material, with very high light power causing an explosion of the nanomotor.

The second case study dealt with three types of nanomotors based on a silica nanorod structure, propelled by the catalytic decomposition of H_2O_2 by Pt and Fe_2O_3 nanoparticles. We discovered that, in this case, the ensemble of particles gave rise to two sub-populations with different motion dynamics, most likely due to a lack of control of the geometry during the deposition of the Pt layer. By dividing these two sub-populations into "high α" and "low α", we discovered that the former were better described as moving by enhanced diffusion and the latter by propulsive and directional motion.

In the third study, hybrid enzymatically propelled micromotors with non-constant velocity profiles were studied. These micromotors can consume their fuel very rapidly and change the pH of the surrounding medium by the release of ammonia, affecting their catalytic reaction and making the speed decrease in an exponential manner. To be able to characterize these types of motors, we developed an analytic formula for the time- and ensemble-averaged MSD that considered these exponential dynamics in the speed, and we proposed a strategic approach to analyze these types of particles in a time-averaged manner without losing information due to a correction factor applied to the ensemble-averaged MSD.

Finally, we continued in the study of hybrid micro- and nanomotors, considering their future applications in biomedicine as active drug carriers, and we investigated their motion in HA, a non-Newtonian viscoelastic medium. For this purpose, we used the DLS technique, that can compute the autocorrelation function of scattered light and calculate the MSD of the particles, from which their diffusivities can be extracted, as well as rheological information about the material at high frequencies. We characterized three types of particles based on core-shell silica nanoparticles, namely bare CS particles, CS particles functionalized with amino groups and CS particles functionalized with

PEG and urease, that can produce active motion. We investigated the effect of the surface charge of the particles in the diffusion in water and HA, as well as the changes produced in terms of apparent viscosity of the material. We discovered that negatively charged particles can diffuse better in HA, showing a higher α exponent in their MSD and the addition of urea increases this diffusivity by decreasing the apparent viscosity of the material. For CS-PEG-Ur nanomotors, moreover, not only the apparent viscosity is decreased, but their α is increased by 10%, indicating an overall enhancement of the motion dynamics. These studies suggest that urease-powered nanomotors should be preferably used with negatively charged particles in order to improve their diffusivity in HA and reach further.

5. Materials and methods

Anomalous diffusion of a nanobottle motor

Fabrication of the nanobottle motor

The synthesis and fabrication of the CNB motors were carried out by Dr. Mingjun Xuan, Dr. Changyon Gao and co-workers at Harbin Institute of Technology, China

The CNB motors were fabricated by a soft-template-based polymerization method, based on previous publications. Briefly, poly-(ethylene glycol)-block-poly(propylene glycol)-block-poly-(ethylene glycol) (EO20-PO70-EO20, P123) and sodium oleate (SO) were dispersed in an aqueous solution to form mixed micelles. Specifically, 0.0075 mM P123 and 0.12 mM sodium oleate were homogeneously mixed in 20 mL of deionized water and stirred slowly to form a transparent solution. Subsequently, ribose was polymerized as a carbon precursor on the surface at 160 °C. For that purpose, 40 mL of an aqueous solution containing 3 g of ribose were added to the previous polymeric solution. The resultant transparent solution was transferred into an autoclave (approximately 85 mL) and hydrothermally treated at 160 °C for 12 h. When the autoclave cooled down to room temperature, the black solid products were collected by centrifugation (9500 rpm, 15 min) and washed for three times with deionized water, and dried at 70 °C in an oven overnight. At the beginning stage of nanobottle formation, the hydration level of the poly(ethylene glycol) (PEO) blocks in the P123 polymer decreases when the temperature increases owing to the rupture of the hydrogen bonds between PEO and water at 160 °C. The PEO blocks tend to penetrate the mixed template through hydrophobic forces, causing a volume expansion that leads to cracking at the thin area of the carbonaceous shell. Ribose diffuses to the core area with low concentration, which in turn expels the inner surfactants. As a result, ribose is polymerized on the inner wall of the cavity and the corresponding inner radius is reduced gradually. Subsequently, the polymerization of ribose occurs in the cracked area by using expelled surfactants as the soft templates, and a carbonaceous open neck is formed, thus resulting in the successful preparation of bottle-structured particles. Sodium oleate (SO), poly(ethylene glycol)-block-poly(propylene glycol)-block-poly-(ethylene glycol) (EO20-PO70-EO20, P123), and ribose were purchased from Sigma-Aldrich.

Recording and tracking of the CNB motor

A two-photon confocal laser scanning microscope (TP-CLSM; 63x, oil objective) was employed with a pulsing femtosecond laser system to supply the 760 nm NIR light ($0.00 \sim 2.36$ W/cm^2) for the CNB motor to trigger on/off the motion (TP-CLSM scanning speed = 1400 Hz (lines per second), scanning area = 256 × 256 pixels). To record the motion frames of CNB motor, 488 nm light was

kept as open state to provide visible light for imaging. In the power on/off motion, 760 nm NIR light was switched on/off to control the motion of CNB motor, while the 488 nm light was open for imaging and recording. An in-house-coded program was designed to track the motion of the CNB motor containing of coordinate information. These tracking data were utilized in conducting motion analysis to calculate the MSD, angular velocity and angle distributions. The instant velocity and directional angle were calculated by the finite element method of second order.

Scanning and transmission electron microscope imaging

Scanning electron microscope (SEM, Hitachi S4800) and transmission electron microscope (TEM, FEI, Tecnai G2 F20) were used to image the morphology of the CNB motor. A two-photon confocal laser scanning microscope (TP-CLSM, Leica SP5) was employed to provide a femtosecond pulsing near infrared laser with continuous-wave to trigger and record the motion of NB motor. The surface plasmon resonance (SPR) effect of CNB motor was measured by UV-Vis-NIR spectrophotometer (PerkinElmer, Lambda 950).

Finite element analysis simulations

The FEA simulations were performed by considering a two-dimensional axisymmetric bottle structure immersed in water. A boundary heat source was applied to the walls of the CNB motor with a flux of 1.36 W/cm^2 and an emissivity efficiency of 0.8 to simulate the heat absorption by the NIR light application. The simulation was carried out in a stationary manner that is assuming the CNB motor was at a fixed position in the medium, in order to reduce the computing power.

Nanomotors based on mesoporous silica nanorods

Synthesis of the MSNRs

The synthesis of MSNRs were carried out and facilitated by Jan Grzelak, from Anna Roig's and Martí Gich's lab at the Institute of Material Science of Barcelona (ICMAB)

MSNRs were synthesized by a sol-gel method that used silica as a precursor and Pluronic P123 as a surfactant. 16.5 g of hydrochloric acid (37% wt/v) was diluted in 81 mL of Milli-Q water and 2 g of Pluronic P123 were subsequently dissolved in it. The mixture was heated up at 40 °C with vigorous stirring of 700 rpm for 3 h. Then, 4.24 g of tetraethyl orthosilicate (TEOS) were added to the previous mixture and stirred for 5 min. The reaction was left to continue for 24 h at 40 °C. Then, the mixture was transferred to an oven at 80 °for another 24 h. Afterwards, the synthesized silica nanorods were filtered and dried at 50 °C overnight. Finally the MSNRs were washed in ethanol in a Soxhlet extractor (24 cycles) in order to remove the surfactant and they were annealed at 500 °C for 5 h.

Synthesis of MSNR-Fe

The synthesis of MSNRs with Fe_2O_3 nanoparticles were carried out and facilitated by Jan Grzelak, from Anna Roig's and Martí Gich's lab at the Institute of Material Science of Barcelona (ICMAB)

Iron oxide (Fe_2O_3) nanoparticles were synthesized using a wet impregnation method. MSNRs and iron (III) nitrate nonahydrate were mixed and heated above the melting temperature of the iron (III) nitrate nonahydrate precursor (47.2 °C). Then a thermal decomposition of the precursor was carried out at 425 °C for 2 h.

Fabrication of MSNR-Pt and MSNR-Fe-Pt

In order to fabricate nanomotors based on Pt, monolayers of MSNR and MSNR-Fe were deposited by adding 50 μL of each type of nanorod at 45° on a glass slide of 24x24 mm, which had been previously washed with acetone and isopropanol, and treated with oxygen plasma, in order to remove contaminants. After the monolayers had dried, Pt was sputtered using a Leica EM ACE600 sputter, at a rate of 0.4 nm/s, with a working distance of 45 mm, a current of 35 mA and achieving a thickness of 10 nm of sputtered Pt.

Characterization of nanorods

The MSNRs and the three types of motors derived from them were characterized by SEM, TEM, DLS and EDX mapping. SEM imaging was performed using a FEI NOVA NanoSEM 230 scanning microscope at 10 kV. TEM imaging was performed with a JEOL JEM-2100 transmission microscope. The electrophoretic mobility of the nanorods was obtained with a Wyatt Möbius DLS machine coupled with an Atlas pressurization system. EDX mapping was performed with a Magellan 400L Field Emission Scanning Electron Microscope with attached X-Max Ultim Extreme EDX (Oxford Instruments).

Optical video recording of MSNRs

The motion of the nanorods and nanomotors was performed with an optical inverted microscope (Leica DMi8), equipped with a 63x water immersion objective (NA = 1.2). Briefly, a concentrated solution of nanomotors was diluted in 1 mL of water. Then, a drop of this solution was mixed in a 1:1 ratio with a H_2O_2 solution to achieve final concentrations of 0 %, 0.5 %, 1 %, 1.5%, 3% and 5% (v/v), and the final solution was placed in a glass coverslip under the microscope. Several videos of 30 s at 25 frames per second (FPS) were recorded for each condition. The trajectories of the particles was obtained by a previously available home-made tracking software based on Python that would locate and track the particles based on image processing techniques, returning the positions of the particles with time[32, 40]. The rest of the analysis was performed with a "Motion Visualization Tool" Python home-made script that was designed for this project. For each of the conditions of nanomotors and fuel concentration, a sample size between N = 50 - 150 was used.

Motion visualization tool

The motion visualization tool was a Python (v. 3.7) script designed to analyze large quantities of data obtained with this project. This tool displayed a graphic user interface (through the module PyQt5) that allowed the user to analyze together large sets of data corresponding to the same conditions (i.e. MSNR-Pt at 3 % fuel) using the trajectory points obtained from the previously available tracking software. The tool extracted the (x, y) positions from each particle and could perform all the following analyses, if selected by the user: 1) computation of the MSD; 2) plotting of the trajectories; 3) calculation of the instantaneous speed by the centered finite difference of second order

method; 4) computation of the MSAD; 5) computation of the velocity autocorrelation function; 6) computation of the local exponent α in terms of time; 7) fit the MSD to a linear, quadratic or logarithmic equation and extract parameters; and 8) fit the MSAD to a linear or quadratic equation and extract parameters. Moreover, the region of interest to perform the MSDs could be indicated (being 10% of the maximum video length the default) as well as the possibility to perform averages between all particles and extract the average values of the parameters of interest. In this case, all the analyses were performed individually and in average and reported in different folders in an organized manner.

Enzymatic micromotors with exponentially decaying speed

Micromotor experiments

The synthesis and video recording of hollow silica micromotors was performed by Xavier Arqué at the Institute of Bioengineering of Catalonia (IBEC)

Experiments of micromotors were performed with urease-coated hollow silica microparticles. Briefly, the silica micro-particles were synthesized from 2 μm polystyrene microparticles (Sigma-Aldrich) by mixing them with an ammonium hydroxide solution, 3-aminopropyltriethoxysilane (APTES) and tetraethylorthosilicate (TEOS) in ethanol. The polystyrene beads with a silica shell were washed with dimethylformamide to remove polystyrene, making them hollow. Functionalization of the micromotors with urease was performed by functionalizing first with gluteraldehyde followed by urease (from Canavalia ensiformis, Type IX, powder, 50.000–100.000 units g^{-1} solid, Sigma-Aldrich). The videos of the enzymatic micromotor motion were recorded using a high speed camera (Hamamatsu Digital Camera C11440) of an inverted optical microscope (Leica DMi8). A 63x water immersion objective (NA = 1.2) was used to record the micromotors at 25 FPS, placed on a glass slide, mixed with urea at a final concentration of 100 mM (Sigma-Aldrich) and covered with a cover slip. For the long time tracking of the micromotors, videos of 30 seconds were recorded at the beginning of each minute from 0 up to 10 minutes, being the minute 0 right after mixing the micromotors with the substrate solution. From second 30 to 60, the recording stopped and that time was used to refocus the particle in the field of view. In the case of drifting particles, the drift was generated by making the solution touch the lateral part of an adhesive tape attached the glass slide, creating a slow flow in the solution.

Enzymatic nanomotors moving in viscoelastic media

Hyaluronic acid

Hyaluronic acid sodium salt from Streptococcus Equi (Sigma-Aldrich cat. no. 53747) was dissolved in pure water at a concentration of 2 mg/mL overnight under stirring conditions to make a stock solution. To obtain the solutions of 1 mg/mL HA, 1 mg/mL HA + 50 mM urea and 1 mg/mL HA + 100 mM urea for DLS experiments, pure water, 100 mM urea and 200 mM solutions were mixed at a concentration of 1:1 with the stock solution of HA and homogenized by pipetting. CS, CS-NH_2 and CS-PEG-Ur particles were added at a concentration of 10 μmg/mL from a stock solution of 3 mg/mL into the HA solutions.

CS nanoparticle synthesis and functionalization

Synthesis of bare CS particles was carried out by Angel Blanco at the Institute for Bioengineering of Catalonia (IBEC)

CS particles were synthetized as reported elsewhere[41]. Briefly, ethanol (7 mL), pure water (10 mL) and ammonium hydroxide (2 mL) were dissolved and stirred for 15 min. Subsequently, 6 mL of tetraethylorthosilicate (TEOS, 99%, Sigma-Aldrich), was added dropwise and the mixture was left stirring for 21 h. The solid silica spheres were collected and washed with ethanol. 60 mg of these silica spheres were dissolved in water (20 mL), triethanolamine (TEOA, 99%, Sigma-Aldrich) and cetyltrimethylammonium bromide (CTAB, 99%, Sigma-Aldrich). The solution was heated to 80 °C and 0.125 mL of TEOS was added dropwise. The solution was stirred for 2 h and the nanoparticles collected by centrifugation and washed in ultrapure water. Finally, the nanoparticles were suspended in a solution of MeOH and HCl (30 mL, 10:0.6) and refluxed for 24 h at 80 °C. The final nanoparticles were collected and washed in ethanol.

CS-NH_2 nanoparticles were obtained by functionalization with 3-aminopropyltriethoxysilane (APTES). A solution of 2 mg/mL of CS particles was suspended in a mixture of Ethanol and APTES (20:1 ratio) and shaken for 24 h in a rotatory shaker. Finally, the particles were collected by centrifugation and washed in ethanol three times.

CS-PEG-Ur nanomotors were functionalized following the amine functionalization with APTES. First, 2 mg of CS-NH_2 nanoparticles were resuspended in 0.9 mL of PBS with 0.1 mL of glutaraldehyde solution (25% in water, Sigma-Aldrich). The mixture was vortexed and left for 2.5 h in a rotatory shaker. Then, the particles were centrifuged and washed three times with PBS. Then, the particles were suspended in a 1-mL solution containing 3 mg of urease (from Canavalia ensiformis, Type IX, powder, 50.000–100.000 units g^{-1} solid, Sigma-Aldrich) and 3 μg of PEG (methoxypolyethylene glycol amine, 5.000, Sigma-Aldrich). The solution was left in a rotatory shaker at room temperature overnight and then centrifuged and washed in PBS.

DLS measurements

DLS measurements were performed with a Möbius DLS system (Wyatt Technology), using disposable cuvettes of 1 mL of volume. Before starting the measurements, the DLS system was left to stabilize at 25 °C and the nanoparticle solution was sonicated for 4 min in order to avoid aggregation. As mentioned before, the solutions of HA with or without urea were prepared by mixing the components in a 1:1 ratio to achieve the final concentrations. Then, the particles were added to a concentration of 10 μg/mL, mixed thoroughly with a pipette while avoiding the generation of bubbles and added to the disposable cuvette. Each measurement was the average of 3 runs of the DLS system. The data was extracted into a .csv file and analyzed manually with a home-made Python program based on the theory described in the main text. Zeta-potential measurements were performed with a dip cell in the Möbius DLS system.

For the q wave vector computation, according to Equation 2.21, the angle θ at which the detector is located, the wavelength λ of the laser and the refractive index n of the medium, are needed. For the Möbius system, $\theta = 163.52°$ and $\lambda = 532$ nm. The refractive index, in the case of water, was taken as $n_w = 1.333$. For HA, based on a previous report[61], its refractive index was estimated to be to be $n_{HA} = 1.563$ for 1 mg/mL.

After the acquisition of autocorrelation functions and during post-processing of the results, filtering of the data was performed. The baseline, B, was calculated, as explained in the text, by averaging the autocorrelation value when the function was completely decorrelated. For water, the averaging was performed between $1 \cdot 10^5$ μs and $5 \cdot 10^5$ μs. For HA, for which the autocorrelation lasted longer, averaging was performed between $1 \cdot 10^6$ μs and $5 \cdot 10^6$ μs. Both in water and in HA, but especially in the latter, the autocorrelations completely decreased to a baseline close to 1, indicating the absence of aggregates, dust or bubbles for water, or a strong caging effect at short times, for HA. A threshold of $B < 1.05$ was applied to filter noiseless data, as higher values of the baseline could indicate the presence of contaminants in the sample.

Macrorheology studies

The rheological properties of HA at different pH and with/without particles were performed with a Discovery HR-2 controlled-stress rheometer (TA Instruments) equipped with a Peltier steel cone geometry of 40 mm of diameter, 26 μm of truncation, and an angle of 1.019°. A flow ramp with shear rate from 100 1/s to 0.01 1/s was performed, in logarithmic mode with 600 s of duration per point, with a pre-conditioning of 30 s and pre-shear of 3 rad/s for 10 s.

Characterization through scanning electron microscopy

To study the internal structure of HA with SEM, a process of liophylization was performed overnight in order to remove all the water content without losing the three-dimensional structure of the material. Briefly, the samples were snap-freezed in liquid nitrogen and subsequently placed in a liophylizer (Virtis Genesis Pilot Lyophilizer) for 24 h. Then, the samples were characterized through SEM (FEI NOVA NanoSEM 230) at 10 kV.

References

[1] M. Xuan, R. Mestre, C. Gao, C. Zhou, Q. He, and S. Sánchez, *Noncontinuous Super-Diffusive Dynamics of a Light-Activated Nanobottle Motor,* Angewandte Chemie - International Edition **57**, 6838 (2018).

[2] P. Romanczuk, M. Bär, W. Ebeling, B. Lindner, and L. Schimansky-Geier, *Active Brownian particles: From individual to collective stochastic dynamics,* European Physical Journal: Special Topics **202**, 1 (2012).

[3] F. Höfling and T. Franosch, *Anomalous transport in the crowded world of biological cells,* Reports on Progress in Physics **76**, 046602 (2013), arXiv:1301.6990 .

[4] C. Bechinger, R. Di Leonardo, H. Löwen, C. Reichhardt, G. Volpe, and G. Volpe, *Active particles in complex and crowded environments,* Reviews of Modern Physics **88**, 045006 (2016), arXiv:1602.00081 .

[5] L. Zhang, J. J. Abbott, L. Dong, K. E. Peyer, B. E. Kratochvil, H. Zhang, C. Bergeles, and B. J. Nelson, *Characterizing the swimming properties of artificial bacterial flagella,* Nano Letters **9**, 3663 (2009).

[6] T. Patiño, X. Arqué, R. Mestre, L. Palacios, and S. Sánchez, *Fundamental Aspects of Enzyme-Powered Micro- and Nanoswimmers,* Accounts of Chemical Research **51**, 2662 (2018).

[7] J. Katuri, X. Ma, M. M. Stanton, and S. Sánchez, *Designing micro-and nanoswimmers for specific applications,* Accounts of Chemical Research **50**, 2 (2017).

[8] S. Sanchez, L. Soler, and J. Katuri, *Chemically powered micro- and nanomotors,* Angewandte Chemie - International Edition **54**, 1414 (2015).

[9] S. Palagi, D. P. Singh, and P. Fischer, *Light-Controlled Micromotors and Soft Microrobots,* Advanced Optical Materials 7, 1 (2019).

[10] L. Xu, F. Mou, H. Gong, M. Luo, and J. Guan, *Light-driven micro/nanomotors: From fundamentals to applications,* Chemical Society Reviews **46**, 6905 (2017).

[11] T. Xu, W. Gao, L. P. Xu, X. Zhang, and S. Wang, *Fuel-Free Synthetic Micro-/Nanomachines,* Advanced Materials **29**, 1603250 (2017).

[12] W. F. Paxton, K. C. Kistler, C. C. Olmeda, A. Sen, S. K. St. Angelo, Y. Cao, T. E. Mallouk, P. E. Lammert, and V. H. Crespi, *Catalytic nanomotors: Autonomous movement of striped nanorods,* Journal of the American Chemical Society **126**, 13424 (2004).

[13] Y. Wang, R. M. Hernandez, D. J. Bartlett, J. M. Bingham, T. R. Kline, A. Sen, and T. E. Mallouk, *Bipolar electrochemical mechanism for the propulsion of catalytic nanomotors in hydrogen peroxide solutions,* Langmuir **22**, 10451 (2006).

[14] N. Mano and A. Heller, *Bioelectrochemical propulsion,* Journal of the American Chemical Society **127**, 11574 (2005).

[15] D. Pantarotto, W. R. Browne, and B. L. Feringa, *Autonomous propulsion of carbon nanotubes powered by a multienzyme ensemble,* Chemical Communications , 1533 (2008).

[16] S. Sanchez, A. A. Solovev, Y. Mei, and O. G. Schmidt, *Dynamics of Biocatalytic Microengines Mediated by Variable Friction Control,* Journal of the American Chemical Society **132**, 13144 (2010).

[17] A. A. Solovev, Y. Mei, E. B. Ureña, G. Huang, and O. G. Schmidt, *Catalytic microtubular jet engines self-propelled by accumulated gas bubbles,* Small **5**, 1688 (2009).

[18] A. A. Solovev, W. Xi, D. H. Gracias, S. M. Harazim, C. Deneke, S. Sanchez, and O. G. Schmidt, *Self-Propelled Nanotools,* ACS Nano **6**, 1751 (2012).

[19] V. Magdanz, G. Stoychev, L. Ionov, S. Sanchez, and O. G. Schmidt, *Stimuli-responsive microjets with reconfigurable shape,* Angewandte Chemie - International Edition **53**, 2673 (2014).

[20] S. Sanchez, A. A. Solovev, S. Schulze, and O. G. Schmidt, *Controlled manipulation of multiple cells using catalytic microbots,* Chemical Communications **47**, 698 (2011).

[21] A. A. Solovev, S. Sanchez, M. Pumera, Y. F. Mei, and O. C. Schmidt, *Magnetic control of tubular catalytic microbots for the transport, assembly, and delivery of micro-objects,* Advanced Functional Materials **20**, 2430 (2010).

[22] L. Soler, V. Magdanz, V. M. Fomin, S. Sanchez, and O. G. Schmidt, *Self-propelled micromotors for cleaning polluted water,* ACS Nano 7, 9611 (2013).

[23] M. Guix, J. Orozco, M. Garcia, W. Gao, S. Sattayasamitsathit, A. Merkoči, A. Escarpa, and J. Wang, *Superhydrophobic alkanethiol-coated microsubmarines for effective removal of oil,* ACS Nano **6**, 4445 (2012).

[24] J. Parmar, D. Vilela, K. Villa, J. Wang, and S. Sánchez, *Micro- and Nanomotors as Active Environmental Microcleaners and Sensors,* Journal of the American Chemical Society **140**, 9317 (2018).

[25] J. Orozco, V. García-Gradilla, M. D'Agostino, W. Gao, A. Cortés, and J. Wang, *Artificial Enzyme-Powered Microfish for Water-Quality Testing,* ACS Nano 7, 818 (2013).

[26] S. Campuzano, D. Kagan, J. Orozco, and J. Wang, *Motion-driven sensing and biosensing using electrochemically propelled nanomotors,* Analyst **136**, 4621 (2011).

[27] J. Katuri, W. E. Uspal, J. Simmchen, A. Miguel-López, and S. Sánchez, *Cross-stream migration of active particles,* Science Advances **4**, eaao1755 (2018).

[28] J. R. Howse, R. A. L. Jones, A. J. Ryan, T. Gough, R. Vafabakhsh, and R. Golestanian, *Self-Motile Colloidal Particles: From Directed Propulsion to Random Walk,* Physical Review Letters **99**, 048102 (2007), arXiv:0706.4406 .

[29] L. S. Palacios, J. Katuri, I. Pagonabarraga, and S. Sánchez, *Guidance of active particles at liquid–liquid interfaces near surfaces,* Soft Matter **15**, 6581 (2019).

[30] J. Simmchen, A. Baeza, D. Ruiz-Molina, and M. Vallet-Regí, *Improving catalase-based propelled motor endurance by enzyme encapsulation,* Nanoscale **6**, 8907 (2014).

[31] X. Ma and S. Sánchez, *Bio-catalytic mesoporous Janus nano-motors powered by catalase enzyme,* Tetrahedron **73**, 4883 (2017).

[32] X. Ma, A. Jannasch, U. R. Albrecht, K. Hahn, A. Miguel-López, E. Schäffer, and S. Sánchez, *Enzyme-Powered Hollow Mesoporous Janus Nanomotors,* Nano Letters **15**, 7043 (2015).

[33] K. K. Dey, X. Zhao, B. M. Tansi, W. J. Méndez-Ortiz, U. M. Córdova-Figueroa, R. Golestanian, and A. Sen, *Micromotors Powered by Enzyme Catalysis,* Nano Letters **15**, 8311 (2015).

[34] P. Schattling, B. Thingholm, and B. Städler, *Enhanced Diffusion of Glucose-Fueled Janus Particles,* Chemistry of Materials **27**, 7412 (2015).

[35] A. Joseph, C. Contini, D. Cecchin, S. Nyberg, L. Ruiz-Perez, J. Gaitzsch, G. Fullstone, X. Tian, J. Azizi, J. Preston, G. Volpe, and G. Battaglia, *Chemotactic synthetic vesicles: Design and applications in blood-brain barrier crossing,* Science Advances **3**, e1700362 (2017).

[36] L. K. E. A. Abdelmohsen, M. Nijemeisland, G. M. Pawar, G.-J. A. Janssen, R. J. M. Nolte, J. C. M. van Hest, and D. A. Wilson, *Dynamic Loading and Unloading of Proteins in Polymeric Stomatocytes: Formation of an Enzyme-Loaded Supramolecular Nanomotor,* ACS Nano **10**, 2652 (2016).

[37] A.-I. Bunea, I.-A. Pavel, S. David, and S. Gáspár, *Modification with hemeproteins increases the diffusive movement of nanorods in dilute hydrogen peroxide solutions,* Chemical Communications **49**, 8803 (2013).

[38] P. S. Schattling, M. A. Ramos-Docampo, V. Salgueiriño, and B. Städler, *Double-Fueled Janus Swimmers with Magnetotactic Behavior,* ACS Nano **11**, 3973 (2017).

[39] X. Arqué, A. Romero-Rivera, F. Feixas, T. Patiño, S. Osuna, and S. Sánchez, *Intrinsic enzymatic properties modulate the self-propulsion of micromotors,* Nature Communications **10**, 2826 (2019).

[40] X. Ma, A. C. Hortelao, A. Miguel-López, and S. Sánchez, *Bubble-Free Propulsion of Ultrasmall Tubular Nanojets Powered by Biocatalytic Reactions,* Journal of the American Chemical Society **138**, 13782 (2016).

[41] A. C. Hortelão, T. Patiño, A. Perez-Jiménez, À. Blanco, and S. Sánchez, *Enzyme-Powered Nanobots Enhance Anticancer Drug Delivery,* Advanced Functional Materials **28**, 1705086 (2018).

[42] T. Patiño, N. Feiner-Gracia, X. Arqué, A. Miguel-López, A. Jannasch, T. Stumpp, E. Schäffer, L. Albertazzi, and S. Sánchez, *Influence of Enzyme Quantity and Distribution on the Self-Propulsion of Non-Janus Urease-Powered Micromotors,* Journal of the American Chemical Society **140**, 7896 (2018).

[43] Z. Wu, X. Lin, X. Zou, J. Sun, and Q. He, *Biodegradable Protein-Based Rockets for Drug Transportation and Light-Triggered Release,* ACS Applied Materials & Interfaces **7**, 250 (2015).

[44] R. Golestanian, T. B. Liverpool, and A. Ajdari, *Propulsion of a molecular machine by asymmetric distribution of reaction products,* Physical Review Letters **94**, 220801 (2005).

[45] R. Golestanian, T. B. Liverpool, and A. Ajdari, *Designing phoretic micro- and nano-swimmers,* New Journal of Physics **9**, 126 (2007), arXiv:0701168 [cond-mat] .

[46] I. A. Pavel, A. I. Bunea, S. David, and S. Gáspár, *Nanorods with biocatalytically induced self-electrophoresis,* ChemCatChem **6**, 866 (2014).

[47] M. De Corato, X. Arqué, T. Patiño, M. Arroyo, S. Sánchez, and I. Pagonabarraga, *Self-Propulsion of Active Colloids via Ion Release: Theory and Experiments,* Physical Review Letters **124**, 108001 (2020).

[48] C.-T. Wu, Y.-W. Lin, and H.-R. Jiang, *Zeta potential dependent Self-electrophoresis of Pt-coated Janus particles in hydrogen peroxide solutions,* (2017), arXiv:1702.03743 .

[49] A. Brown and W. Poon, *Ionic effects in self-propelled Pt-coated Janus swimmers,* Soft Matter **10**, 4016 (2014), arXiv:1312.4130 .

[50] G. Dunderdale, S. Ebbens, P. Fairclough, and J. Howse, *Importance of particle tracking and calculating the mean-squared displacement in distinguishing nanopropulsion from other processes,* Langmuir **28**, 10997 (2012).

[51] G. E. Uhlenbeck and L. S. Ornstein, *On the Theory of the Brownian Motion,* Physical Review **36**, 823 (1930).

[52] A. C. Hortelao, R. Carrascosa, N. Murillo-Cremaes, T. Patino, and S. Sánchez, *Targeting 3D Bladder Cancer Spheroids with Urease-Powered Nanomotors,* ACS Nano **13**, 429 (2019).

[53] D. Walker, B. T. Ka sdorf, H.-H. Jeong, O. Lieleg, and P. Fischer, *Enzymatically active biomimetic micropropellers for the penetration of mucin gels,* Science Advances **1**, e1500501 (2015).

[54] T. Li, S. Kheifets, D. Medellin, and M. G. Raizen, *Measurement of the instantaneous velocity of a brownian particle,* Science **328**, 1673 (2010).

[55] T. Patino, A. Porchetta, A. Jannasch, A. Lladó, T. Stumpp, E. Schäffer, F. Ricci, and S. Sánchez, *Self-Sensing Enzyme-Powered Micromotors Equipped with pH-Responsive DNA Nanoswitches,* Nano Letters **19**, 3440 (2019).

[56] D. Vilela, U. Cossío, J. Parmar, A. M. Martínez-Villacorta, V. Gómez-Vallejo, J. Llop, and S. Sánchez, *Medical Imaging for the Tracking of Micromotors,* ACS Nano **12**, 1220 (2018).

[57] N. Gal, D. Lechtman-Goldstein, and D. Weihs, *Particle tracking in living cells: A review of the mean square displacement method and beyond,* Rheologica Acta **52**, 425 (2013).

[58] S. Palagi, D. Walker, T. Qiu, and P. Fischer, *Microbiorobotics: Biologically Inspired Microscale Robotic Systems*, 2nd ed. (Elsevier Inc., 2017) pp. 133–162.

[59] Q. Xu, N. J. Boylan, J. S. Suk, Y. Y. Wang, E. A. Nance, J. C. Yang, P. J. McDonnell, R. A. Cone, E. J. Duh, and J. Hanes, *Nanoparticle diffusion in, and microrheology of, the bovine vitreous ex vivo,* Journal of Controlled Release **167**, 76 (2013).

[60] T. G. Mason, *Estimating the viscoelastic moduli of complex fluids using the generalized Stokes-Einstein equation,* Rheologica Acta **39**, 371 (2000).

[61] R. Tadmor, N. Chen, and J. N. Israelachvili, *Thin film rheology and lubricity of hyaluronic acid solutions at a normal physiological concentration,* Journal of Biomedical Materials Research **61**, 514 (2002).

[62] M. K. Cowman, H. G. Lee, K. L. Schwertfeger, J. B. McCarthy, and E. A. Turley, *The content and size of hyaluronan in biological fluids and tissues,* Frontiers in Immunology **6**, 261 (2015).

[63] D. Schamel, A. G. Mark, J. G. Gibbs, C. Miksch, K. I. Morozov, A. M. Leshansky, and P. Fischer, *Nanopropellers and Their Actuation in Complex Viscoelastic Media,* ACS Nano **8**, 8794 (2014).

[64] M. K. Cowman, T. A. Schmidt, P. Raghavan, and A. Stecco, *Viscoelastic Properties of Hyaluronan in Physiological Conditions,* F1000Research **4**, 622 (2015).

[65] J. Stetefeld, S. A. McKenna, and T. R. Patel, *Dynamic light scattering: a practical guide and applications in biomedical sciences,* Biophysical Reviews **8**, 409 (2016).

[66] P. Cicuta and A. M. Donald, *Microrheology: a review of the method and applications,* Soft Matter **3**, 1449 (2007).

[67] B. A. Krajina, C. Tropini, A. Zhu, P. Digiacomo, J. L. Sonnenburg, S. C. Heilshorn, and A. J. Spakowitz, *Dynamic Light Scattering Microrheology Reveals Multiscale Viscoelasticity of Polymer Gels and Precious Biological Materials,* ACS Central Science **3**, 1294 (2017).

[68] T. Stylianopoulos, M. Z. Poh, N. Insin, M. G. Bawendi, D. Fukumura, L. L. Munn, and R. K. Jain, *Diffusion of particles in the extracellular matrix: The effect of repulsive electrostatic interactions,* Biophysical Journal **99**, 1342 (2010).

[69] B. J. Berne and R. Pecora, *Dynamic Light Scattering with Applications to Chemistry, Biology, and Physics* (Courier Corporation, 1977).

[70] D. Ferreira, R. Bachelard, W. Guerin, R. Kaiser, and M. Fouché, *Connecting field and intensity correlations: the Siegert relation and how to test it,* (2020), arXiv:2002.05425 .

[71] P. Hopkins, A. Fortini, A. J. Archer, and M. Schmidt, *The van Hove distribution function for Brownian hard spheres: Dynamical test particle theory and computer simulations for bulk dynamics,* Journal of Chemical Physics **133**, 224505 (2010), arXiv:1010.2124 .

[72] J. P. Boon and S. Yip, *Molecular Hydrodynamics* (Courier Corporation, 1980).

[73] B. J. Frisken, *Revisiting the method of cumulants for the analysis of dynamic light-scattering data,* Applied Optics **40**, 4087 (2001).

[74] D. E. Koppel, *Analysis of macromolecular polydispersity in intensity correlation spectroscopy: The method of cumulants,* The Journal of Chemical Physics **57**, 4814 (1972).

[75] M. Doi and M. Makino, *Electrokinetic boundary condition compatible with the Onsager reciprocal relation in the thin double layer approximation,* Journal of Chemical Physics **128**, 044715 (2008).

[76] X. Zheng, B. Ten Hagen, A. Kaiser, M. Wu, H. Cui, Z. Silber-Li, and H. Löwen, *Non-Gaussian statistics for the motion of self-propelled Janus particles: Experiment versus theory,* Physical Review E **88**, 032304 (2013).

[77] M. Naiim, A. Boualem, C. Ferre, M. Jabloun, A. Jalocha, and P. Ravier, *Multiangle dynamic light scattering for the improvement of multimodal particle size distribution measurements,* Soft Matter **11**, 28 (2015).

[78] J. Wang, *Anomalous Diffusion of Active Brownian Particles in Crystalline Phases,* IOP Conference Series: Earth and Environmental Science **237**, 052005 (2019).

[79] T. Guggenberger, G. Pagnini, T. Vojta, and R. Metzler, *Fractional Brownian motion in a finite interval: Correlations effect depletion or accretion zones of particles near boundaries,* New Journal of Physics **21**, 022002 (2019).

[80] S. K. Ghosh, A. G. Cherstvy, D. S. Grebenkov, and R. Metzler, *Anomalous, non-Gaussian tracer diffusion in crowded two-dimensional environments,* New Journal of Physics **18**, 1 (2016), arXiv:1508.02029v1 .

[81] M. Marseguerra and A. Zoia, *The Monte Carlo and fractional kinetics approaches to the underground anomalous subdiffusion of contaminants,* Annals of Nuclear Energy **33**, 223 (2006).

[82] M. T. Valentine, P. D. Kaplan, D. Thota, J. C. Crocker, T. Gisler, R. K. Prud'homme, M. Beck, and D. A. Weitz, *Investigating the microenvironments of inhomogeneous soft materials with multiple particle tracking,* Physical Review E **64**, 9 (2001).

[83] M. Grimm, S. Jeney, and T. Franosch, *Brownian motion in a Maxwell fluid,* Soft Matter **7**, 2076 (2011).

[84] A. Dodero, R. Williams, S. Gagliardi, S. Vicini, M. Alloisio, and M. Castellano, *A microrheological and rheological study of biopolymers solutions: Hyaluronic acid,* Carbohydrate Polymers **203**, 349 (2019).

[85] E. A. Nance, G. F. Woodworth, K. A. Sailor, T. Y. Shih, Q. Xu, G. Swaminathan, D. Xiang, C. Eberhart, and J. Hanes, *A dense poly(ethylene glycol) coating improves penetration of large polymeric nanoparticles within brain tissue,* Science Translational Medicine **4**, 149ra119 (2012).

[86] T. G. Mason and D. A. Weitz, *Optical measurements of frequency-dependent linear viscoelastic moduli of complex fluids,* Physical Review Letters **74**, 1250 (1995).

[87] T. G. Mason, K. Ganesan, J. H. Van Zanten, D. Wirtz, and S. C. Kuo, *Particle tracking microrheology of complex fluids,* Physical Review Letters **79**, 3282 (1997).

[88] D. M. Carberry, M. A. B. Baker, G. M. Wang, E. M. Sevick, and D. J. Evans, *An optical trap experiment to demonstrate fluctuation theorems in viscoelastic media,* Journal of Optics A: Pure and Applied Optics **9**, S204 (2007).

[89] B. Kim, S. Woo, Y.-S. Park, E. Hwang, and M. H. Moon, *Ionic strength effect on molecular structure of hyaluronic acid investigated by flow field-flow fractionation and multiangle light scattering,* Analytical and Bioanalytical Chemistry **407**, 1327 (2015).

III

3D bioprinting and materials for hybrid robotics

Parts of Section 2 of this chapter have been published in *Adv. Mater. Technol.* **2019**, 4, 1800631[1], in *Biomimetic and Biohybrid Systems*. Living Machines **2018**. Lecture Notes in Computer Science, vol 10928[2], and in *Biomimetic and Biohybrid Systems*. Living Machines **2019**. Lecture Notes in Computer Science, vol 11556[3]. Section 3 of this chapter is being filed for a patent.

1. Introduction and state of the art

Material science, the interdisciplinary study of material properties, has become a crucial discipline for recent advances in a wide range of fields, from bioengineering to soft robotics, or even nano- and micro-robotics, since these small robots can interact with the matrices surrounding them in complex ways. A first introduction to the study of the micro-rheological properties of natural polymers and their interactions with active nano-particles was already discussed at the end of the previous chapter, where we could get a glimpse of the heterogeneous parameters that affect the non-Newtonian behavior of naturally-occurring polymers. Nonetheless, at the macroscale, this behavior remains as interesting, and the study of the rheological properties of hydrogels and other polymers can find an enormous variety of applications in the fields of bio-hybrid soft-robotics and tissue engineering, thanks to the advances of 3D bioprinting[4–6].

3D bioprinting is a technique that allows the automated and fast-prototyping printing of cell-laden hydrogels according to different designs, in order to mimic the 3D environment of native tissue[6, 7]. Two-dimensional cultures have been widely used in biological research but, over the years, there is a increasing understanding that they are not appropriate models of native three-dimensional tissue. 3D bioprinting was born, thus, as a way to circumvent this issue, by allowing in a still somewhat futuristic view to recreate whole organs made of actual cells in their native 3D shape[8].

This dream, however, is far more complex that could be envisioned. Cell proliferation or differentiation within an extra-cellular matrix (ECM), either natural or artificial, is highly dependent on numerous macroscopic and microscopic parameters, such as the density of the matrix, the presence of cell-attachment motifs, the surface charge of polymer chains that will interact with the cell and influence the accumulation of water content, their storage and loss moduli that will affect the migration and proliferation of the cells, among others[9]. With such a large number of constraints set on the biomaterials that can be used, the options in terms of biofabrication become slimmer, specially if the three-dimensional native structure of the tissue needs to be maintained[10]. 3D bioprinting enters into play as a promising technique to achieve this.

Several modes of printing try to solve this variability in material properties by proposing different printing strategies (Table 3.1). Pneumatic-extrusion-based bioprinting is the most widely used technique, and it is based on the extrusion of a cell-laden hydrogel (or any other polymer) through a thin nozzle by the application of pressure[6]. This technique is appropriate for materials with enough pseudoplastic or shear-thinning behavior, i.e. their viscosity decreases when shear rate is increased through the printing nozzle. This reduction in viscosity allows printing at lower pressures but also helps protect the cells from high shear stresses[6]. For very low viscosity materials, ink-jet printing[11–13] or laser-assisted bioprinting[7, 14] are more appropriate ways of controlling the flow of material. Especially ink-jet bioprinting, also known as "drop-in-demand", allows very low volumes of liquids to be dispensed by using thermal[13] or acoustic forces[15, 16]. However, this method only enables to dispense cells at specific locations, without any three-dimensional structure due to the low viscosity of the material.

Long-chained biopolymers show strong shear-thinning behavior and are ideal for pneumatic extrusion 3D bioprinting[17]. During 3D bioprinting the free chains of an uncrosslinked polymer are free to re-orient longitudinally in the same direction as increasing shear stress is applied at the nozzle. At this point, the viscosity of the material decreases locally, allowing a smooth printing and, after deposition, the chains take again random orientations increasing its viscosity and retaining the printed shape. Afterwards, the material may be crosslinked to avoid losing the structure of the construct.

Table 3.1: Comparison of 3D bioprinting techniques. Adapted from [6, 7, 14, 17, 21].

	Inkjet	**Extrusion**	**Laser assisted**
Material viscosity	< 10 mPa·s	30 mPa·s to $6 \cdot 10^7$ mPa·s	1 - 300 mPa·s
Cell density	Low (< 10^6 cells/mL)	Very low to very high	Medium (< 10^8 cells/mL)
Resolution	10 - 50 μm	> 100 μm	10 - 100 μm
Cell viability	> 85%	40-95%	>95%
Printer cost	Low	Medium	High
Fabrication speed	High	Low	Medium
3D shape	Low	High	High

Materials like alginate, gelatin, fibrinogen, hyaluronic acid, chitosan, poly(ethylene glycol) diacrylate (PEGDA), collagen, nanocellulose, decellularized ECM, or chemical modifications of these, like gelatin methacrylate (GelMA) or alginate methacrylate (AlgMA) have been widely used alone or in combination with one another for their shear-thinning properties, stiffness modulation or biocompatibility[7, 8, 18–20].

Gelatin is widely used in 3D bioprinting for its shear-thinning properties in gel form at cold temperatures, but it is normally used as sacrificial material, since it dissolves at physiological conditions during cell culture[22]. In order to avoid its dissolution, its methacrylated counterpart, GelMA, can be used to increase the stiffness of the matrix and add cell attachment motives, necessary for cell survival[23]. Different crosslinking methods also call for many different combinations to fulfill any methodological or cell-specific requirements[24]. Alginate and chitosan can be chemically crosslinked, fibrinogen can be converted into fibrin by the enzyme thrombin, GelMA, PEGDA and AlgMA use UV light, while collagen has a slow temperature-dependent crosslinking. Even more, other materials can be bioprinted in parallel to achieve more complex structures. For instance, polycaprolactone is generally printed with high temperature thermo-extrusion for bone tissue regeneration due to its high stiffness[25], while polydimethyilsiloxane (PDMS) is 3D-printed for applications where softer and flexible materials are needed[1, 26]. Pluronic acid, on the other hand, is used as a sacrificial material for overhanging structures or to create vascular channels or complex 3D structures, as it can be easily washed away with cold water or PBS[8].

Most of the examples in the literature have used pneumatic-extrusion-based 3D bioprinting to bioengineer different kinds of tissues. For instance, Kang et al. developed a hydrogel mixture based on gelatin, hyaluronic acid and fibrinogen that could be mixed in specific concentrations to achieve a proper environment for skeletal muscle cells, chondrocytes, and amniotic-fluid-derived stem cells[8]. After successfully 3D-bioprinting these cell-laden hydrogels, they injected them into mice and observed the first indications of reconstruction of ear cartilage, calvarial bone and skeletal muscle. This is just one of the many examples in which 3D bioprinting has been used for organ regeneration purposes. Many other examples include cartilage[8], neural tissue[8], cardiac[18], chondrocyte[27], skin [27], ovarian follicles[27], adipose [18] or musculoskeletal tissues, which involve many cell types in conjunction[27].

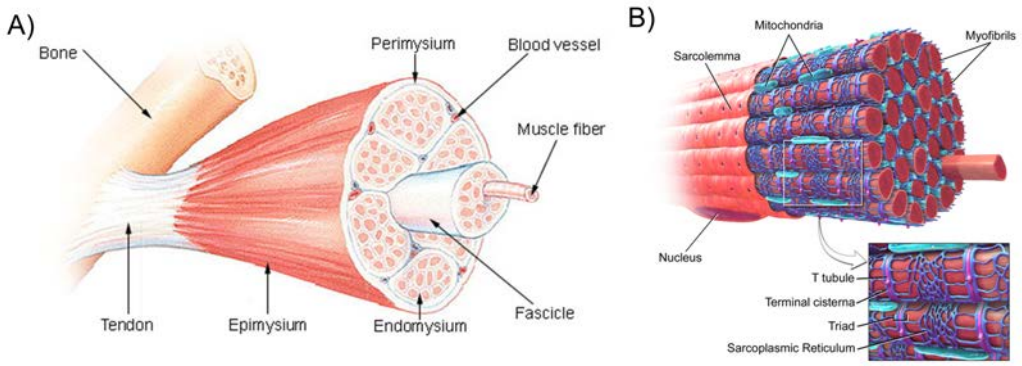

Figure 3.1: 3D structure of muscle tissue. A) At the macroscale, muscle tissues are organized in fascicles that contain several bundles of myocytes. Adapted from wikimedia.org. B) At the microscale, each myocyte contains several myofibrils, which possess a sarcomeric structure that allows muscle contraction. Adapted from [36].

Skeletal muscle tissue, in particular, is a very interesting kind of tissue due to its functionality in the form of contractions. Significant efforts have been dedicated to the reproduction of healthy skeletal muscle tissue for organ regeneration, but many other applications have been envisioned and developed over the last years, by a combination of 3D bioprinting or mold-casting techniques[1, 28–30]. For instance, biological actuators based on skeletal muscle tissue can be used to study muscle development, maturation or healing[31–33], or even act as drug testing platforms for muscle myopathies[34]; and more complex untethered actuators can take the form of bio-hybrid soft-robots, towards the next hybrid generation of soft robotics[28, 35]. These applications will be considered in more detail in the next chapters. Certainly, 3D bioengineering of skeletal muscle tissue, either by 3D bioprinting or a similar technique, is of wide interest for an increasing range of multidisciplinary fields of research, ranging from developmental biology to soft robotics.

Skeletal muscle tissue has an inherently three-dimensional architecture (Figure 3.1). Therefore, any tissue model that aims at recreating its complexity must take a three-dimensional form. Skeletal muscle is composed of bundles of muscle fibers, called myocytes, which are the basic contractile unit of the muscle and are created after fusion of myoblasts, their precursor cells, during the differentiation process. Myocytes within the bundles are densely packed and highly aligned in order to achieve very efficient and longitudinal contractions[37]. Inside each myocyte, groups of internal protein structures, called the myofibrils, are formed. These structures contain periodic units called sarcomeres, the smallest protein contractile unit, which are mainly composed of actin fibers and myosin and have the ability of contracting the myocyte upon certain stimulus under the proposed mechanism of sliding filament[38]. Generally, depolarization of the sarcolemma (the cell membrane of skeletal muscle tissue) by a neuronal action potential in the neuromuscular junction (mediated by acetylcholine) induces a cascade of ionic release[39]. This depolarization of the sarcolemma spreads across the myocyte's network of T-tubules, extensions of the cell's membrane that cover the dense group of myofibrils, having a large concentration of several ion channels and pumps and permits a rapid propagation of the action potential throughout the cells (Figure 3.1B). After this, cell signaling activates the release of Ca^{+2} ions from the sarcoplasmic reticulum, a structure within the myocyte, analogue to the endoplasmic reticulum, that stores Ca^{+2} ions and maintains their concentration at low and stable levels[40]. This calcium release creates a spark, synchronously across the whole cytosol of the myofiber, and finds its way to the a protein called troponin C in the sarcomeric structure[41]. This complex of troponin-Ca^{+2} makes the protein troponin to shift its position in the thin filaments of the myofibril, exposing the myosin-binding sites, and allowing the myosin heads to bind to the actin filaments and contraction to occur.

This is an extremely complex and hierarchical structure, that can only be achieved through natural self-organization. However, 3D bioengineering techniques are getting closer to replicating this complexity. Mouse myoblasts have already been 3D-bioprinted embedded in bio-inks and their differentiation induced in this environment to form multinucleated myotubes[1][8]. Other approaches not based on 3D bioprinting, but mold casting techcniques, have also achieved the same outcomes, and cell morphological and functionality have been more thoroughly analyzed[42]. Nonetheless, these techniques lack the versatility, automation and fast-prototyping capabilities of 3D bioprinting.

Therefore, 3D-bioprinted filaments already resemble the bundle-like organization of packed myocytes present in native tissue and their cells can synchronously contract in a longitudinal axis. The thickness of the tissue constructs that can be achieved with 3D bioprinting or mold casting is in occasions difficult to control, especially if gelatin is involved. As the oxygen diffusion limit within a tissue is around 200 μm, wider tissues can suffer from biocompatibility issues or low cell density in the inner parts of the hydrogel[43]. This causes a great loss of force, as the bundle of myotubes will not be densely packed, but actually depleted, diminishing the total force per cross-sectional area that can be achieved[28]. Moreover, in native tissue each bundle of myocytes is further organized in fascia or fascicles surrounded by the perimysium (Figure 3.1A), a layer of connective tissue (mainly collagen) that stabilizes and separates the bundles of muscle fibers, containing from 10 to 100 of them[37]. This fascicle structure has not been completely mimicked yet with 3D bioprinting, as subsequent layers of 3D-bioprinted fibers fuse with each other to form an even wider construct. The closest analogs to these kinds of structures have relied on sacrificial molds and microfabrication techniques[44]. Although many methods allow for the fabrication of width-controlled fibers, mainly based on co-axial systems dedicated to the creation of vascular channels[45] or on support baths of sacrificial polymers[46, 47], these techniques have not been used for the biofabrication of several individual skeletal muscle bundles that could be assembled like the aforementioned fascicles.

In this chapter, we will dwell more in depth into the properties of biopolymers, paying special attention to their rheological and mechanical properties, their biocompatibility and, naturally, their encapsulation with cells in order to obtain active, functional and alive muscle tissue that can be morphologically and functionally alike to native skeletal muscle tissue. In Section 2 we will demonstrate the capabilities of the 3D bioprinting technique to bioengineer three-dimensional skeletal muscle tissues that share morphological, physiological and functional characteristics with native tissue, such as the presence of multinucleated and aligned fibers, the development of internal sarcomeric structures and the contractile response upon electrical stimulation. In Section 3, we will propose a novel universal technique for the fabrication of thin, homogeneous and width-controlled fibers of virtually any hydrogel, and we will focus on the application for the fabrication of bundle-like skeletal muscle fibers that could be potentially assembled to form fascicles, similar to those present in native tissue.

2. 3D bioprinting of skeletal muscle tissue

2.1. Objectives

Skeletal muscle tissue is inherently three-dimensional. In order to perform relevant studies regarding its development, maturation or effects of different external or internal signals, an appropriate model that can capture its three-dimensional organization, as well as its functional capabilities, needs to be bioengineered. Moreover, if there is interest in its potential applications in bio-hybrid

[1]When talking about multinucleated myocytes from mice, the term myotube is commonly used, while myocyte is reserved for human skeletal muscle.

robotics, and not only in disease modeling or drug-screening for muscle-related disorders, it is necessary to completely understand the challenges and capabilities of the bio-engineered tissue constructs in order to deal with their integration into more complex systems in the future.

This sub-section deals with a first approximation to the development of 3D-bioengineered skeletal muscle tissue by 3D bioprinting. The objectives are as follows: i) to characterize the biomaterials used for their purpose and ensure their printability and biocompatibility; ii) to proof the proper differentiation of myoblasts into myotubes, maintaining the native structure of highly aligned myotube bundles; iii) to ensure their functionality by the stimulation of contractions *via* electric stimulation and their characterization in bright-field imaging and Ca^{+2} imaging; and iv) identify the short-term and long-term challenges of this bio-fabrication approach and of skeletal muscle tissue engineering in general.

2.2. Results and discussion

Material characterization

Skeletal muscle myoblasts were encapsulated and 3D-bioprinted in a hydrogel composed of biocompatible polymers. This bio-ink had to offer specific properties that could support not only in its printability, but also offer the adequate mechanical support for the cells, and correctly mimic the three-dimensional environment of the cells' ECM, with the right mechanical stiffness and sufficient attachment sites in the surrounding polymeric networks. For that reason, based on a previous work by Kang *et al.*[8], we synthesized a bio-ink composed of gelatin, fibrinogen and hyaluronic acid as main components (Figure 3.2). Each of these components had specific properties that fitted into the complex design of a proper bio-ink for skeletal muscle myoblasts: i) fibrinogen was the main biologically relevant element, as it possesses specific sites for cell attachment and proliferation; ii) gelatin provided structural support during printing, as it gels at low temperatures, and allows to retain the shape of the construct during the process; iii) hyaluronic acid provided shear-thinning properties,

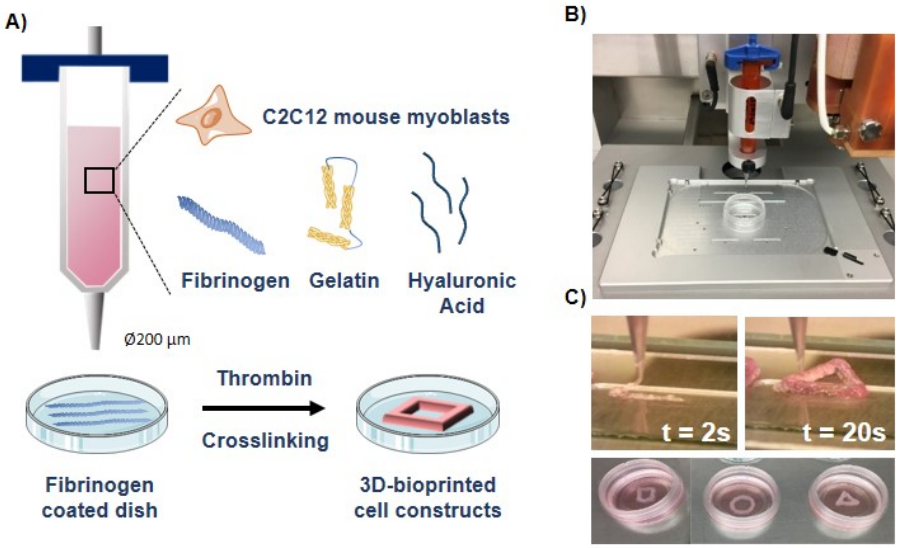

Figure 3.2: Representation of the 3D bioprinting process. A) Schematic of the fabrication of skeletal muscle tissue *via* 3D bioprinting. B) Picture of the 3D bioprinting setup. C) Snapshots of a bioprinting process of a cell-laden hydrogell with different shapes. Adapted with permission from [1].

necessary for an improved printability of the bio-ink, together with a reduction of the shear stress felt by the cells during the printing process[9]. Once printed, fibrinogen was crosslinked into fibrin by the addition of a solution of the enzyme thrombin, which gave further structural support to the printed construct. After this, gelatin and hyaluronic acid could be slowly dissolved and washed away during the incubation process as 37 °C, but the main structural integrity of the 3D-bioprinted tissue was maintained thanks to fibrin.

Rheological characterization of the bio-ink was performed to estimate the best range of temperature for 3D bioprinting. In a rheological experiment, a moving plate rotates over a stationary plate, with the characterized fluid confined between both of them. The moving plate rotates with a certain angular speed and creates a velocity profile between in the fluid as displayed in Figure 3.3A. The shear rate, $\dot{\gamma}$, is defined as the velocity of the moving plate divided by the distance between both plates and represents the rate at which the deformation is applied. The fluid opposes the deformation by applying a certain shear stress, τ, and the relationship between the shear rate and shear stress is the viscosity of the material, η. In simple fluids, like water or glycerol, also called Newtonian fluids, this relationship is linear and the viscosity, defined as the slope of the τ vs $\dot{\gamma}$ curve, is a constant value independent of the shear rate (Figure 3.3A). However, complex fluids may have other types of responses. On the one hand, shear-thinning or pseudoplastic materials decrease the viscosity when the shear rate is increased, and the shear stress vs shear rate relationship decreases its slope at high shear rates. On the other hand, shear-thickening or dilatant fluids increase their viscosity when high shear strains are applied. Therefore, the slope of the τ vs $\dot{\gamma}$ curve increases. There is another relevant type of non-Newtonian fluids, called Bingham plastics. This kind of material, which might have a linear stress vs strain relationship like a Newtonian fluid, does not intercept the shear stress at 0. This means that flow can only occur if a minimum amount of shear stress, called the yield stress, τ_0, is applied. If this fluid, in addition, behaves like a pseudoplastic it is called a Bingham pseudoplastic. This is

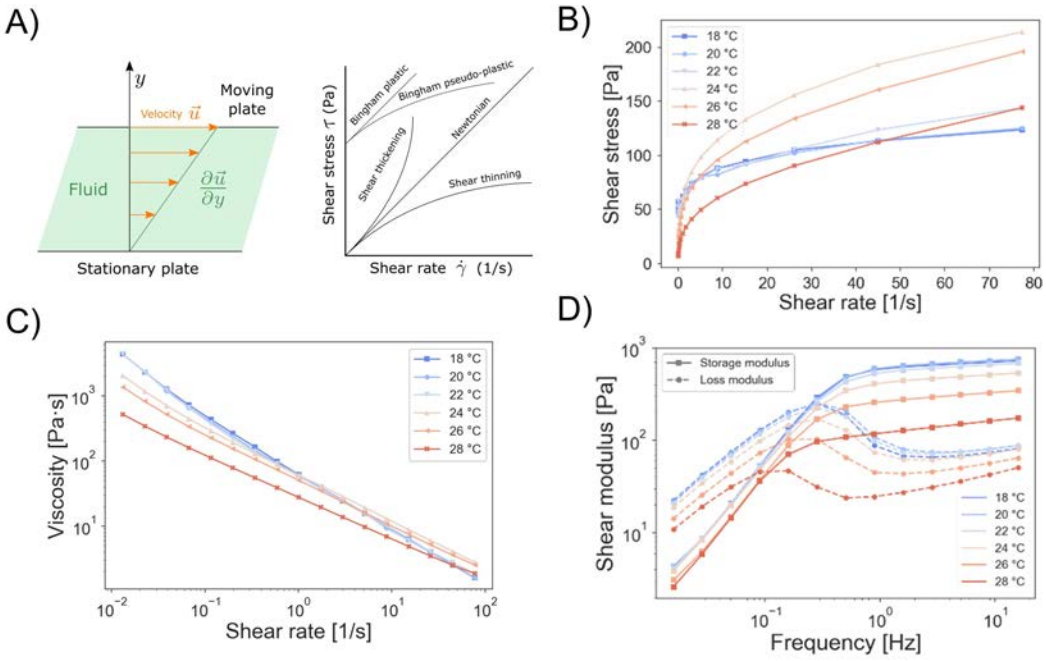

Figure 3.3: Characterization of the bio-ink. A) Shear stress vs shear rate curves for different types of materials and schematic representation of a fluid during a rheological experiment. B) Rheological characterization of the hydrogel in a shear stress vs shear rate flow ramp mode and C) viscosity in terms of the sear rate, for different temperatures. D) Dynamic shear moduli in a frequency sweep for different temperatures. Adapted with permission from [1].

the most interesting type of material for 3D bioprinting for three main reasons: i) the shear-thinning behavior helps protect the cells from from the high shear stresses felt at the tip of the nozzle, since the viscosity is reduced; ii) the fidelity of the printing is improved, because the material can flow with low viscosity through the nozzle but will retain its shape after printing as the viscosity increases; and iii) the presence of a yield stress avoids dripping of the material when no pressure is applied.

Figure 3.3B displays the shear stress vs shear rate curves of the bio-ink at temperatures ranging from 18 °C to 28 °C. Shear-thinning behavior can be clearly observed for all ranges of temperatures, as the slope of the curve decreases for increasing shear rate. However, the higher the temperature, the more linear is the trend of the curve, indicating a tendency towards Newtonian behavior as gelatin becomes liquid. A fitting to the Herschel-Bulkley model ($\tau = \tau_0 + k\gamma^n$), which approximates the behavior of a Bingham pseudoplastic fluid, also picks up this response. The hydrogel at 18 °C yields a shear-thinning parameter $n = 0.32 \pm 0.04$, meanwhile the same material at 28 °C gives $n = 0.408 \pm 0.008$. The main change, however, is the decrease of yield stress with increasing temperature, going from $\tau_0 = 43 \pm 3$ Pa for 18 °C to 3.3 ± 0.7 Pa for 28 °C. Therefore, the higher the temperature, the less pressure is needed to 3D-bioprint the hydrogel, which can result in dripping from the printing nozzle when no pressure is applied if the temperature is too high. Figure 3.3C, additionally, shows how the viscosity of the bio-ink decreases, becoming more linear with shear rate, as the temperature increases. In both Figure 3.3B and C, an overlapping of the low temperature curves can be seen from 18 °C to 22 °C. Therefore, we established 18-20 °C as the minimum temperature at which the cell-laden hydrogel needed to be in order to avoid dripping of the nozzle (low yield stress) and fidelity during printing (high viscosity and high shear-thinning behavior).

Figure 3.3D shows the dynamic modulus of the bio-ink, composed of the storage and loss moduli, which have different frequency-dependent behaviors. The dynamic modulus of elasticity, defined as $G = G' + iG''$, gives information about the viscoelasticity of the hydrogel mixture. G' is called the storage modulus and provides information about the elastic portion of the material (or stored energy) and G'' is called the loss modulus, which represents the dissipating or viscous portion. Viscoelastic materials, such as the ECM of tissues, show strong viscoelastic behaviors with different degree of elasticity or viscosity at different frequencies. This choice of material, therefore, is appropriate to mimic the viscoelastic properties of the ECM, necessary for proper cell proliferation and differentiation[9]. Moreover, compression mechanical testing of the hydrogel yielded a Young's modulus of 2 kPa after reproducing the conditions of the hydrogel in cell culture by crosslinking it with thrombin and leaving in an incubator for 7 days for gelatin to dissolve. This value was slightly lower than those reported for native tissue (around 12 kPa)[48]. However, it is is still within the appropriate range for tissue engineering of muscle tissue, was has been reported to be around 1-14 kPa[48] . Other recent reports, nevertheless, situate the appropriate Young's modulus for 3D bioengineered muscular tissue to be around 1-3 kPa, claiming that 12 kPa is more appropriate for 2D cultures[23, 49].

3D bioprinting of skeletal muscle tissue

3D bioengineering of skeletal muscle tissues by mold-casting techniques is usually a multi-step process, often with specialized equipment or careful manual work, which may hinder the scalability of the approach[42]. In this study, we focused on the application of 3D bioprinting technique as a novel tool to generate different designs of skeletal muscle tissue, which could ultimately be integrated into a soft robotic device or be used to study the development and adaptability of muscle tissue. This technique offers not only speed and ease of design, but a great degree of scalability and customization. Moreover, one of the main advantages of the 3D bioprinting technique is the versatility in terms of

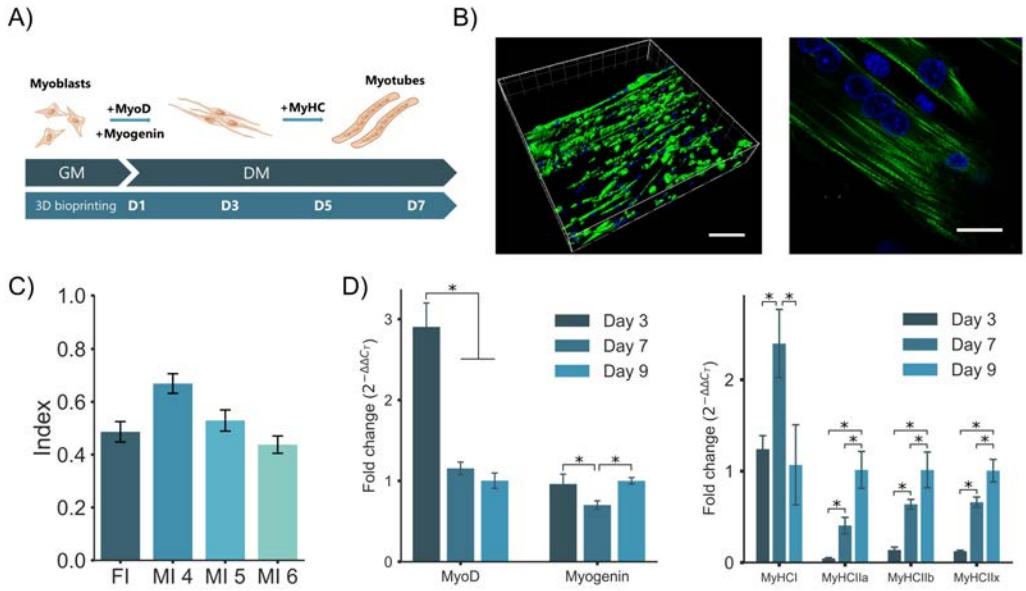

Figure 3.4: Biological characterization of 3D-bioprinted skeletal muscle tissue. A) Schematic representation of the differentiation and maturation process of skeletal muscle cells. B) 3D reconstruction of CLSM images of differentiated myotubes inside the hydrogel (left) and a close-up image at 63x (right), showing striation. Scale bars: 100 μm (left) and 20 μm (right). C) Fusion index (FI) and maturation index (MI) of the 3D-bioprinted tissue. D) Gene expression analysis of 3D-bioprinted muscle tissue, in particular of the differentiation markers MyoD and Myogenin and maturation markers (isoforms of MyHC) during the differentiation process. Adapted with permission from [1].

optimization, allowing immediate redesigns of structures to perform trial and error in a fast manner. The first sketch of the geometry to be printed was designed in a computer-aided design (CAD) software and exported into an .stl file type. This file was loaded into an open source software called Slic3r, commonly used for general-purpose 3D printers, where the geometry was turned into a series of filaments, emulating the 3D printing process. The characteristics of these filaments, such as width, layer separation, speed of printing, among many others, could be optimized at the moment, finally generating a GCode file. GCode is an instruction language that is used to control automated machine tools in computer-aided manufacturing and, in particular, 3D printing. This GCode, which contains the coordinates of the design, can also be fine-tuned during optimization to change parameters such as the speed of the print-head, the opening and closing of pressure, and many other features than can influence the final result.

A commercially available 3D bioprinter (3DDiscovery™ BioSafety by RegenHU) was used for the bioengineering of skeletal muscle constructs. This bioprinter possesses several print-heads that can 3D print with different mechanisms. For our purpose, we used the pneumatic extrusion printhead, using pressure to control the flow of the bio-ink. We designed a 3D bioprinting protocol that could allow production of tissue constructs in a fast, single-step process of high throughput, compared to other methods in the literature, where the cell-laden hydrogel needs to be manually mold-casted. Moreover, the main versatility of this technique consisted in the possibility of rapidly implementing custom-made designs, allowing a fast optimization of the printed structures, without needing to fabricate different types of molds for each specific case.

The culture dishes were coated with fibriongen in order to ensure attachment of the bioprinted hydrogel. After 3D bioprinting, the tissue construct crosslinked with a solution of 5 U/mL of thrombin and was left in growth medium (GM) for two days, in order to induce the proliferation of my-

oblasts for a short time. Afterwards, this medium was switched to differentiation medium (DM), which induced the fusion of myoblasts to form elongated multi-nucleated cells, called myotubes. Both GM and DM were supplemented with 1 mg/mL of 6-aminocaproic acid (ACA), a protease inhibitor that helped maintain the structural integrity of the construct[28]. Moreover, DM was further supplemented with 50 ng/mL of insulin-like growth factor 1 (IGF-1), which can enhance the differentiation of myotubes[28]. The differentiation and maturation of skeletal muscle myoblasts is marked by the expression of several differentiation and maturation markers, as shown in Figure 3.4A. At the biomolecular level, two transcription factors, MyoD and Myogenin, are more expressed during the first days of differentiation. MyoD leads to the terminal exit of the myoblast cell cycle and triggers differentiation, while Myogenin is involved in the formation of multi-nucleated myotubes[50, 51]. After three days in DM, Myosin Heavy Chain I and II (MyHCI and MyHCII) become more expressed as the muscle starts to maturate and form an internal sarcomeric structure and contractile machinery[52].

Differentiation and maturation of the 3D-bioprinted muscle tissue was assessed by immunostaining and the RNA expression of the aforementioned genes. A 3D-reconstructed immunostaining picture of MyHCII and cell nuclei obtained by confocal laser scanning microscopy (CLSM) is shown in Figure 3.4B, where the elongated morphology and multinucleation are visible. The right-hand image shows a close-up of a myotube, where striation (or sarcomeric structure) can be observed. From these immunostaining pictures, the fusion index and maturation index can be defined as metrics to validate the efficiency of the maturation process. Figure 3.4C shows the fusion index (FI) and maturation indices (MI-N) acquired in different layers of the constructs. The FI was defined as the ratio of nuclei within myotubes with 2 or more nuclei with respect to the total number of nuclei and the MI-N was defined as the ratio of myotubes having N or more nuclei with respect to the total number of myotubes. The FI and MI metrics reported values similar to those found in literature for 2D cultures of C2C12 cells[53].

Furthermore, we studied the expression of the differentiation-related transcription factors (MyoD and Myogenin) and of different MyHC isoforms at various time points via reverse transcription polymerase chain reaction (RT-PCR) (Figure 3.4D). We observed downregulation of MyoD and significant changes on Myogenin expression, as expected in late stages of differentiation[50, 51, 54]. Muscle fibers are conventionally classified according the ATPase activity of the myosin that is predominantly expressed[55, 56]. MyHCI is normally expressed on slow-twitch fibers, whereas the different MyHCII on fast-twitch fibers. Therefore, we studied the expression levels of different MyHC isoforms. MyHCI showed an initial upregulation during the first days (from day 3 to day 7 of differentiation) and a subsequent downregulation (from day 7 to day 9 of differentiation), an effect that has already been reported in studies with 2D cultures, in which they found a slow-to-fast transition in the expression of the different MyHC isoforms[57]. On the contrary, the MyHCII isoforms showed a continuous upregulation during the studied differentiation period.

Myotube alignment is crucial for maximal force generation. In order to assess whether the stress produced during the 3D-bioprinting process could induce alignment of myotubes within the constructs, we employed confocal imaging of MyHCII and cell nuclei. Figure 3.5 shows full mosaic images of a square (A), circle (B) and triangle (C) at the glass level, with insets displaying the alignment of the myotubes according to the shape. We analyzed the degree of alignment depending on the distance to the glass coverslip. In Figure 3.5D, three examples of images in a z-stack (3 μm, 28 μm and 56 μm) show how the myotubes were aligned in the direction of the construct at higher distances from the glass slide. The orientation of elongated cell nuclei and the alignment of the myotubes were studied by image processing techniques. For each sample, we selected a reference angle formed by

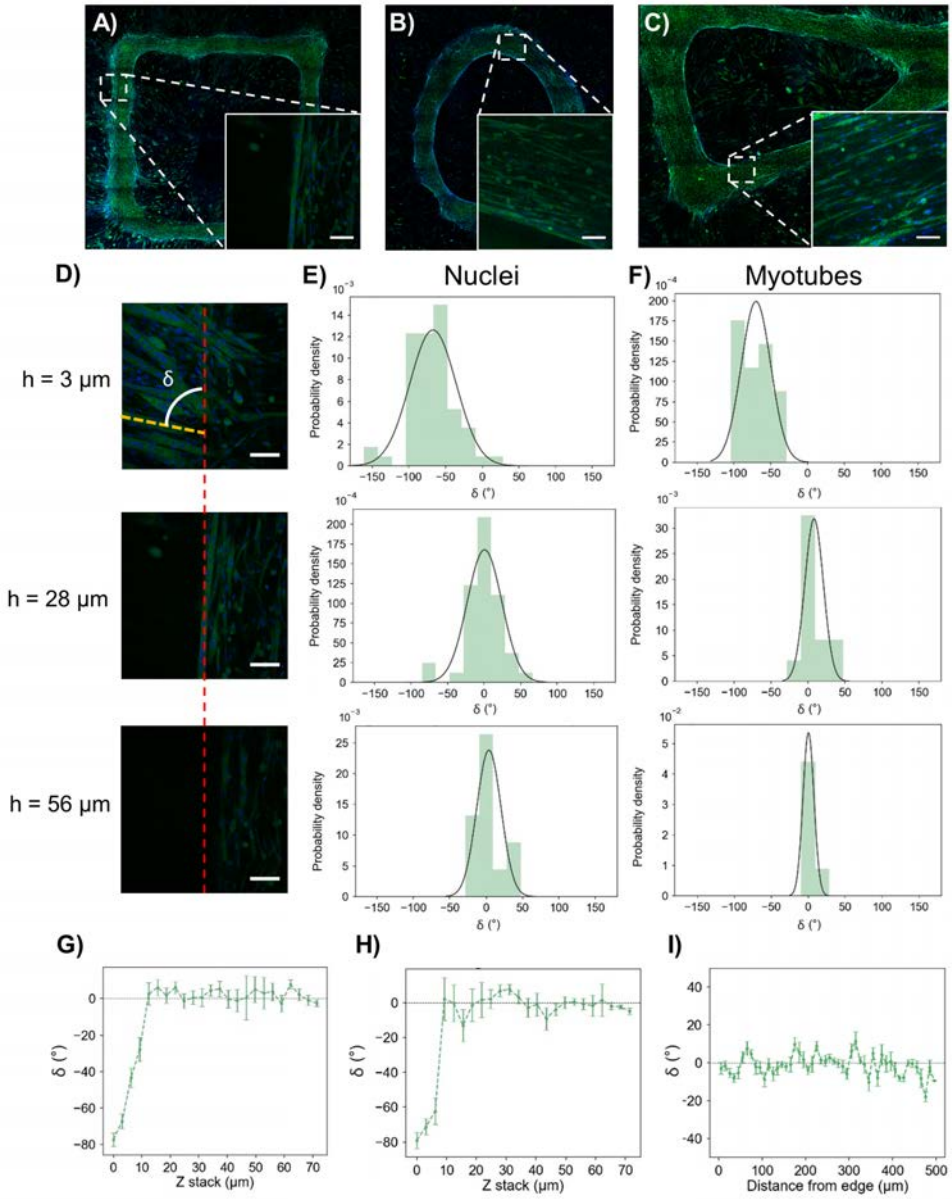

Figure 3.5: 3D myotube alignment within different 3D-bioprinted geometries. A–C) CSLM image reconstruction of the whole bioprinted constructs with different shapes, which were fluorescently immunostained for MyHCII (green) and nuclei (blue). Insets show a magnification of the selected area. Scale bar is 100 μm. D) Representative CSLM single slice images from a z-stack, either at 3 μm (top), 28 μm (middle), and 56 μm (bottom) from the glass slide. Scale bars are 100 μm. E,F) Distribution of cell nuclei alignment and myotube orientation, respectively. G,H) δ angle as a function of the distance to the glass slide for nuclei and myotubes, respectively. I) δ angle as a function of the distance to the tissue edge for cell nuclei. Adapted with permission from [1].

the tissue edge (see red dashed line in Figure 3.5D). Then, we compared the elongation of all cell nuclei and myotubes to this angle (yellow dashed line) to obtain the distance from the reference angle, called δ. Figures 3.5E and 3.5F show the histogram of distribution of δ for the three cases displayed in Figure 3.5D. It can be seen how, at the lowest position, cell nuclei and myotubes were aligned at a random angle. However, at higher distances from the glass slide, the angle δ became zero, meaning that the myotubes were aligned to the shape of the construct. This trend is displayed in Figure 3.5G and 3.5H for cell nuclei and myotubes, respectively, up to 70 μm away from the dish. Finally, Figure 3.5I shows the variation of alignment in terms of the lateral distance to the tissue edge. Although we

Figure 3.6: Compaction of 3D-bioprinted skeletal muscle tissue. When not attached to the bottom of a Petri dish, the tissue constructs compact due to cell migration and activity. Adapted with permission from [1].

did not find significant differences as the distance increased, we generally found a lower density of myotubes in the center of the construct compared to the tissue edges.

It has been reported that there is a lower degree of maturity when myotubes are directly attached to a glass substrate, compared to myotubes in subsequent layers that experience a "tissue-like" stiffness[48]. This effect could be related to the lower alignment to the reference angle that we observed further away from the bottom of the dish. We also found that a simultaneous crosslinking of the tissue with the fibrinogen coating on the dish helped to retain the shape of the printed construct throughout the differentiation period. Myotubes need mechanical restriction during maturation to be completely functional. Samples that were not previously coated with fibrinogen did not properly attach to the glass bottom and completely shrank to a non-uniform structure after some days of culture (Figure 3.6). This phenomenon is generally attributed to the generation of cell traction forces due to the absence of any kind of mechanical constrain[58].

To assess the reasons behind the high alignment of myotubes and to fully characterize the samples at the nanoscale level, we used scanning electron microscopy (SEM) of both 3D-bioprinted hydrogel and cell-laden hydrogel (Figure 3.7). 3D bioprinting of the hydrogel without cells produced highly aligned fibers (Figure 3.7A). A fast Fourier transform (FFT) of the image and subsequent circular profiling revealed a general alignment in one direction, which corresponds to the direction of printing. In addition, cell-laden hydrogel after 14 days of differentiation confirmed the results obtained by immunofluorescence, showing a dense myotube pattern completely aligned in the direction of printing (Figure 3.7B). These results seem to indicate that the shear stress during the extrusion process has an important effect on the alignment of hydrogel fibers, an effect that is maintained after crosslinking and guides longitudinal myotube alignment. Hence, 3D bioprinting entails an induced cellular self-alignment in three-dimensional tissue of arbitrary geometries without the need for adding any other mechanical or biomechanical cues.

Characterization of stimulation setup

A contactless stimulation setup was designed and fabricated for the stimulation of 3D-bioprinted muscle tissue. This setup was based on an interdigitated array (IDA) of electrodes, fabricated by standard photolithography and sputtering of Pt, which ensured a homogeneous propagation of the generated electric field. A schematic representation and an actual picture of the IDA stimulation setup is shown in Figure 3.8A. This setup was fabricated on top of a glass slide, where a well made of PDMS was attached, leaving a region in its center to place a cell-laden hydrogel. Therefore, all parts of

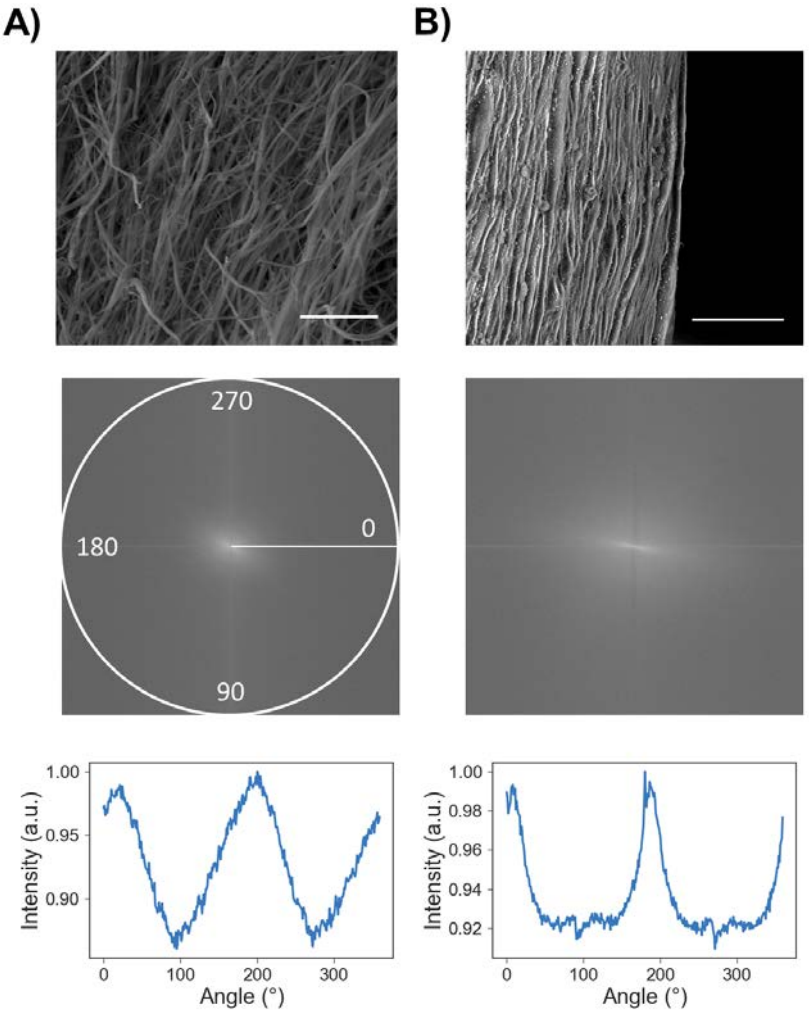

Figure 3.7: SEM characterization of fiber alignment. A) SEM image (top) of a 3D-bioprinted hydrogel without cells (scale bar is 5 μm). FFT of the SEM image (middle) and intensity profile over 360°(bottom). B) SEM image (top) of a 3D-bioprinted cell-laden hydrogel (scale bar is 50 μm). FFT of the SEM image (middle) and intensity profile over 360°(bottom). Adapted with permission from [1].

the tissue felt the same intensity of electric field across the plane and the tissue could remain floating in the culture medium and still get stimulated. The interdigitated electrodes had a width of 100 μm and were separated from each other by 100 μm. Finite element analysis (FEA) simulation of the electric field propagation was performed in order to prove the homogeneous propagation of the electric field intensity. Figure 3.8B shows how after approximately 50 μm, the electric field magnitude can be considered constant throughout the whole stimulating region due to its periodicity. Notice that the simulation was performed in vacuum, not considering the presence of an electrolyte medium, as it was done only to demonstrate the homogeneity of the electric field lines.

Impedance spectroscopy measurements of the IDA of electrodes are shown in Figure 3.8C. Results from a frequency sweep were fitted to an equivalent circuit formed by a series resistance (R) with a capacitance (C_0) in parallel with another resistance (R_0), which represented the geometric capacitance of the system and the parasitic resistance between the interdigitated electrodes, respectively. Least-squares fitting revealed a result of $R = 9 \cdot 10^3 \pm 2 \cdot 10^3\ \Omega$, $C_0 = 8.86 \cdot 10^{-11} \pm 0.13 \cdot 10^{-11}$ F , and $R_0 = 2.01 \cdot 10^8 \pm 0.03 \cdot 10^8\ \Omega$. As can be seen in Figure 3.8C, at very low frequencies,

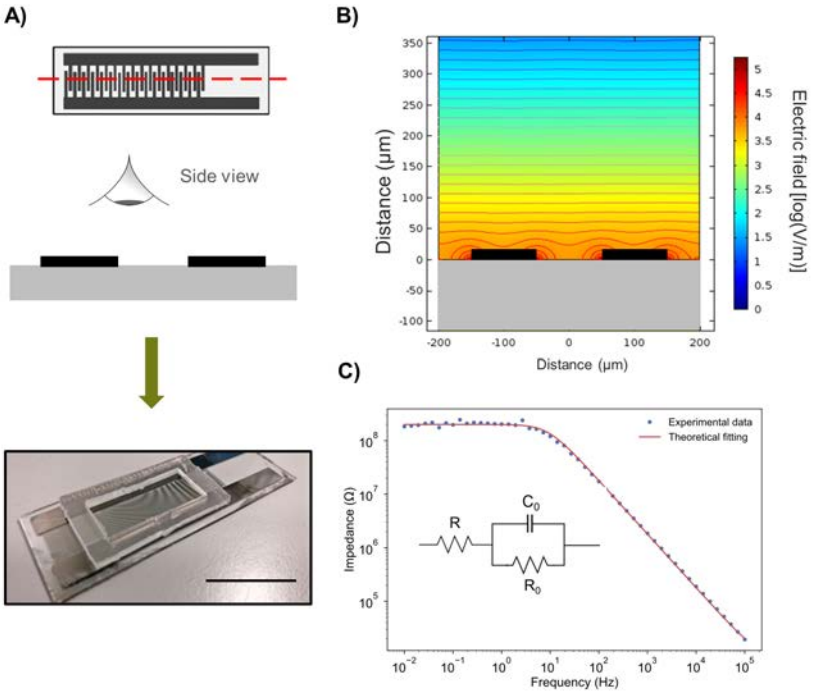

Figure 3.8: Characterization of the IDA of electrodes. A) Scheme of the interdigitated array of electrodes and real picture. After the fabrication, a PDMS well was adhered on top to isolate the culture medium during stimulation. B) FEA simulation of electric field distribution showing a homogenous propagation (stream lines) after very short distances. C) Characterization of the interdigitated array of electrodes and equivalent circuit (inset). Adapted with permission from [1].

the impedance of the setup is dominated by the parasitic resistance, R_0, indicating the presence of Faradaic reactions at the Pt-medium interface. Therefore, this stimulation setup was prone to hydrolysis and corrosion, especially if long-width pulses were applied. For this reason, stimulation pulses were maintained at 1-2 ms to avoid harmful effects to the constructs.

Functionality

Skeletal muscle cells differentiated into myotubes have the ability to contract upon electrical stimuli. In order to assess the functionality of the tissue, we emulated the effect of neuronal action potentials by applying electric pulse stimulation (EPS). At day 14 of differentiation, 3D-bioprinted tissues were lifted from their dishes and placed inside an inverted microscope (at 37 °C and 5% CO2) in the IDA-based stimulation chamber. In this way, thanks to the homogeneous propagation of the electric field, we could demonstrate electrical response in all parts of the cell-laden hydrogel.

The controllability of myotube contraction was evaluated by both quantitative calcium imaging and optical tracking as complementary techniques. The former provided insight into biological aspects in independent cellular units, as calcium streams are known to cause contractions upon electrical stimulation. The latter helped assess the overall contractility of the tissue as a whole, since the simultaneous contraction of aligned myotubes caused visible contractions in bright-field.

In order to assess the presence and synchronicity of calcium transients we performed quantitative calcium imaging using Fluo4, a Ca^{2+}-sensitive dye. This dye is internalized into the cells and, following reception of electrical stimuli and subsequent cell depolarization, an intracellular release of Ca^{2+} is detected by the fluorophore. Live cell imaging allowed us to record changes in the fluores-

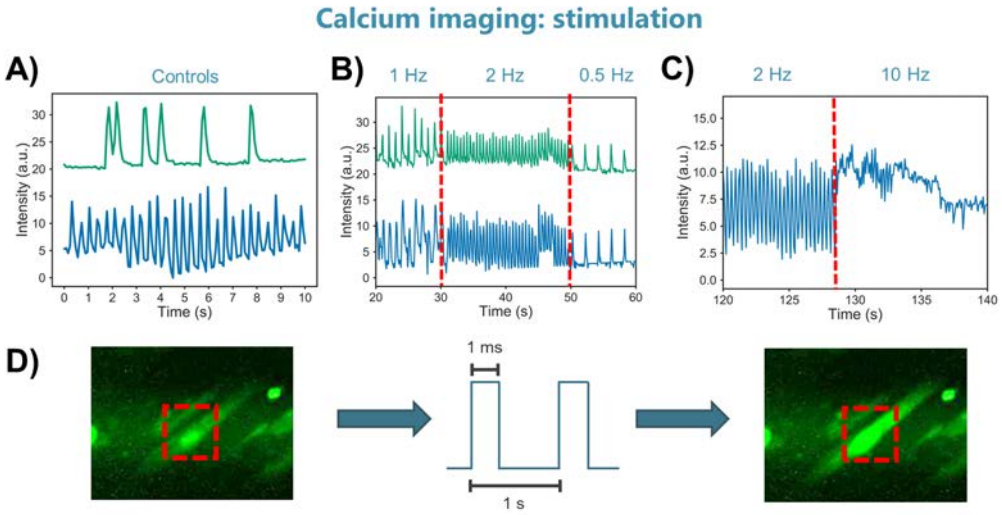

Figure 3.9: Calcium imaging of 3D-bioprinted muscle tissue. A) In a control sample (not stimulated), the calcium transients in different myotubes (green and blue) were completely random and not synchronized. B) Upon electrical stimulation, the calcium transients synchronized even for two distant myotubes (green and blue). C) Tetanic behavior can be observed when passing from low frequencies (2 Hz) to high frequencies (10 Hz). D) Snapshots of a Ca-imaging video under fluorescence microscopy, showing the increase of intensity during depolarization. Adapted from [1].

cence intensity upon electrical stimulation at different frequencies. Without applying EPS, myotubes showed spontaneous calcium sparks, which were not synchronized to each other (Figure 3.9A). However, after application of EPS at different frequencies, the myotubes were synchronized to the applied frequency, as well as to each other (Figure 3.9B). By comparing in a 1 Hz stimulation recorded at 50 frames per second (FPS) the offset between the moment when the fluorescence signal reaches its maximum and the moment it reaches the baseline again, we can compute the raising and relaxation times of the contractions, which yielded $t_{\text{raise}} = 0.17 \pm 0.07$ s and $t_{\text{fall}} = 0.35 \pm 0.08$ s, which agree with other reports in the literature[32]. Calcium imaging also provided an evidence of tetanic contractions at high frequencies (Figure 3.9C), where the calcium concentration was increased and maintained for a few seconds. These results were analyzed with a custom-made Python script that allowed the user to select a region of interest (ROI) around a myotube of interest (Figure 3.9D). Then, the total intensity of the ROI was computed and compared frame by frame, obtaining information about the intensity changes within single myotubes, that allowed us to separate spontaneous sparks in distant parts of the tissue.

Bright-field tracking of the muscle tissue constructs during stimulation revealed the tissue to be functional and responsive. When no electric field was applied, only spontaneous twitch contractions were observed in some parts of the tissue. However, during the experiments, the tissues were contracting following the applied frequencies in a synchronous manner (Figure 3.10A). The quantification of the contractions was performed by bright-field image with custom-made tracking algorithms that detected the displacement of certain features of the tissue (blue square in Figure 3.10B), providing information about the intensity of the contractions and the net movement of the tissue due to them. The total displacement with respect to the first frame was then computed, as shown in Figure 3.10A for a 120 s stimulation. We can see in the two zoomed-in plots that the tissue was able to follow the applied frequencies and even show tetanic contractions at 10 Hz. Moreover, there was an evident drifting of the tissue in time, as can be seen by the increasing slope of the signal in Figure 3.10A. This displacement was most likely due to the contractions induced by EPS and an inherent asymmetry in the shape of the construct, resulting in net motion.

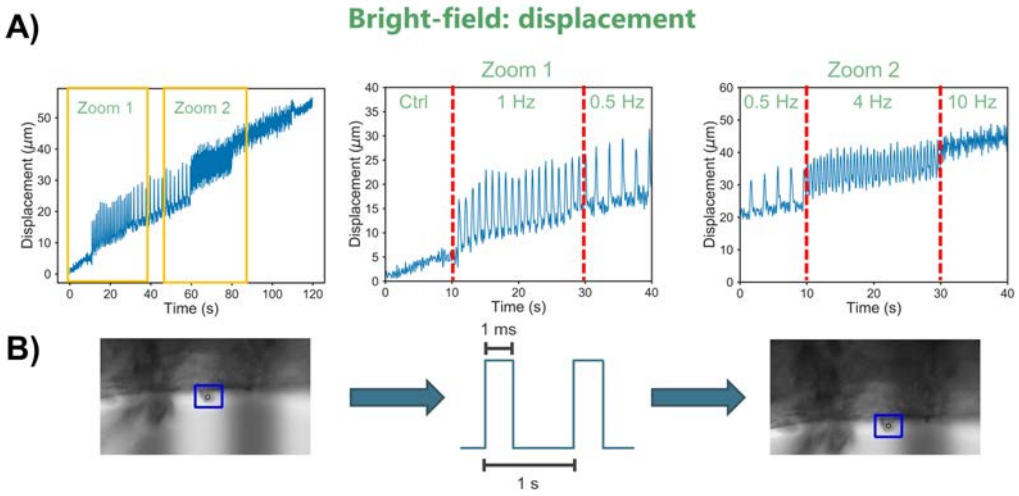

Figure 3.10: Optical tracking of 3D-bioprinted muscle tissue. A) Displacement of the muscle tissue upon different frequencies. A drifting behavior can be observed. B) Tracking snapshots showing a displacement of the tissue in the culture medium due to the contractions. Adapted with permission from [1].

2.3. Conclusions

In this section, we have demonstrated that 3D bioprinting constitutes a rapid prototyping and versatile tool for the fabrication of skeletal muscle tissue with a high degree of controllability over their shape and functionality, in a fast, integrated and scalable manner. The required myotube alignment for efficient contractions was achieved in all bioprinted constructs with varied geometrical designs, without the need for additional microfabrication techniques to guide cellular alignment. Moreover, the bioprinted skeletal muscle constructs showed complete controllability and response to external actuation based on electrical stimuli, which was thoroughly characterized by both optical tracking and calcium transient analysis. Moreover, morphological analysis of the myotubes through MyHCII immunostaining showed high fusion and maturation indices comparable to results reported in the literature and the presence of sarcomeric structure, necessary for contractions to happen. RNA expression analysis showed downregulation of MyoD and Myogenin during differentiation, as expected for the maturation process, and an upregulation of all isoforms of MyHCII.

Many challenges are yet to be overcome, leaving the field open to a full range of research paths in many different directions. For instance, the integration of other types of materials, such as responsive or smart materials[59], together with bioengineered skeletal muscle tissue could be investigated, providing attractive characteristics for future bio-hybrid robotic systems. Finally, there are some long-term challenges in the bio-robotic field related to the viability of the devices. One critical constraint is the limitation of maintaining optimal culture conditions and proper nutrient delivery, which is an essential aspect for tissue survival, especially in regenerative medicine applications. This could be tackled by incorporating vascular channels that are also being investigated by 3D bioprinting[60]. Close to this issue is the biomimicry of the structural conditions of native skeletal muscle, which is based on the self-organization of independent fascicles of differentiated myocytes that do not suffer nutrient diffusion problems due to their thin cross section. Efforts towards the development of an integrated and versatile 3D-bioprinting-based approach to overcome this biomimicry issue will be the focus of the next section.

2.4. Materials and methods

Hydrogel fabrication

The hydrogel mixture based on fibrinogen, gelatin and HA was prepared as described elsewhere[8]. Briefly, a solution of 3 mg/ml HA (Sigma-Aldrich) in DMEM was stirred overnight at 37 °C. Then, glycerol (10% v/v) was added to the mixture and stirred for 1 h, followed by the addition of gelatin (35 mg/ml) and fibrinogen (20 mg/ml). When all components were dissolved in the medium, the hydrogel mixture was sterile-filtered through a 0.2 μm syringe filter (Millipore™) and stored at -20 °C until its use.

Rheological and mechanical characterization of the hydrogel

Rheological properties of the hydrogel mixture were characterized with a Discovery HR-2 controlled-stress rheometer (TA Instruments) equipped with a Peltier steel cone geometry of 40 mm of diameter, 26 μm of truncation, and an angle of 1.019°. The temperature-dependent behavior was studied by increments of 2 °C between 18 °C and 28 °C. In all experiments, the sample was left to acquire the desire temperature for 1 min. Frequency sweeps were performed by keeping the frequency constant in a logarithmically spaced range between 0.1 rad/s and 100 rad/s, and expressed in Hz. In the shear stress vs. shear rate plots, the data was fitted to a Herschel-Bulkley model of a non-Newtonian fluid, following the equation $\tau = \tau_0 + k\gamma^n$, where τ is the shear stress, γ is the shear rate, τ_0 is the yield stress, and n is the shear-thinning parameter.

For the characterization of the hydrogel, several hydrogel structures of cylindrical shape were fabricated by using a circular mold. Uniaxial compression tests were carried out with a mechanical testing machine (Zwick Roell) at a strain rate of 0.05 mm/s and a Young's modulus of $E = 2$ kPa was obtained by fitting the linear region of 15-30%.

Cell culture

C2C12 mouse myoblasts were purchased from ATCC and maintained in growth medium (GM) consisting of high glucose Dullbecco's Modified Eagle's Medium (DMEM; Gibco®) supplemented with 10% Fetal Bovine Serum (FBS), 200 nM L-Glutamine and 1% Penicillin/Streptomycin, in a 37 °C and 5% CO_2 atmosphere. Cells were passaged before reaching 80% confluence in Corning® T-75 flasks. For cell differentiation and myotube formation after the bioprinting process, GM was substituted by DM, consisting of high glucose DMEM containing 10% Horse Serum (Gibco®), 200 nM L-Glutamine (Gibco®), 1% Penicillin-Streptomycin (Gibco®), 50 ng/ml IGF-1 (Sigma-Aldrich) and 1 mg/ml 6-aminocaproic acid (ACA, Sigma-Aldrich).

3D bioprinting of skeletal muscle tissue

C2C12 myoblasts were harvested by a 0.05% (wt/v) Trypsin-EDTA (Gibco™, 15400054), centrifuged at 300g for 5 min and re-suspended at a concentration of $5 \cdot 10^6$ cells/mL in the hydrogel mixture, at 37 °C. The cell-laden hydrogel was loaded into a 3 mL plastic syringe (Nordson®, ref. 7012085) coupled to a 200-μm (G27) plastic conic nozzle (Optimum® SmoothFlow™ tapered tips, Nordson®, ref. 7018417). For the 3D bioprinting process, we used the RegenHU's pneumatic-extrusion-based 3D bioprinter with a class II biosafety cabinet (3DDiscovery™ BioSafety). In all

cases, the pressure was set at 50 kPa and a cooler system (RegenHU) was used to maintain the cartridge temperature at 18 °C. As a substrate, glass-bottom 35-mm μ-Dishes (ibidi, ref. 81158), precoated with fibrinogen, were used. For the coating, the dishes were incubated with a solution of 0.5 mg/ml fibrinogen in 1× phosphate buffered saline (PBS) overnight at 4 °C. After that, the fibrinogen solution was removed, washed twice in PBS and air-dried. After printing, the 3D constructs were crosslinked by the addition of a 5 U/ml solution of thrombin (T4648, Sigma-Aldrich) for 15 min at 37 °C. The excess of thrombin was washed out by two washes in PBS (2 min each) and the structures were maintained in GM at 37 °C and 5% CO_2. At 48 h, GM was replaced by DM and refreshed every two days for 14 days. For the design of different bioprinted structures, BioCAD 1.1 (RegenHU) software was used.

Cell viability and MyHCII immunofluorescence

Cell viability was analyzed at 24 h and 48 h by the dual-fluorescence Live/Dead® Viability/Cytotoxicity kit for mammalian cells (Life Technologies), following the manufacturer's instructions. Fluorescently labeled cells were imaged under a Leica DMi8 inverted fluorescence microscope equipped with a 37 °C and 5% CO_2 chamber, using a 20× air objective. A series of z-stack images were captured to analyze the viability of cells in the three dimensions of the bioprinted constructs. The percentages of live and dead cells were calculated by using ImageJ software ver.1.47q (National Institutes of Health, Bethesda, MD). For immunostaining, 3D-bioprinted constructs were washed twice in PBS and fixed by incubating them with a 3.7% paraformaldehyde in PBS solution for 15 min at RT, followed by three washes in PBS. Then, cells were permeabilized by using 0.2% Triton-X-100 in PBS. After two washes in PBS, the constructs were incubated with 5% Bovine Serum Albumin (BSA) in PBS (PBS-BSA) to block unspecific bindings. Then, bioprinted structures were incubated for 2 h at RT and dark conditions with a 1/400 dilution of Alexa Fluor®-488-conjugated Anti-Myosin Heavy Chain II antibody (eBioscience) in 5% PBS-BSA. The unbound antibodies were washed out with PBS, and cell nuclei were counterstained with 1 μL/mL Hoechst 33342 (Life technologies). Finally, samples were washed twice in PBS, ProLong® (Life technologies) antifade mounting medium was added and they were stored at 4 °C until their analysis. Fluorescently immunostained bioprinted constructs were imaged under an LTE-ZEISS confocal scanning laser microscope (CSLM). For the detection of Alexa Fluor® 488 labeled myotubes, and Hoechst 33342 stained nuclei, a diode laser at 488 nm and 405 nm excitation wavelength were used, respectively.

Myotube alignment analysis

Myotube alignment analysis at different levels of height and separation from the tissue border was performed with a homemade Python (v. 3.7) script based on image processing techniques with OpenCV (v. 4.1.2). First, the bright field image was used to manually select the angle that the tissue was forming, designated as the reference angle. Then, the z-stacks of fluorescence images were pre-processed with smoothing, erosion and adaptive thresholding to obtain binarized images of myotubes and nuclei. For myotubes, a watershed segmentation approach was used to label myotubes that were considered to be independent from each other. The orientation was computed from the spatial moments of each labeled myotube as the orientation angle of an ellipse with the same second-order moments. For nuclei, individual nucleus contours were fitted to an ellipsoidal shape and its orientation with respect to the reference angle was computed. For each z-value, the histogram of orientations was calculated and the mean value with standard error of the mean was displayed. To analyze the change in alignment with respect to the separation from the tissue border, the centroids of each individual nucleus or myotube were compared to the tissue border. In order to increase the

statistical significance of the results, images of different heights were used, starting from a point where the alignment was already achieved (Figures 3.5G and 3.5H).

For the scanning electron microscopy (SEM) characterization of the hydrogel and the cell-laden hydrogel, samples were fixed with 2.5% glutaraldehyde (grade I, Sigma-Aldrich, G6257), washed several times with increasing concentrations of ethanol and critical point dried. The different samples were visualized under a low vacuum scanning electron microscope (FEI NOVA NanoSEM 230) at 10 kV.

Fabrication and characterization of electrodes

The stimulation of tissue constructs of different shapes floating in the medium were performed with an interdigitated array (IDA) of electrodes to ensure a better propagation of the electric field. The IDA of electrodes was fabricated by standard photolithography techniques. A positive mask was designed and printed on acetate sheets (Selba S.A.). A positive photoresist (AZ® 5214) was spin-coated (WS-650Mz-23NPPB, Laurell Technologies Corporation) on crystal glass slides (BPB016, RS France) and baked for 3 min at 90 °C. Then, a mask aligner (SÜSS Microtec) was used to irradiate the samples with a power of 25 mW/m^2. The patterned features were revealed with an AZ® 100 remover for 7 s. Metals were deposited with a sputtering machine (EM ACE600, Leica). First, a 5 nm Ti layer was deposited to improve adhesion, and then, a thicker 100 nm Pt layer. Finally, the design was revealed by removing the excess materials via lift-off. A PDMS (Sylgard 184, Dow Corning) well was attached to the electrodes so that only a small amount of culture medium was necessary. The interdigitated electrodes had a width of 100 μm and were separated from each other by 100 μm. Finite element analysis (FEA) simulation of the electric field propagation was performed by setting one electrode to ground and the other one to a finite voltage and imposing periodic boundary conditions on both sides, in order to prove the homogeneous propagation of the electric field intensity. Impedance spectroscopy measurements of the IDA of electrodes were done with Autolab (PGSTAT204, Metrohm) in a two-probe setup, at the frequency range of 0.01 – 10.000 Hz, using sinusoidal waves of 20 mV of AC voltage and 250 mV of DC voltage.

Optical tracking of myotube response to electrical stimulation

A waveform generator (PM8572, Tabor Electronics) was used to stimulate the 3D-bioprinted tissue in the IDA of electrodes. Square waves of a width of 1 ms and a voltage amplitude of 2.5 V were applied at different frequencies, ranging from 0.5 Hz to 10 Hz. An oscilloscope (DS1104Z, Rigol) was used to check the applied signals. The tissue was always stimulated inside an inverted microscope (Leica's DMi8), equipped with a chamber to maintain an atmosphere of 37 °C and 5% CO2. The bright field displacement of the 3D-bioprinted tissue was performed with a home-made Python (v. 3.7) script based on tracking algorithms using OpenCV (v. 4.1.2). Videos were recorded during stimulation with an inverted microscope and a 10× objective and loaded into the script with the function VideoCapture. Then, the user was asked to select a region of interest (ROI) in an area with distinctive features with the function SelectROI. The position of the ROI in the following frames was tracked with a machine learning algorithm based on the detection of features by an online-boosted multiple instance learning approach[61], using the function TrackerBoosting_create. The displacement of the tracked rectangle at time t with respect to the initial ROI was displayed as a function of time. In order to quantify the quality of the tracking and make sure that the observed drift was not due to a drifting of the tracked ROI, all the frames were compared pairwise with the initial frame of the video. The error was computed by the $\mathcal{L}_2$-norm of the image pixels. This error also showed the char-

acteristic peaks at different frequencies and the drift that could be observed during the tracking of displacement. Likewise, the error between all the detected images (as compared to the initial ROI) was fairly constant in time, indicating that the detection and tracking was working adequately.

Quantitative analysis of calcium transients upon stimulation

At 14 days of differentiation, 3D-bioprinted C2C12 cells were stained with calcium-sensitive Fluo4 dye (Life technologies), according to the manufacturer's instructions. Cells were imaged under an inverted fluorescence microscope in culture conditions and using a 10× dry objective and a standard FITC filter. To analyze the changes in calcium intensity produced by the electrical stimulation of the cells, different videos at 12.5 FPS were recorded. The quantification of fluorescence intensity changes was performed with a home-made Python script. The user was asked to select a small ROI and the average intensity value of all the pixels of the ROI was displayed over time. Since the drift in intensity is related to photo-bleaching effect and does not contain any information, the signals were normalized to their baseline by fitting it with a linear function. To quantify the actual frequency of stimulation, a fast Fourier transform (FFT) algorithm was applied to the signal. To calculate the rising and falling times of the calcium transients for the 1 Hz stimulation, we used videos taken with 50 FPS to avoid sampling errors. The script used the baseline-normalized calcium transients to calculate the relationship between the peaks (maximum values of intensity) and baseline (points where intensity changes were smaller than a certain threshold).

Gene expression analysis

Total RNA of at least two independent experiments was extracted using the RNeasy mini kit (QIAGEN, 74134) according to manufacturer's instructions. The concentration and purity of RNA were assessed with a Nanodrop ND-1000 (Thermo Scientific). A total quantity of 500 ng of extracted RNA were converted into cDNA using the ReverAid First Strand cDNA Synthesis Kit (Thermo Scientific, K1622). The qPCR reactions were performed in a final volume of 10 μL with PowerUp SYBR Green Master Mix (Applied Biosystems, A25742), used according to manufacturer's instructions in a StepOnePlus Real-Time PCR System (Applied Biosystems, 4376600). The following primers were used:

- GAPDH: FW (5' ATGGTGAAGGTCGGTGTGAA 3')
  GAPDH: RV (5' GAGGTCAATGAAGGGGTCGT 3')
- MyoD: FW (5' CCACTCAGGTCTCAGGTGTAAC 3')
  MyoD: RV (5' TCGCCCGCTTGAGGAATAA 3')
- Myogenin: FW (5' CCCTACAGACGCCCACAATC 3')
  Myogenin: RV (5' ACCCAGCCTGACAGACAATC 3')
- MyHCI: FW (5' GCCCCAAGCACAAGGAGT 3')
  MyHCI: RV (5' AGCCCCAAGAAATAAGGACAG 3')
- MyHCIIa: FW (5' GCAGAGACCGAGAAGGAG 3')

MyHCIIa: RV (5' CTTTCAAGAGGGACACCATC 3')

- MyHCIIb: FW (5' GAAGGAGGGCATTGATTGG 3')
  MyHCIIb: RV (5' TGAAGGAGGTGTCTGTCG 3')

- MyHCIIx: FW (5' GCGACAGACACCTCCTTCAAG 3')
  MyHCIIx: RV (5' TCCAGCCAGCCAGCGATG 3')

All genes were normalized to the expression levels of GAPDH, whose expression was constant across all experiments. Melt-curve analyses were performed to ensure that only one amplicon was being produced.

Statistical analysis

The comparative quantitative reverse-transcription polymerase chain reaction (qRT-PCR) statistical analysis were performed using the $2^{-\Delta\Delta CT}$ method[62]. All the samples are compared related to a control sample of the same stiffness condition. A Holm-Sidak test was used to compare multiple groups. The level of significance was set to $p \leq 0.05$. All significance analyses were performed using GraphPad Prism Version 7.00 for Windows (GraphPad Software, San Diego, CA).

3. Co-axial 3D bioprinting

3.1. Objectives

The previous section dealt with the bioengineering of three-dimensional skeletal muscle tissue using 3D bioprinting to obtain a faithful tissue model that considers the three-dimensional organization of native muscle and can mimic its functionality. However, despite the general advantages of the technique and encouraging results, there was still room for improvement. One of the main remaining challenges was the diffusion of nutrients within the tissue construct, since the density of cells found at the center of the cell-laden hydrogel was lower than at the edges. This is expected as the oxygen diffusion limit within tissues is considered to be around 100-200 μm and it can be lower for other nutrients[43, 63]. Therefore, myoblasts are likely to migrate from the center to the borders, forming myotubes at these regions, rendering the central cells dead or undifferentiated. Eventually, the total force per cross-sectional area of the tissue will be low, especially if the construct is much thicker than the oxygen diffusion limit.

A hydrogel-based gelatin, as the one used in the previous section, will not make possible the reduction of the cross-sectional area. Gelatin is used due to its gel properties, which allow printing with fidelity at low temperatures, maintaining the structural shape until the other components (e.g. fibrinogen) are crosslinked[8]. This material, however, is known to produce irregular printing, making it rather difficult to control the thickness of the construct[64], and is usually accompanied by other materials that help stabilize the printing, like alginate[65]. Moreover, since the crosslinking of the hydrogel is produced after printing, it is not possible to attain individual fibers that can mimic the fascicles in native tissue, since 3D bioprinting of several layers will cause their fusion to form an even thicker structure.

Therefore, in this section, we present a novel strategy towards overcoming the nutrient diffusion problem and the creation of individual fibers. The objectives of this section are the following: i) to obtain a method to carefully control the thickness of the bioprinted constructs in the micro-meter range, and reaching values comparable to the oxygen diffusion distance; ii) to obtain a method to 3D-bioprint individual fibers that are not fused with each other, improving the biomimicry of the organizational structure of skeletal muscle tissue; and iii) to obtain a universal method of bioprinting that can potentially include different types of hydrogels and different crosslinking strategies, in particular focusing on the inclusion of collagen, one of the main components of the skeletal muscle ECM. To reach these objectives, a pluronic-assisted co-axial 3D bioprinting system was envisaged, characterized and finally employed. This technique allows the fabrication of free-standing, individual and thin fibers based on diverse types of hydrogels, paving the way towards an improved biomimetic model of skeletal muscle tissue for basic developmental research or biomedical applications.

3.2. Results and discussion

Working principle

Co-axial 3D bioprinting is a method that allows printing cell-laden hydrogels surrounded by a shell of another hydrogel, usually assisting in the crosslinking of the inner one. One of the most common strategies for co-axial printing is the use of alginate, which is crosslinked *in situ* during the extrusion process by the presence of calcium chloride in the external needle. This method, nonetheless, can be difficult to regulate, as the flow of the calcium chloride in solution is difficult to control, and it might need the use of syringe pumps to achieve sufficiently small and controlled flows. Moreover, due to this lack of control, obstruction of the internal nozzle due to the accumulation of crosslinked alginate at the exit is also very common[66].

Here, in order to overcome all these difficulties, we considered an approach based on a sacrificial material, the block co-polymer pluronic acid F-127, as a supporting structure during 3D bioprinting. While this material has been successfully used as a sacrificial ink for structures that need infilling or three-dimensional support before crosslinking[47], it has never been used in a co-axial system to act as shell to control the thickness of the inner hydrogel. As we will report in this sub-section, this sacrificial material offers high versatility to implement several crosslinking strategies, potentially amplifying its use for many kinds of tissues that might require different hydrogel compositions, and not only skeletal muscle cells.

Figure 3.11A shows a schematic of the working principle, which is always based on the extrusion of a cell-laden hydrogel through an inner nozzle, surrounded by pluronic in an outer nozzle, working as a shell. Pluronic is liquid at low temperatures (~4°), but it undergoes a sol-gel transition at room temperature, making it ideal for 3D printing and obtaining a fine control of its extrusion. Based on these properties, two different hydrogel confinement strategies were envisaged:

i) a chemical method, based on the *in situ* crosslinking of alginate inside the hydrogel with $CaCl_2$ present in the pluronic solution, and

ii) a physical method, based on physical repulsion by gelatin inside the hydrogel and pluronic outside of it.

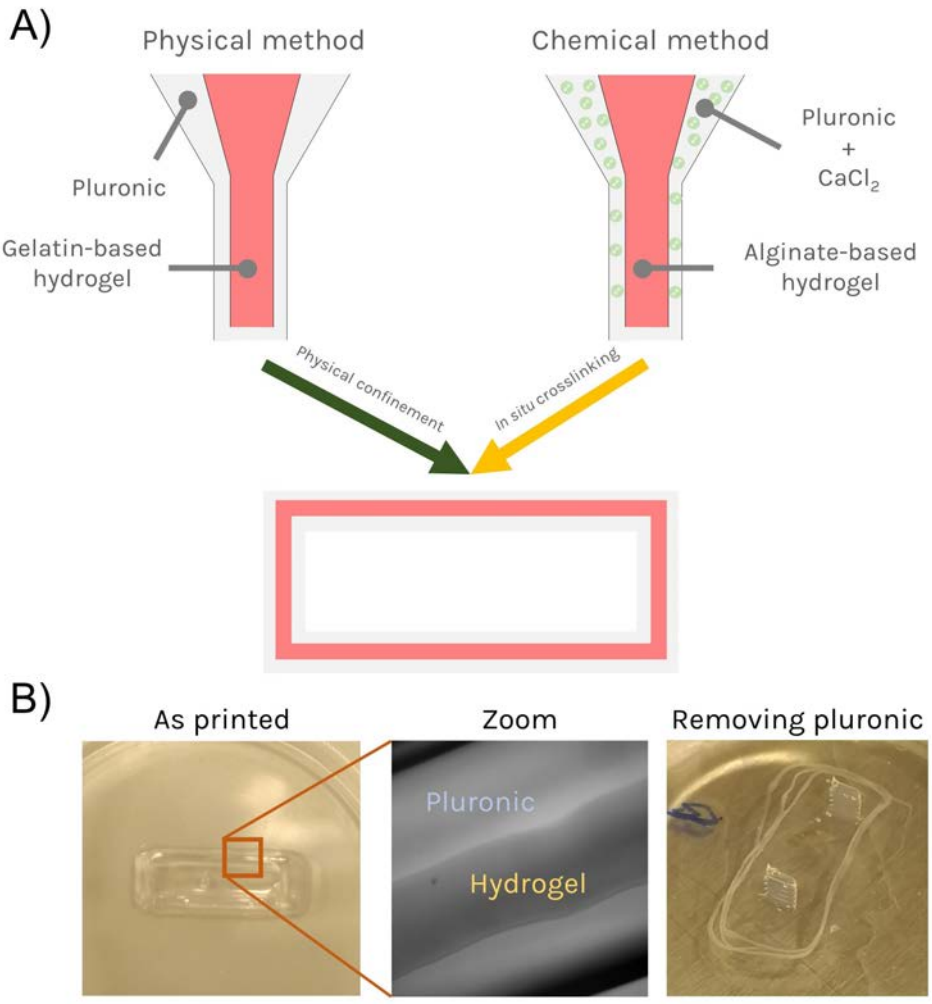

Figure 3.11: Schematic representation of the co-axial bioprinting working principle. A) The inner needle extrudes the cell-laden hydrogel and the outer needle pluronic acid. By using two different confinement methods (chemical and physical), individual and thin fibers can be achieved. B) Representative pictures of the final outcome, showing how the fiber is confined by the pluronic and the resulting individual fibers obtained after dissolving pluronic with cold PBS.

By applying one of these two strategies, thin, individual and width-controlled fibers can be printed, and the composition of the cell-laden hydrogel can be adjusted for specific needs of cell lines or even different crosslinking methods, although always maintaining the core materials, as we will see later on. With the chemical method, $CaCl_2$ ions must be dissolved at the desired molarity concentration in pluronic at low temperature; parallel, alginate needs to be a part of the cell-laden hydrogel. Upon extrusion at room temperature, Ca^{+2} ions from pluronic get in contact with alginate at the borders of the fiber, chemically crosslinking it to achieve a homogeneous fiber. With the physical method, there is no crosslinking of the hydrogel during extrusion, but simple physical repulsion between the two materials. A pre-chilled gelatin-based hydrogel and pluronic at room temperature both have gel properties which can ensure the confinement of the hydrogel. Both strategies provide initial stability of the 3D-bioprinted fibers and allow for a second-level and final crosslinking by any available approach, namely: i) UV-crosslinking; ii) temperature-assisted crosslinking; iii) enzymatic crosslinking; or iv) ionic crosslinking. Once the cell-laden hydrogel is crosslinked, pluronic can be removed by the addition of cold PBS, making it dilute in low temperature, and finally removing it by several washes (Figure 3.11B).

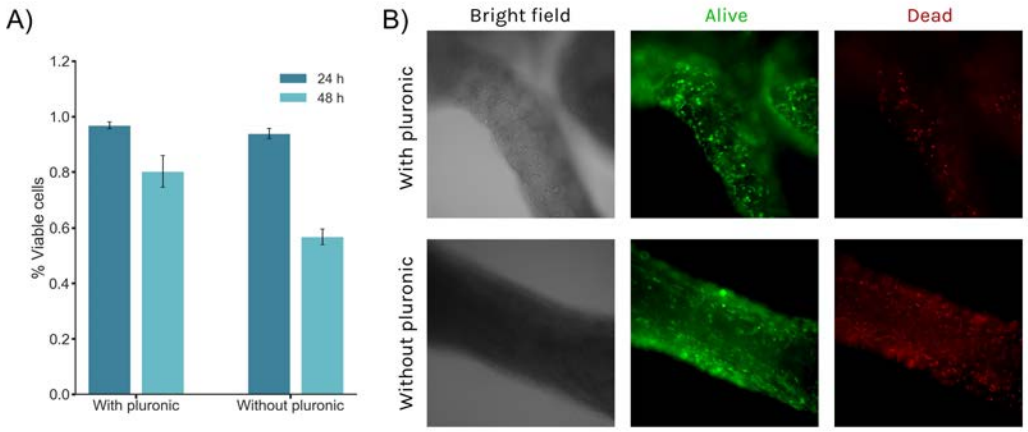

Figure 3.12: Cell viability after co-axial printing. A) When the cell-laden is printed without pluronic confinement, the width of the hydrogel cannot be properly controlled, yielding thicker fibers. Despite having similar viability after 24 h, there is a higher decrease of variability after 48 h for the case without pluronic confinement. B) Fluorescence images of the live/dead assay show a greater quantity of dead cells after 24 h for the printing without pluronic. It can also be observed in bright field how the tissue is thicker in this case, being responsible for less oxygen and nutrient diffusion within the matrix.

The fabrication of thin fiber constructs is crucial to obtain high biocompatibility. Figure 3.12 shows the viability after 3D bioprinting C2C12 myoblasts in a co-axial system with and without pluronic as a confinement material. After 24 h, the percentage of viable cells in the co-axial system using pluronic has been slightly reduced to 80%; however, without using pluronic the viability is much lower after the same time, reaching almost 50% (Figure 3.12A). In this case, the thickness of the cell-laden hydrogel cannot be fully controlled, yielding a very wide construct. As can be appreciated in the bright-field images of Figure 3.12B, without pluronic the tissue appears darker and wider due to its higher thickness. In the corresponding Live/Dead snapshots, we can see how the amount of dead cells (red) is much higher in that case.

Optimization of the co-axial needles

The printing fidelity of a hydrogel is highly dependent on the type of nozzle used and, particularly, on its gauge. Conical nozzles, usually fabricated in plastic, provide better stress profiles for 3D bioprinting since the point of maximum stress is only found at the tip. Cylindrical nozzles made of stainless steel could be potentially harmful for cells, as the shear stress increases significantly when they are too long. Previous reports on the literature of co-axial or core-shell printing have used cylindrical needles, as they are easier to assemble[66–68]. Here, however, we searched for a strategy that could include conical needles, posing less damage for cells.

Different types of co-axial nozzles were manually fabricated, as shown in Figure 3.13A. These needles consisted of a primary nozzle, where the cell-laden hydrogel would pass through, and a secondary nozzle through which pluronic would be extruded. The primary nozzle was always a 200-μm conical plastic nozzle, in order to ensure viability of the printed cells. The challenge, therefore, was to assemble the secondary external needle. For this purpose, a disposable micropipette P1000 tip was cut off and the conical nozzle introduced inside of it, gluing them together. A heated puncher was used to make a hole at one of the sides of the micropipette tip, leaving room for the insertion of the secondary nozzle that would allow the flow of pluronic around the primary conical nozzle. The zoomed-in picture displays the state of the tip after assembly, where we can see how the inner nozzle protrudes surrounded by the outer one.

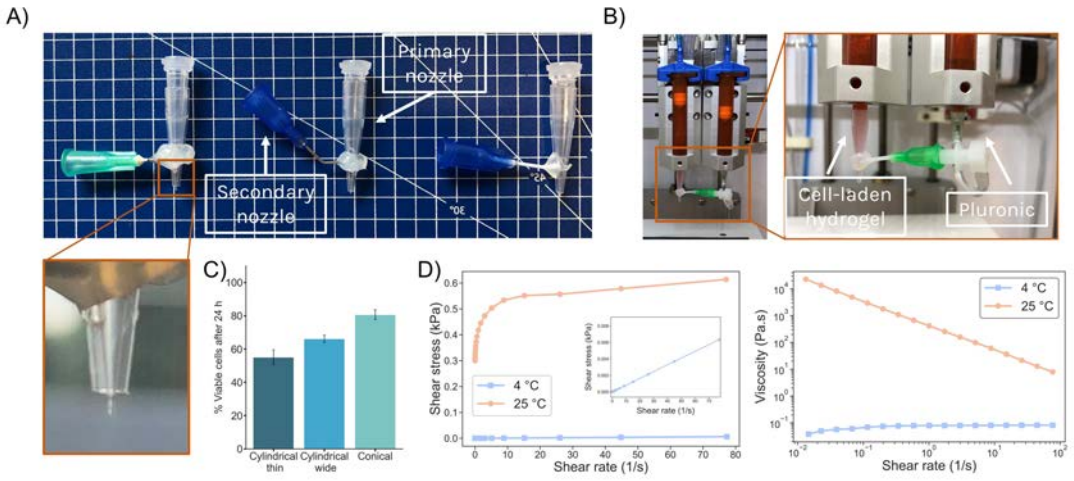

Figure 3.13: Optimization of the co-axial system. A) Several types of co-axial nozzles based on conical needles were considered, offering different degrees of versatility by modifying the outer needle to obtain different angles of insertion or flexibility. B) Both cartridges of the 3D bioprinter are used to control the flow of both materials, connecting the outer needle to the second cartridge with a microfluidic tubing. C) Cell viability after 24 h shows that conical needles provide less cell damage due less amount of shear stress. D) Rheological characterization of pluronic acid at 35% wt/v for two different temperatures. At low temperature, pluronic behaves as a Newtonian liquid with constant viscosity (inset). At room temperature, it shows a strong shear-thinning behavior.

Several secondary nozzles for pluronic were considered: a straight steel nozzle, a bent nozzle and a flexible cylindrical nozzle (Figure 3.13A). A straight steel nozzle (left) was not compatible with the bioprinting setup, as it would crash with the walls of the Petri dish during printing. A bent steel nozzle would partially solve this issue (center), but it would leave less room for versatility and it might still collide with the walls of the dish. Finally, a flexible nozzle (right) solved the problem, as it would adapt to the geometry around the Petri dish it without any collisions. The assembled co-axial nozzle was adapted to 3D bioprinting setup in order to control both flows of materials (Figure 3.13B). The inner nozzle was directly connected to the first cartridge and would receive pressure control from the first printhead. The external nozzle was connected through a silicone tubing to the second printhead in order to control the flow of pluronic.

Straight cylindrical co-axial needles are easier to assemble due to their simpler shape, but they pose more damage for cells due to increased shear stress. Figure 3.13C show a Live/Dead characterization that proves this statement. We 3D-bioprinted a cell-laden hydrogel with the pluronic-based co-axial system, considering three different primary nozzles: i) a thin cylindrical nozzle of gauge 19G (approximately 700 μm of diameter); ii) a wide cylindrical nozzle of gauge 18G (approximately 840 μm of diameter); iii) and a plastic conical nozzle of 200 μm of diameter at the tip. After 24 h, cell viability was higher for the cells printed using the conical nozzle, despite having a smaller diameter at its final point.

Finally, rheological characterization of pluronic acid was performed at low and room temperatures, to investigate the use of this material as a sheath (Figure 3.13E). At 4 °C, pluronic behaves as a Newtonian liquid, with no yield stress and a constant viscosity over the range of shear rate tested. At room temperature, however, it shows a strong shear-thinning effect with a finite yield stress and a decreasing viscosity for higher shear rates, explaining its smooth printability and shape retaining.

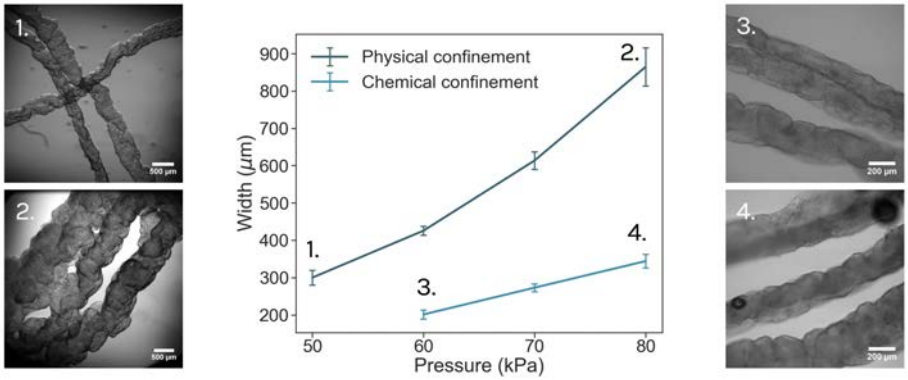

Figure 3.14: The fiber diameter of the hydrogel can be carefully controlled by modifying the extrusion pressure of the hydrogel. Error bars represent standard error of the mean. N = 8-12

The confinement methods

With any of the two confinement methods proposed, fiber width could be carefully controlled to the desired dimensions by simply modifying the pressure applied on the hydrogel. Figure 3.14 shows the range of width that was available for each case. For the chemical confinement method, the control was finer than for the physical one, achieving diameters as low as the nozzle diameter (200 μm) for 60 kPa of pressure. The physical confinement method, on the other hand, could go from around 300 μm of width to more than 800 μm, revealing a wider range of possibilities. Lower diameters for each of the methods could still be achieved, but the fibers were often not continuous and the data is not shown. In any case, the variability was low, as demonstrated by the error bars, indicating the production of homogeneous fibers.

Such a versatility for the adaptation of different confinement schemes and crosslinking methods leads to a great variety of combinations of materials, potentially covering a wide area of applications, depending on the specific requirements of cell lines. Table 3.2 gathers several combinations of confinement methods and biomaterials with different crosslinking strategies for some of the materials most commonly used in 3D bioprinting, like GelMA, fibrinogen, and collagen or Matrigel®. The column fiber quality is influenced by both the homogeneity of the printing and the stability of the fibers. For instance, physical confinement of a hydrogel only containing Matrigel® or collagen might give homogeneous fibers if the concentration of gelatin is high enough, but their stability is low, as their stiffness of the construct after temperature crosslinking is low. Therefore, thin and homogeneous fibers can be printed with this combination, but they are easily broken. Adding fibrinogen to the mixture increases their long term stability, as fibrin is more robust, creating high quality fibers. A similar effect occurs with the chemical confinement method. If the main biomaterial is too liquid, like Matrigel®, it will diffuse through the pluronic before the Ca-crosslinking of alginate can form homogeneous fibers, unless the concentration of alginate is increased to accelerate this process. Since alginate does not have cell attachment motives, it is advisable to keep its concentration as low as possible; in that case, however, the quality of the fiber will not be high. One of the best strategies to follow is the combination of both methods by adding a small amount of gelatin or GelMA to alginate, using a hybrid chemical-physical method of confinement. With this combination, as it can be seen in the table, the quality of the fibers is much improved and virtually any material can be used with it.

Collagen and Matrigel®, which are crosslinked slowly at 37 °C during approximately 30 min in an irreversible manner, deserve special consideration. Collagen is one of the main components of many tissue's ECM and, in particular, of skeletal muscle tissue, making it especially interesting for 3D

Table 3.2: Relation of different strategies to obtain thin independent fibers, combining different biomaterials, confinement strategies and crosslinking methods.

Confinement material	Type of confinement	Biomaterial	Crosslinking	Support material	Fiber quality
Gelatin	Physical	Collagen	Temperature	Pluronic	Low
Gelatin	Physical	Matrigel®	Temperature	Pluronic	Low
Gelatin	Physical	Fibrinogen	Enzymatic	Pluronic	High
Gelatin	Physical	Fibrinogen Matrigel®	Enzymatic Temperature	Pluronic	High
Alginate	Chemical	Matrigel®	Temperature	Pluronic + $CaCl_2$	Medium
Gelatin Alginate	Physical/chemical	Matrigel®	Temperature	Pluronic + $CaCl_2$	High
Gelatin Alginate	Physical/chemical	Fibrinogen	Enzymatic	Pluronic + $CaCl_2$	High
Gelatin Alginate	Physical/chemical	Fibrinogen Matrigel®	Enzymatic Temperature	Pluronic + $CaCl_2$	High
GelMA Alginate	Physical/chemical	Fibrinogen	UV Enzymatic	Pluronic + $CaCl_2$	High
GelMA Alginate	Physical/chemical	Fibrinogen Matrigel®	UV Enzymatic Temperature	Pluronic + $CaCl_2$	High

bioengineering applications[69]. Also, Matrigel® is one of the most widely used basement membrane matrices for 2D and 3D cultures, since it is rich in collagen and many other ECM proteins, but shares the same difficulties. However, their irreversible and low temperature-dependent crosslinking makes difficult their bioprinting, as opposed to gelatin, which has reversible crosslinking. Both materials are liquid at room temperature and cannot be 3D-bioprinted by pneumatic extrusion, but if they are crosslinked at 37 °C, they are also too stiff to be extruded. Although the most promising approaches in the literature have dealt with the mixture of alginate and collagen to achieve proper extrusion[70], better strategies are necessary in the field. One of the main difficulties with these approaches comes from the slow crosslinking of these materials. Because of this, the printed construct can easily lose its shape before the crosslinking has taken place. For that reason, collagen or Matrigel® have been mainly used with casting molds, which can retain the shape of the construct until the hydrogel is fully crosslinked[42]. With the pluronic-assisted co-axial printing method, however, these materials can be protected during crosslinking at 37 °C, avoiding its diffusion in the media. As pluronic does not dissolve at this temperature, the fibers can be incubated in physiological temperatures for 30-45 min until Matrigel® or collagen have been crosslinked, and then pluronic can be removed with cold PBS. Both confinement methods (either chemical or physical) could potentially be used in combination with this type of hydrogel, followed a tertiary crosslinking with fibrinogen to improve the mechanical stability of the fibers.

The summary presented in Table 3.2 is a fast guide to understand the possible combinations of materials according to their confinement method, but the reality is much more complex. The relative concentrations of the confinement materials, as well as that of pluronic and even $CaCl_2$, will greatly influence the applicability of the co-axial printing. Figure 3.15 focuses on the description of these possibilities. Regarding the physical confinement method, the concentration of gelatin with respect to the concentration of pluronic needs to be adjusted to avoid diffusion of the bio-ink. In

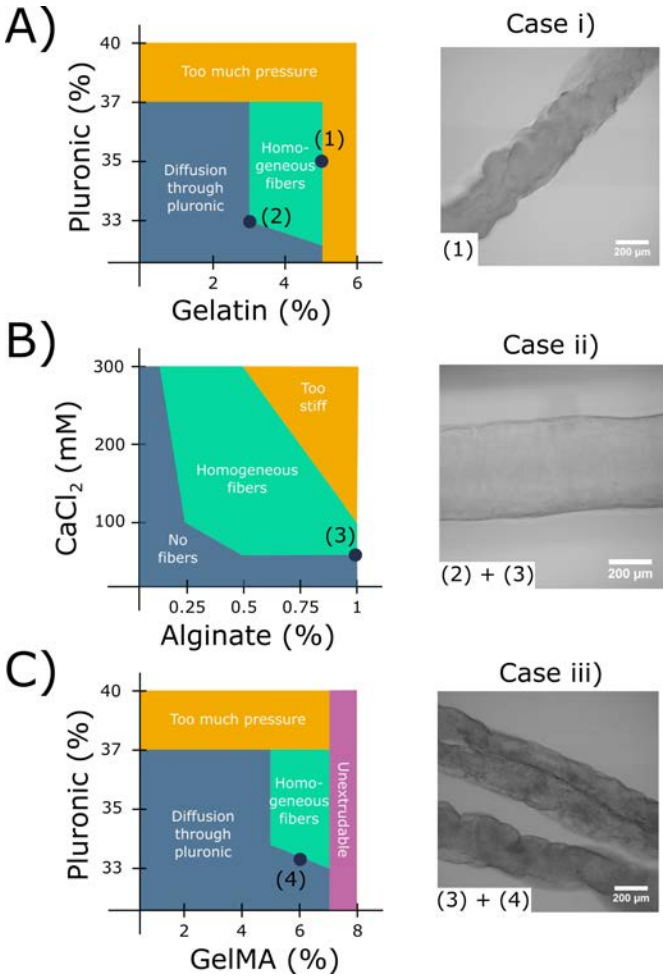

Figure 3.15: Ranges of application of different materials according to their confinement method. A) For physical confinement, the concentration of gelatin with respect to that of pluronic needs to be adjusted to avoid diffusion of the gelatin through the pluronic or having too high pressure that makes extrusion difficult. B) For the chemical confinement method, alginate and calcium chloride need to be adjusted. Low concentrations of alginate are preferred and have been proven to be enough to get homogeneous fibers. C) Gelatin could be exchanged for GelMA, in order to have UV crosslinking of this material. In this case, however, the concentrations of GelMA need to be much higher, due to different gel properties.

general, gelatin at concentrations below 3% (wt/v) is liquid enough to diffuse through pluronic (Figure 3.15A). At the same time, pluronic at concentrations below 33% (wt/v) causes the same problem. The ideal range of concentrations for gelatin to get homogeneous fibers, as the one shown in case i), is between 3-5% (wt/v); for pluronic, it is between 33-37 % (wt/v). Higher concentrations of both pluronic and gelatin can still be used successfully; however, they might require pressures too high for the 3D bioprinter (this depends on the specific system) and cells might suffer too much shear stress during extrusion.

The chemically assisted method, based on alginate crosslinking on extrusion, provides the best homogeneity of fibers compared to physical confinement, as shown in Figure 3.14. Moreover, it does not present clogging problems, since the flow of pluronic can be carefully controlled by the applied pressure. However, alginate also depends on the concentration of pluronic in the same way as gelatin, but is more dependent on the concentration of $CaCl_2$ dissolved in it with respect to its own concentration (Figure 3.15B). Alginate concentrations ranging from as low as 0.25% (wt/v) can yield homogeneous fibers if the concentration of $CaCl_2$ is high enough and other materials that increase the

viscosity are present in the mixture. Higher concentrations of alginate, even surpassing 1% (wt/v) can, naturally, produce very homogeneous fibers, but its stiffness might be too high for the cells, taking into account that other biocompatible polymers with attachment sites, like fibrinogen or collagen, should be included in the mixture. If the presence of alginate is a problem for cell proliferation or differentiation due to low biocompatibility, alginate can be removed after crosslinking of the main biomaterial by the addition of ethylenediaminetetraacetic acid (EDTA) for 5 min[67, 71]. EDTA is a calcium chelator that will attract the Ca^{+2} ions that reversibly crosslink alginate, making it dissolve in the culture medium. In this case, it would be advisable to keep the concentration of alginate low, for instance around 0.5 % (wt/v), with $CaCl_2$ molarities between 100-200 mM, in order to make it easier to remove.

Finally, often the best strategy consists on a hybrid chemical-physical confinement method that uses both gelatin and alginate at smaller quantities. Case ii) in Figure 3.15 shows one of those instances, where alginate at 1% (wt/v) was ionically crosslinked with 50 mM of $CaCl_2$ (point 3), with gelatin at 3% (wt/v) as extra support (point 2). Notice how the fiber is much more homogeneous than case i), in which 5% (wt/v) of gelatin was used (point 1). Therefore, decreasing the concentration of gelatin together with the addition of some alginate gave it a smoother shape. GelMA can also be used to achieve physical confinement, as it also has gel properties (Figure 3.15C). However, it should be considered that the gellification of gelatin and GelMA are comparable, due to the processes to which gelatin is subjected for methacrylation[64]. This can be seen by the relationship between pluronic and GelMA concentrations (Figure 3.15C). GelMA gels at higher concentrations than gelatin, and a minimum concentration of 5% (wt/v) should be used, compared to the minimum of 3% (wt/v) for gelatin. This creates a smaller range to obtain homogeneous fibers, between 5-7% (wt/v). For concentrations higher than this, the mixture is completely unextrudable. Nevertheless, homogeneous fibers can be obtained with this method by carefully choosing the concentrations, and perhaps using alginate in it, as case iii) shows. If GelMA is crosslinked with UV light, the material will remain in the bio-ink, providing cell attachment sites, instead of being washed away, as in the case of gelatin. Further optimization can be achieved by mixing both gelatin and GelMA, as reported in the literature for regular 3D bioprinting[64], to regulate density of GelMA that will remain in the mixture after UV crosslinking.

Skeletal muscle tissue fibers

The descriptions of the previous sub-section are of a universal character; this co-axial system, together with any of the confinement methods, or their hybrid combination, can be used to create thin and homogeneous fibers of controlled width. Moreover, a wide variety of biomaterials, such as fibrinogen, Matrigel®, collagen, or GelMA, with different crosslinking strategies, like enzymatic, ionic, UV light or temperature, can be used to provide the suitable three-dimensional environment for cell survival, depending on the specific needs of each cell type. The confinement materials, gelatin or alginate, can be dissolved if their presence is not needed anymore: gelatin dissolves at physiological temperatures during cell incubation and alginate can be removed with a short wash in EDTA. But they can also be maintained, for instance if GelMA and UV crosslinking are used instead of gelatin. One of the most straightforward applications of this technique is found in the 3D bioprinting of skeletal muscle cells, which can benefit the most from the fibrillar structure, inducing a self-organization in a fascicle-like manner, as in native tissue.

As presented in Table 3.2, virtually any material that is commonly used in the literature for tissue engineering purposes can be used in combination of this co-axial system to produce thin homogeneous fibers. For skeletal muscle tissue, in particular, fibrinogen has been extensively used, sometimes

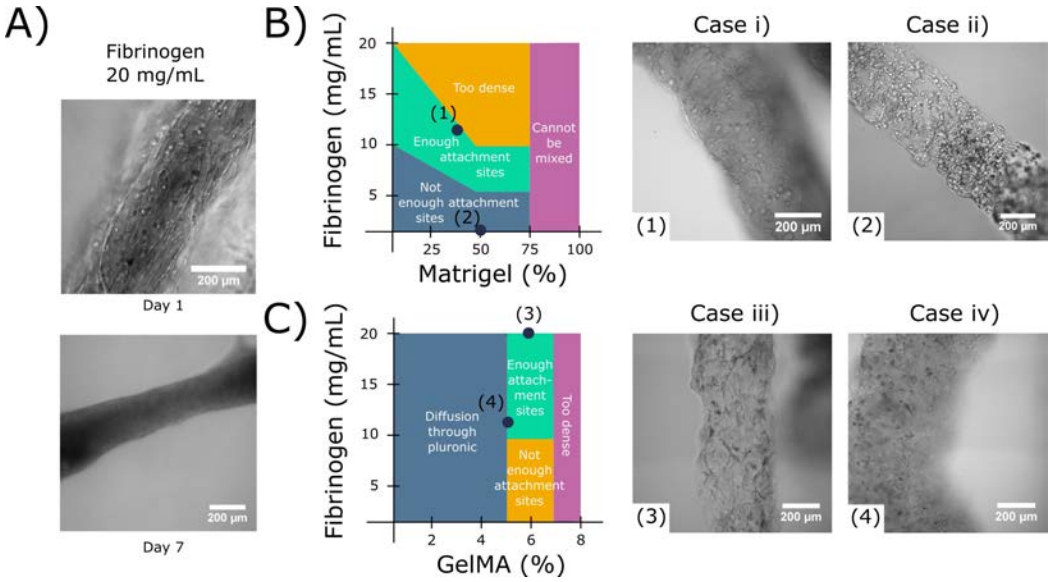

Figure 3.16: Ranges of application of materials according to their attachment sites. A) Fibrinogen, when used alone in combination with gelatin for physical confinement, works best with a higher concentration of at least 20 mg/mL. Pictures below show attachment and alignment of the cells after 1 day that yield a fully compacted and differentiated fiber after 7 days. B) If used in combination with other materials like Matrigel® to increase the attachment sites, it is recommended to decrease the concentration of fibrinogen so that the hydrogel is not too dense. The concentration of Matrigel® should also not be kept higher than 50-75%, since that level of dilution cannot be obtained when mixed with fibrinogen or other components. Examples show a case with good attachment of cells and low attachment when Matrigel® is used by itself. It can be seen how in this case the density of the hydrogel is much lower, being more transparent. C) Fibrinogen can also be mixed with GelMA, taking into account similar conditions to the previous case.

by itself, but others in combination with Matrigel® or collagen[8, 42]. Figure 3.16 shows the ranges of application of some of these cases, focusing on their concentrations as a function of the attachment sites that they provide and the density of the matrix. Fibrinogen, if used alone as the main component of the myoblast-laden hydrogel, together with the chemical, physical or hybrid confinement method, should be kept at a high concentration, with 20 mg/mL being an ideal value for cell differentiation, as previously reported in the literature and in the previous section (Figure 3.16A)[8]. At this concentration, the cells are already elongated longitudinally after 1 day and form a compacted fiber that can contract upon electrical stimulation at day 7.

Since the local microenvironment (the perimysium) of skeletal muscle tissue is mainly composed of collagen, it is a good strategy to combine fibrinogen and Matrigel®, as displayed in Figure 3.16B. However, the relative combination of both materials needs to be carefully considered, as the resulting matrix after crosslinking might be too dense for cell proliferation. For instance, if Matrigel® is mixed at a 50% (v/v) concentration, fibrinogen should be decreased to the range of 10 mg/mL. However, if fibrinogen is reduced too much, the density of attachment sites of Matrigel®, as well as its stiffness, is not high enough for proper cell differentiation, as case ii) shows (50% (v/v) Matrigel® and no fibrinogen). Finally, if GelMA is used as a confinement material, its proportionality with respect to fibrinogen is also crucial. As already mentioned, GelMA concentrations below 5% (wt/v) do not produce homogeneous fibers, since they dissolve through the pluronic. In this range of applicability, fibrinogen should be kept between 10-20 mg/mL to have enough attachment sites. In case iii), the cells are elongated since fibrinogen at 20 mg/mL and GelMA at 6% (wt/v) provide enough attachment sites, while case iv) shows more cells with round shapes, as the concentrations are lower.

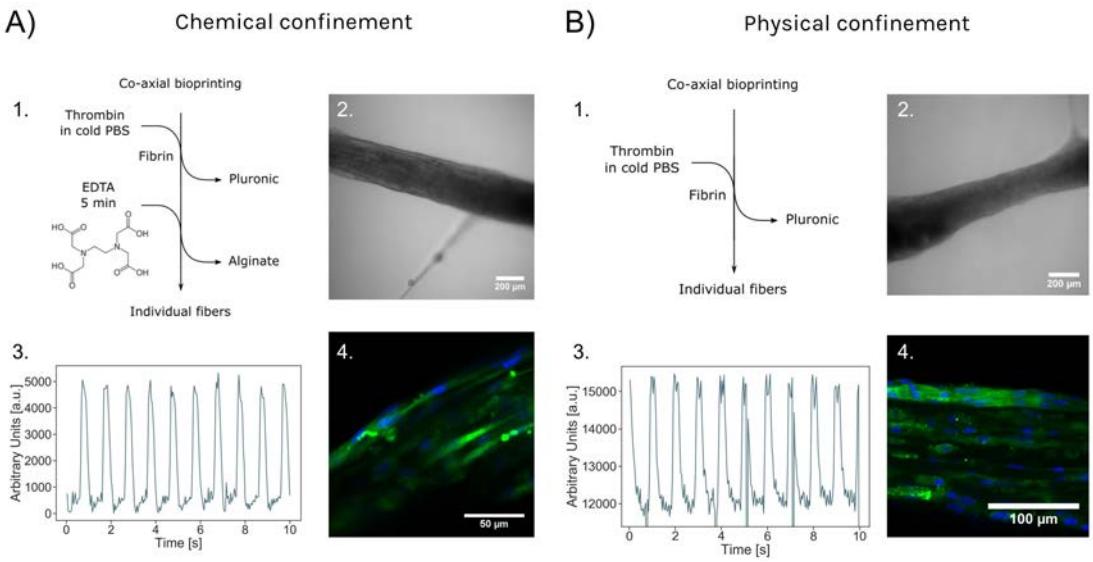

Figure 3.17: Two cases of chemical and physical confinement strategies taken forward. A) A hydrogel laden with C2C12 myoblasts was co-axially 3D-bioprinted embedded in a hydrogel containing alginate, gelatin and fibrinogen. After *in situ* crosslinking of alginate with $CaCl_2$ dissolved in pluronic, thrombin was used to crosslink fibrinogen and pluronic was dissolved with cold PBS (1). Later, EDTA was used to dissolve alginate, improving cell attachment and compaction of the tissue, finally yielding thin fibers (2). After seven day of differentiation, the tissue could contract upon applying electrical stimulation (3) and immunostaining of MyHCII and nuclei showed aligned myotubes within the fiber (4). B) In the physical confinement case, a cell-laden hydrogel composed of gelatin and fibrinogen was co-axially 3D-bioprinted (1) to yield thin fibers (2) after crosslinking of fibrinogen and dissolution of pluronic. After seven days of differentiation, the fibers could also contract (3) and immunostaining showed aligned myotubes as well (4).

Finally, Figure 3.17 shows two cases of successful bioengineering of thin skeletal muscle fibers with each of the confinement methods. The chemical confinement strategy (Figure 3.17A) was carried out with C2C12 myoblasts at a concentration of 5 million/mL and an hydrogel composed of 0.5% (wt/v) of alginate, 3% (wt/v) of gelatin to increase its viscosity and help with the homogeneity of the fibers and 20 mg/mL of fibrinogen for cell attachment sites, similar to the hydrogel already described and validated in Section 2. Pluronic at 33% (wt/v) with 300 mM $CaCl_2$ was used as support material. After 3D bioprinting, a cold solution of thrombin (5 U/mL) was added to the construct for 5 min at 4 °C. At this temperature, pluronic dissolved while fibrinogen was being crosslinked into fibrin. After this time, 3-5 washes with cold PBS were able to completely remove the remaining pluronic.

The use of this confinement method based on alginate, although it produces very homogeneous fibers (as described in Figure 3.14), does not provide the best environment for myoblast differentiation. 3D-bioengineered skeletal muscle tissue generally shows passive compaction during the differentiation process, as it was commented in the previous section and shown in Figure 3.6. Alginate is a polysaccharide which does not possess cell attachment motifs. Therefore, individual fibers crosslinked with alginate, even at low a concentration of 0.5% (wt/v), did not show much compaction, something necessary for the proper differentiation of the cells. As a solution, crosslinking of alginate methacrylate (AlgMA) to a main network formed out of GelMA, for instance, has been proven to provide a suitable environment for this tissue[23]. Likewise, chemically modifying alginate to insert cell attachment sites (such as RGD sequences) would also help in the compaction issue while taking advantage of this crosslinking method[72]. This problem, nonetheless, could be solved without chemical modifications by the dissolution of alginate after fibrinogen crosslinking took place by the addition of a chelating agent, such as EDTA, for 5 min (Figure 3.17A-1). EDTA can sequester

calcium ions involved in the irreversible ionic crosslinking of alginate, therefore rendering it soluble. This strategy has been previously proven to remove most of the alginate present in the hydrogel without disturbing the attachment of cells (strongly affected by calcium chelators) in such a short time frame[67, 71]. In our experiments, 3D-bioprinted fibers shown compaction after incubation with EDTA (Figure 3.17A-2), indicating the removal of alginate and the progression of the differentiation process. After 7 days, EPS could induced contractions in the fibers, as shown in Figure 3.17A-3 and immunostaining of MyHCII and cell nuclei showed thin fibers with aligned myotubes (Figure 3.17A-4).

The physical confinement method, on the other hand, produces less homogeneous fibers, but they are still highly controlled in thickness and can yield thin skeletal muscle constructs (Figure 3.17B). This method, as opposed to the chemically assisted one, only requires the presence of gelatin in the cell-laden hydrogel, although at a higher concentration to ensure physical confinement within the pluronic sheath. In Figure 3.17B, the hydrogel consisted gelatin at 5% (wt/v) with fibrinogen at 20 mg/mL and myoblasts at a density of 5 million cells/mL. The protocol after co-axial bioprinting was the same as for the chemical confinement method, except without the addition of EDTA: the fiber constructs were left in a solution of cold thrombin (5 U/mL) for 5 min at 4°C for fibrinogen to crosslink to fibrin and pluronic to dissolve (Figure 3.17B-1). After this, additional washes with cold PBS removed the remaining pluronic and the constructs were left to proliferate in GM in a cell incubator. As before, the fibers could compact during maturation of the tissue (Figure 3.17B-2) and after several days of differentiation, they could respond to electrical stimulation with contractions, as shown in Figure 3.17B-3. Immunostaining of MyHCII and cell nuclei revealed thin fibers packed with aligned myotubes (Figure 3.17B-4).

3.3. Conclusions

In this section, we have presented a pluronic-assisted co-axial 3D bioprinting strategy for the generation of thin, homogeneous fibers that can be used with a wide variety of cell-laden hydrogels for tissue engineering purposes. This technique is based on the extrusion of a main inner hydrogel through a plastic conical nozzle, surrounded by a secondary support material, pluronic acid, which acts as a sheath and control the width of the extruded polymer. Two main hydrogel confinement methods were envisaged: the first one based on chemical crosslinking of alginate upon extrusion thanks to the presence of $CaCl_2$ within pluronic, and the second one based on physical repulsion between gellified gelatin and pluronic. Both of these strategies can be used in combination with any kind of biopolymer, such as fibrinogen, Matrigel®, GelMA, and others, making it an universal 3D bioprinting method to obtain thin, individual and width-controlled fibers. The possible combinations of a selection of materials were studied and described in detail, focusing on their concentrations with respect to each other and their crosslinking methods.

Finally, this strategy is used for the 3D bioengineering of skeletal muscle fibers of approximately 200 μm, which can be printed individually and homogeneously. In fact, both the chemical and physical confinement strategies yielded differentiated myotubes that could contract upon electrical stimulation and were aligned longitudinally. This strategy brings the state of the art one step closer to recreating the complexity of the skeletal muscle tissue architecture, composed of several layers or organized tubular structures that are densely packed. Previous efforts have only demonstrated the bioengineering of highly aligned myotube fibers, mimicking the bundles of myotubes found in native tissue, but their large thickness prevented them from taking advantage of their full cross-sectional area, showing dead cells or depleted areas in the center, due to low diffusion of oxygen and nutrients. Moreover,

individual fibers were difficult to obtain, as the crosslinking of the hydrogel normally happens after 3D bioprinting. With this strategy, however, fibers are formed and stabilized at the moment of extrusion, opening the possibility to fabricate individual fibers of small diameter, that could be later packed together to form fascicles of myotube bundles, as it occurs in native tissue.

However, several challenges are still to be overcome. Although this technique can successfully yield homogeneous and thin fibers, their small thickness makes them easy to break if they are poorly handled. Investigation of new biocompatible materials for tissue engineering that are less fragile, but still highly porous and of low stiffness, is necessary to attain more stable fibers. For this reason, their packing in the form of muscle fascicles might be difficult at the moment and an automated method that avoided manual assembly should be investigated. One solution could be taking advantage of the natural compaction of the muscle fibers to let them self-assemble in this manner. Another possible solution could be printing in pre-defined wide channels that prevented the fibers to freely float in the medium, similar to a classical mold casting technique, but still taking advantage of the diameter control. In any case, close contact between the hydrogel fibers could result in a small degree of fiber fusion, specially if the cells produce their own ECM, diminishing the advantages of the technique. Native skeletal muscle tissue has small capillaries running around the fascicles, ensuring delivery of oxygen and nutrients, so further research into vascular tissue bioengineering could provide solutions to this problem.

Nevertheless, this pluronic-assisted co-axial bioprinting offers a novel approach for the bioengineering of thin and individual fibers that can avoid the pervasive oxygen diffusion problems and can work universally for virtually any type of hydrogel, being adaptable to many different crosslinking methods to accommodate the necessities in terms of biomaterials of specific cell types. Moreover, in particular, it offers a valuable new strategy especially useful in skeletal muscle 3D bioengineering, where thin and homogeneous fibers are needed to recreate native tissue.

3.4. Materials and methods

Fabrication of the co-axial nozzles

The co-axial nozzles were manually fabricated using different types of commercially available nozzles and tips. The inner nozzle, where the cell-laden hydrogel passed through, was a 200-μm (G27) plastic conical nozzle (Optimum® SmoothFlow™ tapered tips, Nordson®, ref. 7018417). The luer lock of this nozzle was left free to be connected to the first bioprinting barrel, where the cell-laden hydrgel woud be loaded. The outer nozzle that covered the inner one was a filtered P1000 pipette tip (Labclinics, ref. LAB1000ULFNL), cut approximately at 5 cm from its end. The tip was trimmed to increase its diameter at the final point. Both nozzles were assembled and glued together. When the glue was dry and the assembly stable, a hot puncher was used to create a hole in the outer nozzle, at approximately 1.5 cm from its ending, with care to not create another whole in the internal nozzle. The secondary nozzle, where pluronic flowed, was inserted inside this hole. This secondary nozzle was a flexible polypropylene 800-μm nozzle (G18) from Nordson® (EFD® 7018138). A silicone tubing of 0.8 mm of diameter (ibidi, ref. 10841) was attached to this external nozzle through a male elbow luer connector (ibidi, ref. 10802). A 1.1-mm (19G) nozzle (BBraun Sterican®, ref. 4657799) was inserted through the other end of the tubing, so that its luer lock connector could be connected to the second bioprinting barrel, containing pluronic acid.

Hydrogel fabrication

For the fabrication of the different combinations of hydrogels, the following materials were used: gelatin from porcine skin, type A (Sigma-Aldrich, G2500), fibrinogen from bovine plasma (Sigma-Aldrich, F8630) with thrombin from bovine plasma (Sigma-Aldrich, T4648) as crosslinker, Matrigel® Basement™ membrane matrix (Corning®, 354234), sodium alginate (Sigma-Aldrich, W201502), GelMA with lithium phenyl-2,4,6-trimethylbenzoylphosphinate (LAP) at 0.25% (wt/v) as photoinitiator (CELLINK®, LIK-3050V-1), collagen type I high concentration (Corning®, 354249), and Pluronic® F-127 powder (Sigma-Aldrich, P2443).

Pluronic was dissolved at concentrations ranging from 30-40% (wt/v) in Mili-Q water with $CaCl_2$ (at molar concentrations ranging from 50 mM to 300 mM) under stirring in a refrigerator (4 °C) until fully dissolved. For hydrogels containing gelatin, alginate and/or GelMA in the same composition, this components were mixed together in PBS at the desired concentrations. If the hydrogel contained fibrinogen, this component was dissolved in PBS at a 2x concentration and then added to the hydrogel containing alginate and/or gelatin, also at a 2x concentration, in order to avoid pipetting this very viscous mixture. If the hydrogel also contained Matrigel®, the concentrations were also adjusted to achieve the desired concentrations reducing the need for pipetting (for instance, at 1:1:1 ratios, or 2:1:1 ratios, etc.).

Co-axial 3D bioprinting

C2C12 myoblasts were harvested by a 0.25% (wt/v) Trypsin-0.53 mM EDTA solution, centrifuged at 300g for 5 min and the pellet re-suspended at a concentration of $5 \cdot 10^6$ cells/mL in the hydrogel mixture, at 37 °C. The cell-laden hydrogel was loaded into a 3-mL plastic syringe (Nordson®, ref. 7012085) coupled to the inner nozzle of the co-axial nozzle. Pluronic was loaded while cold into a secondary barrel and left at RT to gel beforehand. CELLINK® Inkredible+ 3D bioprinter was used to bioprint the hydrogel fibers. The cell-laden hydrogel was inserted in the first cartridge and the pluronic barrel to the second barrel, and all the nozzles connected as previously explained. The pressure for the pluronic barrel was kept between 250-350 kPa and adjusted manually, although these values are highly dependent on the diameter and length of the silicone tubing and the concentration of pluronic. For the hydrogel, the pressures were kept between 40-80 kPa, also adjusted manually, depending on the type of hydrogel. The designs were directly written in GCode with the help of the open-source software Slic3r (v. 1.2.9) and the bioprinter was controlled with RepetierHost (v. 2.0.5). After 3D bioprinting, if the hydrogel contained fibrinogen, a solution of 5 U/mL of thrombin was added to the Petri dish for 5 min in a refrigerator at 4 °C. At this point, pluronic would dissolve and fibrinogen would crosslink to form fibrin. After this, several washes with cold PBS were done to completely remove pluronic, GM supplemented with ACA was added and the constructs left in a cell incubator at 37 °C and 5% CO_2 atmosphere. If the hydrogel contained Matrigel®, the as-printed constructs were left in an incubator for at least 30 min, without removing pluronic. After this, a cold solution of PBS (or thrombin, if fibrinogen was also in the mixture) was added to dissolve pluronic after several washes. If the chemical confinement method based on alginate was used, and this material wanted to be removed, a solution of 20 mM EDTA (Sigma-Aldrich, E6758) adjusted with NaOH to pH 7, was added to the Petri dish after crosslinking for 5 min.

Rheological characterization of pluronic acid

Rheological characterization of pluronic was performed using a Discovery HR-2 controlled-stress rheometer (TA Instruments) equipped with a Peltier steel cone geometry of 40 mm of diameter, 26 μm of truncation, and an angle of 1.019°. The Peltier element was set to 4 °C and 25 °C to demonstrate the behavior of the block co-polymer at low and room temperatures. In all experiments, the sample was left to acquire the desire temperature for 1 min. A flow ramp with shear rate from 100 1/s to 0.01 1/s was performed, in logarithmic mode with 600 s of duration per point, with a pre-conditioning to the temperature of 30 s and pre-shear of 3 rad/s for 10 s.

Cell culture, differentiation and electrical stimulation

C2C12 mouse myoblasts were purchased from ATCC and maintained in growth medium (GM) consisting of high glucose Dullbecco's Modified Eagle's Medium (DMEM; Gibco®) supplemented with 10% Fetal Bovine Serum (FBS), 200 nM L-Glutamine and 1% Penicillin/Streptomycin, in a 37 °C and 5% CO_2 atmosphere. Cells were passaged before reaching 80% confluence in Corning® T-75 flasks. For cell differentiation and myotube formation after the bioprinting process, GM was substituted by DM, consisting of high glucose DMEM containing 10% Horse Serum (Gibco®), 200 nM L-Glutamine (Gibco®), 1% Penicillin-Streptomycin (Gibco®), 50 ng/ml IGF-1 (Sigma-Aldrich) and 1 mg/ml 6-aminocaproic acid (ACA, Sigma-Aldrich). 3D-bioprinted fibers were stimulated with a set of carbon-made electrodes attached to the cover of a Petri dish (a detailed characterization can be found in Chapter IV) under an inverted microscope (Leica's DMi8) with pulses of 2 ms and 1 V/mm. Analysis of the contractions was performed with a home-made Python algorithm based on computer vision techniques that computed the distance between frames of a selected ROI by applying an $\mathcal{L}_2$-norm to the image pixels.

Cell viability and MyHCII immunofluorescence

Cell viability was analyzed by the dual-fluorescence Live/Dead® Viability/Cytotoxicity kit for mammalian cells (Life Technologies), following the manufacturer's instructions. Fluorescently labeled fibers were imaged under a Leica DMi8 inverted fluorescence microscope equipped with a 37 °C and 5% CO2 chamber, using a 20× air objective. The percentages of live and dead cells were calculated by using ImageJ software ver.1.47q (National Institutes of Health, Bethesda, MD). For immunostaining, 3D-bioprinted constructs were washed twice in PBS and fixed by incubating them with a 3.7% paraformaldehyde in PBS solution for 15 min at RT, followed by three washes in PBS. Then, cells were permeabilized by using 0.2% Triton-X-100 in PBS. After two washes in PBS, the constructs were incubated with 5% Bovine Serum Albumin (BSA) in PBS (PBS-BSA) to block unspecific bindings. Then, bioprinted structures were incubated for 2 h at RT and dark conditions with a 1/400 dilution of Alexa Fluor®488-conjugated Anti-Myosin Heavy Chain II antibody (eBioscience) in 5% PBS-BSA. The unbound antibodies were washed out with PBS, and cell nuclei were counterstained with 1 μl/mL Hoechst 33342 (Life technologies). Finally, samples were washed twice in PBS and they were stored at 4 °C until their analysis. Fluorescently immunostained fiber constructs were imaged under an Zeiss LSM 800 confocal scanning laser microscope (CSLM), with a diode laser at 488 nm and 405 nm excitation wavelength for Myosin Heavy Chain II and cell nuclei.

References

[1] R. Mestre, T. Patiño, X. Barceló, S. Anand, A. Pérez-Jiménez, and S. Sánchez, *Force Modulation and Adaptability of 3D-Bioprinted Biological Actuators Based on Skeletal Muscle Tissue,* Advanced Materials Technologies **4**, 1800631 (2019).

[2] R. Mestre, T. Patiño, M. Guix, X. Barceló, and S. Sanchez, *Design, Optimization and Characterization of Bio-Hybrid Actuators Based on 3D-Bioprinted Skeletal Muscle Tissue,* in *Martinez-Hernandez U. et al. (eds) Biomimetic and Biohybrid Systems. Living Machines 2019. Lecture Notes in Computer Science*, Vol. 11556 (Springer, Cham, 2019) pp. 205–215.

[3] R. Mestre, T. Patiño, X. Barceló, and S. Sanchez, *3D bioprinted muscle-based bio-actuators: Force adaptability due to training,* in *Vouloutsi V. et al. (eds) Biomimetic and Biohybrid Systems. Living Machines 2018. Lecture Notes in Computer Science*, Vol. 10928 (Springer, Cham, 2018) pp. 316–320.

[4] T. Patino, R. Mestre, and S. Sánchez, *Miniaturized soft bio-hybrid robotics: a step forward into healthcare applications,* Lab Chip **16**, 3626 (2016).

[5] M. M. Stanton, C. Trichet-Paredes, and S. Sanchez, *Applications of three-dimensional (3D) printing for microswimmers and bio-hybrid robotics.* Lab on a chip **15**, 1634 (2015).

[6] S. V. Murphy and A. Atala, *3D bioprinting of tissues and organs.* Nature biotechnology **32**, 773 (2014).

[7] I. Donderwinkel, J. C. M. van Hest, N. R. Cameron, M. Duocastella, B. Pippenger, S. Bellance, R. Bareille, M. Remy, L. Bordenave, J. Amedee, F. Guillemot, P. Strippoli, S. Canaider, A. Tamayol, A. Khademhosseini, M. R. Dokmeci, A. Atala, A. Khademhosseini, G. H. Zhu, X. Y. Jin, S. R. Shin, M. R. Dokmeci, and A. Khademhosseini, *Bio-inks for 3D bioprinting: recent advances and future prospects,* Polym. Chem. **31**, 7250 (2017).

[8] H.-W. Kang, S. J. Lee, I. K. Ko, C. Kengla, J. J. Yoo, and A. Atala, *A 3D bioprinting system to produce human-scale tissue constructs with structural integrity,* Nature Biotechnology **34**, 312 (2016).

[9] O. Chaudhuri, *Viscoelastic hydrogels for 3D cell culture,* Biomater. Sci. **5**, 1480 (2017).

[10] M. M. Stanton, J. Samitier, and S. Sánchez, *Bioprinting of 3D hydrogels,* Lab Chip **15**, 3111 (2015).

[11] T. Xu, W. Zhao, J. M. Zhu, M. Z. Albanna, J. J. Yoo, and A. Atala, *Complex heterogeneous tissue constructs containing multiple cell types prepared by inkjet printing technology,* Biomaterials **34**, 130 (2013).

[12] T. Xu, J. Jin, C. Gregory, J. J. Hickman, and T. Boland, *Inkjet printing of viable mammalian cells,* Biomaterials **26**, 93 (2005).

[13] X. Cui, T. Boland, D. D.D'Lima, and M. K. Lotz, *Thermal Inkjet Printing in Tissue Engineering and Regenerative Medicine,* Recent Patents on Drug Delivery & Formulation **6**, 149 (2012).

[14] K. Hölzl, S. Lin, L. Tytgat, S. Van Vlierberghe, L. Gu, and A. Ovsianikov, *Bioink properties before, during and after 3D bioprinting,* Biofabrication **8**, 032002 (2016).

[15] T. Xu, H. Kincaid, A. Atala, and J. J. Yoo, *High-throughput production of single-cell microparticles using an inkjet printing technology,* Journal of Manufacturing Science and Engineering, Transactions of the ASME **130**, 0210171 (2008).

[16] T. Okamoto, T. Suzuki, and N. Yamamoto, *Microarray fabrication with covalent attachment of DNA using Bubble Jet technology,* Nature Biotechnology **18**, 438 (2000).

[17] J. Malda, J. Visser, F. P. Melchels, T. Jüngst, W. E. Hennink, W. J. A. Dhert, J. Groll, and D. W. Hutmacher, *25th anniversary article: Engineering hydrogels for biofabrication,* Advanced Materials **25**, 5011 (2013).

[18] F. Pati, J. Jang, D.-h. Ha, S. W. Kim, J.-w. Rhie, J.-h. Shim, D.-h. Kim, and D.-w. Cho, *Printing three-dimensional tissue analogues with decellularized extracellular matrix bioink,* Nature Communications **5**, 1 (2014).

[19] Y. B. Kim, H. Lee, and G. H. Kim, *Strategy to Achieve Highly Porous/Biocompatible Macroscale Cell Blocks, Using a Collagen/Genipin-bioink and an Optimal 3D Printing Process,* ACS Applied Materials and Interfaces **8**, 32230 (2016).

[20] B. H. Lee, N. Lum, L. Y. Seow, P. Q. Lim, and L. P. Tan, *Synthesis and characterization of types A and B gelatin methacryloyl for bioink applications,* Materials **9**, 1 (2016).

[21] Z. Yue, X. Liu, P. T. Coates, and G. G. Wallace, *Advances in printing biomaterials and living cells: Implications for islet cell transplantation,* Current Opinion in Organ Transplantation **21**, 467 (2016).

[22] X. Wang, Q. Ao, X. Tian, J. Fan, H. Tong, W. Hou, and S. Bai, *Gelatin-based hydrogels for organ 3D bioprinting,* Polymers **9**, 401 (2017).

[23] A. García-Lizarribar, X. Fernández-Garibay, F. Velasco-Mallorquí, A. G. Castaño, J. Samitier, and J. Ramon-Azcon, *Composite Biomaterials as Long-Lasting Scaffolds for 3D Bioprinting of Highly Aligned Muscle Tissue,* Macromolecular Bioscience **18**, 1800167 (2018).

[24] S. Knowlton, B. Yenilmez, S. Anand, and S. Tasoglu, *Photocrosslinking-based bioprinting: Examining crosslinking schemes,* Bioprinting **5**, 10 (2017).

[25] L. Shor, S. Güçeri, R. Chang, J. Gordon, Q. Kang, L. Hartsock, Y. An, and W. Sun, *Precision extruding deposition (PED) fabrication of polycaprolactone (PCL) scaffolds for bone tissue engineering,* Biofabrication **1**, 015003 (2009).

[26] J. U. Lind, T. A. Busbee, A. D. Valentine, F. S. Pasqualini, H. Yuan, M. Yadid, S. J. Park, A. Kotikian, A. P. Nesmith, P. H. Campbell, J. J. Vlassak, J. A. Lewis, and K. K. Parker, *Instrumented cardiac microphysiological devices via multimaterial three-dimensional printing,* Nature Materials **16**, 303 (2017).

[27] H. Martínez Ávila, S. Schwarz, N. Rotter, and P. Gatenholm, *3D bioprinting of human chondrocyte-laden nanocellulose hydrogels for patient-specific auricular cartilage regeneration,* Bioprinting **1-2**, 22 (2016).

[28] C. Cvetkovic, R. Raman, V. Chan, B. J. Williams, M. Tolish, P. Bajaj, M. S. Sakar, H. H. Asada, M. T. A. Saif, and R. Bashir, *Three-dimensionally printed biological machines powered by skeletal muscle,* Proceedings of the National Academy of Sciences of the United States of America **111**, 10125 (2014).

[29] Y. Morimoto, H. Onoe, and S. Takeuchi, *Biohybrid robot powered by an antagonistic pair of skeletal muscle tissues,* Science Robotics **3**, eaat4440 (2018).

[30] L. Madden, M. Juhas, W. E. Kraus, G. A. Truskey, and N. Bursac, *Bioengineered human myobundles mimic clinical responses of skeletal muscle to drugs,* eLife **2015**, 4:e04885 (2015).

[31] R. Raman, L. Grant, Y. Seo, C. Cvetkovic, M. Gapinske, A. Palasz, H. Dabbous, H. Kong, P. P. Pinera, and R. Bashir, *Damage, Healing, and Remodeling in Optogenetic Skeletal Muscle Bioactuators,* Advanced Healthcare Materials **6**, 1700030 (2017).

[32] M. S. Sakar, D. Neal, T. Boudou, M. A. Borochin, Y. Li, R. Weiss, R. D. Kamm, C. S. Chen, and H. H. Asada, *Formation and optogenetic control of engineered 3D skeletal muscle bioactuators,* Lab on a Chip **12**, 4976 (2012).

[33] Y. Sun, R. Duffy, A. Lee, and A. W. Feinberg, *Optimizing the structure and contractility of engineered skeletal muscle thin films,* Acta Biomaterialia **9**, 7885 (2013).

[34] H. Vandenburgh, J. Shansky, F. Benesch-Lee, V. Barbata, J. Reid, L. Thorrez, R. Valentini, and G. Crawford, *Drug-screening platform based on the contractility of tissue-engineered muscle,* Muscle and Nerve **37**, 438 (2008).

[35] V. Chan, K. Park, M. B. Collens, H. Kong, T. A. Saif, and R. Bashir, *Development of miniaturized walking biological machines.* Scientific Reports **2**, 857 (2012).

[36] B. Staff, *Medical gallery of Blausen Medical 2014,* WikiJournal of Medicine **1** (2014), 10.15347/wjm/2014.010.

[37] R. L. Lieber, *Skeletal Muscle Structure, Function, and Plasticity* (2011).

[38] R. Horowits, E. S. Kempner, M. E. Bisher, and R. J. Podolsky, *A physiological role for titin and nebulin in skeletal muscle,* Nature **323**, 160 (1986).

[39] S. Ahadian, S. Ostrovidov, V. Hosseini, H. Kaji, M. Ramalingam, H. Bae, and A. Khademhosseini, *Electrical stimulation as a biomimicry tool for regulating muscle cell behavior.* Organogenesis **9**, 87 (2013).

[40] L. N. Van Kann and A. J. Bakker, *Effect of tumor necrosis factor α on electrically induced calcium transients elicited in C2C12 skeletal myotubes,* Muscle and Nerve **35**, 251 (2007).

[41] C. S. Farah and F. C. Reinach, *The troponin complex and regulation of muscle contraction,* The FASEB Journal **9**, 755 (1995).

[42] R. Raman, C. Cvetkovic, and R. Bashir, *A modular approach to the design, fabrication, and characterization of muscle-powered biological machines,* Nature Protocols **12**, 519 (2017).

[43] J. Rouwkema, B. F. Koopman, C. A. van Blitterswijk, W. J. Dhert, and J. Malda, *Supply of Nutrients To Cells in Engineered Tissues,* Biotechnology & Genetic Engineering Reviews **26**, 163 (2009).

[44] D. Neal, M. S. Sakar, L.-L. S. Ong, and H. Harry Asada, *Formation of elongated fascicle-inspired 3D tissues consisting of high-density, aligned cells using sacrificial outer molding,* Lab Chip **14**, 1907 (2014).

[45] S. C. Millik, A. M. Dostie, D. G. Karis, P. T. Smith, M. McKenna, N. Chan, C. D. Curtis, E. Nance, A. B. Theberge, and A. Nelson, *3D printed coaxial nozzles for the extrusion of hydrogel tubes toward modeling vascular endothelium,* Biofabrication **11**, 045009 (2019).

[46] D. L. Cohen, E. Malone, H. Lipson, and L. J. Bonassar, *Direct Freeform Fabrication of Seeded Hydrogels in Arbitrary Geometries,* Tissue Engineering **12**, 1325 (2006).

[47] W. Wu, A. Deconinck, and J. A. Lewis, *Omnidirectional printing of 3D microvascular networks,* Advanced Materials **23**, 178 (2011).

[48] A. J. Engler, M. A. Griffin, S. Sen, C. G. Bönnemann, H. L. Sweeney, and D. E. Discher, *Myotubes differentiate optimally on substrates with tissue-like stiffness: Pathological implications for soft or stiff microenvironments,* Journal of Cell Biology **166**, 877 (2004).

[49] M. Costantini, S. Testa, E. Fornetti, A. Barbetta, M. Trombetta, S. M. Cannata, C. Gargioli, and A. Rainer, *Engineering Muscle Networks in 3D Gelatin Methacryloyl Hydrogels: Influence of Mechanical Stiffness and Geometrical Confinement,* Frontiers in Bioengineering and Biotechnology **5**, 22 (2017).

[50] S. J. Tapscott, R. L. Davis, M. J. Thayer, P. F. Cheng, H. Weintraub, and A. B. Lassar, *MyoD1: A nuclear phosphoprotein requiring a Myc homology region to convert fibroblasts to myoblasts,* Science **242**, 405 (1988).

[51] W. E. Wright, D. A. Sassoon, and V. K. Lin, *Myogenin, a factor regulating myogenesis, has a domain homologous to MyoD,* Cell **56**, 607 (1989).

[52] M. G. Cusella-De Angelis, G. Lyons, C. Sonnfno, L. De Angelis, E. Vifvarelli, K. Farmer, W. E. Wright, M. Molifnaro, M. Bouchè, M. Buckfngham, and G. Cossu, *MyoD, Myogenein Independent Differnentiation of Primordial Myoblasts in Mouse Somites,* Journal of Cell Biology **116**, 1243 (1992).

[53] P. Bajaj, B. Reddy, L. Millet, C. Wei, P. Zorlutuna, G. Bao, and R. Bashir, *Patterning the differentiation of C2C12 skeletal myoblasts.* Integrative Biology **3**, 897 (2011).

[54] J. B. Miller, *Myogenic programs of mouse muscle cell lines: Expression of myosin heavy chain isoforms, MyoD1, and myogenin,* Journal of Cell Biology **111**, 1149 (1990).

[55] S. Schiaffino, A. C. Rossi, V. Smerdu, L. A. Leinwand, and C. Reggiani, *Developmental myosins: Expression patterns and functional significance,* Skeletal Muscle **5**, 1 (2015).

[56] O. Delbono, *Myosin - still a good reference for skeletal muscle fibre classification?* Journal of Physiology **588**, 9 (2010).

[57] D. M. Brown, T. Parr, and J. M. Brameld, *Myosin heavy chain mRNA isoforms are expressed in two distinct cohorts during C2C12 myogenesis,* Journal of Muscle Research and Cell Motility **32**, 383 (2012).

[58] A. M. De Jesús and E. A. Sander, *Observing and quantifying fibroblast-mediated fibrin gel compaction,* Journal of Visualized Experiments , 50918 (2014).

[59] Z. X. Khoo, J. E. M. Teoh, Y. Liu, C. K. Chua, S. Yang, J. An, K. F. Leong, and W. Y. Yeong, *3D printing of smart materials: A review on recent progresses in 4D printing,* Virtual and Physical Prototyping **10**, 103 (2015).

[60] P. Datta, B. Ayan, and I. T. Ozbolat, *Bioprinting for vascular and vascularized tissue biofabrication,* Acta Biomaterialia **51**, 1 (2017).

[61] B. Babenko, Ming-Hsuan Yang, and S. Belongie, *Visual tracking with online Multiple Instance Learning,* in *2009 IEEE Conference on Computer Vision and Pattern Recognition* (IEEE, 2009) pp. 983–990.

[62] T. D. Schmittgen and K. J. Livak, *Analyzing real-time PCR data by the comparative CT method,* Nature Protocols **3**, 1101 (2008).

[63] L. Ricotti, B. Trimmer, A. W. Feinberg, R. Raman, K. K. Parker, R. Bashir, M. Sitti, S. Martel, P. Dario, and A. Menciassi, *Biohybrid actuators for robotics: A review of devices actuated by living cells,* Science Robotics **2**, eaaq0495 (2017).

[64] J. Yin, M. Yan, Y. Wang, J. Fu, and H. Suo, *3D Bioprinting of Low-Concentration Cell-Laden Gelatin Methacrylate (GelMA) Bioinks with a Two-Step Cross-linking Strategy,* ACS Applied Materials and Interfaces **10**, 6849 (2018).

[65] B. Duan, L. A. Hockaday, K. H. Kang, and J. T. Butcher, *3D Bioprinting of heterogeneous aortic valve conduits with alginate/gelatin hydrogels,* Journal of Biomedical Materials Research - Part A **101 A**, 1255 (2013).

[66] M. G. Yeo, J. S. Lee, W. Chun, and G. H. Kim, *An Innovative Collagen-Based Cell-Printing Method for Obtaining Human Adipose Stem Cell-Laden Structures Consisting of Core-Sheath Structures for Tissue Engineering,* Biomacromolecules **17**, 1365 (2016).

[67] Q. Pi, S. Maharjan, X. Yan, X. Liu, B. Singh, A. M. van Genderen, F. Robledo-Padilla, R. Parra-Saldivar, N. Hu, W. Jia, C. Xu, J. Kang, S. Hassan, H. Cheng, X. Hou, A. Khademhosseini, and Y. S. Zhang, *Digitally Tunable Microfluidic Bioprinting of Multilayered Cannular Tissues,* Advanced Materials **30**, 1706913 (2018).

[68] S. Hong, J. S. Kim, B. Jung, C. Won, and C. Hwang, *Coaxial bioprinting of cell-laden vascular constructs using a gelatin-tyramine bioink,* Biomaterials Science **7**, 4578 (2019).

[69] T. H. Qazi, D. J. Mooney, M. Pumberger, S. Geißler, and G. N. Duda, *Biomaterials based strategies for skeletal muscle tissue engineering: Existing technologies and future trends,* Biomaterials **53**, 502 (2015).

[70] G. Kim, S. Ahn, Y. Kim, Y. Cho, and W. Chun, *Coaxial structured collagen-alginate scaffolds: Fabrication, physical properties, and biomedical application for skin tissue regeneration,* Journal of Materials Chemistry **21**, 6165 (2011).

[71] W. Jia, P. S. Gungor-Ozkerim, Y. S. Zhang, K. Yue, K. Zhu, W. Liu, Q. Pi, B. Byambaa, M. R. Dokmeci, S. R. Shin, and A. Khademhosseini, *Direct 3D bioprinting of perfusable vascular constructs using a blend bioink,* Biomaterials **106**, 58 (2016).

[72] U. Hersel, C. Dahmen, and H. Kessler, *RGD modified polymers: Biomaterials for stimulated cell adhesion and beyond,* Biomaterials **24**, 4385 (2003).

IV

Skeletal muscle tissue bio-actuators

Parts of Section 2 of this chapter have been published in *Adv. Mater. Technol.* **2019**, 4, 1800631[1], in *Biomimetic and Biohybrid Systems*. Living Machines **2018**. Lecture Notes in Computer Science, vol 10928[2], and in *Biomimetic and Biohybrid Systems*. Living Machines **2019**. Lecture Notes in Computer Science, vol 11556[3]. Section 3 of this chapter can be found as pre-print in *biorXiv*[4].

1. Introduction and state of the art

Engineering of bio-hybrid robots, which combine biological entities with artificial materials, has found in muscle-based bio-actuators excellent candidates towards the development of complex devices, encountering a wide variety of applications during their evolution. Recent advances in 3D bioprinting and tissue engineering have opened the possibility of mimicking native tissue[5–8] by the biofabrication of three-dimensional bio-actuators that can act as muscle models, offering opportunities for studies in muscle development or muscular diseases, thus avoiding the need for animal models that can carry ethical issues. Moreover, their use as force measurement platforms have brought them to applications ranging from biosensing[9] to drug screening platforms[8, 10], as they can provide information about contraction kinetics of three-dimensional muscle tissue, as well as their maturation, adaptability or self-healing[11–14].

Muscle-based bio-actuators usually consist of a 3D bio-engineered skeletal muscle strip or ring surrounded by two or more cantilevers that provide mechanical support to assist in the differentiation and maturation of these cells[15]. Different models employ cantilevers that mimic muscular structures, using their deflection to give estimates of the forces generated during tissue formation and compaction, as well by active contractions[16, 17]. Electrical or optical stimulation of 3D-bioengineered muscle tissues can give insightful information about the contraction dynamics and the generation of force, which can then be used to analyze how specific drugs affect these parameters[10, 15], provide useful data for tissue engineering and, in particular, for the fabrication of relevant skeletal tissue models.

The integration of living tissue into bio-hybrid robotic devices has reported exciting outcomes in terms of controllability, sensing and response to dynamic environmental stimuli[18]. However, out of all the outstanding properties that are attributed to bio-hybrid actuators, which include self-healing, biosensing, or adaptability, among others, very little of them have been extensively studied. In particular, Raman *et al.* analyzed damage and healing of bio-bots by the addition of fresh myoblasts[11] and their increase in force after applying different stimulation regimes[13]. Moreover, Orfanos *et al*. studied the effect of *in vitro* exercise in the breaking of sarcomeres in 2D cultures[14]. Although the use of biochemical cues[19–21], topographical features[22–24] and 3D-printed molds [17, 25] have proven to be suitable and effective techniques for the fabrication of bio-actuators, the field is still lacking a technique that can increase its versatility, speed and scalability.

Both forces and contraction kinetics can provide valuable information in the study of muscle functionality. For instance, there is a wide range of myopathies, neuromuscular diseases or autoimmune diseases that can affect skeletal muscle tissue, and they could all be very heterogeneous, showing differences from patient to patient[26]. Consequently, there is a need for human tissue models to perform efficient screenings of different treatments by measuring physiological parameters, such as force and contraction kinetics of diseased tissue[8]. Three-dimensional models of skeletal muscle tissue have been mainly focused on murine primary cells or cell lines, with increasing applications in the hybrid bio-robotics field, although some cases have been dedicated to pharmacological testing or biomolecule monitoring[9, 10]. Nonetheless, bio-engineering of human muscle cells has received some attention, yet most of the studies have primarily aimed at studying the effects of mechanical stretching[27], cycling[28] or cell density[27]. In this regard, related to the study of forces in human skeletal muscle tissue, Madden *et al.* successfully developed a human myobundle platform from myoblasts, focusing on obtaining clinically relevant responses and analyzing the tetanic and twitch behaviors of their models[29].

Complex muscle models usually contain more than one type of cells in the form of co-cultures, usually to mimic the neuromuscular junction (NMJ) of native tissue[30]. Some bio-actuators have started to include motor neurons[31–34], although mainly based on murine cell lines. Nonetheless, some groups have started to use human-derived cells. For instance, Osaki *et al.* used induced pluripotent stem cell (iPSC)-derived muscle cells to create a microphysiological 3D model of muscle tissue that included optogenetic motor neurons[8, 35], and other groups have followed similar approaches[26, 36]. However, although many of these platforms offer the possibility of measuring muscle force thanks to the deflection of micro-cantilevers, the study of the kinematics of contraction has not received much attention.

Moreover, studies on cell aging, despite being of great importance for muscle tissue research, have not been deeply investigated in 3D models. Senescence, defined as an irreversible cell cycle arrest during aging[37], has been found to have a primary role in muscle regeneration in inflammatory myopathies[38] and chronically aged skin[37, 39]. Senescent cells secrete a variety of paracrine molecules, called senescence-associated secretory phenotype (SASPs) factors, which include pro-inflammatory cytokines, growth factors and proteases, among others, and can induce aging features to surrounding tissues[40, 41]. Tumor necrosis factor α (TNF-α) is the best known SASPs component in skeletal muscle tissues, whose expression increases with age. This cytokine has been described as one of the main drivers for the known morphological changes that take place in senescent muscles[42–44], and has been linked to the development of sarcopenia affecting satellite cells[45]. In mouse cell lines, differences in TNF-α have been related to changes in calcium transients[46, 47] and reduction of contractile force[44]. Furthermore, *in vitro*, this cytokine is known to have an effect on myogenesis inhibition[48] and cause atrophy[49], as demonstrated in C2C12 cell lines, as well as having an important effect in muscle regeneration after injury *in vivo*[50]. Sarcopenia has also been linked to the presence of macrophage-secreted TNF-α in men during aging[51]. Moreover, the study of aging in skeletal muscle tissue has also relevant applications in the cosmetic field, since skin manifestations of aging have been linked to physiological and functional changes of subcutaneous tissues, such as adipose tissue and skeletal facial muscle[51, 52]. Hence, by treating healthy human myocytes with this cytokine, it might be possible to mimic the morphological and functional characteristics of aged muscle in order to obtain a more accurate model for screening studies that account for the subject's age.

In the present chapter, we report fully functional 3D-bioprinted bio-actuators that can be used as a force measuring platform. We prove that this bio-actuator also represents a relevant tissue model of murine, human and aged human muscle tissue. Besides, these platforms are easy to fabricate, versatile and of high-throughput, unlike many other micro-platforms in the literature. As proof of concept, we carry out several studies to evaluate this muscle tissue models. First, by studying the evolution of force and dynamic gene expression of murine muscle constructs depending on different exercising protocols, we prove that 3D-bioprinted bio-actuators can adapt in multiple ways by modifying the stimulation frequencies and stiffness of mechanical constraints. Moreover, we 3D-bioengineer biological actuators based on human myoblasts to study its feasibility as a drug-testing platform for human diseases, by analyzing not only the force generation, but also the contraction kinetics under different types of stimulation. We validate the capabilities of this drug testing platform by the treatment of human tissue constructs with TNF-α, thus obtaining a model of skeletal muscle tissue affected by aging (senescence-like), characterized by a decrease in force generation, cell diameter and disruption of cell sarcolemma. Finally, as a proof of concept, we verify the 3D-printed testing platform by evaluating the efficacy of a cosmetic ingredient in development, Argireline® Amplified peptide. In this study, we evaluate its impact in both aged and non-aged 3D muscle models, focusing on its relaxing effects after electrical-stimulation-induced muscle contractions. Overall, these stud-

ies demonstrate the versatility of this bio-actuator to act as a force measurement platform for both murine and human muscle for the study of muscle functionality during processes like adaptability or aging, which can also have applications for drug screening in the biomedical or cosmetic fields.

2. Adaptability of 3D-bioengineered skeletal muscle tissue upon simulated exercise

2.1. Objectives

In the previous chapter, we demonstrated the possibility of using 3D bioprinting to fabricate functional muscle tissue that retained native capabilities, such as the ability to contract upon electrical stimulation. These results could be of importance for muscle regeneration after injury, but it also finds numerous applications in bio-hybrid robotics and disease modeling. The applications of three-dimensional muscle tissue in fully untethered bio-hybrid robotics will be considered in Chapter V. However, before diving into this topic, it is essential to discuss the capabilities of bio-actuators as powerful tools for studies in muscle development or drug testing.

In this section, we will discuss the fabrication of a multi-material hybrid bio-actuator platform based on skeletal muscle tissue, by using the 3D bioprinting technique. This bio-actuator consists of two PDMS posts surrounded by a functional muscle tissue ring that can be activated by electrical pulse stimulation (EPS) to contract and bend the posts, simulating an actual muscle-tendon unit. The deflection of these cantilevers can be used to measure the force applied by the muscle, obtaining a force measurement platform. We hypothesize that this platform could be of interest to perform basic studies in muscle development, which could be useful for applications in muscle tissue engineering and to understand the capabilities of bio-hybrid robots, thanks to its high throughput, ease of fabrication and fast prototyping. As adaptability to system requirements in one of the key features of muscle-based bio-robots, we performed a study on the adaptability of muscle tissue upon short-term and long-term exercising with EPS.

Therefore, the objectives of this section are the following: i) to demonstrate the fabrication and functionality of 3D bio-actuators based on muscle tissue; ii) to design a force measurement protocol based on optical microscopy and computer vision techniques; iii) to design and characterize a stimulation setup that is safe for long-term EPS in sterile environment; iv) to study the short-term and long-term adaptability of the bio-actuators according to different frequencies; and v) to investigate the effect of the stiffness of the PDMS posts by modifying its curing agent/base ratio, and considering "soft" and "stiff" conditions. To fulfill the last two objectives, the total forces exerted by the muscle tissue, as well as their changes in expression of related proteins, namely different isoforms of myosin heavy chain I and II, were examined in detail.

2.2. Results and discussion

Characterization of PDMS

As it was mentioned in the objectives, one of the main purposes of this study was the fabrication of a bio-actuator that could be used as a force measurement platform of the contractions of the tissue, so that this hybrid device could be turned into a tool to study the development and maturation of

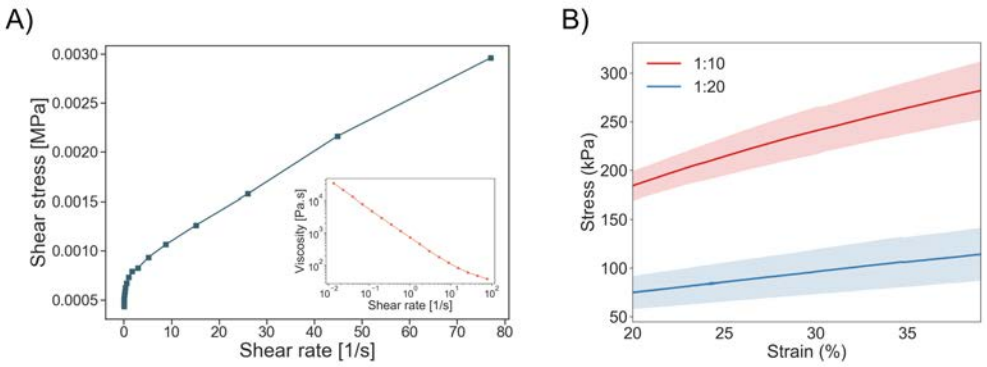

Figure 4.1: Characterization of PDMS. A) Rheological characterization of PDMS in a shear stress vs. shear rate flow ramp mode and (inset) viscosity in terms of the sear rate. B) Tensile mechanical characterization of PDMS after curing at 37 °C for different crosslinking ratios.

skeletal muscle tissue, as well as a drug screening platform for muscle-related diseases. The bioprinting of functional muscle tissue was presented in the previous chapter, and therefore, the printing of PDMS as anchoring posts, as well as the simultaneous multi-material printing, remained to be demonstrated.

The PDMS ink was mechanically and rheologically characterized (Figure 4.1). The PDMS used for this purpose was a variation of the common version used for micro-fluidic applications and mold casting, which is fluid at room temperature. This PDMS ink, termed SE1700, contains fumed silica nanoparticles, which increase its viscosity, making it completely solid at room temperature and with ideal rheological properties for 3D printing. These particles can move inside the polymeric network and rearrange their positions due to the shear stress felt in the nozzle. Due to this, a pseudo-plastic or shear-thinning effect emerges, and the viscosity of the material decreases when the shear stress increases (Figure 4.1A). This allows the material to easily flow when the pressure is increased, but still retains its final shape once the pressure has been removed and the polymeric network and the nanoparticles have come back to their initial positions. A Herschley-Bulkley fluid model is a generalized model of a non-Newtonian fluid with pseudo-plastic and Bingham characteristics that can capture the behavior of PDMS, following the equation $\tau = \tau_0 + k\gamma^n$, where τ is the shear stress, τ_0 is the yield stress, γ is the shear rate, k is the consistency index and n is the shear-thinning parameter. A fitting to this model gave the following results: $\tau_0 = 524 \pm 24$ Pa, $k = 123 \pm 18$ Pa·s^n, and $n = 0.68 \pm 0.03$. These results display the presence of a strong yield stress, transforming this material into a Bingham pseudo-plastic. Theoretically, for these kinds of materials, when $\tau < \tau_0$, it behaves as a solid, explaining the high pressures that are necessary to 3D print it and its stability of the constructs. When $\tau > \tau_0$, the material can flow with a strong shear-thinning behavior characterized by the parameter n.

PDMS is a material composed of two elements, a base and a curing agent that induces the crosslinking of PDMS at high temperatures. The higher the amount of curing agent present in the mixture, the higher the Young's modulus of the crosslinked material. At the same time, the higher the temperature used for curing, the higher the Young's modulus. In this particular case, we were interested in finding a single-step process for the fabrication of the hybrid bio-actuators, and therefore the PDMS posts should not be fabricated beforehand and cured at high temperature before 3D bioprinting the cell-laden hydrogel, as it would add more unnecessary steps to the fabrication. For that purpose, the 3D-printed posts were slowly cured at 37 °C in a cell incubator during the differentiation process of the myoblasts. Figure 4.1B shows a tensile mechanical characterization of PDMS with two different

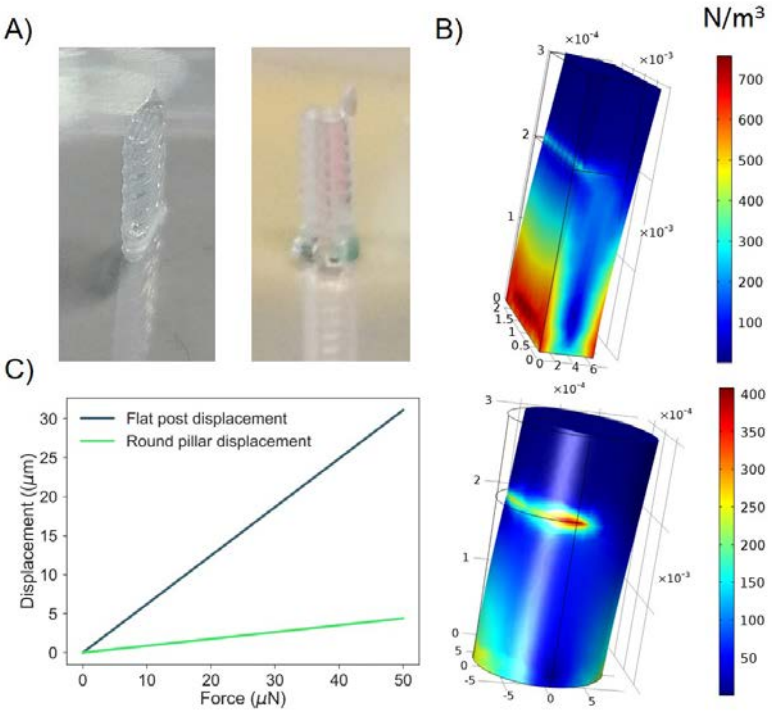

Figure 4.2: Optimization of the 3D-printed posts. A) Two images of posts designed as a flat slab (left) and a hollow pillar (right). B) Stresses generated by a simulated edge force on the two designs, leading to deformation. C) Displacement of the top part of the post for different applied forces and for each design. Adapted with permission from [2].

curing agent/base ratios, slowly crosslinked at 37 °C in an incubator, in order to mimic the exact same conditions of the experimental setup. A linear fitting on the 20-40% region of the strain rate revealed Young's modulus of the range of 622 kPa for the "stiff" condition (1:10 ratio) and 206 kPa for the "soft" condition (1:20 ratio).

Modeling and optimization

Optimization of the post design was carried out by the finite element analysis simulations, considering two different designs: i) a thin flat slab; and ii) a circular hollow pillar. Both structures were tested beforehand in the 3D bioprinter (Figure 4.2A), in order to ensure their feasibility and stability. For instance, it was found that a flat slab of less than 500 μm of width was not stable enough after several layers of printing, so the minimum thickness had to be set to 500 μm. On the other hand, a hollow pillar also had an intrinsic limitation due to stability, and the minimum possible external diameter was of 6 mm. However, due to its hollowness and the small width of their walls (also 500 μm), it might still offer a low enough geometrical stiffness for the tissue to deform it.

Details of the simulations are reported in Figure 4.2. Both structures, taking into account the fabrication limitations just mentioned, were designed within with a total height of 3 mm and, for the flat slab, a lateral length of 2 mm. To simulate the loading exerted by a tissue during contraction, a force sweep in the range 0-50 μN, which were values of force in the expected range according to previous publications in the field[13], were applied as a total load at a distance of 2 mm. The displacement of the highest tip of each geometry was plotted as a function of the load, as shown in Figure 4.2C, demonstrating that the flat slab was the most optimal geometry, as it would offer the most sensitive results in the considered range.

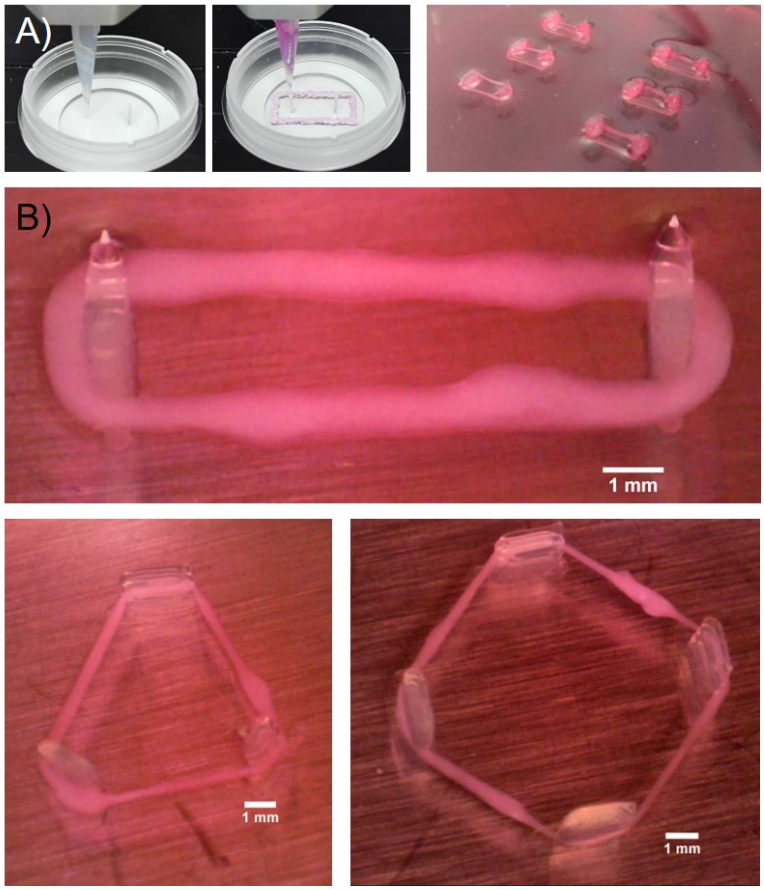

Figure 4.3: Versatility and scalability of 3D bioprinting to fabricate bio-actuators. A) 3D bioprinting process of a bio-actuator (left) and six bio-actuators printed in parallel (right). B) Several examples of bio-actuators formed out of 2, 3 or 4 posts. Adapted with permission from [1].

In order to obtain an analytical formula that allowed us to transform displacement values into force measurement, we used Euler-Bernoulli's beam bending theory to estimate the tension applied by the tissue to the posts. We approximated the tension to be a singular force concentrated on a point at a height a from the base of the post. Beam bending equations tell us that, for a post of height h, the displacement has the following form:

$$\begin{aligned} y(x) &= \frac{Px^2}{6EI_z}(3a - x) \quad \text{for } 0 < x < a \\ y(x) &= \frac{Pa^2}{6EI_z}(3x - a) \quad \text{for } a < x < h, \end{aligned} \tag{4.1}$$

where P is the applied force, E is the Young's modulus of the PDMS, I_z is the second moment of area around the z-axis, a is the height at which the tissue is pulling from and $y(x)$ is the displacement of the tissue at height x. If we assume that the displacement of the post is measured at the same position where the tissue is pulling, that is, $x = a$, then we can simplify the formula to:

$$P = \frac{3EI_z y(a)}{a^3} \tag{4.2}$$

The second moment of area around the z-axis for this geometry was calculated as:

$$I_z = \frac{w^3 L}{12}, \tag{4.3}$$

where $w = 0.64$ mm and $L = 2$ mm were the two lateral dimensions of its base.

3D bioprinting of bio-actuators

In order to demonstrate the versatility of the process to produce bio-actuators in a fast manner, we designed different scenarios of application. Figure 4.3A, shows a mass production of six bio-actuators, produced in the same process and in a single step, showing the scalability options of this technique. Likewise, Figure 4.3B shows different cases, as for instance bio-actuators made out of 2, 3 or 4 posts, which could also be easily located at different positions, and even have different widths, so that the geometrical stiffness could be altered in different sections of the bio-actuator to study differential or local maturation of the tissue due to the geometrical constrains. For our following studies, focused on the adaptability process of skeletal muscle cells in a three-dimensional environment, we decided to use the two-post system as a minimal model to perform the desired studies.

One of the first issues to consider during 3D bioprinting is the biocompatibility of the process. As it was mentioned before, in order to maintain the process integration of the approach PDMS was slowly cured at 37 °C in a cell incubator during the myoblast differentiation process. Due to this temperature-assisted chemical crosslinking, the diffusion of toxic by-products into the cell medium was a possibility. However, Figure 4.4B shows how the viability of the three-dimensional cell culture was high after 48 h of culture, both with and without posts, suggesting that the simultaneous crosslinking of PDMS did not alter the viability of the cells. Moreover, we can see how the post-printing viability (24 h) was also high, around 90%, indicating that the shear stress suffered by the cells during the bioprinting process was not harmful thanks to the shear-thinning properties of the materials used.

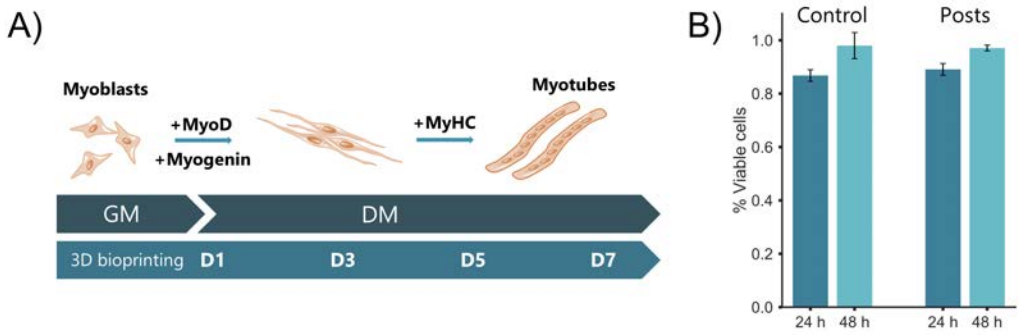

Figure 4.4: Differentiation and maturation of skeletal muscle tissue in bio-actuators. A) Schematic of the differentiation and maturation process of the 3D-bioprinted skeletal muscle tissue, showing the upregulation or downregulation of several genes that are involved in the process. B) Live/Dead results for post samples and control samples (without post), demonstrating that the simultaneous curing of PDMS is not harmful for the cells. Adapted with permission from [1].

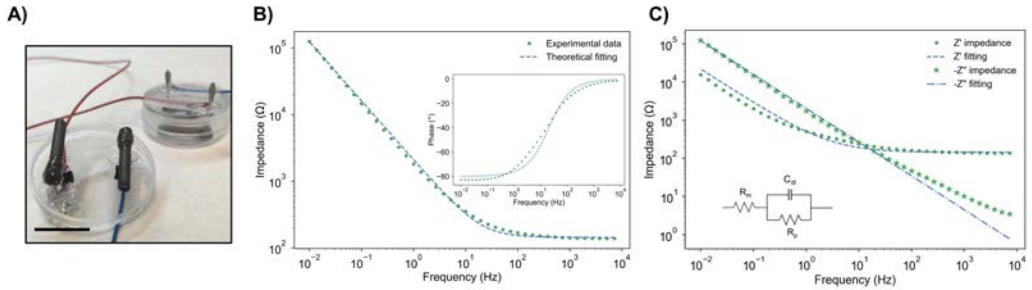

Figure 4.5: Characterization of the carbon-rod stimulation setup. A) Picture of the home-made carbon electrodes. Scale bar: 12 mm. B) Bode plot of the carbon electrodes with phase plot as inset. C) Plot of the real and imaginary impedance, Z' and Z'', with their respective fittings according to the equivalent circuit (inset). Adapted with permission from [2].

IV

Characterization of stimulation setup

A home-made electrode setup for safe and long-term stimulation was designed and fabricated (Figure 4.5A). This setup consisted on two carbon rods attached to the cover of a Petri dish that could be closed to ensure sterility during the stimulation in the inverted microscope, as carbon electrodes have been shown to be safe for long-term stimulation[53, 54]. Impedance spectroscopy was performed, and the results displayed in Figure 4.5B and 4.5C. The bode plot was fitted to the equivalent circuit (inset schematic in Figure 4.5C), consisting on a series resistance (R) that corresponds to the resistance of growth medium and cables, together with a pseudo-capacitance (represented by a constant phase element, C_{dl}) to account for the double-layer capacitance at the electrode interface and a polarization resistance (R_0) in parallel. The fitting to the bode plot was accurate and gave results of $R_m = 143 \pm 3\ \Omega$, $C_{dl} = 9.4 \cdot 10{-}5 \pm 0.2 \cdot 10^{-5}\ \mathrm{F} \cdot \mathrm{s}^{n-1}$, and $n = 0.887 \pm 0.009$. The polarization resistance, R_p, was too large to be fitted by this model at this frequency range. This indicates that: i) the electrodes effectively behaved as having a very small medium resistance in series with a pseudo-capacitance; and ii) the reactions that occurred at the interface did not cause severe corrosion or hydrolysis (since the polarization resistance was too high). However, the phase of the impedance (inset of Figure 4.5B) and Z' and Z'' were not perfectly fitted, which might indicate small deviations of this model, but it was observed that the trend was generally well maintained.

Therefore, these results demonstrated the the carbon electrodes were not prone to corrosion, specially if short-lived pulses were applied, making them ideal for long-term stimulation. Moreover, as the lid could be completely closed, sterility was ensured if the setup was assembled inside a biosafety cabinet and the electrodes properly sterilized prior stimulation.

Force measurement

The versatility of the 3D bioprinting technique allowed a fast prototyping and fabrication of multi-material systems in a very short time and scalable manner. In this case, our proof-of-concept design consisted on two PDMS posts surrounded by a ring of cell-laden hydrogel (Figure 4.6A). The process of 3D bioprinting of a bio-actuator consisted on the 3D printing of the PDMS posts followed by the 3D bioprinting of the myoblast-laden hydrogel, in a single step. Then, a solution of 5 U/mL of thrombin was added to the dish for 5 min at room temperature to crosslink fibrinogen and growth medium (GM) supplemented with 6-aminocaproic acid (ACA) as added (see Chapter III for more details regarding 3D bioprinting of skeletal muscle tissue). After three days in GM, the tissue had already shrunk and was in contact with the posts due to the passive forces that compact the tissue, and the medium was switched to differentiation medium (DM), supplemented with ACA and

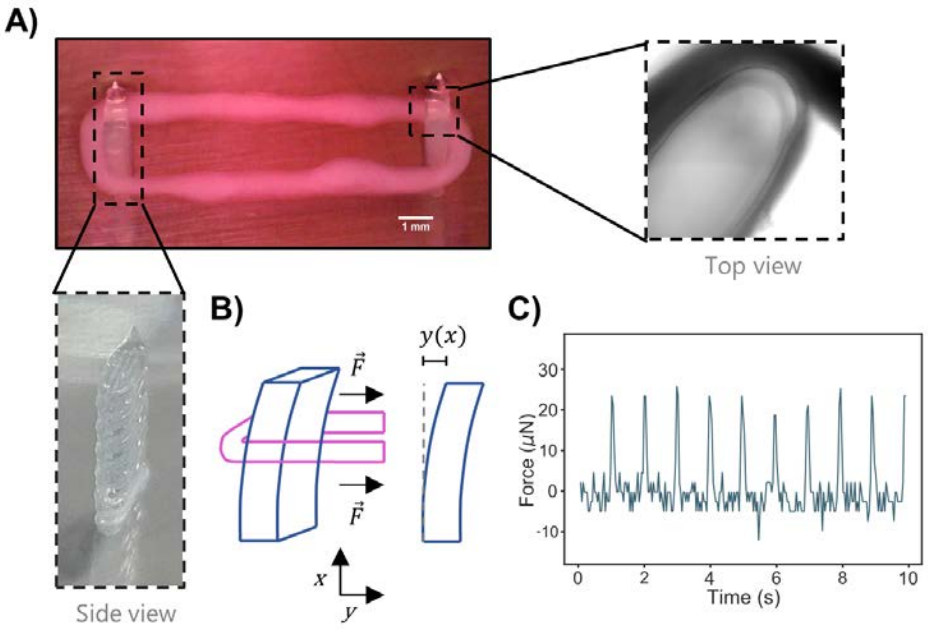

Figure 4.6: Principle of force measurement of bio-actuators. A) The 3D-bioprinted bio-actuator, based on two PDMS posts and skeletal muscle tissue around it. B) When EPS is applied, the tissue can contract and produce a displacement in the posts, which can be measured to compute the force generated. C) Force measurement during a 1 Hz stimulation of a bio-actuator. Adapted with permission from [1].

insulin-like growth factor 1 (IGF-1). When the tissue was mature and functional, EPS could generate contractions to bend the two PDMS posts. The displacement of the posts could be correlated to forces by using the classical Euler–Bernoulli beam bending theory (Figure 4.6B and Equation 4.2) and this relationship allowed us to compute the force exerted by the tissue, as can be observed in Figure 4.6C for a 1 Hz stimulation.

A characterization protocol based on computer vision techniques was developed to characterize the performance of the bio-actuators (in terms of force generation) in order to better understand their behavior. During electrical stimulation, the samples were being recorded with an inverted microscope with a micrometric z-axis stage. Firstly, the exact position of the tissue with respect to the bottom of the Petri dish was calculated by performing a z-stack imaging. Secondly, the video was focused at the point of the applied force to record the deformations of the post (Figure 4.7A). After acquisition, a home-made Python script based on image processing and computer vision algorithms was used to track the displacement of the posts. Briefly, a Sobel operator was applied to find the edges of the image, which were binarized afterwards (Figure 4.7A). The threshold of the Sobel operator could be modified on-line in order to account for different brightness in the videos. The user was then asked to draw a straight, perpendicular line, to one of the outer edges of the post (Figure 4.7B). A Bresenham's line algorithm was then applied to approximate the drawn line to a set of pixels. As depicted in Figure 4.7C, the intersection between the edge pixels (gray squares) with the Bresenham's approximation (pink squares) would define the location of the edge. A profile along the Bresenham's line would reveal a square jump at the position of the edge (as in a binarized image, the only two possible pixel intensity values are 0 and 255). This profile was then fitted to a Gaussian function and its mean was computed. For each frame of the video, the line coordinates were kept constant, while the position of the edge was moving with the contractions. Time evolution of the Gaussian means of the profile projection could be used to compute the displacement of the posts due to the contractions and, by using Equation 4.2, the force generated by the muscular tissue could be measured.

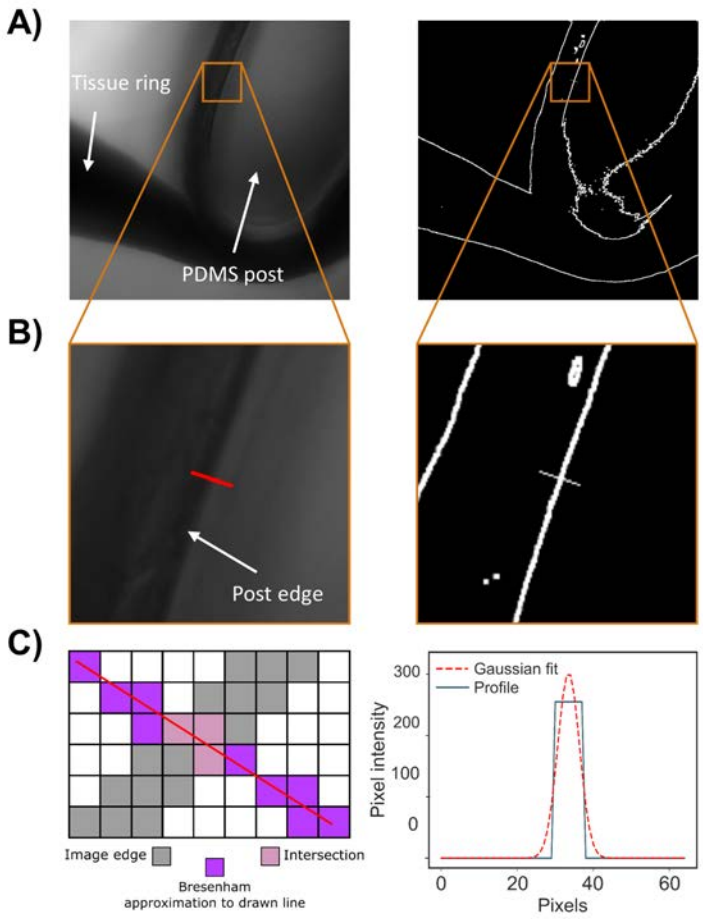

Figure 4.7: Protocol for force measurement of bio-actuators based on computer imaging. A) Left: Image from a movie during an electrical stimulation of a bio-actuator, where the tissue (darker section) and the post (lighter section) are shown. Right: Binarization after edge detection of the left image. B) Left and right: zoomed-in sections of the respective images where the user has drawn a line. C) Left: schematic representing the Bresenham's line algorithm. Right: profile along the line showing the detection of the edge and the fitting to a Gaussian function. Adapted with permission from [2].

Independently of the force reached by the stimulation protocol, we found that its value could be modulated by changing the pulse width and applied electric field (Figure 4.8A and B). The inverse relationship between pulse width and applied voltage or current is already well known in the literature[55]. In our case, we could modulate the amount of force generated, within a specific range (established by the degree of maturation of the bio-actuator), by changing these parameters. In particular, we noticed that the maximum values of force generation could be achieved with a pulse width around 1 ms. For larger values, however, the maximal force saturated to the same value for every voltage. This is hypothesized to be an effect of the strong depolarization suffered by the myotubes, which decrease their resting time and Ca^{2+} cannot be completely replenished[56]. In general, this modulation is likely due to the recruitment of a different amount of myotubes when low voltages or short-time currents are applied, and it could lead to a higher degree of force controllability of bio-hybrid actuators, independently of being previously exercised or not. Moreover, during the course of 1 h, we discovered that the force kept increasing with time (i.e. from 10 μN to 25 μN in Figure 4.8C), showing short-term modulation of the force output.

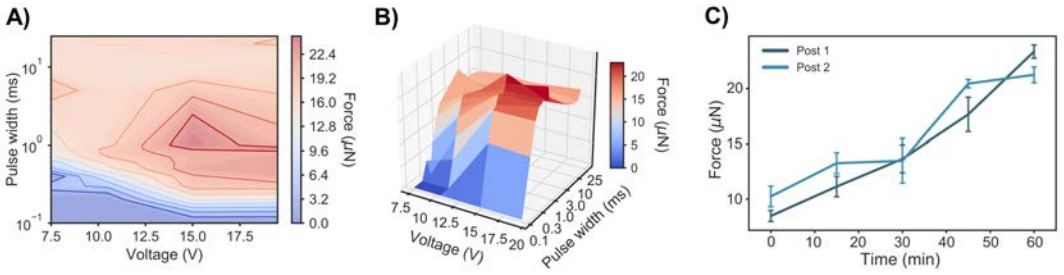

Figure 4.8: Modulation of the force through stimulation parameters and short-term adaptability. A) Heatmap of the force generated by a bio-actuator when the pulse width and the voltage are modified. B) Surface plot of the force generated vs the voltage and pulse width, showing how modulation can be achieved from 0 μN to the peak force, 25 μN. C) Force measurement for both posts of a bio-actuator in terms of time, showing short-term adaptability. Adapted with permission from [1] and [2].

Force modulation and adaptability after long-term training

After observing the effects in performance of a short-term stimulation, we analyzed the effects in the long term by changing parameters like the stimulation frequency and the stiffness of the mechanical constraints. For that purpose, we designed stimulation protocols consisting on 1 h EPS for 4 days, starting on day 6 and finishing on day 9 of differentiation, as illustrated in the scheme of Figure 4.9A. All stimulations were carried out in an inverted microscope with culture conditions and using the sterile custom-made, carbon-based stimulation setup. We chose day 6 of differentiation as the starting point since it was the first day where we could observe contractions strong enough to move the posts. Figure 4.9B shows the force at the end of a stimulation session ($t = 60$ min) for four consecutive days, for a set of four frequencies (0.1 Hz, 1 Hz, 5 Hz and 10 Hz) and for two different post stiffnesses (stiff and soft, achieved by changing the relative curing agent ratio of PDMS). Figure 4.9C shows the fold change in force, F^{D9}/F^{D6} , where F^{D6} and F^{D9} are the forces at the end of the first and last stimulation sessions, respectively. We can see that not all stimulation frequencies resulted in steady increases of force. For stiff posts, only very low frequencies (0.1 Hz) could produce a significant increment, while for soft posts, medium to low frequencies (0.1 Hz and 1 Hz) created a 2-fold increment.

By comparing the force output of a trained sample with a control (non-stimulated) sample, we could better understand how this force modulation was related to the stiffness of the mechanical constraints and the applied frequency. We defined the control sample as a bio-actuator that was not trained during the 4 days and, on the last day, was stimulated for the first time (Figure 4.10A). Initially (at $t = 0$ min), the control bio-actuator would exert a certain force, called $F^{D9}_{ctrl,0}$. After 60 min of continuous 1 Hz stimulation, the force would increase up to $F^{D9}_{ctrl,60}$. We later compared the improvement achieved by the different training protocols at day 9 of stimulation (F^{D9}_{train}) by comparing their force output with a control sample that was never stimulated before ($F^{D9}_{train}/F^{D9}_{ctrl,0}$) and with a sample that was simply stimulated once for 60 min on the last day ($F^{D9}_{train}/F^{D9}_{ctrl,60}$). In the first case, we would understand if the training was effective in increasing the force beyond the values of a non-trained bio-actuator. In the second case, we would know if the training was worthwhile, as it could be the case that the control bio-actuator would achieve the same values as their trained counterparts after only 60 min. Figures 4.10B and 4.10C show these results for stiff and soft posts, respectively.

The greatest improvement was observed for softer mechanical constrains, reaching values as high as 8-fold, compared to increments of 2.5-fold for stiff conditions. However, even though there was a clear enhancement in force generation for all frequencies, it was not always practical to apply a 4-

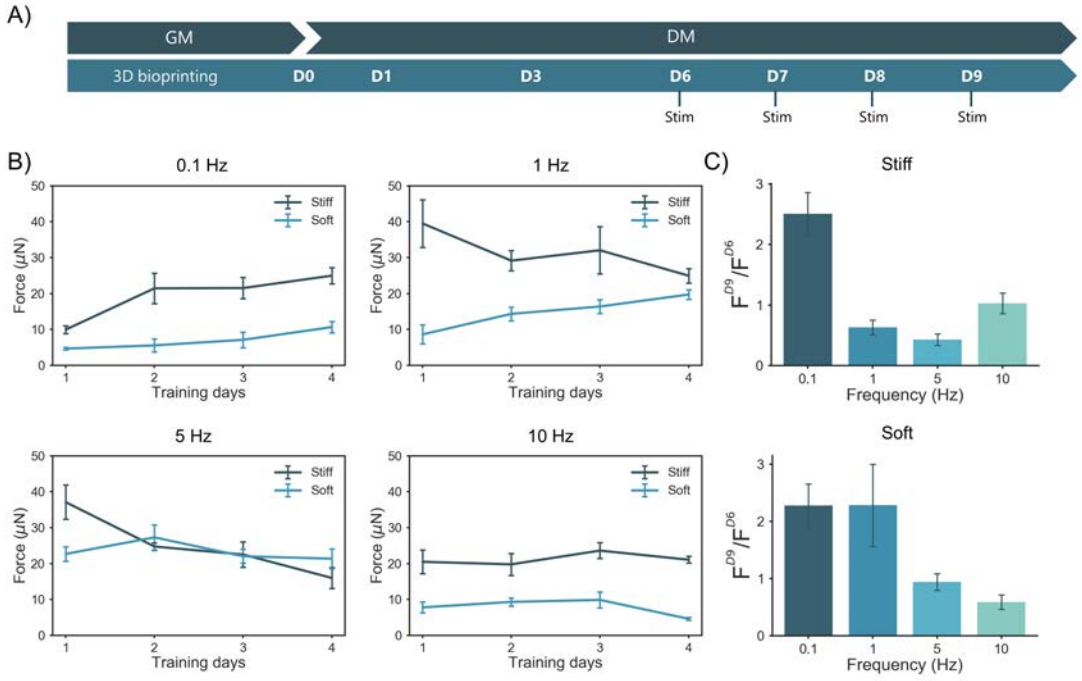

Figure 4.9: Force changes after long-term stimulation. A) Scheme representing the differentiation and training protocol. B) Force evolution during the training days for different frequencies and post stiffnesses. Error bars represent standard error of the mean. C) Fold increment of the force from the first day of stimulation to the last day. Error bars represent standard error of the mean. Adapted with permission from [1].

day training protocol. For instance, for every training protocols on stiff posts, stimulating a control sample only on the fourth day for 60 min at 1 Hz ($F^{D9}_{ctrl,60}$) achieved the same amount of force as the rest of the trained samples, as reported in Figure 4.10B. Thus, applying a long-term training protocol was impractical, as one could achieve the same amount of force by stimulating for only 60 min. This could be due to two reasons: i) the mechanical stimulation provided by stiffer posts was sufficient to achieve large forces, independently of the frequency, or ii) the accumulated stress produced by high frequencies together with stiff mechanical constrains led to harmful effects on the tissue, as supported by the fact that only a very low stimulation frequency (0.1 Hz) resulted in an enhancement during the 4-day period (Figure 4.10C). We hypothesize this last option to be more probable, as in general we observed a decrease in the thickness of the tissue rings, which were likely caused by the deterioration and damage of the bio-actuator due to the highly stressful conditions. Long-term stimulation with soft posts was, on the contrary, advantageous when compared to a sample stimulated for 60 min on the last day (Figure 4.10C). When medium to high frequencies (1 Hz and 5 Hz) were used, there was a 2-fold increment in force generation, proving that these parameters of training could achieve the greatest improvement in performance. However, when using a low frequency (0.1 Hz), the initial enhancement of 4-fold decreased to barely 1-fold.

All in all, these comparative results point out that the combination of large stiffness with high frequency in long-time stimulations might be harmful for the bio-actuators, most likely due to the breakage of sarcomeres that cannot be repaired[14]. Even though higher forces are obtained with stiffer posts (Figure 4.9A), they do not generally increase after prolonged stimulation (Figure 4.9B). Only stimulation at medium frequencies with softer posts can induce an actual enhancement on the force output.

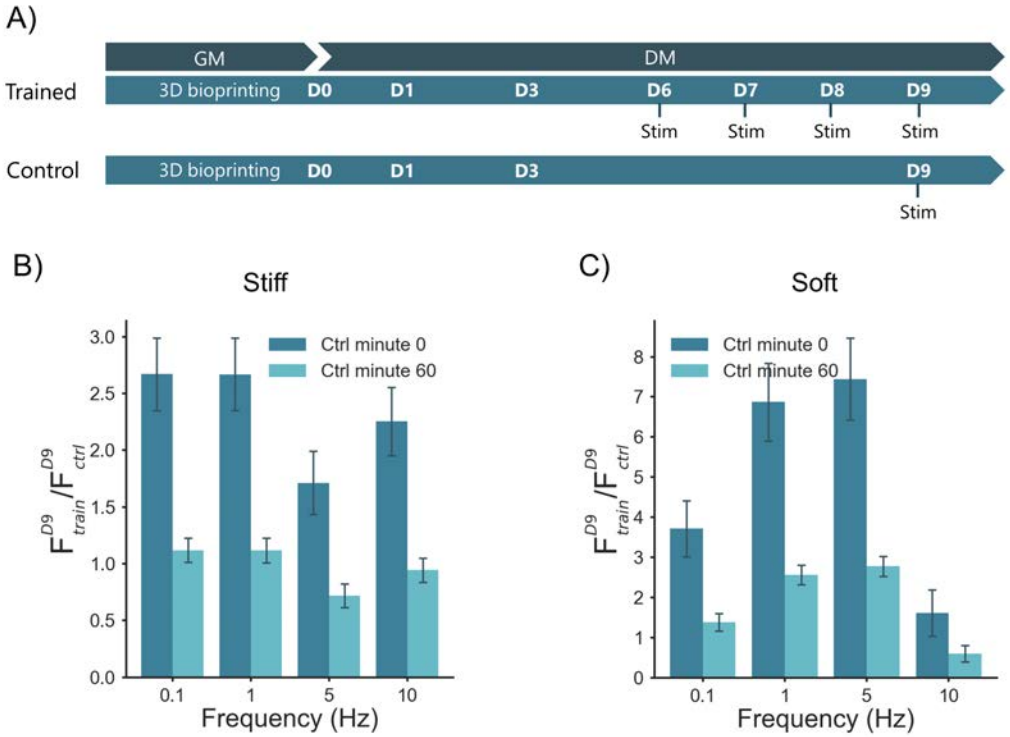

Figure 4.10: Force modulation of trained bio-actuators compared to control samples. A) Timeline of the differentiation process of a trained and control sample, indicating the days where stimulation was applied. B-C) Force fold increase of a trained sample compared to a control sample. "Ctrl minute 0" refers to a control sample not stimulated at all during the 4 days ($F^{D9}_{ctrl,0}$) and "Ctrl minute 60" to a control sample stimulated only the last day for 60 min at 1 Hz ($F^{D9}_{ctrl,60}$). Adapted with permission from [1].

Gene expression after long-term training

The study of the expression pattern of the different myosin heavy chain (MyHC) isoforms helps us understand the events modulating the actuation of these bio-hybrid systems. Dynamic gene expression of stimulated samples for all the different frequencies are displayed in Figure 4.11. In each case, the values were normalized to a control sample on day 9 with the same stiffness condition that was not stimulated for the whole 4-day period (named D9 in Figure 4.11). Although for stiff posts the slow-twitch MyHCI isoform did not show significant differences in its expression, the fast MyHCII isoforms were mostly downregulated when compared to a non-stimulated sample (Figure 4.11B). Regarding soft posts, the same behavior occurred, except in the expression of MyHCIIa, in which the 5 Hz stimulation showed an upregulation (Figure 4.11C). Interestingly, this frequency was the one showing a greater force fold increase (together with 1 Hz, which did not show a downregulation on MyHCIIa) when compared to the non-stimulated sample (Figure 4.10C). As per previous reports in the literature, the lack of changes in the expression pattern of MyHCI could be simply due to the end of a slow-to-fast transition, a period in which the expression levels of the slow-twitch MyHCI isoforms decrease meanwhile those of the fast-twitch MyHCII continue increasing[57].

Simultaneous analysis of gene expression and force evolution seems to indicate different mechanisms taking place. On the one hand, the downregulation of MyHCII in stiff posts, together with constant force output throughout the training, could indicate that the tissue reached a terminal maturation state, where no more proteins were being synthesized, since MyHC, mRNA and protein

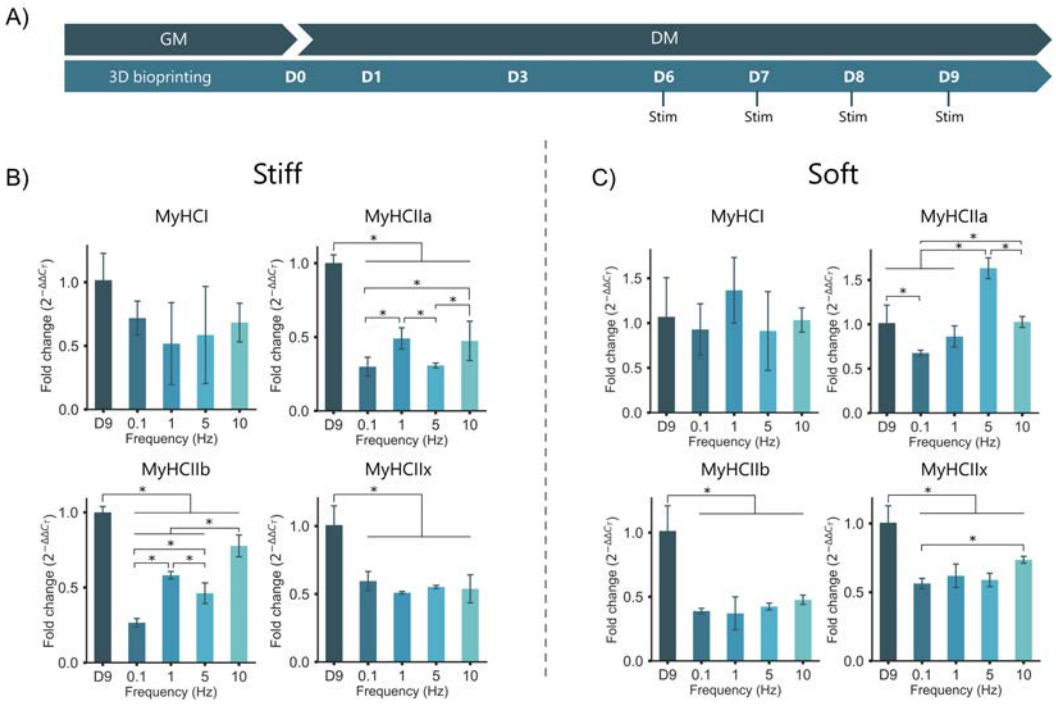

Figure 4.11: Gene expression analysis after training. A) Scheme representing the differentiation and training protocol. B-C) Expression levels of different isoforms of MyHC for different frequencies and post stiffness. All of them are normalized to a control sample of the same stiffness condition. Error bars represent standard error of the mean. Adapted with permission from [1].

levels are closely matched[58]. On the other hand, the downregulation of MyHCII isoforms in soft posts, together with the increased force output that we observe, could indicate protein remodeling of the internal structure of myotubes. However, one may also speculate that downregulation on the expression of the different MyHCII isoforms in trained samples could be linked to sarcomeric lesions due to the continuous exercise and high eccentric stresses[14]. In any case, further studies at the protein level could shed more light onto the specific mechanism behind the reported change on the muscle-based actuator's capabilities.

2.3. Conclusions

This research proves one of the key aspects of the next generation of 3D-bioprinted bio-actuators: force modulation and adaptability according to specific requirements. We 3D bioprinted a proof-of-concept bio-actuator that could actively bend two posts. This bio-actuator is a fast, versatile system for force measurement that can be readily designed and fabricated in different shapes and for different purposes. In particular, the results presented above give some indications about the best training conditions to achieve different levels of force output. Although dynamic mRNA expression studies proved the adaptability of bio-actuators to different frequencies and mechanical stiffnesses, the precise mechanisms behind these changes are not yet fully understood. In particular, it should be investigated whether the observed force increase comes from an enhanced maturation of the tissue, internal remodeling or actual hypertrophy, and if this level of maturation can also be achieved by passive bio-actuators without prolonged stimulation. To study this, future experiments should consider the force monitoring several days after stimulation and the characterization of myotube development at the protein level, which would give hints about muscle hypertrophy and atrophy. Fur-

ther studies focused on applications of bio-actuators should aim at translating these results to train and optimize muscle-based bio-robots. Although our approach of using a fixed bio-actuator is more convenient for this fundamental study and biomedical applications, more research should be carried out into exploiting this technique to develop fully printed and untethered bio-robots with different architectures that can lead to efficient motion, bringing this versatility and scalability into the bio-robotics field. Moreover, more research in the material science field could help integrate other kinds of materials, such as responsive or smart materials, or improve the current ones to obtain enhanced performance and features. Finally, there are some long-term challenges in the bio-robotic fields related to the viability of the devices. For instance, the lifetime of bio-actuators, which could hinder future applications, has not been extensively investigated. In addition, another critical constraint is the limitation of maintaining optimal culture conditions and proper nutrient delivery, which is an essential aspect for the bio-actuator survival. This could be tackled by incorporating the bio-actuators inside bioreactors and by using micro-fluidic channels. In this regard, recent advances of 3D printing in microfluidics and bio-engineering could be combined to obtain fully integrated bio-actuating devices. Despite all these challenges, we believe this work opens up new avenues not only for the fabrication and understanding of the adaptation of biological actuators in bio-hybrid soft robotic devices, but also for biomedical or pharmacological studies interested in the development of native three-dimensional skeletal muscle tissue.

2.4. Materials and methods

Cell culture

C2C12 mouse myoblasts were purchased from ATCC and maintained in GM consisting of high glucose Dullbecco's Modified Eagle's Medium (DMEM; Gibco®) supplemented with 10% Fetal Bovine Serum (FBS), 200 nM L-Glutamine and 1% Penicillin/Streptomycin, in a 37 °C and 5% CO_2 atmosphere. Cells were passaged before reaching 80% confluency in Corning® T-75 flasks. For cell differentiation and myotube formation after the bioprinting process, GM was substituted by DM, consisting of high glucose DMEM containing 10% Horse Serum (Gibco®), 200 nM L-Glutamine (Gibco®), 1% Penicillin-Streptomycin (Gibco®), 50 ng/ml insulin-like growth factor 1 (IGF-1, Sigma-Aldrich) and 1 mg/ml 6-aminocaproic acid (ACA, Sigma-Aldrich).

Hydrogel fabrication

The hydrogel mixture based on fibrinogen, gelatin and hyaluronic acid (HA) was prepared as described elsewhere[59]. Briefly, a solution of 3 mg/ml HA (Sigma-Aldrich) in DMEM was stirred overnight at 37 °C. Then, glycerol (10% v/v) was added to the mixture and stirred for 1 h, followed by the addition of gelatin (35 mg/mL) and fibrinogen (20 mg/mL). When all components were dissolved in the medium, the hydrogel mixture was sterile-filtered through a 0.2 μm syringe filter (Millopore™) and stored at -20 °C until its use.

Multi-material 3D bioprinting of bio-actuators

For the multi-material 3D bioprinting process, we used the Inkredible+ bioprinter (CELLILNK®) with two pneumatic extrusion cartridges. C2C12 myoblasts were harvested by a 0.05% (wt/v) Trypsin-EDTA (Gibco^{TM}, 15400054), centrifuged at 300g for 5 min and re-suspended at a concentration of $5\dot{1}0^6$ cells/mL in the hydrogel mixture, at 37 °C. The cell-laden hydrogel was loaded into a 3 mL plas-

tic syringe (Nordson®, ref. 7012085) coupled to a 200-μm (G27) plastic conic nozzle (Optimum® SmoothFlow™ tapered tips, Nordson®, ref. 7018417). The PDMS precursor was prepared by mixing SE 1700 (Dow Corning®) base and cross-linker at a 10:1 (stiff) or 20:1 (soft) ratio, depending on the experiment. The designs were made with the 3D modeling software SketchUp, converted into GCode with the open-source software Slic3r (v. 1.2.9) and the bioprinter was controlled with RepetierHost (v. 2.0.5). The posts and the hydrogel were simultaneously printed in the same process at 200 kPa and 50 kPa, respectively. As a substrate, glass-bottom 35-mm μ-Dishes (ibidi, ref. 81158) were used. After printing, the 3D constructs were crosslinked by the addition of a 5 U/ml solution of thrombin (T4648, Sigma-Aldrich) for 5 min at 37 °C. The excess of thrombin was washed out by two washes in PBS (2 min each) and the structures were maintained in GM supplemented with ACA at 37 °C and 5% CO2 for 3 days. Then, GM was replaced by DM supplemented with ACA and replenished every two days.

Mechanical and rheological characterization of PDMS

To characterize the PDMS, dog-bone shape elements where 3D-printed with the Inkredible+ 3D bioprinter (CELLILNK®) with a 580 μm nozzle diameter and left to cure slowly at 37 °C inside an incubator in order to emulate the experiment's curing conditions. The shapes were designed according to a scaled-down version of the ASTM D638 standard. Then, tensile tests were performed with a mechanical testing machine (Zwick Roell) with a strain rate of 0.05 mm/s. The Young's modulus was calculated from the linear region in the 20-40% range.

Long-term stimulation of biological actuators

Bio-actuators with PDMS posts were 3D-bioprinted as explained in the main text. They were left in GM supplemented with ACA for 3 days, once the tissue had de-attached from the glass-bottom and was surrounding the PDMS posts. At that point, it was switched to DM supplemented with ACA and IGF-1. Long-term stimulation was conducted from day 6 to 9 of differentiation with stimulation platforms consisting on 2 graphite rods (Ladd Research, 30250) attached to the cover 33 mm μ-Dishes (Ibidi, 81158). All stimulations were carried out for 1 h inside an inverted microscope in culture conditions and videos of the displacement of the posts were taken every 15 min. Bio-actuator's culture medium was changed before and after each stimulation to allow for nutrient replenishment and remove possible toxic components, although carbon rods are less reactive than Pt electrodes, and are a safe stimulation method for long-term periods[54]. The stimulation platforms were connected to a waveform generator (Tabor Electronics, PM8572). The pair of electrodes were separated a distance of 12.5 mm and square wave pulses of 12.5 V (achieving 1 V/mm) and 1 ms of width (unless specified otherwise) were applied at different frequencies according to the needs of the experiment.

Stimulation videos were processed with a home-made Python (v. 3.7) script to obtain the displacement of the posts and Euler-Bernoulli's beam bending equation was used to estimate the forces and stresses exerted against the posts to the tissue during electrical stimulation. Briefly, microscope videos were loaded into the script using OpenCV (v. 4.1.2) and the VideoCapture function. Then, a binary thresholding was applied to the first frame using the Treshold function from OpenCV with a random threshold value. A Sobel operator was applied using the Sobel function in the x- and y-axes of the image. This operator is a filter that can detect edge differences in the images, especially if it has been thresholded before. Both edge detections in x and y were put together using the Bitwise_or function of OpenCV. The binarized edges of the first frame were prompted on screen with trackbars

that allowed to manually modify the threshold value, the scaling of the image (only for visualization purposes) and the dilation level of the edges. If the edges were too noisy, a dilation using the Dilate function of OpenCV was applied to make them smoother. Normally, the thresholding would be manually changed to account for differences in illumination between samples until the edges detected with the Sobel filter were adequately representing the actual edges of the posts. Then, the user could draw a line in the image, perpendicular to the edge of the post, where the displacement of such edge would be evaluated in time. The line was transformed with a Bresenham algorithm (using a module of the same name) into a list of pixels. Finally, the whole video would be processed with the same filters (keeping the selected threshold value and dilation) and the intensity projection (with only values of 0 or 255, as the image was binarized) in the drawn line would be stored. After processing the video, every projection of the edge was fitted to a Gaussian function and its mean (indicating the position of the post) was stored. In this way, by plotting the means vs time, we could obtain a function of post displacement vs time. Since a z-stack of the posts was taken to calculate the exact height of the tissue, that value, together with the displacement and the information about Young's modulus and post dimensions were used to calculate the exerted force by using Equation 4.2.

Electrical characterization of the carbon-rod electrodes was performed with Autolab (PGSTAT204, Metrohm) in a two-probe setup, at the frequency range of 0.01 – 10,000 Hz, using sinusoidal waves of 20 mV of AC voltage and 250 mV of DC voltage.

Gene expression analysis

Total RNA of at least two independent experiments was extracted using the RNeasy mini kit (QIAGEN, 74134) according to manufacturer's instructions. The concentration and purity of RNA were assessed with a Nanodrop ND-1000 (Thermo Scientific). A total quantity of 500 ng of extracted RNA were converted into cDNA using the ReverAid First Strand cDNA Synthesis Kit (Thermo Scientific, K1622). The qPCR reactions were performed in a final volume of 10 μL with PowerUp SYBR Green Master Mix (Applied Biosystems, A25742), used according to manufacturer's instructions in a StepOnePlus Real-Time PCR System (Applied Biosystems, 4376600). The following primers were used:

- GAPDH: FW (5' ATGGTGAAGGTCGGTGTGAA 3')
  GAPDH: RV (5' GAGGTCAATGAAGGGGTCGT 3')

- MyoD: FW (5' CCACTCAGGTCTCAGGTGTAAC 3')
  MyoD: RV (5' TCGCCCGCTTGAGGAATAA 3')

- Myogenin: FW (5' CCCTACAGACGCCCACAATC 3')
  Myogenin: RV (5' ACCCAGCCTGACAGACAATC 3')

- MyHCI: FW (5' GCCCCAAGCACAAGGAGT 3')
  MyHCI: RV (5' AGCCCCAAGAAATAAGGACAG 3')

- MyHCIIa: FW (5' GCAGAGACCGAGAAGGAG 3')
  MyHCIIa: RV (5' CTTTCAAGAGGGACACCATC 3')

- MyHCIIb: FW (5' GAAGGAGGGCATTGATTGG 3')
  MyHCIIb: RV (5' TGAAGGAGGTGTCTGTCG 3')

- MyHCIIx: FW (5' GCGACAGACACCTCCTTCAAG 3')
  MyHCIIx: RV (5' TCCAGCCAGCCAGCGATG 3')

All genes were normalized to the expression levels of GAPDH, whose expression was constant across all experiments. Melt-curve analyses were performed to ensure that only one amplicon was being produced.

Statistical analysis

The comparative quantitative reverse-transcription polymerase chain reaction (qRT-PCR) statistical analysis were performed using the $2^{-\Delta\Delta CT}$ method[60]. All the samples are compared related to a control sample of the same stiffness condition. A t-test was used to compare two groups, while Holm-Sidak test was used to compare multiple groups. The level of significance was set to $p \leq 0.05$. All significance analyses were performed using GraphPad Prism Version 7.00 for Windows (GraphPad Software, San Diego, CA).

3. A 3D model of aged human skeletal muscle tissue

3.1. Objectives

Bio-actuators can represent faithful models of skeletal muscle tissue, as they possess the necessary three-dimensional organization of native tissue and show functional adaptability. For this reason, they could be useful as drug testing platforms, in order to understand the effects that certain drugs could have, both morphologically and functionally, in the development or the response of muscle tissue. Moreover, the versatility of this force measurement platform could offer the possibility of using patient-derived myoblasts to understand the development of rare myopathies or neuromuscular diseases.

However, the previous bio-actuator was based on murine skeletal muscle myoblasts and, in order to properly be used to test the efficacy of drug treatments, the biofabrication with human myoblasts should be demonstrated. Hence, the objectives of this section are the following: i) to successfully fabricate a bio-actuator based on human skeletal muscle myoblasts; ii) to demonstrate morphological and functional relevant characteristics, similar to those of native tissue; iii) to test the effect of a cytokine, TNF-α, as means to induce an aging effect in the muscle tissue and obtain a relevant model of aged muscle; and iv) to test the efficacy of a commercially available cosmetic peptide that is known to have relaxing effects in muscle and compare the differences between aged and non-aged tissue. In order to achieve these objectives, not only the force generation of the tissue was analyzed, but also the kinetics of the contraction under high frequency stimulation, so that the relaxing effects in these highly demanding conditions could be analyzed.

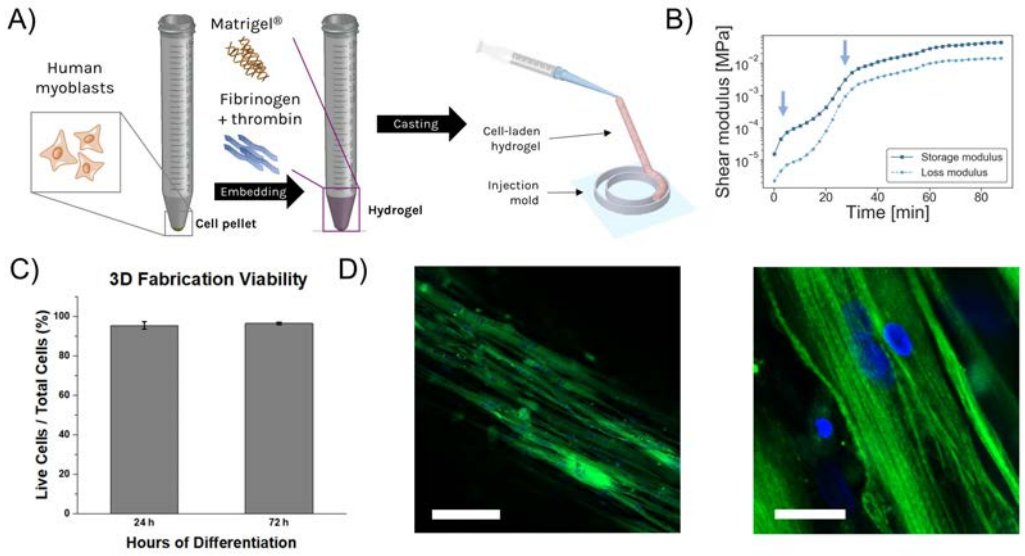

Figure 4.12: Fabrication of three-dimensional human skeletal muscle bio-actuators. A) Schematic of the fabrication method, based on casting on 3D-printed molds and subsequent transfer into 3D-printed PDMS posts, fabricated as described in the previous section. B) Shear modulus of the hydrogel during crosslinking at 37 °C. Arrows represent the fast crosslinking of fibrinogen into fibrin and the slow Matrigel® crosslinking after 30 min. C) Viability studies of the hSMTs after casting (N=2; mean ± standard error of the mean). D) Immunostaining after 10 days of differentiation showing well aligned myotubes and (zoom) sarcomeric structure. Scale bars: 125 μm (left) and 20 μm (right).

3.2. Results and discussion

Bioengineering of human skeletal muscle tissues

Human skeletal muscle tissues (hSMTs) were bioengineered by embedding human myoblasts in a mixture of biopolymers mimicking the ECM found in native tissue. The mixture consisted of Matrigel® and fibrinogen as the main components, adapted from a previously reported protocol for murine skeletal muscle cells[25]. As already discussed in the previous chapter, collagen is one of the main components of the sarcolemma of skeletal muscle tissue. Therefore, the collagen contained within Matrigel®, as well as its other components, helps recreate this environment. Fibrinogen, also rich in cell-attachment motifs, helps modulating the final stiffness of the matrix (after crosslinking with thrombin) to achieve the right mechanical properties for cell survival and tissue manipulation (Figure 4.12).

Human myoblasts were embedded in the hydrogel mixture at a final concentration of 5 million cells/mL. Thereafter, fibrinogen was added, mixed thoroughly, and 80 μL of the solution was casted in a 3D-printed mold made of PDMS, rapidly in order to avoid the crosslinking of fibrinogen into fibrin induced by thrombin (Figure 4.12A). Afterwards, the cell-laden hydrogels were left in an incubator for 30 min until Matrigel® was fully crosslinked. These crosslinkings can be observed in a time sweep of the rheological properties of the hydrogel, indicated by the blue arrows in Figure 4.12B. For this experiment, the hydrogel was mixed, including thrombin, and immediately placed into a Peltier plate at 37 °C for an oscillatory test in a rheometer. Both the storage and loss modulus of the hydrogel suffer a small increase of their value right after the start of the test, indicating the fast dynamics of the fibrinogen crosslinking with thrombin. After approximately 30 min, a second increase illustrates the crosslinking of collagen inside Matrigel® and reaches a plateau for longer times.

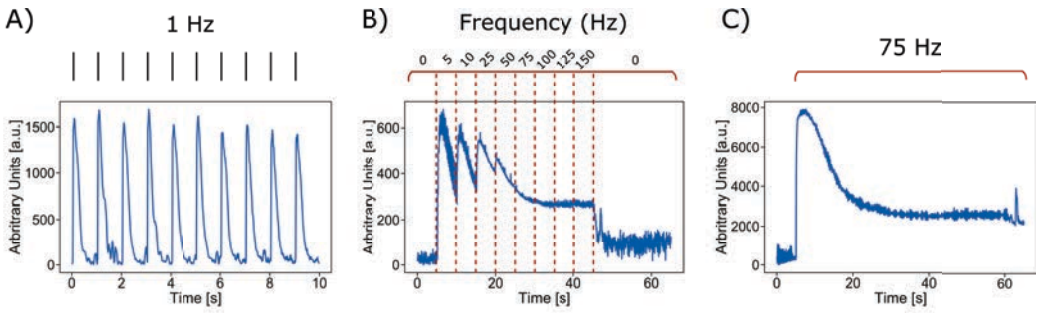

Figure 4.13: Response of hSMT constructs after different types of electrical stimulation, mimicking the behavior of native skeletal muscle tissue, at day 6 of differentiation. A) A constant stimulation at equally spaced intervals (1 Hz) produces single-twitch contractions, where the muscle has enough time to fully relax between contractions. B) An increasing frequency sweep in intervals of 5 s exhibits the effect of wave summation, where one stimulation wave builds up over the next one, not allowing the muscle to relax. It is interesting to notice how, for a single frequency, there is a fast decrease in the contraction. C) This effect can be clearly observed in a sustained high-frequency contraction of 75 Hz for 55 s, where the muscle achieves a peak of maximum contraction, followed by a slow decrease, remaining at a baseline level.

GM supplemented with ACA was added and maintained for 2 days. As it occurred with murine skeletal muscle tissue, the addition of the anti-fibrinolytic agent ACA was a crucial step in order to obtain long-lasting hSMTs, due to the strong degradation of collagen and fibrin by plasmin, cysteine cathepsins and other proteases[61]. We found that, after 5 days of differentiation, the tissue would completely degrade due to the action of these proteases. Inhibition of serine protease by the addition of ACA ensured structural integrity for the duration of all our experiments. Beforehand, we performed studies of cell growth, proliferation and differentiation of human myoblasts in 2D, which showed no differences when the media were supplemented with ACA. Moreover, previous reports in the literature show beneficial aspects of using ACA to increase the lifetime of bio-actuators without loss of function[61].

After 2 days in GM, the hSMTs were carefully transferred to a 3D-printed two-post system and the media changed to DM supplemented with ACA. Tissue compaction after transfer into the two-post system was minimal. This differs particularly from the 3D bioengineering of murine skeletal muscle tissue, where tissue compaction was a key element in the self-assembly of the bio-actuator (see Section 2). Since static mechanical stimulation of myocytes[1] is crucial for proper differentiation and necessary for post deflection and force measurement, the dimensions of the molds had to be carefully designed for the tissue to perfectly adapt to the two-post system. Moreover, on the first day after casting the tissues were gently separated from the outer wall of the molds due to the high adhesion of the hydrogel to PDMS. On the second day, before transfer, some compaction of the tissue was already be observed. For this reason, 3D bioprinting was not a suitable technique to fabricate bio-actuators made of human skeletal muscle tissue, since it is not possible to bioprint the tissue construct very close to the posts due to the conical shape of the nozzles. We hypothesize that these human myoblasts are less active than their murine counterparts, perhaps due to their larger size, something also supported by the low release of cells from the scaffold into the bottom of the dish, a very common occurrence with C2C12 cells.

Biocompatibility of the whole process was checked by using a fluorescence Live/Dead viability kit (Figure 4.12B). One day after casting, we observed high viability > 95%, which was still maintained on the third day, after switching to DM. During myogenesis, the tissue slightly compacted against the posts and multinucleated myocytes could form (Figure 4.12C). Immunostaining of MyHC and

[1]In the literature, the term myocyte is reserved to name multinucleated skeletal muscle cells of humans, while myotube is used for mice. Therefore, in this section, we will use the term myocyte.

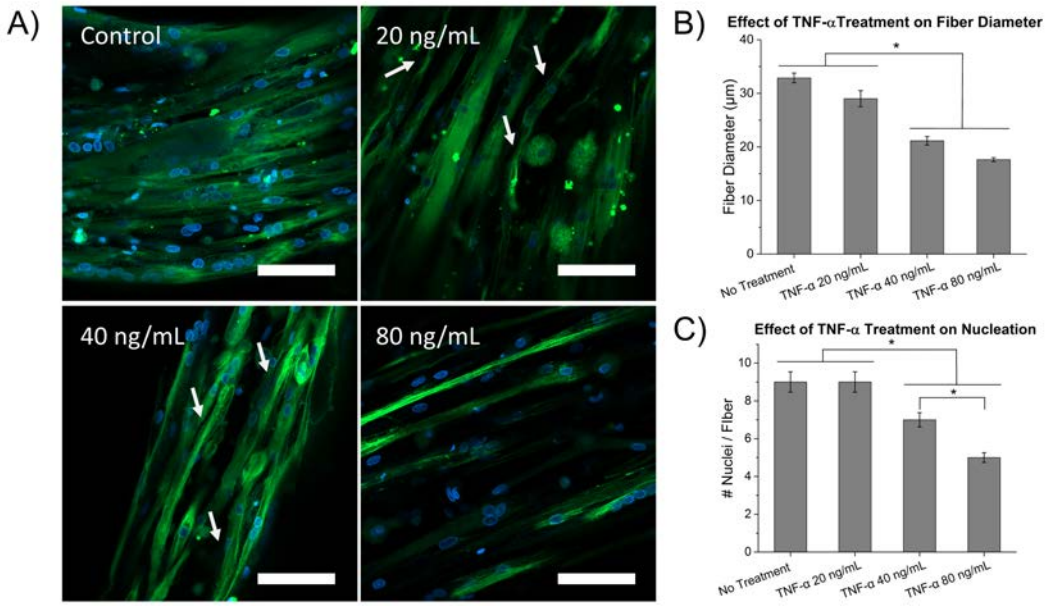

Figure 4.14: Effects of the addition of TNF-α to three-dimensional hSMC constructs. A) Upon the addition of higher concentrations of TNF-α, the myotubes seem to show a significant decrease in their width and shape distortions (white arrows). Scale bars: 80 μm. B) The diameter of the myotubes decreases with increasing concentrations of TNF-α (N=12; mean $\pm$ standard error of the mean). C) The number of nuclei per fiber is also affected by the concentration of TNF-α (N=12; mean $\pm$ standard error of the mean).

nuclei showed elongated and aligned myocytes, and sarcomeric structures could be observed under high magnification, indicating maturation of the tissue. Spontaneous contractions were not observed during differentiation, which poses another difference between bioengineering of human and murine muscle tissue.

Maturation of the hSMT was confirmed via electrical stimulation (Figure 4.13). By using the home-made setup of carbon-rod electrodes characterized in Section 2, we performed electrical stimulation of the hSMTs in the two-post platform after 6 days of differentiation. As expected, the tissues could contract following the applied frequency, as can be observed in Figure 4.13A, after a 1 Hz stimulation that produced twitch contractions. Other behaviors related to different frequency profiles were also investigated. Figure 4.13B shows the contractile response after a frequency sweep from 5 Hz to 150 Hz in 5 s intervals. A behavior similar to that of wave summation in native tissue can be observed[62]. However, for higher frequencies (50 Hz and beyond), this response disappears, and a steady tetanic state is maintained until stimulation is stopped. In order to get a grasp on this high frequency response, we examined the contraction kinetics under a high frequency stimulation of 75 Hz for 55 s (Figure 4.13C). When stimulation starts, there is an initial contraction of high force, which gradually decreases and remains in a tetanic state until stimulation stops. In general, we observed this kind of behavior for all frequencies in the testing range of 10-75 Hz, as well as from day 5 to 12 of differentiation, when our experiments took place. Moreover, this behavior differs from that observed in 3D-bioengineered C2C12 cells, which only show a sustained tetanic contraction for frequencies higher than 10 Hz without an initial stroke (see Chapter III).

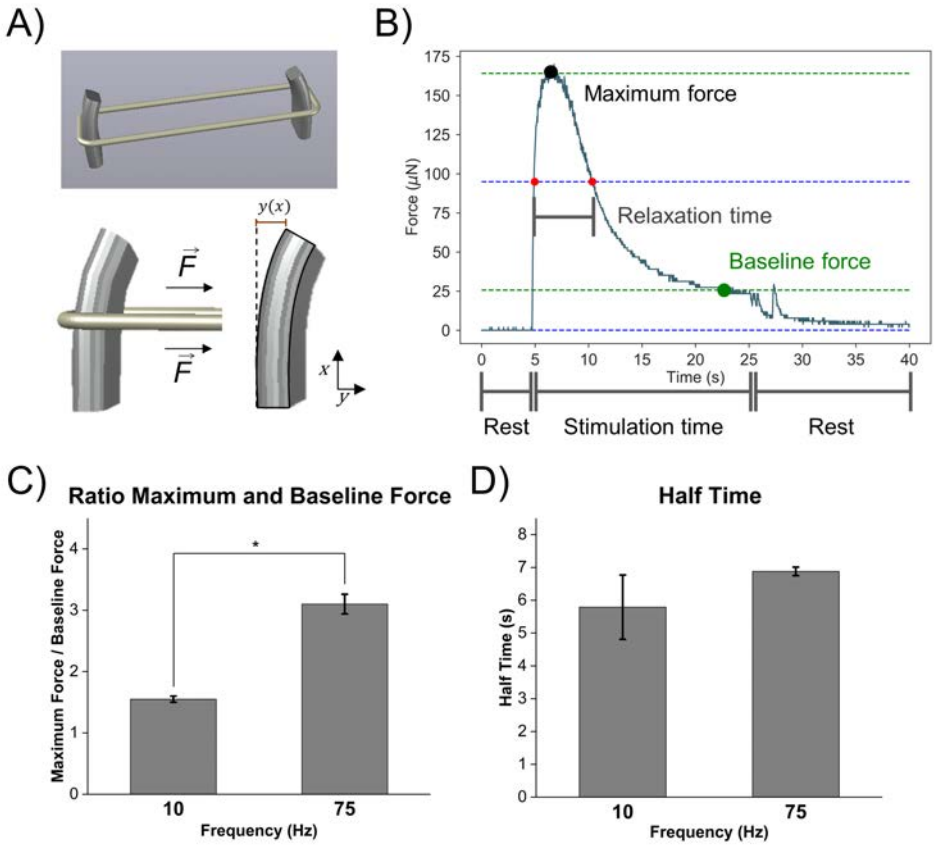

Figure 4.15: Force measurement and contraction kinetics of bioengineered human muscle tissue. A) Representation of the mechanism of force monitoring with the drug testing platform. B) The maximum force, baseline force and relaxation time are extracted from 30 s high frequency stimulations (10 Hz or 75 Hz) in order to study differences in contraction kinematics. C) The ratio of maximum to baseline force indicate that 75 Hz stimulation produces a higher force stroke (N=4; mean ± standard error of the mean). D) The relaxation half time, however, is not affected by the frequency (N=4; mean ± standard error of the mean).

Effect of TNF-α

TNF-α is a proinflammatory cytokine known to be related to sarcopenia, or loss of muscle mass and function in aging, as well as reduction of cell fusion[44–50]. Hence, we examined whether addition of this cytokine could be used to model aged skeletal muscle tissue in our muscle platform. We evaluated three different concentrations of TNF-α in the culture media: 20 ng/mL, 40 ng/mL and 80 ng/mL. Morphological and physiological changes were assessed by immunostaining of MyHC and cell nuclei (Figure 4.14). All concentrations showed multinucleated and aligned myocytes, although morphological differences could be observed with higher concentrations (Figure 4.14A). White arrows indicate areas where the myocytes show thinning of the fibers with uncharacteristic distortions. Besides, there was a decrease in myocyte diameter, going from more than 30 μm for control (untreated) samples to less than 20 μm for the highest concentration (Figure 4.14B). Nucleation was also affected by the cytokine, since the number of nuclei per visible fiber was reduced from 9 to 5 for the concentration of 80 ng/mL (Figure 4.14C). All these morphological changes were consistent with those related to sarcopenia induced by TNF-α[44, 45, 49, 63]. In order to test whether functional changes were also compatible, we set the concentration of TNF-α to 40 ng/mL for the remaining experiments, since it was the concentration for which some effects could be observed without becoming too adverse.

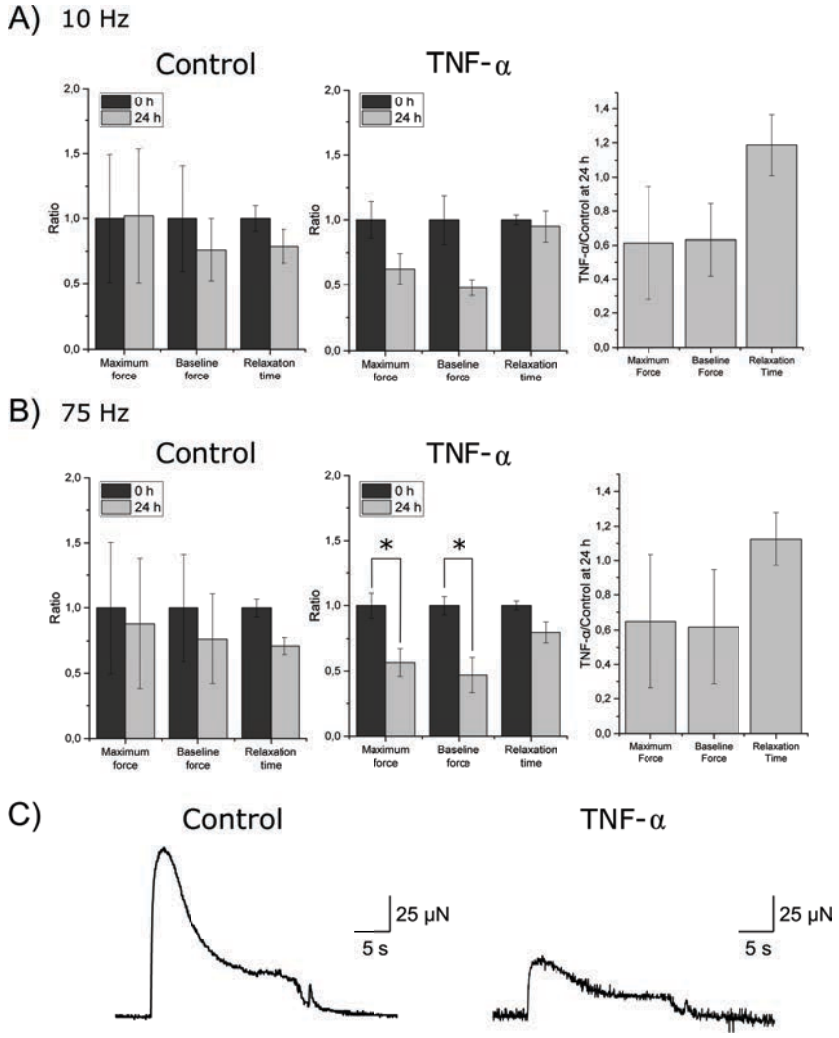

Figure 4.16: Effect of TNF-α on the contraction parameters. A) Results for a sustained stimulation of 10 Hz and B) 75 Hz, both for control and TNF-α-treated samples. On the right side, the ratio of each parameter for TNF-α vs control at 24 h are compared to better see the differences between models. All data are normalized with respect to the initial conditions before any treatment (0 h). C) Representative example of the contraction profiles (75 Hz) for a control and TNF-α with the same scaling, to better appreciate the differences produced. N=3-6. All results are shown with mean $\pm$ standard error of the mean.

Having obtained a morphologically relevant model of native and aged hSMT, we proceeded to use this system as a force measurement platform for drug testing (Figure 4.15). The contractions of the skeletal muscle induced by electrical stimulation could deflect the two PDMS posts, as depicted in Figure 4.15A. This displacement could then be translated into force generation, as described in Section 2. In this way, we could not only assess the kinetics of the contraction, but also the total force generated by the muscle in a quantitative manner.

Due to the interesting contraction profiles reported in Figure 4.13, we focused on the study of the kinetics and force generation of a high- (75 Hz) and a low-frequency stimulation (10 Hz) for 20 s. We extracted three main parameters from the contraction profiles: the maximum force achieved, the baseline force maintained until stimulation was stopped and the relaxation time, defined as the time until achieving the median force between maximum and baseline after the onset of stimulation (Figure 4.15B). Initial observations reported differences in the maximum/baseline force ratio for 10 Hz and 75 Hz, confirming that higher frequencies produced a stronger initial twitch, as already re-

ported (Figure 4.15C)[44, 49]. The relaxation time, however, did not significantly differ between both frequencies (Figure 4.15D).

These contraction parameters were monitored before and after the addition of 40 ng/mL of TNF-α in order to test functional changes compatible with skeletal tissue aging. Figure 4.16 shows these results for both frequencies, as well as control (untreated) and TNF-α-treated samples, before (0 h) and after (24 h) treatment with the cytokine. All contraction parameters for each sample were normalized to the average value in the pre-treatment state (0 h) in order to reduce initial variability common in replicas of biological studies. Control samples, in general, did not show significant changes in the contraction parameters, although there was high inherent sample variability, despite standardizing culture conditions by fixing exact concentration of cells and always using the same passage (Figure 4.16B). Samples treated with TNF-α, however, showed a marked decrease in maximum and baseline forces after 24 h of treatment, reaching half of their pre-treatment values (Figure 4.16C). This was statistically significant for the 75 Hz stimulation, although the same tendency was observed for 10 Hz, with higher variability. The graphs at the right-hand side compare the ratios of control and TNF-α-treated samples at 24 h. It can be seen how the maximum and baseline forces were also reduced in TNF-α compared to controls, therefore eliminating temporal effects related to the natural maturation of the tissue. Moreover, there was a slight tendency to increase the relaxation time after TNF-α treatment, although not significantly. The comparison of these ratios at 24 h (right-hand side plots) revealed that the addition of TNF-α seemed to increase the relaxation time of the hSMTs when compared to control samples. Finally, Figure 4.16C shows representative examples of the contraction profiles for 75 Hz of samples with and without TNF-α after 24 h. Here, it can be seen how the cytokine TNF-α affects both the strength of the fast twitching response and the baseline tetanic force in the short term (24 h), and also slightly increases its relaxation time. This is consistent with previous studies, which show that muscle aging is associated to an increase in relaxation time and a decrease in the force output[44, 62, 64, 65]. Thus, a high-frequency stimulation of 75 Hz resembles muscle dysfunctional changes that occur during aging.

Drug testing of a cosmetic peptide

To further exploit the possibilities of our drug testing platform, we tested the effects of Argireline® Amplified peptide, as cosmetic ingredient in development. As a first approach, the peptide was added to healthy 3D muscle models for 48 h, with a replenishment after 24 h at a concentration of 2 mg/mL. Figure 4.17 shows the impacts on the contraction parameters after 24 h and 48 h of addition to non-aged muscle, where all parameters were normalized to the average value in the pre-treatment state (0 h). The results point at a frequency-dependent effect. For low frequencies (10 Hz), the maximum twitch force was increased after 48 h, while it was decreased for high frequencies (75 Hz). This decrease was especially prominent in the baseline force, which was radically reduced until reaching total inhibition of tetanic contraction for 75 Hz. For 10 Hz, however, baseline force was not significantly changed, although slightly increased. The relaxation time was reduced for both frequency conditions, although more strongly for 75 Hz after 48 h. Representative contraction profiles of a 75 Hz stimulation can be seen in Figure 4.17C. It can be readily observed how, after 48 h, the tetanic contraction was partially inhibited despite having a continuous electrical stimulation. Only a short-lived twitch contraction remained, which decreased rapidly to a relaxed state. Therefore, Argireline® Amplified peptide showed relaxing effects by inhibiting maximum and baseline forces, and also reducing relaxation time in young/healthy muscles, leading to an inhibition of sustained contractions upon high frequency stimulations (75 Hz).

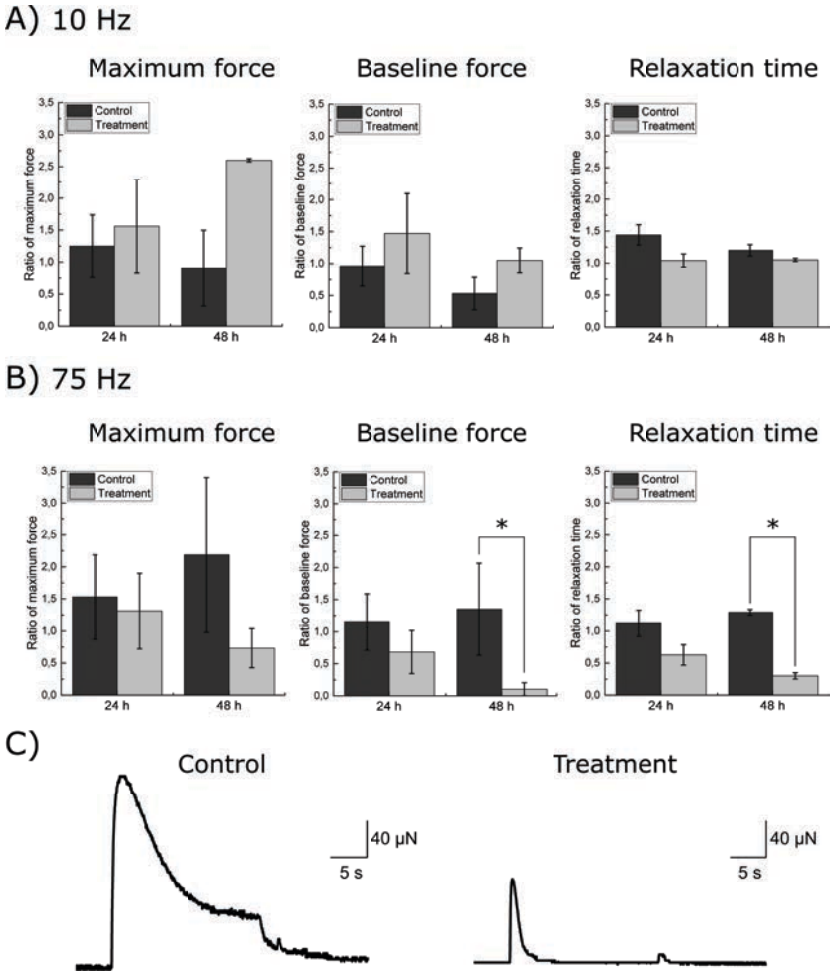

Figure 4.17: Effect of the Argireline® Amplified peptide on the contraction parameters. A) Results for a sustained stimulation of 10 Hz and B) 75 Hz, both for control and peptide-treated samples for 48 h. All data are normalized with respect to the initial conditions before any treatment (0 h). C) Representative example of the contraction profiles (75 Hz) for a control and a sample treated with the peptide with the same scaling, to better appreciate the differences produced. N=3-6. All results are shown with mean ± standard error of the mean.

The effects of this peptide were also studied on a model of aged hSMT, also revealing frequency-dependent responses (Figure 4.18). In this study, TNF-α was introduced in the culture media for 24 h in order to induce the aging attributes revealed in the previous figures (Figure 4.18A). Here, this point was considered the initial phase for this study (0 h), and all contraction parameters were normalized to the average value of the corresponding samples at this stage. Subsequently, the samples were treated with the peptide for two additional days (time-points 24 h and 48 h). For 10 Hz stimulations, both the maximum twitch and baseline forces increased when the peptide was added (Figure 4.18B), in contrast to samples to which no treatment was applied, similar to the results obtained for the same frequency in Figure 4.17. The relaxation time, however, did not show considerable changes after 48 h of peptide treatment. At 75 Hz, the condition previously described to mimic muscle physiological state during aging, peptide treatment lead to a decrease in the maximum force generation after 48 h (Figure 4.18C). Likewise, the baseline force decreased significantly after 48 h of treatment with the peptide, as reported in Figure 4.17, although it did not reach a complete inhibition of the contraction. The relaxation time was modestly decreased after addition of the peptide, as also shown in Figure 4.17. Considering these results, our data seem to indicate that treatment with the peptide at 75 Hz can reduce maximal force and provides faster relaxation in both young and aged-induced muscle.

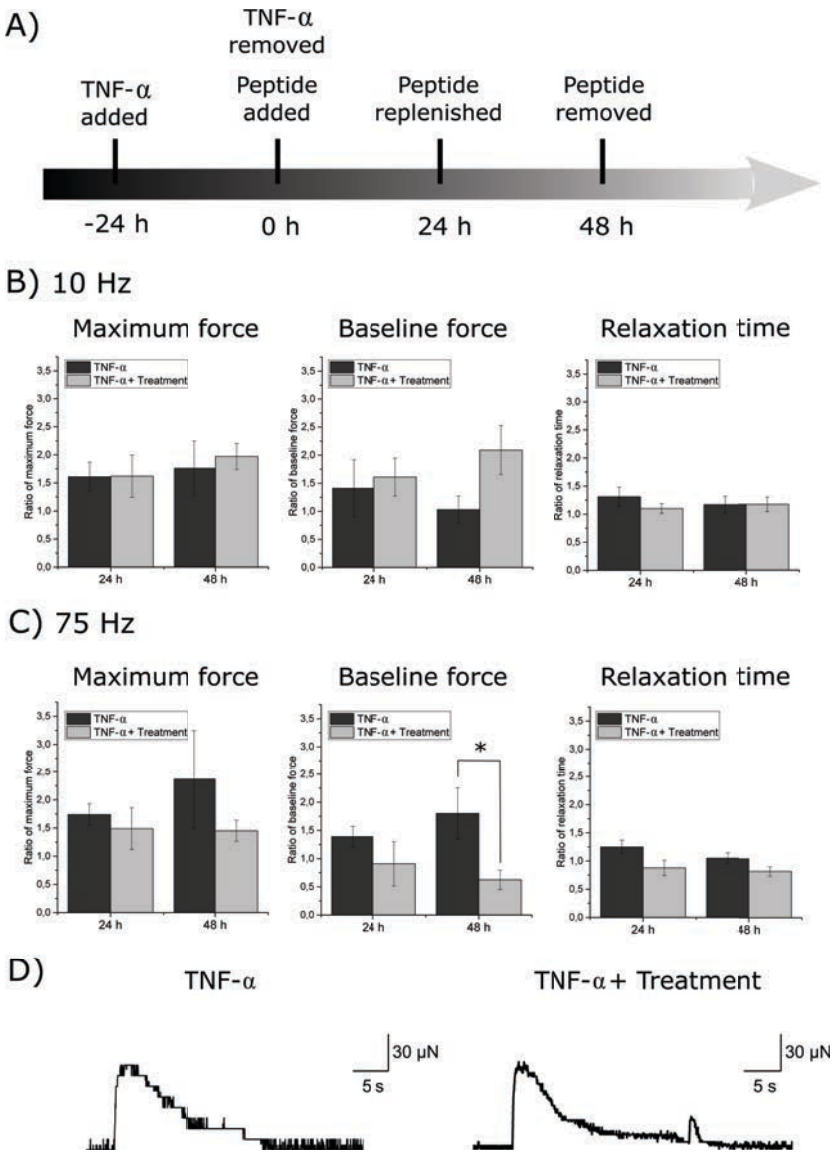

Figure 4.18: Combined effect of TNF-α and the Argireline® Amplified peptide in the contraction parameters. A) Experimental time-line of the addition of each molecule. B) Results for sustained stimulation of 10 Hz and C) 75 Hz. All data are normalized with respect to the initial conditions of aged muscle before the treatment with the peptide (0 h). D) Representative example of the contraction profiles (75 Hz) for a sample treated with TNF-α and a sample treated with TNF-α and the peptide with the same scaling, to better appreciate the differences produced. N=3-6. All results are shown with mean ± standard error of the mean.

3.3. Conclusions

In this work, we presented a 3D-printed and versatile platform for the study of young and aged human muscle functionality and its potential applications as a drug testing platform. We 3D-bioengineered a model of aged or senescence-like hSMT by the addition of TNF-α, and we showed its effects both in morphology (by immunostaining) and functionality (by contraction profiles), characterized by a reduction in fiber diameter and disruption of the sarcolemma, as well as loss of maximum and baseline forces. To further illustrate the possibilities of the testing platform, we tested, as a proof of concept, the impacts of Argireline® Amplified peptide in the contraction kinetics of bioengineered human muscle, showing model-dependent effects (aged vs non-aged). We believe that this drug-testing platform could have a potentially positive impact for the development of new drugs

in the biomedical or cosmetic fields, as it can mimic the 3D environment of native hSMT, as well as extract useful information of all kinds of stimulation profiles, both acute and chronic. Nevertheless, more advanced models of aging could include satellite cells, which seem to be especially affected by TNF-α[45], or motor neurons, in order to study neuromuscular disorders and their relationship with aging[35]. Moreover, in order to get more specialized treatment, human myoblasts or induced pluripotent stem cells from patients suffering from rare muscular disorders could be used to understand their development and treatment[8].

3.4. Materials and methods

Cell culture

Purchased cryopreserved Human Skeletal Myoblasts were obtained from the abdominal area of a Caucasian female donor aged 28 (Zenbio, # cat. SKB-F-1). Their GM was Skeletal Muscle Cell Growth Medium (PromoCell, # cat. C-23060) supplemented with Skeletal Muscle cell Growth Medium SupplementMix (PromoCell, # cat. C-39365) and DM was Skeletal Muscle Cell Differentiation Medium (PromoCell, # cat. C-23061) supplemented with Skeletal Muscle Cell Differentiation Medium SummplementMix (PromoCell, # cat. C-39366). Both of these media were supplemented with 1% Penicillin-Streptomycin (Gibco®). Cryovials were thawed and 2D cultures were expanded and passaged until reaching passage 4. Once the cells reached a confluence of 50-70% (approximately after 5-6 days growth) they were recollected. In this process, T-75 flasks were rinsed twice with PBS 1x and 3 mL of trypsin were added to each flask for 2 min. After cells detached, trypsin was neutralized with 9 mL of supplemented Skeletal Muscle Cell Growth Medium and final volume was centrifuged at 300g for 5 min. Supernatant was discarded and the pellet was resuspended in supplemented Skeletal Muscle Cell Growth Medium for cell counting. Eventually, the resuspended pellet was once again centrifuged at 300g for 5 min and the resulting pellet used for the sample 3D fabrication.

3D printing of molds and posts

In order to fabricate the PDMS molds for cell-laden hydrogel casting and posts for the force measurement platform, the 3D bioprinter Inkredible+ from CELLINK® was used. Both structures were made of PDMS with a crosslinker ratio of 1:20. After printing, the molds were cured at 80 °C for 16 h and the posts were cured at 37 °C for 72 h. The walls of the molds were 1 mm high and their inner and outer diameters were 10 mm and 13 mm, respectively. The posts were 3 mm high, 0.5 mm wide and with 2 mm of lateral width.

3D bioengineering of human skeletal muscle tissues

For the fabrication of the hydrogel, a mixture GM (32.5% v/v) supplemented with 1 mg/mL of ACA (Sigma-Aldrich), 50 U/mL of thrombin (7.5% v/v), Matrigel® (60% v/v) and fibrinogen 8 mg/mL (50% v/v) were used. First, cultured human skeletal myoblasts at passage 4 and reaching 80% confluency were detached with trypsin as previously described. The resulting cell pellet after centrifugation was mixed with all the components except fibrinogen at a temperature in a cold ice bath, when Matrigel® is fluid. Once the solution was homogenized, fibrinogen was added and then, 80 μL of the final mixture was poured inside the mold, fast enough to avoid coagulation due to the fibrinogen to fibrin crosslinking. The density of cells in each mold was always 5 million/mL. After this, molds were incubated for 30-60 min to allow Matrigel® to crosslink. Then, 1.5 mL of Skeletal

Muscle Cell Growth Medium with 1 mg/mL of ACA was added to the Petri dish. Samples were put into the incubator for 48 h. At 24 h samples were gently lifted from the outer wall of the mold to enhance tissue compaction.

After 48 h samples were entirely lifted from the mold and carefully transferred to Petri dishes containing the 3D-printed posts. The ring of cells should encircle both pillars. DM supplemented with 1 mg/mL of ACA was added, and the samples were put into the incubator until they have reached optimum compaction and were able to contract under electrical stimulation. During this time, medium was changed every 38-72 h.

Electrical pulse stimulation

The setup for the electrical pulse stimulation was composed by a waveform generator (PM8572, Tabor Electronics), a signal amplifier x15, an oscilloscope (DS1104Z, Rigol) and a set of handmade electrodes based of graphite rods. The electrodes are made of two cylindrical graphite rods (cat. number 30250, Ladd Research) placed on opposite sides of the Petri dish (see Section 2 for more details). The recording was carried out inside an inverted microscope (DMi8, Leica) and samples are placed in a chamber that allows to mimic physiological conditions (37 °C and 5% CO2). Pulses of different frequencies (depending on experiment) of 2 ms were applied, keeping a constant electric field of 1 V/mm between the electrodes.

Measurement of force and contraction kinetics

Force measurement was carried from the displacement of the posts normalized by the height of the post at which the sample was applying the force, as carefully described in Section 2. From the contraction profiles, a home-made Python script was used to compute the maximum force from the initial stroke, the baseline force by averaging the force values at around 20 s of stimulation, and the half relaxation time as the time it took the sample to relax to the median value between the maximum and baseline forces. For contraction kinetics initially studied in Figure 4.13, a home-made Python (v. 3.7) script based on a tracking algorithm was applied using OpenCV (v. 4.1.2) Briefly, the function SelectROI was used to manually select a region of the tissue in the first frame of the video. Then, the image distance between the ROI of the first frame and the remaining frames (defining the distance as the pixel difference) was computed to obtain the contraction kinetics in arbitrary units.

Tumor necrosis factor α and peptide treatment

Some samples are treated with HumanKineTM Tumor Necrosis Factor α (TNF-α), human recombinant, expressed in HEK 293 cells (Sigma-Aldrich, # cat. H8916). The cytokine was added at different concentrations (20 ng/mL, 40 ng/mL or 80 ng/mL) in the culture media for 24 h. Argireline® Amplified peptide obtained from Lipotec™ Active Ingredients was added, when corresponding, at a concentration 2 mg/mL in the culture media for 24 h. Then, it was replenished for an additional 24 h.

Live/dead and immunostaining

Different types of analysis were performed in order to extract information about the viability of the 3D fabrication method and the correct differentiation and maturation of the tissue. Cell viability

was assessed by the Live/Dead™ Viability/Cytotoxicity assay for mammalian cells (Invitrogen™) kit. For the visualization of differentiated myoblasts, samples were immunostained using Myosin 4 Monoclonal Antibody (MF20) conjugated with Alexa Fluor 488 (eBioscience™) and Hoechst staining to label myosin and nuclei, respectively. ImageJ/Fiji software was used to process the results.

Statistical analysis

The statistical test used to perform multiple data comparison between myocyte diameter and number of nuclei per fiber (Figure 4.14) was one-way ANOVA followed by post hoc analysis (Tukey's Multiple Comparison test; N=12). To analyze the difference in contraction parameters at different frequencies between two group (Figure 4.15), a student's t-test was performed (N=4). Homoscedasticity was checked by the normal Q-Q plot and the equality of variances by the residuals versus fit plot. For the remaining experiments, data from the different contraction parameters were collected for each sample at different frequencies and for several days, as explained in the results section. For each of the three figures reporting comparisons between these data (Figures 4.16, 4.17 and 4.18), the following data treatment was applied. For Figure 4.16, whose aim was to detect differences after the addition of TNF-α after 24 h, each value of maximum force, baseline force or relaxation time was normalized to the average value within its sample group (control or TNF-α) at 0 h (before adding the cytokine). In this way, we wanted to reduce the initial variability in replicates, since we were only interested in the time evolution of the samples. A t-test of dependent (paired) samples was used to detect statistical differences between samples at 0 h and 24 h. A variance test (F-test) was performed beforehand to check whether we could account for equal variances or not in the t-test and the Kolmogorov-Smirnov (K-S) test to check for normality. For Figure 4.17, whose aim was to detect differences between control and peptide-treated groups at different time-points, all contractions parameters were also normalized to the average value for each group at 0 h (before adding the peptide). To test for significance, an independent-sample t-test was performed, also preceded by a variance F-test and normality K-S test. Finally, for Figure 4.18, whose aim was to detect differences in the contraction parameters when the peptide was added in aged muscle models, the values were normalized to their group average at 0 h, the time-point when TNF-α was removed and the peptide not added yet (see time-line in Figure 4.18A). As in the previous case, an independent-sample t-test was performed to check for statistical differences, preceded by a variance F-test to confirm or not variance equality and a normality K-S test. Statistical tests were carried out by R. The level of significance was set to p-value ≤ 0.05. For every experiment of Figures 4.16, 4.17 and 4.18, the population was N = 3-6.

References

[1] R. Mestre, T. Patiño, X. Barceló, S. Anand, A. Pérez-Jiménez, and S. Sánchez, *Force Modulation and Adaptability of 3D-Bioprinted Biological Actuators Based on Skeletal Muscle Tissue,* Advanced Materials Technologies **4**, 1800631 (2019).

[2] R. Mestre, T. Patiño, M. Guix, X. Barceló, and S. Sanchez, *Design, Optimization and Characterization of Bio-Hybrid Actuators Based on 3D-Bioprinted Skeletal Muscle Tissue,* in *Martinez-Hernandez U. et al. (eds) Biomimetic and Biohybrid Systems. Living Machines 2019. Lecture Notes in Computer Science*, Vol. 11556 (Springer, Cham, 2019) pp. 205–215.

[3] R. Mestre, T. Patiño, X. Barceló, and S. Sanchez, *3D bioprinted muscle-based bio-actuators: Force adaptability due to training,* in *Vouloutsi V. et al. (eds) Biomimetic and Biohybrid Systems.*

Living Machines 2018. Lecture Notes in Computer Science, Vol. 10928 (Springer, Cham, 2018) pp. 316–320.

[4] R. Mestre, N. Garcia, T. Patiño, M. Guix, M. Valerio-Santiago, N. Almiñana, and S. Sanchez, *3D-printed drug testing platform based on a 3D model of aged human skeletal muscle,* bioRxiv (2020), 10.1101/2020.06.18.158659.

[5] J. Malda, J. Visser, F. P. Melchels, T. Jüngst, W. E. Hennink, W. J. Dhert, J. Groll, and D. W. Hutmacher, *25th anniversary article: Engineering hydrogels for biofabrication,* Advanced Materials **25**, 5011 (2013).

[6] Y. J. Choi, T. G. Kim, J. Jeong, H. G. Yi, J. W. Park, W. Hwang, and D. W. Cho, *3D Cell Printing of Functional Skeletal Muscle Constructs Using Skeletal Muscle-Derived Bioink,* Advanced Healthcare Materials **5**, 2636 (2016).

[7] A. García-Lizarribar, X. Fernández-Garibay, F. Velasco-Mallorquí, A. G. Castaño, J. Samitier, and J. Ramon-Azcon, *Composite Biomaterials as Long-Lasting Scaffolds for 3D Bioprinting of Highly Aligned Muscle Tissue,* Macromolecular Bioscience **18**, 1800167 (2018).

[8] T. Osaki, S. G. Uzel, and R. D. Kamm, *On-chip 3D neuromuscular model for drug screening and precision medicine in neuromuscular disease,* Nature Protocols **15**, 421 (2020).

[9] M. A. Ortega, X. Fernández-Garibay, A. G. Castaño, F. De Chiara, A. Hernández-Albors, J. Balaguer-Trias, and J. Ramón-Azcón, *Muscle-on-a-chip with an on-site multiplexed biosensing system for in situ monitoring of secreted IL-6 and TNF-α,* Lab on a Chip **19**, 2568 (2019).

[10] H. Vandenburgh, J. Shansky, F. Benesch-Lee, V. Barbata, J. Reid, L. Thorrez, R. Valentini, and G. Crawford, *Drug-screening platform based on the contractility of tissue-engineered muscle,* Muscle and Nerve **37**, 438 (2008).

[11] R. Raman, L. Grant, Y. Seo, C. Cvetkovic, M. Gapinske, A. Palasz, H. Dabbous, H. Kong, P. P. Pinera, and R. Bashir, *Damage, Healing, and Remodeling in Optogenetic Skeletal Muscle Bioactuators,* Advanced Healthcare Materials **6**, 1700030 (2017).

[12] R. M. Duffy and A. W. Feinberg, *Engineered skeletal muscle tissue for soft robotics: Fabrication strategies, current applications, and future challenges,* Wiley Interdisciplinary Reviews: Nanomedicine and Nanobiotechnology **6**, 178 (2014).

[13] R. Raman, C. Cvetkovic, S. G. Uzel, R. J. Platt, P. Sengupta, R. D. Kamm, and R. Bashir, *Optogenetic skeletal muscle-powered adaptive biological machines,* Proceedings of the National Academy of Sciences of the United States of America **113**, 3497 (2016).

[14] Z. Orfanos, M. P. Gödderz, E. Soroka, T. Gödderz, A. Rumyantseva, P. F. Van Der Ven, T. J. Hawke, and D. O. Fürst, *Breaking sarcomeres by in vitro exercise,* Scientific Reports **6**, 1 (2016).

[15] T. Boudou, W. R. Legant, A. Mu, M. A. Borochin, N. Thavandiran, M. Radisic, P. W. Zandstra, J. A. Epstein, K. B. Margulies, and C. S. Chen, *A Microfabricated Platform to Measure and Manipulate the Mechanics of Engineered Cardiac Microtissues,* Tissue Engineering Part A **18**, 910 (2012).

[16] M. S. Sakar, D. Neal, T. Boudou, M. A. Borochin, Y. Li, R. Weiss, R. D. Kamm, C. S. Chen, and H. H. Asada, *Formation and optogenetic control of engineered 3D skeletal muscle bioactuators,* Lab on a chip **12**, 4976 (2012), arXiv:NIHMS150003 .

[17] C. Cvetkovic, R. Raman, V. Chan, B. J. Williams, M. Tolish, P. Bajaj, M. S. Sakar, H. H. Asada, M. T. A. Saif, and R. Bashir, *Three-dimensionally printed biological machines powered by skeletal muscle,* Proceedings of the National Academy of Sciences of the United States of America **111**, 10125 (2014).

[18] T. Patino, R. Mestre, and S. Sánchez, *Miniaturized soft bio-hybrid robotics: A step forward into healthcare applications,* Lab on a Chip **16**, 3626 (2016).

[19] Y. Sun, R. Duffy, A. Lee, and A. W. Feinberg, *Optimizing the structure and contractility of engineered skeletal muscle thin films,* Acta Biomaterialia **9**, 7885 (2013).

[20] S. Alom Ruiz and C. S. Chen, *Microcontact printing: A tool to pattern,* Soft Matter **3**, 168 (2007).

[21] P. Bajaj, B. Reddy, L. Millet, C. Wei, P. Zorlutuna, G. Bao, and R. Bashir, *Patterning the differentiation of C2C12 skeletal myoblasts.* Integrative Biology **3**, 897 (2011).

[22] K. Nagamine, T. Kawashima, T. Ishibashi, H. Kaji, M. Kanzaki, and M. Nishizawa, *Micropatterning contractile C2C12 myotubes embedded in a fibrin gel,* Biotechnology and Bioengineering **105**, 1161 (2010).

[23] P. Y. Wang, H. T. Yu, and W. B. Tsai, *Modulation of alignment and differentiation of skeletal myoblasts by submicron ridges/grooves surface structure,* Biotechnology and Bioengineering **106**, 285 (2010).

[24] V. Hosseini, S. Ahadian, S. Ostrovidov, G. Camci-Unal, S. Chen, H. Kaji, M. Ramalingam, and A. Khademhosseini, *Engineered contractile skeletal muscle tissue on a microgrooved methacrylated gelatin substrate,* Tissue Engineering - Part A **18**, 2453 (2012).

[25] R. Raman, C. Cvetkovic, and R. Bashir, *A modular approach to the design, fabrication, and characterization of muscle-powered biological machines,* Nature Protocols **12**, 519 (2017).

[26] J. M. Faustino Martins, C. Fischer, A. Urzi, R. Vidal, S. Kunz, P. L. Ruffault, L. Kabuss, I. Hube, E. Gazzerro, C. Birchmeier, S. Spuler, S. Sauer, and M. Gouti, *Self-Organizing 3D Human Trunk Neuromuscular Organoids,* Cell Stem Cell **26**, 172 (2020).

[27] C. A. Powell, B. L. Smiley, J. Mills, and H. H. Vandenburgh, *Mechanical stimulation improves tissue-engineered human skeletal muscle,* American Journal of Physiology - Cell Physiology **283**, 1557 (2002).

[28] D. G. Moon, G. Christ, J. D. Stitzel, A. Atala, and J. J. Yoo, *Cyclic mechanical preconditioning improves engineered muscle contraction,* Tissue Engineering - Part A **14**, 473 (2008).

[29] L. Madden, M. Juhas, W. E. Kraus, G. A. Truskey, and N. Bursac, *Bioengineered human myobundles mimic clinical responses of skeletal muscle to drugs,* eLife **2015**, 4:e04885 (2015).

[30] M. Demestre, M. Orth, K. J. Föhr, K. Achberger, A. C. Ludolph, S. Liebau, and T. M. Boeckers, *Formation and characterisation of neuromuscular junctions between hiPSC derived motoneurons and myotubes,* Stem Cell Research **15**, 328 (2015).

[31] C. D. Kaufman, S. C. Liu, C. Cvetkovic, C. A. Lee, G. Naseri Kouzehgarani, R. Gillette, R. Bashir, and M. U. Gillette, *Emergence of functional neuromuscular junctions in an engineered, multicellular spinal cord-muscle bioactuator,* APL Bioengineering **4**, 026104 (2020).

[32] J. Sala-Jarque, F. Mesquida-Veny, M. Badiola-Mateos, J. Samitier, A. Hervera, and J. A. del Río, *Neuromuscular Activity Induces Paracrine Signaling and Triggers Axonal Regrowth after Injury in Microfluidic Lab-On-Chip Devices,* Cells **9**, 302 (2020).

[33] O. Aydin, A. P. Passaro, M. Elhebeary, G. J. Pagan-Diaz, A. Fan, S. Nuethong, R. Bashir, S. L. Stice, and M. T. A. Saif, *Development of 3D neuromuscular bioactuators,* APL Bioengineering **4**, 016107 (2020).

[34] O. Aydin, X. Zhang, S. Nuethong, G. J. Pagan-Diaz, R. Bashir, M. Gazzola, and M. T. A Saif, *Neuromuscular actuation of biohybrid motile bots,* Proceedings of the National Academy of Sciences of the United States of America **116**, 19841 (2019).

[35] T. Osaki, S. G. Uzel, and R. D. Kamm, *Microphysiological 3D model of amyotrophic lateral sclerosis (ALS) from human iPS-derived muscle cells and optogenetic motor neurons,* Science Advances **4**, 1 (2018).

[36] M. A. Bakooshli, E. S. Lippmann, B. Mulcahy, N. Iyer, C. T. Nguyen, K. Tung, B. A. Stewart, H. Van Den Dorpel, T. Fuehrmann, M. Shoichet, A. Bigot, E. Pegoraro, H. Ahn, H. Ginsberg, M. Zhen, R. S. Ashton, and P. M. Gilbert, *A 3d culture model of innervated human skeletal muscle enables studies of the adult neuromuscular junction,* eLife **8**, 1 (2019).

[37] A. S. Wang and O. Dreesen, *Biomarkers of cellular senescence and skin aging,* Frontiers in Genetics **9**, 1 (2018).

[38] Y. Saito, T. S. Chikenji, T. Matsumura, M. Nakano, and M. Fujimiya, *Exercise enhances skeletal muscle regeneration by promoting senescence in fibro-adipogenic progenitors,* Nature Communications **11**, 1 (2020).

[39] B. G. Childs, M. Gluscevic, D. J. Baker, R. M. Laberge, D. Marquess, J. Dananberg, and J. M. Van Deursen, *Senescent cells: An emerging target for diseases of ageing,* Nature Reviews Drug Discovery **16**, 718 (2017).

[40] S. Watanabe, S. Kawamoto, N. Ohtani, and E. Hara, *Impact of senescence-associated secretory phenotype and its potential as a therapeutic target for senescence-associated diseases,* Cancer Science **108**, 563 (2017).

[41] B. Childs and J. van Deursen, *An evolving picture of cell senescence,* Nature **566**, 46 (2019).

[42] Y.-P. Li, Y. Chen, J. John, J. Moylan, B. Jin, D. L. Mann, and M. B. Reid, *TNF-α acts via p38 MAPK to stimulate expression of the ubiquitin ligase atrogin1/MAFbx in skeletal muscle,* The FASEB Journal **19**, 362 (2005).

[43] J. De Larichaudy, A. Zufferli, F. Serra, A. M. Isidori, F. Naro, K. Dessalle, M. Desgeorges, M. Piraud, D. Cheillan, H. Vidal, E. Lefai, and G. Némoz, *TNF-α- and tumor-induced skeletal muscle atrophy involves sphingolipid metabolism,* Skeletal Muscle **2**, 2 (2012).

[44] V. Adams, N. Mangner, A. Gasch, C. Krohne, S. Gielen, S. Hirner, H. J. Thierse, C. C. Witt, A. Linke, G. Schuler, and S. Labeit, *Induction of MuRF1 Is Essential for TNF-α-Induced Loss of Muscle Function in Mice,* Journal of Molecular Biology **384**, 48 (2008).

[45] Y. Wang, S. S. Welc, M. Wehling-Henricks, and J. G. Tidball, *Myeloid cell-derived tumor necrosis factor-alpha promotes sarcopenia and regulates muscle cell fusion with aging muscle fibers,* Aging Cell **17**, e12828 (2018).

[46] S. Ding, J. Zhang, S. Yin, J. Lu, M. Hu, J. Du, J. Huang, and B. Shen, *Inflammatory cytokines tumour necrosis factor-α and interleukin-8 enhance airway smooth muscle contraction by increasing L-type Ca2+ channel expression,* Clinical and Experimental Pharmacology and Physiology **46**, 56 (2019).

[47] L. N. Van Kann and A. J. Bakker, *Effect of tumor necrosis factor α on electrically induced calcium transients elicited in C2C12 skeletal myotubes,* Muscle and Nerve **35**, 251 (2007).

[48] R. C. Langen, A. M. Schols, M. C. Kelders, J. L. Van Der Velden, E. F. Wouters, and Y. M. Janssen-Heininger, *Tumor necrosis factor-α inhibits myogenesis through redox-dependent and -independent pathways,* American Journal of Physiology - Cell Physiology **283**, 714 (2002).

[49] D. T. Wang, Y. Yin, Y. J. Yang, P. J. Lv, Y. Shi, L. Lu, and L. B. Wei, *Resveratrol prevents TNF-α-induced muscle atrophy via regulation of Akt/mTOR/FoxO1 signaling in C2C12 myotubes,* International Immunopharmacology **19**, 206 (2014).

[50] R. A. Collins and M. D. Grounds, *The role of tumor necrosis factor-alpha (TNF-α) in skeletal muscle regeneration: Studies in TNF-α(-/-) and TNF-α(-/-)/LT-α(-/-) mice,* Journal of Histochemistry and Cytochemistry **49**, 989 (2001).

[51] U. Wollina, R. Wetzker, M. B. Abdel-Naser, and I. L. Kruglikov, *Role of adipose tissue in facial aging,* Clinical Interventions in Aging **12**, 2069 (2017).

[52] M. Kaur, R. K. Garg, and S. Singla, *Analysis of facial soft tissue changes with aging and their effects on facial morphology: A forensic perspective,* Egyptian Journal of Forensic Sciences **5**, 46 (2015).

[53] D. R. Merrill, M. Bikson, and J. G. Jefferys, *Electrical stimulation of excitable tissue: Design of efficacious and safe protocols,* Journal of Neuroscience Methods **141**, 171 (2005).

[54] N. Tandon, C. Cannizzaro, P.-H. G. Chao, R. Maidhof, A. Marsano, H. T. H. Au, M. Radisic, and G. Vunjak-Novakovic, *Electrical stimulation systems for cardiac tissue engineering,* Nature Protocols **4**, 155 (2009).

[55] A. Khodabukus and K. Baar, *Defined electrical stimulation emphasizing excitability for the development and testing of engineered skeletal muscle,* Tissue Engineering - Part C: Methods **18**, 349 (2012).

[56] H. Fujita, T. Nedachi, and M. Kanzaki, *Accelerated de novo sarcomere assembly by electric pulse stimulation in C2C12 myotubes,* Experimental Cell Research **313**, 1853 (2007).

[57] D. M. Brown, T. Parr, and J. M. Brameld, *Myosin heavy chain mRNA isoforms are expressed in two distinct cohorts during C2C12 myogenesis,* Journal of Muscle Research and Cell Motility **32**, 383 (2012).

[58] C. DeNardi, S. Ausoni, P. Moretti, L. Gorza, M. Velleca, M. Buckingham, and S. Schiaffino, *Type 2X-myosin heavy chain is coded by a muscle fiber type-specific and developmentally regulated gene,* Journal of Cell Biology **123**, 823 (1993).

[59] H.-W. Kang, S. J. Lee, I. K. Ko, C. Kengla, J. J. Yoo, and A. Atala, *A 3D bioprinting system to produce human-scale tissue constructs with structural integrity,* Nature Biotechnology **34**, 312 (2016).

[60] T. D. Schmittgen and K. J. Livak, *Analyzing real-time PCR data by the comparative CT method,* Nature Protocols **3**, 1101 (2008).

[61] C. Cvetkovic, M. Ferrall-Fairbanks, E. Ko, L. Grant, H. Kong, M. Platt, and R. Bashir, *Investigating the Life Expectancy and Proteolytic Degradation of Engineered Skeletal Muscle Biological Machines,* Scientific Reports **7**, 1 (2017).

[62] S. Hunter, M. White, and M. Thompson, *Techniques to Evaluate Elderly Human Muscle Function: A Physiological Basis,* The Journals of Gerontology Series A: Biological Sciences and Medical Sciences **53A**, B204 (1998).

[63] D. J. Wilkinson, M. Piasecki, and P. J. Atherton, *The age-related loss of skeletal muscle mass and function: Measurement and physiology of muscle fibre atrophy and muscle fibre loss in humans,* Ageing Research Reviews **47**, 123 (2018).

[64] S. Chan and S. I. Head, *Age- and gender-related changes in contractile properties of non-atrophied EDL muscle,* PLoS ONE **5**, 20 (2010).

[65] S.-J. Choi, *Age-related functional changes and susceptibility to eccentric contraction-induced damage in skeletal muscle cell,* Integrative Medicine Research **5**, 171 (2016).

V

Bio-hybrid robots based on skeletal muscle tissue

1. Introduction and state of the art

BIOLOGICAL systems have evolved throughout millennia to develop sophisticated mechanisms of self-organization, actuation and sensing that are difficult to replicate in the field of robotics. In particular, biomimetic soft robotics is emerging as a sub-field of the robotics field that aims at overcoming some of the challenges related to the mechanical properties of the materials, such as compliance, flexibility and overall safety for human interaction, as the rigidity and stiffness of conventional materials limit their applications into certain healthcare or biomedical disciplines[1–3]. Recent developments in material science have made possible the fabrication of biomimetic soft robots that are able to perform some simple types of actuation[4], including crawling[5, 6] or grasping[7], but they are still far from the degree of complexity and sophistication of animals.

One of the most investigated applications of soft robotics is the development of artificial muscles that can mimic the performance of native muscle tissue in mammals. Muscle tissue is inherently complex, as it is simultaneously strong and fast and can enable a wide variety of movements through an efficient self-organization of its fiber bundles. However, current materials still lack the ability to fully replicate these properties[8]. Even more, other features from biological tissues, such as self-healing, energy efficiency, power-to-weight ratio, adaptability or bio-sensing, to name only a few, are strongly desired but difficult to achieve with artificial soft materials[9]. Bio-hybrid robotics is born at this point as a synergistic strategy to integrate the best characteristics of biological entities and artificial materials into more efficient and complex systems that can overcome the difficulties that current soft robots face. Several strategies to unify the development of bio-hybrid devices have emerged, such as the robotic taxonomic key (RTK), that identifies four main elements that an autonomous robotic system can have: structure, actuation, sensing and control[9]. From this starting point, one can analyze the capabilities of a bio-hybrid system, defining the artificial or organic nature of the four key elements, to help in the classification and further development on the field. By finding more efficient ways of unifying the most suitable features of current technologies and living organisms, the field could reach a change of paradigm to boost the performance and efficiency of robotic systems.

In this short introduction, we will focus on bio-hybrid robotic systems based on mammalian muscle tissue. Although this sub-field is still at its infancy, many examples of muscle-powered bio-robots have appeared in the last decade, and current efforts are now being dedicated to the integration of several kinds of tissue, such as the formation of neuromuscular junctions (NMJ) to obtain more sophisticated systems. First efforts in the field were based on cardiomyocytes or cardiac muscle cells. This type of cells are strong and can synchronize their contractions spontaneously, avoiding the need of an external control system to obtain autonomous bio-hybrid robots. For instance, Tanaka *et al.* fabricated a micro-spherical heart pump that was powered by cultured cardiomyocytes[10]. Park *et al.* fabricated micro-devices based on 2D cultures of cardiac cells that could deform polydimethylsiloxane (PDMS) cantilevers for real life measurement of their forces, opening the way for the development of untethered hybrid devices[11, 12]. Indeed, a two-legged[13] and a six-legged[14] crawling bio-robots, made of thin layers of cardiomyocytes on thin structures were also fabricated. Moreover, Chat *et al.* used a stereolithography (SLA) 3D printer to fabricate custom-designed skeletons of a bio-hybrid robot based on cardiac cells that could move at different speeds depending on the design, reaching up to 200 μm/s[15].

Despite the variety of examples using cardiac cells to power bio-robot devices, some inherent limitations might hinder their applicability into more complex systems. For instance, most of the fabricated bio-robots have been focused on some type of thin film, normally PDMS, seeded with cardiac cells[16], since the natural organization of this type of tissue in the heart is to form two-

dimensional layers. Nevertheless, swimming bio-hybrid devices, mimicking the motion seen in the depths of oceans, have resulted in great examples biomimetic bio-robots that can swim[17, 18], especially a bio-hybrid soft robotic sting-ray that could swim due to cardiac cells optogenetically modified to respond to light[19], and cardiac-based medusoids that could mimic the thrusting mechanism of jellyfish[20]. The presence of spontaneous contractions in cardiac cells, that can be stimulated and synchronized at a certain frequency, but cannot be stopped, is also one of the limitations that this kind of tissue finds. Skeletal muscle tissue, thus, possesses a wider range of adaptability and controllability, since these cells adopt a three-dimensional structure that can be accommodated to different substrates and their contractions are induced on demand by means of an external electrical or optical actuation.

Initial examples of bio-hybrid robots based on skeletal muscle tissue were bio-actuators based on the deflection of cantilevers by single myotubes or full tissue, similar to the cases described in the previous chapter[21–25], or used as grippers [26, 27]. Untethered bio-hybrid robots, on the other hand, have been mainly based on crawling mechanisms[28]. Cvetkovic *et al.* developed a 3D-printed bio-bot composed of two legs joined by a beam structure that could walk on the bottom of a Petri dish by differences in friction between two asymmetric legs[29]. Indeed, they demonstrated, both experimentally and by simulations, that adding an asymmetry in the design was necessary for motion. Later on, Raman *et al.* presented the same bio-robotic device controlled by light after optogenetically modifying the skeletal muscle cells to contract upon blue light illumination, obtaining a cable-free and remote control system[30]. Other examples with the same platform have been dedicated to the investigation of some of the features that bio-hybrid integration can offer, such as self-healing[31], adaptability[30], the addition of neurons [32], their long-time preservation [33, 34], their scalability[35] or their integration with micro-electrodes[36]. In particular, recent efforts are being dedicated to the integration of neuronal tissue and skeletal muscle tissue, in order to better resemble native muscle and obtain an improved controllability of these bio-robots[37, 38]. On this subject, recently, Aydin *et al.* presented a bio-hybrid swimmer with functional NMJ that could swim with flagellar dynamics, although at low speeds due to the difficulty of motion at low Reynolds number[39].

Advances in the field of smart materials could bring another level of complexity and applicability into this kind of devices with the integration of responsive or nanocomposite hybrid substrates[40–42]. Gold nanoparticles or nanowires, for instance, have been widely investigated for the development of cardiac patches[43, 44], but little attention has been paid to their applications in skeletal muscle tissue bioengineering or hybrid bio-robots based on them[45]. Likewise, graphene, graphene oxide (GO) or reduced graphene oxide (rGO) can provide benefits in tissue engineering of skeletal muscle thanks to improvements in the mechanical and conductive properties of the scaffolds[46, 47]. For instance, Du *et al.* used rGO in a biodegradable polycitrate-based elastomer, increasing its tensile strength and improving the differentiation and regeneration of skeletal muscle cells through the physicochemical properties or rGO[48]. Likewise, GO increased the viability and metabolic activity of encapsulated C2C12 cells in GO-alginate scaffolds[49] and graphene sheets have been used to regulate the differentiation of skeletal muscle cells in 2D[46] or to control the actuation of bio-bots as embedded electrodes[36].

Piezoelectric nanocomposites, on the other hand, could be excellent candidates for the next generation of nano-engineered bio-hybrid robots, due to the possibility of converting sound waves into voltage differences and provide remote actuation of skeletal muscle tissue[50, 51]. Moreover, they could offer benefits in the differentiation and maturation of these cells. For instance, the integration of nanogenerators based on ZnO nanosheets with piezoelectric properties, can trigger the opening of

ion channels in osteoblast-like cells, when seeded on 2D cultures that are sensible to the motility of the cells[52]. Piezoelectric boron nitride nanotubes (BNNTs)[53], although they have received less attention in biomedical applications compared to carbon nanotubes[54–56], have been proven to increase the metabolic activity of C2C12 cells in 2D cultures, although their differentiation was not significantly affected[57]. Moreover, Ricotti *et al.* employed BNNTs in a 2D co-culture of muscle cells and fibroblasts to induce intracellular electrical stimuli *via* ultrasound waves, using their piezoelectric effect[58].

In this chapter, we will gather all the knowledge from the previous chapters into the fabrication of a functional hybrid bio-robot based on skeletal muscle tissue that can swim upon electric pulse stimulation (EPS) in Section 2. The skeleton of this bio-robot is fabricated by 3D printing of PDMS and its design optimized through finite element analysis (FEA) simulations. We characterize the motion between symmetric and asymmetric skeletons, demonstrating the need for asymmetry to achieve reliable swimming. Moreover, in Section 3 we show some preliminary results towards the integration of nanocomposites into these bio-hybrid systems, by using the bio-bots designed by Bashir *et al.* as fundamental backbone[28]. By integrating piezoelectric BNNTs into the cell-laden hydrogel of the bio-bots, we will discover that they can acquire faster walking speed and stronger force outputs when compared to control samples, thus confirming the hypothesis that self-stimulation of the myotubes during differentiation in the form of spontaneous contractions can induce piezoelectric effect and further stimulation in a feedback loop.

2. A swimming bio-hybrid robot based on skeletal muscle tissue

2.1. Objectives

This section presents the fabrication and characterization of a bio-hybrid swimmer based on skeletal muscle tissue. Most examples of hybrid swimmers in the literature have been based on cardiac cells, biomimicking the motion mechanism of invertebrate animals or certain fish[19, 20], while most of skeletal-muscle-based bio-robots have been actuators or walkers[27, 29]. For the purpose of fabricating a bio-hybrid swimmer based on skeletal muscle tissue, all the knowledge acquired about the 3D bioengineering of muscle and 3D printing of artificial skeletons to create hybrid structures were brought together into the optimization, fabrication and motion characterization of an untethered spring-like bio-hybrid robot that could swim in a fluid by inertial strokes upon electrical stimulation.

The objectives of this section are, thus, the following: i) to optimize the design and fabrication of skeleton of a spring-like bio-robot, based on PDMS, using a serpentine design as foundation; ii) to apply the knowledge about 3D skeletal muscle tissue engineering to assemble such a robot, with differentiated and responsive myotubes; iii) to design a tracking protocol to characterize the motion of the bio-hybrid swimmer; and iv) to compare the efficiency of the motion of symmetric and asymmetric bio-robots.

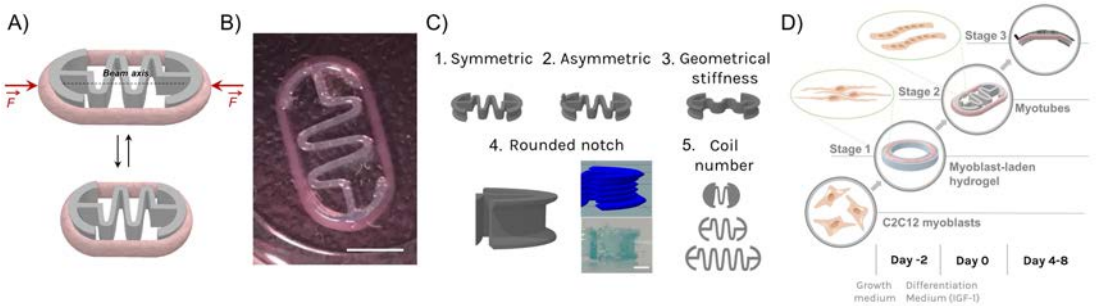

Figure 5.1: Design and fabrication of a bio-swimmer based on skeletal muscle tissue. A) Schematic representation of the working principle of the spring-like bio-robot, composed of a serpentine skeleton made of PDMS surrounded by a tissue ring of skeletal muscle tissue. Upon EPS, the tissue contracts and compresses the skeleton. B) Real image of a self-assembled bio-robot. Scale bar: 3 mm. C) Different designs and features were considered for the optimization of the bio-robot skeleton. D) Schematic of the fabrication process, from myoblast embedding in the hydrogel until formation of the bio-robot.

V

2.2. Results and discussion

Bio-swimmer fabrication

The untethered bio-hybrid robot based on skeletal muscle cells consisted on a serpentine-like skeleton, surrounded by a muscle tissue that could apply a longitudinal force along the beam axis upon EPS. The compliant nature of the serpentine structure allowed its deformation with low geometrical stiffness and a restoring force that brought the bio-robot back to its original state, acting like a spring (Figure 5.1A). The bio-robot could move freely due to its untethered nature (Figure 5.1B) and the hydrodynamic flows created by the contractions and subsequent deformation produced a swimming-like motion. Moreover, we hypothesize that the compliant structure provided a beneficial differentiation support of the muscle tissue due to the presence of the restoring force, which added a further level of mechanical stimulation in the form of a feedback loop.

The skeleton was composed of PDMS and fabricated by extrusion-based 3D printing, in a similar way to the two posts that composed the force measurement platform from Chapter IV. The use of the 3D printing technique provided with versatility and fast prototyping, useful to generate and optimize different geometries and configurations of the artificial skeleton (Figure 5.1C). This allowed us to consider symmetric (1) and asymmetric (2) designs by the inclusion of a small post bulging out of one of the sides, in order to generate an asymmetric compaction of the skeleton of the bio-robot, which is necessary to achieve directional motion. The overall stiffness of the skeleton could be changed by varying the curing-agent-to-base ratio of PDMS, but an extra level of optimization could be attained by modifying its geometrical stiffness by considering different types of springs in the central part (3). A rounded notch at both ends of the skeleton was carefully designed and 3D-printed (4) in order to accommodate the tissue ring and avoid its accidental release. Finally, further optimization could be achieved by including different number of coils in the design to create bio-robots with different properties and sizes (5).

Following the 3D encapsulation and differentiation protocols developed in the previous chapters, C2C12 myoblasts were embedded at a final concentration of 10 million cells/mL in a hydrogel composed of Matrigel® and fibrin as main components, as already discussed in Chapter IV (Figure 5.1D). The cell-laden hydrogel was manually casted on a 3D-printed PDMS injection mold with a circular shape (Stage 1). The tissue construct was left in a cell incubator at 37 °C and 5% CO_2 atmosphere until Matrigel® was fully crosslinked ($\sim$ 30 min). Growth medium (GM) supplemented with

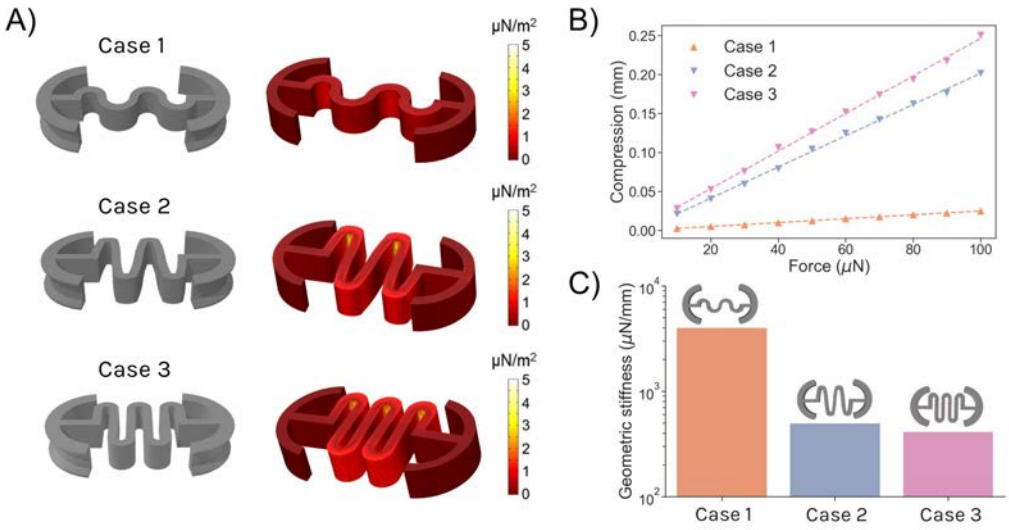

Figure 5.2: FEA simulations of mechanical deformation of symmetric skeletons. A) Three different cases were considered to optimize the coil curvature and shape, depending on the geometrical stiffness of the construct. On the right side, von Mises stresses of each of the structure after a symmetrical load of 100 μN on each side. B) Maximum compression of the skeleton in terms of the applied force, for each of the three cases. C) Geometrical stiffness obtained from the linear spring response of B) for each of the three cases.

6-aminocaproic acid (ACA) to avoid degradation of collagen by proteases was added and kept for 2 days. Then, the tissue was gently lifted from the mold and transferred to the 3D-printed compliant skeleton (Stage 2). At this point, the culture medium was changed to differentiation medium (DM) supplemented with ACA and insulin-like growth factor 1 (IGF-1) to promote the fusion and differentiation of myoblasts into myotubes. The natural compaction of myoblast-laden hydrogels during cell differentiation and maturation allowed the tissue to perfectly adapt to the shape of the compliant skeleton thanks to the rounded edges, avoiding the formation of stresses that could damage the tissue. Due to these compaction forces and to the rounded notch that prevented disassembly, the bio-robot could adopt a buckling structure that was more efficient for motion (Stage 3).

Optimization of the skeleton

Optimal geometrical parameters on the compliant skeleton were evaluated by using finite element analysis (FEA), while considering different serpentine geometries. To study the effect of the type of spring on the compression efficiency, we designed three different geometries: i) case 1, with a low-degree variation along the serpentine, creating low amplitude oscillations; ii) case 2, with much larger amplitude in the oscillations, allowing a better distribution of the stresses; and iii) case 3, with large amplitude, but a strict 90°angle at the points of curvature (Figure 5.2). In order to mimic the contractions of the skeletal muscle tissue that induced compression of the spring-like skeleton, two uni-axial point forces of the same magnitude were applied at both sides of the structure in a 3D simulation, assuming static conditions and only mechanical and linear deformations. For a more meaningful simulation of the contraction kinetics, the profile of a real twitch contraction was measured by image difference as described in Chapter IV and were normalized in a way that the maximum value was 100 μN. The right-hand side of Figure 5.2A shows the von Mises stresses in the skeletons for a compression force of 100 μN. The von Mises stress represents the equivalent stress across the structure and gives information about the distribution of these. As can be expected, the highest stress is felt at the inner part of the structure. With small forces in the range of hundreds of μN, the yield

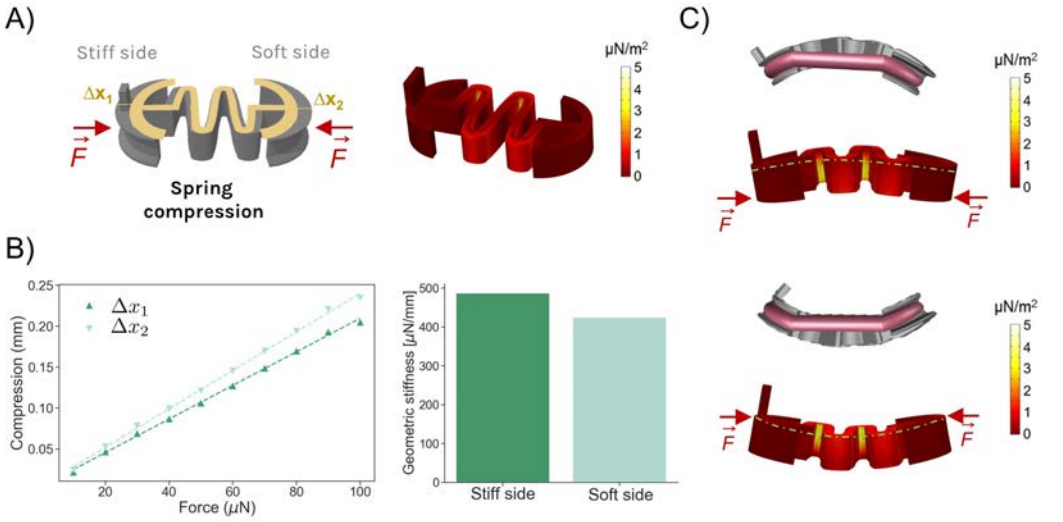

Figure 5.3: FEA simulations of mechanical deformation of asymmetric skeletons. A) An asymmetric skeleton, based on the medium geometric stiffness obtained in the previous figure, was designed with a post bulging out of one of its sides. Compression forces simulating the tissue contraction compressed the skeleton in an asymmetric manner. B) The maximum compression of both sides of the actuator (Δx_1 and Δx_2) in terms of the applied force. On the right, the geometric stiffness of each of the sides labeled in A). C) The buckling behavior was demonstrated to be possible in each direction by applying an asymmetrically distributed load out of the center, as the force vectors indicate.

criterion of the von Mises stress is not fulfilled, as the maximum stress is much lower than the yield stress of PDMS[59], and therefore a linear analysis is appropriate to model the deformations of the material. The higher stress values obtained for cases 2 and 3 already indicate that these structures can probably compress easier than case 1, although a better characterization of this can be obtained by calculating the geometric stiffness of the designs.

The geometric stiffness of the skeletons gives information about the stiffness of the structure taking only into consideration the geometry. We performed a force sweep using the aforementioned contraction profile with a maximum force in the range of 10-100 μN (symmetrically at both edges), based on reported forces in the literature[29, 60]. The maximum uni-axial compression of the compliant skeleton, which coincided in time with the maximum force of the contraction profile, was plotted in terms of the force (Figure 5.2B), revealing a linear elastic response dictated by Hooke's law, that allowed us to calculate the geometrical stiffness of the material, k, by the equation $F = kx$, where F is the applied force and x the compression. The inverse of the slope of Figure 5.2B yields the geometrical stiffnesses of Figure 5.2C, where we can see that case 1, with a soft curvature in its coil, had much larger geometrical stiffness than the other two cases, which presented slightly similar values. Further experiments with 3D-printed skeletons revealed that case 3 was too easily compressible and would collapse, making the serpentine coils touch and stick to each other. Therefore, the design of case 2 provided the appropriate stiffness conditions for muscle-induced compression in the expected force ranges.

Having defined the ideal serpentine structure, the asymmetry of the bio-hybrid robot was also studied by FEA simulations (Figure 5.3A). Likewise, by simulating two uni-axial equivalent contraction profiles at both sides of the skeleton, we discovered that the presence of a small post bulging out of one of the sides induced a differential compression of the structure, as demonstrated in Figure 5.3B. In this compression vs force plot, it can be seen how the maximum compression of the stiffer side (with the induced asymmetry), termed Δx_1, was larger than the compression in the softer side,

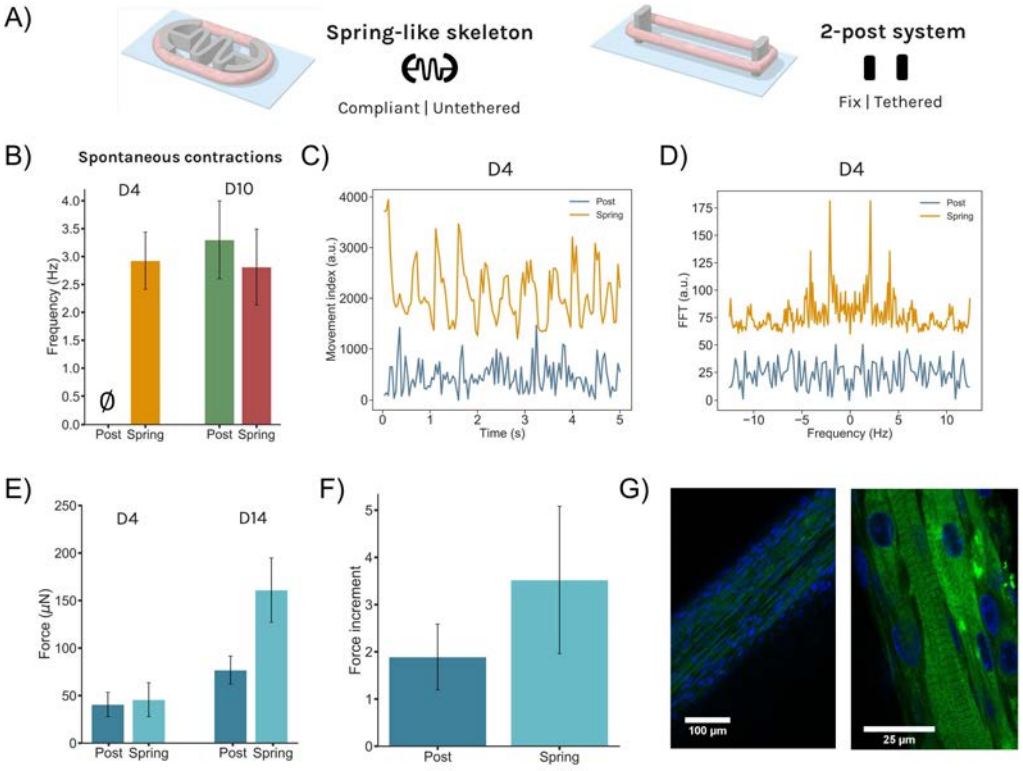

Figure 5.4: Force characterization of bio-robots. A) In order to demonstrate the benefits of differentiation in a compliant skeleton system, we compared the force outputs of tissues differentiated in a bio-robot (left) and a bio-actuator (right) based on a 2-post system. B) Spontaneous contractions were shown much earlier in bio-robots than in bio-actuators, which were only showing strong and synchronized spontaneous contractions at D10 of differentiation. C) The intensity of the contractions in arbitrary units for each system at D4 shows defined contractions for the bio-robot and only noise for the bio-actuator. D) This is further demonstrated by a FFT, where only the spring-like system shows a main peak at approximately 3 Hz. E) The forces upon EPS of both systems were similar at D4. However, at D14, there was a force increment of 3-fold for the bio-robot compared to the bio-actuator, as shown in F). G) Immunostaining images of MyHCII (green) and cell nuclei (blue) of the bio-robot, showing the formation of sarcomeric structures inside the myotubes.

Δx_2. As in the previous figure, the geometrical stiffness was extracted from the force-compression relationship and quantitatively demonstrated that the side with the post was stiffer than the other side. As it is known that an asymmetry is necessary for motion[29], we expected that this differential compression would produce a difference in the flow fields, leading to directional motion.

Finally, we demonstrated the feasibility of the buckling behavior experimentally observed and presented in Figure 5.1D. For this purpose, we simulated uni-axial compression force at both sides of the skeleton, but out of center, as indicated by the force vectors in Figure 5.3D. These forces mimicked the passive compaction of the tissue that occurs during myogenesis[29, 60]. We hypothesize that this effect could be caused by a spontaneous symmetry breaking during tissue compaction, probably due to a combination of the heterogeneity of the muscle constructs that could lead to an asymmetric distribution of the compression forces and the interaction with close interfaces, as we will see later.

Differentiation and force evaluation

It is known that dynamic mechanical stimulation is beneficial for the differentiation and maturation of skeletal muscle cells, as it mimics the conditions of native tissue[61, 62]. Therefore, we hypothesized that the spring-like configuration of the serpentine skeleton provided dynamic stimu-

lation after spontaneous contractions by reacting with an opposite restoring force that could further expand the tissue, offering mechanical stretching in the form of a feedback loop. To demonstrate this, we compared two types of bio-robots: i) the compliant and untethered spring-like skeleton, and ii) a 2-post system that was tethered and less compliant (Figure 5.4A). During myogenesis, we checked for the presence of spontaneous contractions *via* optical microscopy revealing that, after 4 days of differentiation (D4), only spring-like bio-bots were showing strong spontaneous contractions, fully synchronized and at a frequency of approximately 3 Hz, while bio-actuators in the 2-post system were not showing any spontaneous contractions(Figure 5.4B). At D8 of differentiation, the muscle tissue in the 2-post system showed small localized contractions that were not synchronized and, eventually, at D10, the spontaneous contractions were strong and globally distributed, as in the bio-hybrid robot (Figure 5.4B).

The movement index of the contractions, defined as the image difference in a small region of interest (ROI) in the tissue, is shown in Figure 5.4D at D4 of differentiation. It can be seen how only the bio-robot in a spring-like skeleton showed periodic spikes in its movement index (representing the spontaneous contractions), while the signal of the 2-post system was mainly noise. A fast Fourier transform (FFT) of this signal (Figure 5.4D) further confirmed that only the former showed synchronized and defined contractions at 3 Hz, while the signal of the latter did not have any defined frequencies and was just noise.

The strength of the contractions was also evaluated and compared (Figure 5.4E). Although the bio-actuator in the 2-post system did not present spontaneous contractions at D4, EPS could induce contractions in the tissue, which were of a similar magnitude to those induced in the bio-robot. However, force measurements after several days in differentiation demonstrated that the muscle tissue of the spring-like bio-robot had increased its force almost 4-fold, while the 2-post bio-actuator only by 2-fold, indicating an enhanced maturation of the tissue (Figure 5.4F). Confocal immunostaining of myosin heavy chain II (MyHCII) and cell nuclei showed well aligned myotubes with the presence of sarcomeric structures in the hybrid bio-robot (Figure 5.4G).

Motion evaluation with tracking algorithms

Motion evaluation of the bio-hybrid robot was performed with a home-made Python tracking script based on computer vision algorithms that could characterize the motion of the bio-robots after being recorded with any type of smartphone camera (Figure 5.5). In brief, the video file of the recorded bio-robot was loaded into the script and the first frame was prompted for the user to manually select an ROI covering the whole bio-robot area (Figure 5.5A). Then, an object tracking algorithm based on an online AdaBoost feature selection[63] was applied to this ROI through every frame of the video. This algorithm is based on machine learning and extracts identifying features from the object to track its position through time, even if the bio-robot rotates and changes direction. As smartphone videos can be located at different distances and are not calibrated, the script also allowed manual calibration of the video by using a grid paper as background. Before starting the tracking, the user could manually draw a line along one of the squares and the script would find the conversion pixel/mm to calibrate the displacements and create a scale bar at the top of the image. Moreover, time in seconds and frames per second (FPS) of the original video were displayed on top, as well as a close-up image of the tracked object online, to ensure that the tracking was capturing the bio-bot properly during the video. The central position of the ROI in mm was stored and used to generate a color-coded trajectory on the images (Figure 5.5B), as well as to plot the total displacement and compute the speed of motion. As average from all the trackings, we found that both symmetric and asymmetric bio-robots were able to achieve motion. In general, symmetric designs could move

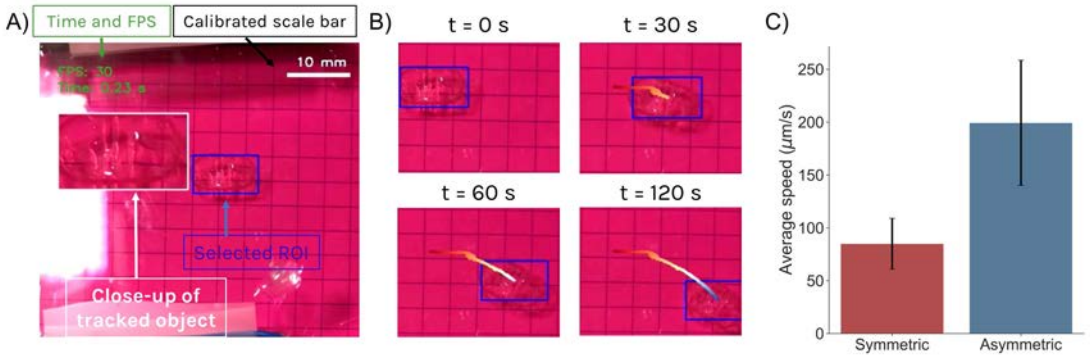

Figure 5.5: Home-made script for tracking of bio-bots. A) Snapshot of the initial frame of the tracking, in which several features can be observed: i) the time and FPS of the video are stamped on the top left corner of the video; ii) an ROI is manually selected to contain the bio-robot, or part of it, which is tracked along the video; iii) the grid paper below the Petri dish is used to calibrate the spatial dimensions; and iv) a close-up of the tracked object inside the ROI is displayed to make sure that the bio-robot is being properly tracked. B) Snapshots of a tracking, showing a color-coded trajectory, going from red (short time) to blue (long time). C) The average speed of symmetric and asymmetric bio-robots shows that having an asymmetric skeleton results in more efficient swimming.

only under certain conditions that broke its symmetry at speeds lower than 100 μm/s, as we will see in the next subsection, but asymmetric bio-robots could swim at much higher speeds and in a consistent manner, although with great variability between samples (Figure 5.5C).

Motion evaluation of symmetric bio-robots

Due to the hydrophobicity of PDMS and surface tension at the air-liquid interface, symmetric bio-robots could remain floating without showing any buckling behavior (Figure 5.6A). However, asymmetry could be induced with the symmetrical skeletons by forcing the bio-robot inside the culture medium, while working in a plastic Petri dish, during the differentiation process. Without the high surface tension of the air-liquid interface, buckling deformation was spontaneously generated due to the heterogeneity of the muscle construct yielding a net compaction force outside its axis of symmetry (Figure 5.6B). Interactions between PDMS and the plastic surface close to the solid-liquid interface favored this kind of conformation, as working with glass substrates did not produce the same effect. This spontaneous symmetry breaking and thus the degree of deformation could not be controlled, but it was dependent on the stiffness of the material, given by the curing-agent-to-base ratio of PDMS. In Figure 5.6B, we can see that low stiffness PDMS (left) would completely compress and collapse the structure, while higher stiffnesses (medium and right) would allow some freedom of movement that could result in net motion.

Hydrodynamics simulations were performed to demonstrate that symmetric spring-like skeletons should produce no net motion upon muscle contractions. Due to the high computational power of simulating the deformation of three-dimensional structures coupled with hydrodynamics, a 2D model was used instead (Figure 5.6C). The flow fields of an incompressible liquid surrounding the symmetric design, governed by the Navier-Stokes equations, were numerically computed by FEA simulations considering the deformations that the tissue contractions exert on the skeleton. Since the deformations along the scaffold are small and can be considered linear (Figure 5.3), the boundary conditions could be applied directly in the undeformed shape of the skeleton, thus avoiding mesh deformations and greatly reducing computational time. The contractions of the tissue were approximated by a continuous function, $g(t)$, that closely followed the shape an actual contraction profile (with a fast increase and a lower relaxation) to ensure derivability of the function (see Materials and

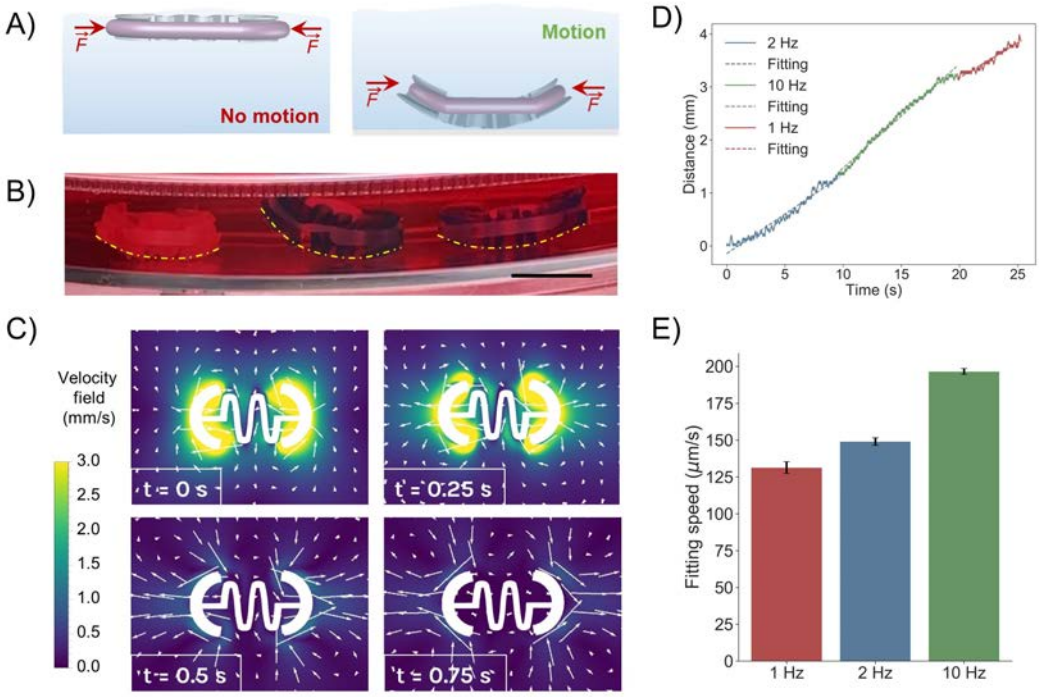

Figure 5.6: Motion analysis of symmetric bio-robots. A) When floating in the surface thanks to surface tension, buckling behavior is not observed, and therefore the symmetry of the design is maintained, showing no motion. When the bio-robots are forced into the medium, buckling develops and some motion can be observed. B) Image of several bio-robots displaying buckling behavior. Scale bar: 8 mm. C) Hydrodynamic simulations of 1-Hz contractions show symmetric flow fields at the beginning and after the contraction. D) Distance traveled by one instance of a symmetric bio-robot with buckling moving close to the surface and, E) speeds obtained by a fitting to the previous plot, showing how larger frequencies produce faster swimming.

Methods for more details). At both the left and right side of the skeleton, the deformations were defined as $d_l(t) = \Delta_l g(t)$ and $d_r(t) = -\Delta_r g(t)$, respectively, where Δ_l and Δ_r were the deformations achieved at the state of maximum compression for left and right size, respectively. In this case, due to the symmetry of the design, $\Delta_l = \Delta_r$. These two values were obtained from the previous mechanical simulations of the skeleton (Figure 5.3), assuming a force of 100 μN, the same order of magnitude of the forces measured in Figure 5.4. On the rest of the bio-robot, namely the spring section, the deformation was approximated by a function $d(t)$, which varied linearly between $d_l(t)$ and $d_r(t)$, a characteristic that was also demonstrated by mechanical simulations. Finally, the x-component of the fluid flow on the bio-robot boundary was computed as the derivative of the deformation due to the incompressibility of the fluid, $v_x(t) = \frac{\mathrm{d}d(t)}{\mathrm{d}t}$.

As the snapshots in Figure 5.6C show, the distribution of the velocity field around the bio-robot during 1 s is completely symmetrical, as would be expected, and cannot generate any net motion. Indeed, when the symmetry of the skeleton was maintained at the air-liquid interface, no motion was observed. Nevertheless, when buckling was induced by pushing the bio-robots to the bottom of the dish, motion could be observed for some of the symmetric skeletons upon EPS. Although our simulation model indicated the opposite, since it could not account for 3D buckling deformation due to its complexity, we hypothesize that the generated asymmetry together with the coupling of flow fields between the structure and the bottom surface could induce a spontaneous symmetry breaking that could propel the bio-robot at low speeds. Figure 5.6D shows an example of the displacement of the best-case scenario of symmetric swimming, which could reach maximum speeds of 100-200

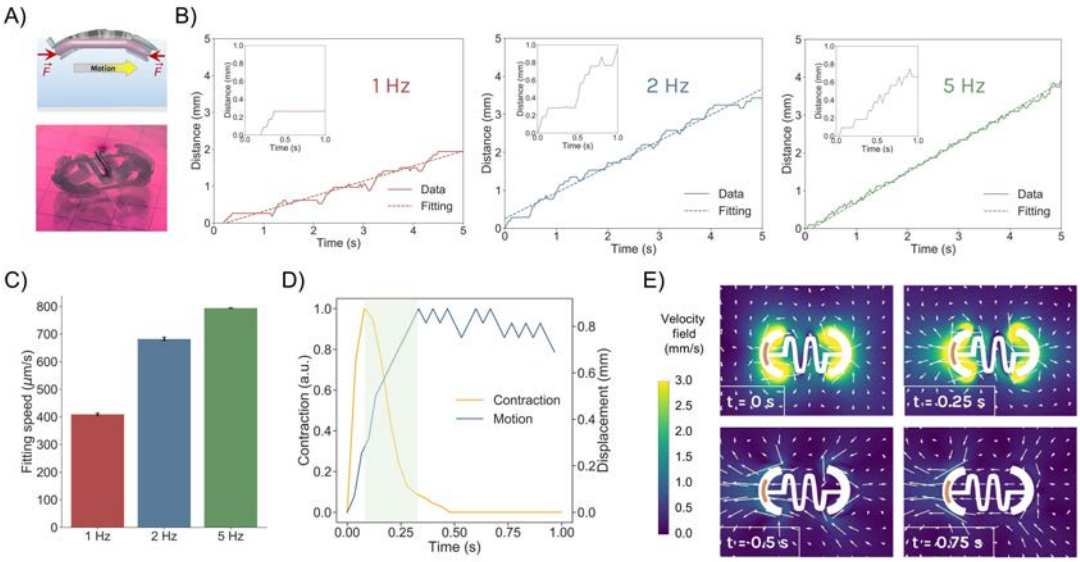

Figure 5.7: Motion analysis of asymmetric bio-robots. A) Because of the asymmetry induced by the post on one of the legs, buckling behavior can be observed at the surface due to differential surface tension. B) Distance traveled by one symmetric bio-robot at different frequencies. Inset shows the displacement after 1 s, where we can see how the motion at 1 Hz and 2 Hz occurs step-wise, while the motion at 5 Hz is more continuous. C) Speeds attained by the bio-robot by a linear fitting to the previous equations. D) Superposition of a measured contraction (yellow) with the motion of a bio-robot after one contraction (right), obtained from B). The green-shadowed portion represents the region of motion that can only be explained by inertia. E) Hydrodynamic simulations show that, after the contraction has finished ($t = 0.75$ s) there is a different velocity profile in the bio-robot that pushes it towards the direction opposite to the post.

μm/s, increasing with frequency (Figure 5.6E). This type of motion could resemble the swimming style of certain fish near surfaces, such as the burst-and-coast behavior of zebra-fishes, characterized by sporadic bursts followed by coasting phases[64, 65]. Moreover, the strong hydrodynamic couplings between the flow field around the bio-robot and the bottom surface could play a significant role in this movement. For instance, it is known that hydrodynamic couplings can induce the alignment of bacteria[66] or active particles near a wall[67], the creation of vortices near a bottom surface can induce the motion of magnetic rollers[68] and the speed of bacteria can be increased in confined channels[69]. It should be considered, however, that the motion resulting from symmetric skeletons was not predictable, as it strongly depended on the degree of curvature, which could not be controlled. Moreover, both the speed and the direction of motion were not clearly defined, as they relied on spontaneous symmetry breaking of the structure and its interactions with the surfaces. Therefore, consistent and controllable motion could only be obtained if an asymmetry was previously incorporated in the design.

Motion evaluation of asymmetric bio-robots

Motion with asymmetric skeletons proved to be predictable in terms of yield and direction of swimming. The movement of this type of bio-robots was always consistent in the direction opposite to the post and their speed was, in average, much higher than the speed of symmetric ones. The presence of the post bulging out of one of the sides created an asymmetry in the surface tension of the skeleton at the air-liquid interface, generating buckling deformation while floating, unlike in the case of the symmetric bio-robots that required to be drawn to the bottom (Figure 5.7A). Three tracking examples at different stimulation frequencies are shown in Figure 5.7B, where speeds of more than 700-800 μm/s for frequencies of 2 Hz and 10 Hz, and 550 μm/s for 1 Hz can be observed (Figure

5.7C). In the insets of 1 Hz and 2 Hz, we can see how the motion occurs in a step-wise manner, while for 5 Hz it is more continuous.

This step-wise motion is consistent with swimming driven by inertia. In fluid mechanics, the relationship between inertial forces and viscous forces during the motion of a swimmer is known as the Reynolds number (Re). This dimensionless quantity allows to differentiate between regimes of motion in which laminar flows (typical of viscous motion) or turbulence flows (typical of inertial motion) are dominant. At low Re ($\ll 1$), where viscous forces dominate, the fluid dynamics are described by the time-independent Stokes equation, in which inertial components are considered negligible. At this scale, the "scallop theorem" by Purcell dictates that a swimmer must perform non-reciprocal or time-irreversible motion to achieve a net displacement different from zero[70]. Microorganisms manage to break this time-reversal symmetry by rotatory motions, like those of bacterial flagella[71], which have been mimicked by artificial micropropellers[72] or bio-hybrid swimmers based on cardiac cells[73]. In our case, the compression mechanism of the skeletal muscle tissue against the skeleton cannot be considered time-reversible, since the shape changes are identical if time is reversed. This bio-swimmer, therefore, should not present motion at low Re.

The Re number is exactly defined as Re$= \frac{vL}{\nu}$, where v is the fluid flow, L is the characteristic length of the swimmer and ν the kinematic viscosity of the fluid. Given an approximated size of $\sim$ 10 mm, speeds of the bio-robot between 100-500 μm/s and the kinematic viscosity of water approximated to $1 \cdot 10^{-6}$ m^2/s, we find Re numbers of the order of 1-5. At this range, both viscosity and inertia play a significant role, and the motion cannot be considered neither purely viscous nor purely inertial. To better understand this type of motion, Figure 5.6D shows a simultaneous comparison of a twitch contraction and the bio-robot displacement during a 1 s cycle. This contraction profile is typical of skeletal muscle tissue, as it is known to go through a fast period of contraction followed by a slower relaxation[60]. In motion purely dominated by viscous forces, as in low Re, the displacement of the bio-robot should closely follow the contraction kinetics and, if time-reversal symmetry is not broken, the swimmer should go back to its initial position during the relaxation phase. However, in this case, the overlapping region between tissue relaxation and continuous motion, highlighted in green, can only be explained by inertial forces.

The different geometrical stiffnesses of both sides of the asymmetric skeleton that lead to a different maximum compression (Figure 5.3) are enough to obtain inertial net motion. Hydrodynamics simulations considering asymmetric compression were performed and are shown in Figure 5.6E. In this case, the compression at the left side, $d_l(t) = \Delta_l g(t)$, and the right side, $d_r(t) = \Delta_r g(t)$, of the skeleton are not equal, since the maximum compressions Δ_l and Δ_r depend on the presence of the post. It can be seen how, by the end of the relaxation of the tissue, at $t = 0.5$ s and $t = 0.75$ s, the flow field around the skeleton is not symmetric, showing a residual flow towards the left-hand side. Motion of the bio-robot, hence, should be directed towards the opposite direction of the flow field, contrary to the post side and consistent with the motion observed experimentally.

2.3. Conclusions

Here, we report an example of a bio-hybrid robot based on skeletal muscle cells that can swim at high speeds. We use 3D printing of PDMS to fabricate serpentine-like skeletons that can act as a spring when a muscle ring compresses them, resulting in compliant scaffolds that aid in the differentiation of the tissue. The optimization of the designs, based on several features like asymmetry or coil curvature, was performed *via* FEA simulations, that allowed us to find the appropriate geometrical

stiffnesses of each case and then experimentally test them. We found that differentiation in a compliant spring-like skeleton was beneficial when compared to other static tethered skeletons, such as a 2-post system. The muscle tissue under these conditions showed earlier spontaneous contractions and greater increments of force during the differentiation process. We hypothesizes that the dynamic compliance of the skeleton, reacting to the compression with a restoring force, provided an additional level of cyclic mechanical stimulation that helped to achieve a better degree of differentiation.

Finally, we characterized the motion of two types of bio-hybrid robots: a symmetric swimmer and an asymmetric swimmer. For the former, we found that motion at the air-liquid interface was not possible due to the generated symmetric flow fields, which was supported by hydrodynamic simulations. However, when the symmetric bio-robots were forced into the culture medium, a buckling behavior could be observed, and the swimmer adopted a curved structure that allowed motion, although at low speeds and unreliably, most likely due to interactions between the generated flow fields and the surface. Asymmetric bio-swimmers, however, showed much more reliable and consistent motion, as they already displayed buckling when floating in the air-liquid interface. Stimulation with EPS showed high speeds, going up to 800 μm/s and motion tracking, as well as hydrodynamic simulations, were consistent with inertia playing a crucial role in the mechanism of motion. This bio-hybrid swimmer based on skeletal muscle cells can move at speeds faster than the largest skeletal-muscle-based bio-bots up to date[35] and comparable to other cardiomyocyte-based bio-swimmers[19]. Future work should aim at understanding the interactions between the skeleton and surfaces, to comprehend the exact parameters governing this type of motion. In order to decrease the variability, the designs could be optimized to include the buckling behavior already in their fabrication to not rely on surface interactions to induce spontaneous symmetry breaking. Moreover, the scalability of these bio-robots could be investigated by comparing the motion of swimmers with different number of coils or to include additional control systems by the integration of magnetic or piezoelectric nanoparticles in their PDMS skeleton to guide their motion or control their contractions *via* ultrasonic waves.

2.4. Materials and methods

Cell culture

C2C12 mouse myoblasts were purchased from ATCC. Growth medium (GM) consisted of high glucose Dullbecco's Modified Eagle's Medium (DMEM; Gibco®) supplemented with 10% Fetal Bovine Serum (FBS), 200 nM L-Glutamine and 1% Penicillin/Streptomycin. Cells below passage 4 were used before reaching 80% confluency in Corning® T-75 flasks. Differentiation medium (DM) consisted of high glucose DMEM containing 10% Horse Serum (Gibco®), 200 nM L-Glutamine (Gibco®), 1% Penicillin-Streptomycin (Gibco®), 50 ng/ml insulin-like growth factor 1 (IGF-1, Sigma-Aldrich) and 1 mg/ml 6-aminocaproic acid (ACA, Sigma-Aldrich).

For the biofabrication of the myoblast-laden hydrogel, C2C12 cells were harvested from the flask by a 0.25% (wt/v) Trypsin-0.53 mM EDTA solution and centrifuged at 300g for 5 min. A centrifuged cell pellet with 3 million cells in total was mixed with 54 μL of cold GM (32.5% v/v) supplemented with 1 mg/mL of ACA (Sigma-Aldrich), 12 μL of a stock solution of 50 U/mL of thrombin (7.5% v/v), 90 μL of Matrigel® (60% v/v) and 150 μL of a stock solution of fibrinogen at 8 mg/mL (50% v/v), in that order. The mixture was immediately casted into the PDMS mold before fibrinogen was crosslinked by the action of thrombin. The mixture was performed in an iced water bath to avoid early crosslinking of Matrigel®.

3D printing of molds, skeletons and posts

The 3D bioprinter Inkredible+ from CELLINK® was used to fabricate the casting molds, the skeletons and the posts for force measurement. The casting molds were fabricated with PDMS (SE1700, Dow Corning) with a ratio of 1:10 and crosslinked at 80 °C overnight. The walls of the molds were 1 mm high and their inner and outer diameters were 10 mm and 13 mm, respectively. Spring-like skeletons of different ratios (1:20, 1:15 or 1:10, depending on the experiment) were cured at 80 °C overnight. In order to make easier the visualization of the bio-robot for video tracking, PDMS was vigorously mixed with a commercial dye of different colors. The designs of the skeletons were done with AutoCAD (v. 2019) and exported as .stl files. Then, the designs were transformed into GCode with the help of the open-source software Slic3r (v. 1.2.9) and the bioprinter was controlled with RepetierHost (v. 2.0.5). The 2-post system was 3D-printed with PDMS of a 1:20 and crosslinked at 37 °C for at least 3 days. The posts were 3 mm high, 0.5 mm wide and with 2 mm of lateral width and were manually written in GCode.

Electrical pulse stimulation

The setup for EPS was composed by a waveform generator (PM8572, Tabor Electronics), an oscilloscope (DS1104Z, Rigol), a signal amplifier x15, and a set of carbon-based handmade electrodes. The electrodes consisted of two graphite rods (cat. number 30250, Ladd Research) placed on opposite sides of a plastic Petri dish of 90x14 mm (ThermoFischer), fabricated and characterized as described in Chapter IV. For force measurement, the recording was carried out inside an inverted microscope (DMi8, Leica) in a chamber that allowed to mimic physiological conditions (37 °C and 5% CO2). For force measurement of the bio-robots in Figure 5.4, the tissue was gently transferred at D4 or D14, depending on the experiment, into a 2-post system, and their force measured by deflection of the posts in an inverted microscope, as carefully explained in Chapter IV. Motion videos of the bio-robots were recorded with a smartphone, keeping a grid paper below the Petri dish for calibration. Pulses of different frequencies of 2 ms were applied, keeping a constant voltage of 15 V.

Tracking algorithm

The script for tracking the motion of the bio-robots was developed in Python 3.7 using the library OpenCV (v. 4.1.2). Videos recorded with a smartphone camera were loaded into the script using the VideoCapture function. Then, the first frame was prompted in the screen and the user had to manually draw a line along one of the squares of the background grid paper. Knowing the actual size of these squares and the pixel length of the line, the calibration of the image in mm/px was performed. The first frame was prompted again and the user had to select an ROI around the bio-robot tracking algorithms with the SelectROI function. A BOOSTING tracker type was created (function TrackerBoosting_create) by initializing it with the selected ROI and it was then applied throughout the whole length of the video, frame by frame. The central position of the ROI was stored and the trajectory was added in the video with a color code to indicate time. The current time, FPS, calibration bar and a zoomed-out online image of the tracked object were also added to the video with OpenCV options. Finally, a linear fitting of the form $x = v \cdot t$ was applied to the displacement vs time data to obtain the speed of the bio-robot.

Mechanical deformation simulations

Simulations of mechanical deformation in 3D were performed using the .stl files of the designs generated by AutoCAD. The equilibrium equations for solid mechanics given by Newton's second law were solved:

$$\rho \frac{\partial^2 \boldsymbol{u}}{\partial^2 t} = \nabla \cdot \boldsymbol{S}, \tag{5.1}$$

where ρ is the density of the material, $\boldsymbol{u}$ is the displacement vector and $\boldsymbol{S}$ is the second Piola-Kirchhoff stress tensor. The Young's modulus of the material was set to $E = 255$ kPa and the poisson ratio to $\nu = 0.495$, as PDMS is nearly incompressible. Two point loads following the dynamics of a single twitch contraction, measured experimentally, were applied on both sides of the skeleton in the x-axis, normalized with a maximum value in the range 10-100 μN. These boundary loads model the contraction force applied by the tissue. The material was assumed to be isotropic and linear, due to the small forces and deformations that yielded von Mises stresses that were well below the yield stress of PDMS. These time-dependent equations were solved for the approximate duration of a contraction ($t = 0.5$ s) using the finite element method. The volume of the skeleton was meshed with tetrahedral elements and a MUMPs solver was used.

To obtain the compression vs force relationship, the maximum displacement along the x-axis, which coincided with the time of maximum force, was computed for the left side, $x_l = \mathsf{max}(u_{x,l})$, and the right side, $x_r = \mathsf{max}(u_{x,r})$ and plotted in terms of the force. A linear least-squares fitting to the equation $x = k^{-1}F$, allowed us to obtain the inverse of the geometrical stiffness, k^{-1}, for each side of the skeleton.

Hydrodynamic simulations

Hydrodynamic simulations were performed by Dr. Marco de Corato at the Institute for Bioengineering of Catalonia (IBEC)

Hydrodynamics simulations of the motion of the bio-robot in a fluid were performed 2D simulations to reduce computational power. As shown in Figure 5.8, the computational domain was a square of side L from which the section of the bio-robot was carved out. We considered a cartesian coordinate system that fixed to the center of the bio-robot. The motion of the incompressible liquid surrounding the bio-robot was governed by the Navier-Stokes equations:

$$\begin{gathered} \rho \left(\frac{\partial \boldsymbol{v}}{\partial t} + \boldsymbol{v} \cdot \nabla \boldsymbol{v} \right) = \eta \nabla^2 \boldsymbol{v} - \nabla p, \\ \nabla \cdot \boldsymbol{v} = 0, \end{gathered} \tag{5.2}$$

where $\rho = 1000$ kg/m^3 is the density of the liquid and $\eta = 10^{-3}$ Pa·s its shear viscosity. The motion of the bio-robot is driven by the shape deformations of the PDMS skeleton generated by the muscle tissue. These deformations generate fluid flows, which then drive the motion of the bio-robot. Experiments and finite elements simulations (Figure 5.2) showed that the shape deformations were small and therefore we could apply the boundary conditions directly at its undeformed shape. This assumption greatly simplified the simulations, since mesh deformation could be avoided.

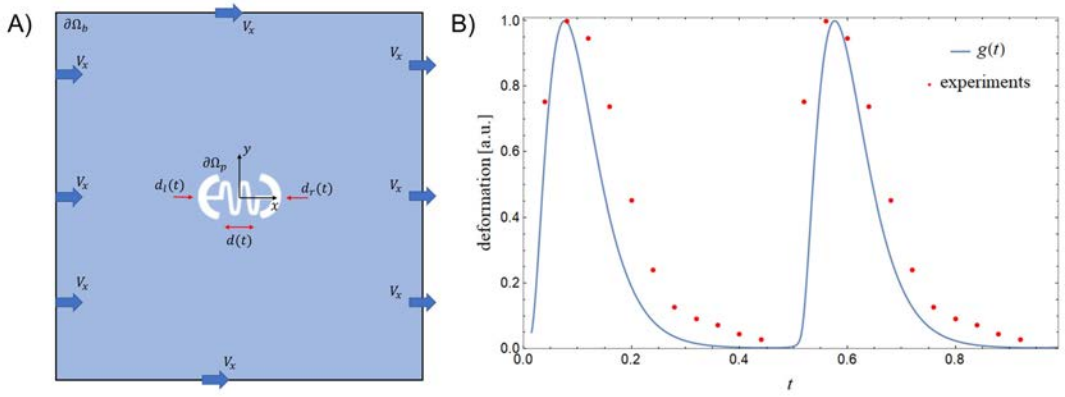

Figure 5.8: Schematics of the hydrodynamics simulations. A) Schematics of the compuational domain considered. B) Displacement prescribed by the function $g(t)$ compared to that measured in experiments for the case $f = 2$ Hz.

Numerical simulations of the deformation of the bio-robot showed that the deformation was concentrated in the spring part of the skeleton. Under the load applied by the tissue, the two curved parts on either side of the bio-robot were displaced as a rigid body with the deformation being concentrated in the spring. We used this finding to assume that the two curved sides were displaced as a function of time along the x-axis. We then assumed that the displacement varied linearly along the skeleton. The deformation on the left side was given by $d_l(t) = \Delta_l g(t)$ and on the right side it was given by $d_r(t) = -\Delta_r g(t)$, where Δ_l and Δ_r are the amplitudes of the displacement of the left and of the right part of the bio-robot. Experimentally, Δ_l and Δ_r could be different if the skeleton has a left-right asymmetric stiffness (Figure 5.3). The deformation on the rest of the bio-robot was denoted by $d(t)$ and it varied linearly between $d_r(t)$ and $d_l(t)$ along the x coordinate, something that was also demonstrated by previous simulations (see Figure 5.8A for a schematic representation).

The dimensionless function $g(t)$ determined the time variation of the deformation. To mimic the periodic nature of the loading and relaxation of the muscle cells, we approximated the contraction by $g(t) = e^{3g^*(t)-3}$ where $g^*(t)$ is specified by the nonlinear implicit equation:

$$g^*(t) = \sin\left[2\pi f t + 0.8 g^*(t)\right], \tag{5.3}$$

with f being the frequency of the tissue stimulation. As it is shown in Figure 5.8B, the normalized displacement prescribed by $g(t)$ closely follows that of measured experiments. The advantage of using $g(t)$ over an interpolation of the experimental data is that $g(t)$ is periodic and the average over one period of its time derivative is zero. The latter property is important to guarantee that the velocity on the boundary of the bio-robot caused by the deformation was zero when averaged over one period.

We assumed that the fluid velocity was equal the velocity due to the deformation of the bio-robot, due to the incompressibility of the fluid. Since the bio-robot was only deforming along the x coordinate and the deformations were small, we had $v_x = \frac{\mathrm{d}d_l(t)}{\mathrm{d}t}$ on the left curved part, $v_x = \frac{\mathrm{d}d_r(t)}{\mathrm{d}t}$ on the right curved part and $v_x = \frac{\mathrm{d}d(t)}{\mathrm{d}t}$ along the rest of the skeleton. This velocity was generated by the boundary actuation of the bio-robot. Moreover, as we considered a reference frame that moves with the bio-robot, the velocity at the edges of the square domain is given by $v_x = -V_x$, where V_x is the instantaneous velocity of the bio-robot. For simplicity, we assumed that the bio-robot only moves along the x axis. V_x is an additional unknown that must be computed considering the balance of forces on the bio-robot:

$$m\frac{\mathrm{d}V_x}{\mathrm{d}t} = F_{H,x}, \tag{5.4}$$

where m is the mass of the bio-robot and $F_{H,x}$ is the hydrodynamic force acting on it in the x direction. $F_{H,x}$ is computed as the integral of the stress tensor along the contour of the bio-robot:

$$F_{H,x} = \int_{\partial\Omega_p} \left[\eta\left(\nabla \boldsymbol{v} + \nabla \boldsymbol{v}^T\right) - p\boldsymbol{I}\right] : \boldsymbol{n} \cdot \boldsymbol{e_x} \mathrm{d}\Omega_p, \tag{5.5}$$

where $\boldsymbol{n}$ is the vector normal to the boundary of the skeleton and pointing outwards, $\boldsymbol{e_x}$ is the unit vector along the x axis and the integral runs along the contour of the bio-robot $\partial\Omega_p$. By solving Equations 5.2 to 5.5, one finds the velocity field and the pressure field around the bio-robot and its velocity along the x axis. The equations are nonlinear because of the convective term in the Equation 5.2, which can lead to a net displacement of the bio-robot over one cycle. We solved these equations using the finite element method. We divided the computational domain in triangular elements, with more elements near the bio-robot. We considered a quadratic interpolation of the velocity field and a linear interpolation for the pressure field. We used a second order implicit Runge-Kutta time integration scheme.

Immunostaining

Tissue constructs were washed three times in PBS and then fixed with a 3.7% paraformaldehyde in PBS for 15 min at RT, followed by three washes in PBS and stored until use. For immunostaining, cells were permeabilized by 0.2% Triton-X-100 in PBS. After washing thrice in PBS, the constructs were incubated with 5% Bovine Serum Albumin (BSA) in PBS (PBS-BSA) to block unspecific bindings. Then, the tissues were incubated for 2 h at RT and dark conditions with a 1/400 dilution of Alexa Fluor®-488-conjugated Anti-Myosin Heavy Chain II antibody (eBioscience) in 5% PBS-BSA. The unbound antibodies were washed out with PBS, and cell nuclei were stained with 1 μL/mL Hoechst 33342 (Life technologies). Finally, the tissue samples were washed thrice in PBS and stored at 4 °C until their analysis. The fluorescently labeled tissue constructs were imaged under an Zeiss LSM 800 confocal scanning laser microscope (CSLM), with a diode laser at 488 nm and 405 nm excitation wavelength for Myosin Heavy Chain II and cell nuclei.

3. Nanocomposite bio-bots with piezoelectric nanotubes

3.1. Objectives

Biological robots are becoming increasingly complex by the integration of different types of cells, likes neurons[32, 37, 39], the design of more sophisticated structures[19], the accomplishment of controlled and complicated tasks[27] or the integration of smart materials or nanocomposites into the skeletons[36]. On this regard, this section aims at providing proof-of-concept preliminary results towards the combination of muscle cells and piezoelectric nanocomposites that could improve the maturation of the tissue and provide additional levels of control in the future. Thus, the objectives of this section were the following: i) to obtain functional walking bio-bots following a well-established protocol; ii) to find a stable and homogeneous dispersion of BNNTs and integrate

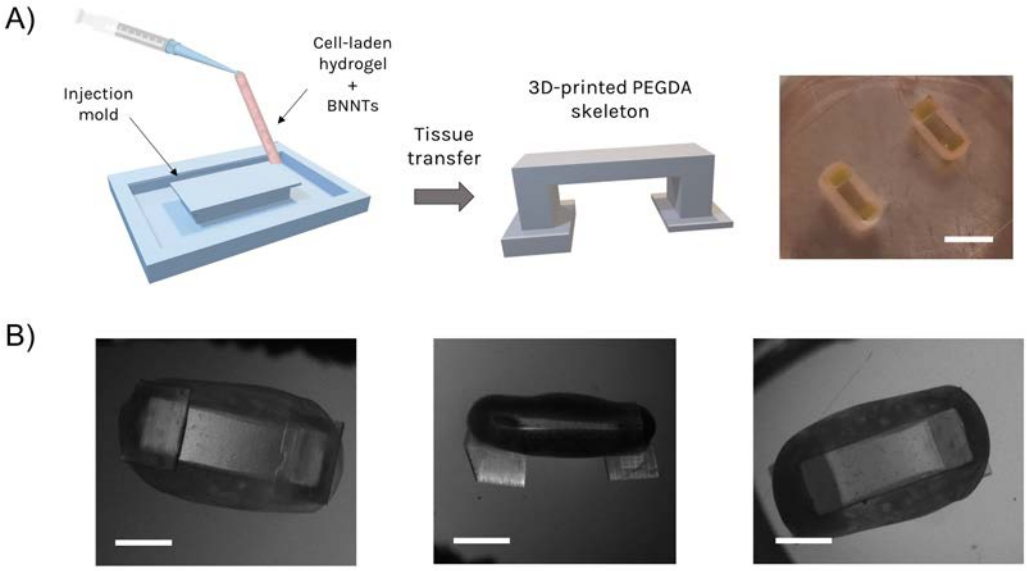

Figure 5.9: Biofabrication of BNNT bio-bots. A) A cell-laden hydrogel was mixed with a solution of BNNTs and loaded into an injection mold made of PDMS. After 2 days in GM, the tissue was transferred to 3D-printed PEGDA skeleton with an induced asymmetry in its legs to form a walking bio-bot. Scale bars: 5 mm. B) Microscope images of the assembled walking bio-bot upside down (left), from the side (center) and in walking position (right). Scale bars: 3 mm.

them into the cell-laden hydrogel to obtain BNNT-loaded bio-bots; iii) to compare the performance between BNNT-loaded bio-bots and control bio-bots in terms of their speed; and iv) in terms of their force generation, to demonstrate the benefits of piezoelectric nanocomposites for myotube differentiation.

These results were obtained at the University of Illinois at Urbana-Champaign (UIUC) during a 3-month stay in Prof. Bashir's group, pioneers in the fabrication and development of miniaturized biological walking machines, also called bio-bots.

3.2. Results and discussion

A bio-hybrid walker was fabricated following the protocol described in the previous section. Briefly, a myoblast-laden hydrogel composed of Matrigel®, fibrinogen and thrombin was casted into an injection mold made of PDMS (Figure 5.9A). Later, after 2 days in GM supplemented with ACA, the tissue was gently transferred into a skeleton made of PEGDA, 3D printed *via* SLA. This skeleton was based on previous designs reported by the research group, consisting on two small T-shaped legs joined together by a thin bridge[29]. The mechanism of motion was based on friction between the legs and the substrate[35]. Unlike in the swimming bio-robot reported in Section 2, which was made of PDMS and its hydrophobicity and material density allowed it to swim on the surface, PEGDA is a porous hydrogel that sinks and therefore the bio-bot can walk on the surface. An asymmetry was introduced in the design by making one of the legs thicker, as can be seen in Figure 5.9A. In this way, the difference between friction coefficients on both sides of the bio-robot produced a net movement towards the side of the thicker leg[29, 35]. Figure 5.9B shows several microscope images of an assembled bio-robot facing upwards (left), where the base of its legs can be observed, sideways (center) and in walking position (right).

Piezoelectric nanocomposites

The addition of nanocomposites into cell-laden hydrogels have been demonstrated to provide beneficial aspects in the differentiation or maturation of muscle cells. In particular, conductive nanocomposites, such as gold nanoparticles[45] or nanowires[43], graphene[46], GO[49] or rGO[74] can improve the mechanical properties of the scaffolds, provide mechanical cues for better alignment, as well as enhance their conductivity for a more efficient propagation of depolarization potentials, which can help in the synchronization of the cell's contractions[47]. Piezoelectric nanocomposites provide an additional level of benefits that can be consider dynamic due to the combination of piezoelectricity and the active and passive forces exerted by skeletal muscle tissue during myogenesis. The piezoelectric effect is the creation of voltage difference in certain materials when a mechanical strain is applied or, inversely, the deformation of a material when an external electric field is applied. Skeletal muscle tissue can generate two types of stress: a passive stress during myogenesis when myoblasts pull from the surrounding hydrogel chains and compact the tissue, which helps in the self-assembly of bio-actuators or bio-robots; and an active stress in the form of contractions, which can be induced by electric fields but can also occur spontaneously during tissue differentiation[29, 60]. Besides, electrical stimulation during myogenesis can improve the differentiation and maturation of skeletal muscle[60, 75]. For these reasons, the integration of piezoelectric nanocomposites within the cell-laden hydrogel could potentially transform the stresses generated by the tissue into small voltage differences that could, in turn, provide electrical stimulation to the myotubes during differentiation, in a feedback loop.

Piezoelectric nanomaterials have already been used to generate local electric fields to induce self-stimulation of cells and modulate their activity. Murillo *et al.* presented piezoelectric nanogenerators made of 2D ZnO nanosheets as an active substrate for cell attachment[52]. They found that the mechanical forces exerted by macrophages during attachment and proliferation could apply a stress on the nanosheets and induce a local electric field that depolarized the cell, releasing intracellular Ca^{+2}. Likewise, Kitsara *et al.* used poly(vinylidene fluoride) (PVDF) to mimic the inherent piezoelectric properties of bone, also observing an increase in intracellular calcium compared to control samples[76]. Piezoelectric BNNTs, in particular, have been used in combination with skeletal muscle cells in 2D cultures to improve the differentiation. Ciofani *et al.* investigated the interactions between BNNTs coated with poly-L-lysine and C2C12 cells, finding an increased protein synthesis and no adverse effects in differentiation markers like MyoD or fusion index of myotubes, demonstrating their suitability for biomedical applications[57]. Later on, Ricotti *et al.* described engineered polyacrilamide gels with micro-grooves in which fibroblasts and myoblasts were co-cultured. They supplemented the culture medium with BNNTs and applied ultrasonic stimulation to the samples, thus creating stress on the nanotubes that would be translated into local electric fields that could stimulate the cells, achieving longer, thicker and more functional myotubes[58]. These promising results, only obtained in 2D cultures, point towards the benefits of the addition of BNNTs in three-dimensional cell-laden hydrogels. For this reason, we studied the integration of this type of piezoelectric nanocomposites into skeletal muscle tissue constructs to improve the performance and force generation of bio-robots.

BNNTs characterization and dispersion

BNNTs are a type of one-dimensional structures, similar to carbon nanotubes (CNTs), which have gained significant attraction in the past years due to their outstanding properties. For instance, they possess high chemical stability[77] and excellent thermal conductivity[78], superior to CNTs[57], a Young's modulus in the TPa range[53] and they are electrically insulating with a bandgap of $\sim 5 - 6$ eV[53, 79]. Analogously to CNTs, BNNTs are composed of hexagonal B-N bonds with a

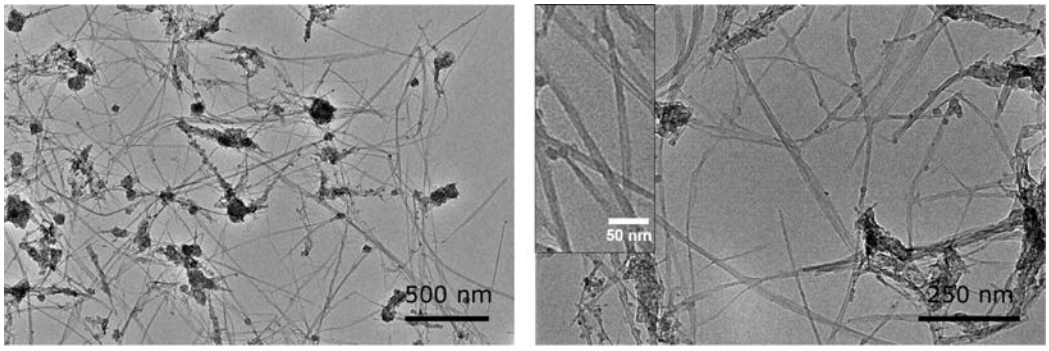

Figure 5.10: TEM images at different magnifications of a dispersion of BNNTs. Darker aggregates correspond to boron nanoparticle impurities.

partial ionic character and almost the same atomic spacing[53, 80]. The nature of the piezoelectricity of single-walled BNNTs has been demonstrated experimentally, although it is not completely understood[53]. Numerical and molecular mechanics simulations, however, have been able to approximate the resultant dipolar vector in sigle-walled nanotubes after an applied stress[53, 81], while others have found theoretical piezoelectric response values higher than those of piezoelectric polymers [82]. Likewise, multi-walled BNNTs have also shown experimental signs of piezoelectricity[83]. Although these characteristics are especially attractive for the aerospace or energy generation industries [53], their applications in the biomedical field have been generally unexplored[57, 80].

Commercially available BNNTs are synthesized by a high temperature-pressure method[53] and come in the form of a puffball of very low density. These nanotubes were characterized by transmission electron microscope (TEM), as shown in Figure 5.10. This characterization revealed an inhomogeneous mixture of BNNTs with some impurities in the form of hexagonal boron-nitride (h-BN) nanoparticles, as reported by the manufacturer[53]. The nanotubes were in general straight and organized in bundles, with diameters as small as tens of nanometers (inset). While one of the key aspects of BNNTs is their chemical stability, this can make their dispersion in aqueous solutions difficult to achieve, hindering their applications in biomedicine[80]. To improve the dispersion, previous reports have used non-covalent wrapping of BNNTs in poly-L-lysine[57, 84] or glycol chitosan[58]. Here, we chose an alternative method based on dispersion in organic solvents, followed by subsequent solvent transfers until achieving a stable dispersion in ethanol.

Firstly, we dissolved the foam-like material in dimethylformamide (DMF) at 0.5 mg/mL under vigorous stirring overnight, until obtaining a brown solution with small aggregates. Then, the samples were sonicated for at least 2 h in an ice-cold bath, until all the aggregates were completely dissolved[58]. Afterwards, the sample was centrifuged and resuspended in a solution of 1:1 of ethanol and DMF at the same concentration, and sonicated in cold until achieving dissolution. Finally, the sample was again centrifuged and resuspended in pure ethanol at 0.5 mg/mL. The dispersion was found to be stable for several weeks in ethanol at 4 °C, although small aggregates were formed. Before mixing with the cell-laden hydrogel, the ethanol dispersion of BNNTs had to be sonicated in a cold bath for at least 1-2 h until the dispersion was again homogeneous.

Performance of bio-bots loaded with BNNTs

BNNT-loaded bio-bots were fabricated following the same cell encapsulation protocol, but dispersing the nanocomposites in the hydrogel before mold casting at a concentration of 5 μg/mL (Fig-

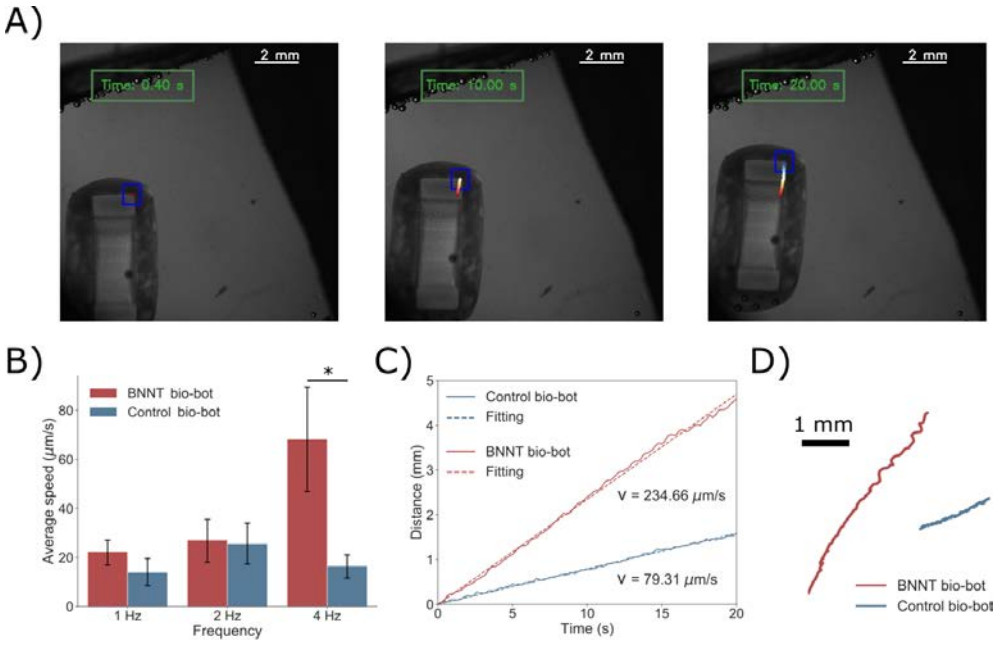

Figure 5.11: Motion analysis and comparison of control and BNNT bio-bots. A) Snapshots of a tracking of a bio-bot moving at 1 Hz upon EPS. B) Average speeds reached by control and BNNT bio-bots according to different frequencies. C) Examples of the two best cases of motion of control and BNNT bio-bots for a period of 20 s at 4 Hz, showing how the BNNT bio-bots

ure 5.9A). This concentration was chosen since it was previously demonstrated to be biocompatible and show the highest increase in protein content per μg of DNA, when compared to 0 μg/mL and 10 μg/mL[57]. While being kept in ice after sonication, 2.86 μL of the 0.5 mg/mL stock solution of BNNTs in ethanol was mixed with the hydrogel and homogenized thoroughly with the pipette, without creating any bubbles. Then, the BNNT- and cell-laden hydrogel was manually casted into the injection molds and left in a cell incubator for 1 h, until Matrigel was fully crosslinked. Then, GM supplemented with ACA was added and maintained for two days, just like control bio-bots. Then, all tissue constructs were gently lifted from the molds and positioned around the PEGDA skeletons, while their media was changed to DM supplemented with ACA.

The performance of BNNT-loaded bio-bots in terms of speed was compared to control bio-bots at day 6 of differentiation. Figure 5.11A shows a tracking example of a bio-bot walking at a 1-Hz pace upon EPS. The tracking algorithm described in Section 2 was applied to follow a corner in the skeleton of the bio-bots and their speeds were computed from the trajectory. Despite showing great variability between samples, BNNT-loaded bio-robots showed generally higher speeds than control bio-bots, with values comparable to those reported previously[29]. In particular, the average speed at 1 Hz was slightly higher for BNNT bio-bots but the speed at 4 Hz was greatly increased, showing statistically significant differences compared to the control cases (Figure 5.11B). The best two cases of motion for each kind of bio-robot are shown in Figure 5.11C, where a fitting was performed to obtain their speeds. It can be seen how BNNT-loaded bio-bots could reach speeds up to 234 μm/s, three times higher than the control cases at roughly $\sim$ 80 μm/s. Figure 5.11D displays the tracked trajectories of the examples of Figure 5.11C, where it can be observed how they are completely directional. However, several of the bio-bots showed significant rotational motion, probably due to inhomogeneities in the skeleton during 3D printing. These bio-bots, therefore, were not included in the speed calculations, but only directional ones.

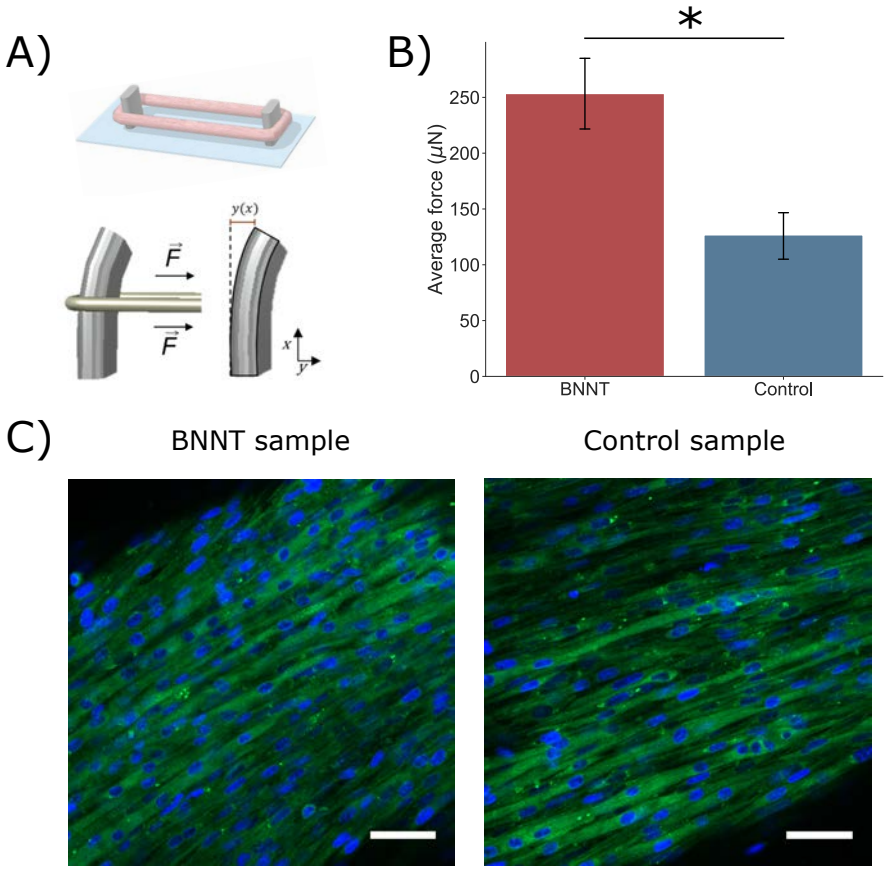

Figure 5.12: Force measurement of control and BNNT bio-bots. A) Schematic representation of the force measurement setup, based on deflection of PDMS cantilevers. B) At day 6 of differentiation, BNNT muscle tissues showed a significant enhancement in their force generation, compared to control samples. C) Immunostaining of MyHC (green) and cell nuclei (blue) did not reveal any qualitative differences between samples. Scale bars: 50 μm.

Finally, force measurements on control and BNNT-loaded skeletal muscle tissues were performed by deflection of two PDMS posts, as carefully described in Chapter IV. Tissue constructs were fabricated following the same protocol and then transferred into the two-post system for differentiation (Figure 5.12A). After 6 days in DM, control samples showed forces in the range of $\sim$ 80 μN, similar to previous reports[29, 30]. However, BNNT-loaded muscle tissues showed more than a two-fold increase in their force generation, reaching values of 250 μN, with statistically significant differences (Figure 5.12B). Immunostaining of MyHCII and cell nuclei showed no differences between BNNT and control samples, since both of them exhibit elongated and well-aligned myotubes (Figure 5.12C), as previous reports in the literature also showed[57]. The effects on force generation and bio-bot performance, hence, could come from differences at the protein level, such as remodelling of the sarcomeric structure and the expression of different MyHC proteins due to an exercise effect, such as the one described in Chapter IV.

3.3. Conclusions

In this section, we have demonstrated the feasibility of fabricating nanocomposite bio-hybrid robots with enhanced capabilities, by integrating piezoelectric BNNTs into the cell-laden hydrogel of walking bio-bots. A dispersion of BNNTs was obtained by dissolution in DMF and several solvent changes until reaching a stable solution in ethanol. Bio-bots loaded with BNNTs at a concentration

of 5 μg/mL showed enhanced motion, as demonstrated by tracking of bio-bots actuated by EPS. This effect was particularly significant for a frequency of 4 Hz, reaching speeds up to 234 μm/s after only six days of differentiation. Moreover, we demonstrated that these improvements in the motion were a result of a stronger force output of the nanocomposite-laden muscle tissue. By performing force measurements, we found that the average force of BNNT-loaded tissues was 250 μN, a 2.5-fold increase with respect to control samples. Finally, immunostaining of MyHCII and nuclei did not show any differences in the differentiation of the tissue.

These preliminary results pave the way was towards a more complex actuation of bio-hybrid robots by the integration of nanocomposites with different capabilities, in this case, piezoelectric nanoparticles that improve the performance of the tissue. Future studies should investigate the piezoelectric effect for remote actuation of these bio-bots by the application of ultrasonic waves. Other nanocomposites could be also combined to boost the performance and efficiency, such as magnetic nanoparticles in the cell-laden hydrogel or the artificial scaffold, to guide the bio-hybrid robots through magnetic fields or graphene-based nanocomposites that could improve the mechanical and conductive properties of the hydrogels. The multidisciplinary integration of recent advances in smart materials, nanotechnology, tissue engineering and soft robotics will be key for the future development of advanced bio-hybrid robotics

3.4. Materials and methods

Bio-bot skeleton fabrication

PEGDA with a number average molecular weight (Mn) of 700 (Sigma-Aldrich) was mixed with PEGDA 575 Mn in a 1:1 ratio. A solution of PEGDA 700/575 at 16% v/v in ultrapure water with lithium phenyl-2,4,6-trimethylbenzoylphosphinate (LAP; Sigma-Aldrich) at 0.1% wt/v was prepared. A red dye, Sudan I (Sigma-Aldrich) was included in the solution at a 0.15% wt/v and sonicated until fully dissolved. The skeletons, based on previous CAD designs[29], were 3D printed with the PICO2 SLA 3D printer from Asiga. Sudan I dye was necessary to improve the definition of the structures by scattering of the white light source used by the printer. After printing, the skeletons were soaked in 10% bleach to remove the dye, left in isopropanol overnight and then maintained in PBS until use.

Cell culture

C2C12 mouse myoblasts were purchased from ATCC. Growth medium (GM) consisted of high glucose Dullbecco's Modified Eagle's Medium (DMEM; Gibco®) supplemented with 10% Fetal Bovine Serum (FBS; ThermoFisher), 200 nM L-Glutamine and 1% Penicillin/Streptomycin (Lonza). Cells below passage 6 were used before reaching 80% confluency in T-75 flasks. Differentiation medium (DM) consisted of high glucose DMEM containing 10% Horse Serum (Gibco®), 200 nM L-Glutamine (Gibco®), 1% Penicillin-Streptomycin (Gibco®), 50 ng/ml insulin-like growth factor 1 (IGF-1, Sigma-Aldrich) and 1 mg/ml 6-aminocaproic acid (ACA, Sigma-Aldrich).

Fabrication of control and BNNT-loaded bio-bots

Myoblast-laden hydrogel were composed of Matrigel® (ThermoFischer), fibrinogen (Sigma-Aldrich) and thrombin (Sigma-Aldrich) in GM supplemented with ACA. Cells at 80% confluence were harvested by adding 3 mL of TrypLE Express (ThermoFischer) for 5 mL and then neutralized with

3 mL of GM. Then, cells were centrifuged at 300g for 5 min and separated into 15-mL Falcon tubes with 3 million cells in each on. For cell encapsulation, 115 μL of GM + ACA were added to a pellet with 3 million cells and homogenized thoroughly. Then, 6 μL of a 100 U/mL solution of thrombin and 90 μL of Matrigel® were added and homogenized. Finally, 75 μL of stock solution of fibrinogen at 16 mg/mL was added, homogenized fast, and 120 μL of solution was casted in one injection mold, preparing a total of two each time. The tissue constructs were left in a cell incubator at 37 °C and 5% CO_2 atmosphere for 1 h until Matrigel® was crosslinked and GM supplemented with ACA was added.

BNNTs (product code R2-beta) were purchased from BNNT, LLC. The material came in the form of a puffball and small quantities of it were dispersed in DMF at a concentration of 0.5 mg/mL, as described in the main text, by first leaving it under vigorous stirring overnight and then sonicating in ice for at least 2 h. The sample was centrifuged at 1400 rpm in Eppendorfs and the solvent was changed to DMF and ethanol in a 1:1 ratio, maintaining the same concentration of BNNTs. The process of sonication and centrifuging was repeated until obtaining a solution in pure ethanol. After solvent change to ethanol, the sample could be stored at 4 °C in cold. Before mixing with the hydrogel, the dispersion was again sonicated in cold for at least 1 h or until it was completely homogeneous and without aggregates. Taking into account that the total amount of hydrogel needed was 286 μL (as per last paragraph's quantities), 2.86 μL of the stock solution of 0.5 mg/mL BNNTs in ethanol was added to achieve a final concentration of 5 μg/mL in the hydrogel. The addition of the BNNT dispersion was performed right before addition of fibrinogen and homogenized thoroughly, without observing presence of aggregates.

Motion analysis of bio-bots and force measurement of muscle tissue

Motion characterization was performed under an up-right microscope with a set of home-made stimulation electrodes composed of two platinum rods. A waveform generator with an amplifier (AD797) were used to apply squared biphasic pulses by connecting a capacitor in series to minimize electrolysis created by the Pt electrodes. Bio-bots were recorded at different frequencies after placing them in fresh, warm DMEM and the motion was analyzed with the home-made tracking script described in the previous section.

Force measurement was performed as described in Chapter IV. Briefly, control and BNNT-loaded tissues were transferred into a 2-post system instead of into a bio-bot skeleton and they were left to differentiate for 6 days in DM supplemented with ACA. Force measurement was done at 1 Hz and recorded under an inverted microscope.

Immunostaining

Tissue constructs were washed three times in PBS and then fixed with a 3.7% paraformaldehyde in PBS for 15 min at RT, followed by three washes in PBS and stored until use. For immunostaining, cells were permeabilized by 0.2% Triton-X-100 in PBS. After washing thrice in PBS, the constructs were incubated with 5% Bovine Serum Albumin (BSA) in PBS (PBS-BSA) to block unspecific bindings. Then, the tissues were incubated overnight at RT and in dark conditions with a 1/400 dilution of Myosin 4 Monoclonal Antibody (MF20; eBioscience) as primary antibody and 4′,6-diamindino-2-phenylindole (DAPI; Sigma-Aldrich) at 1:5000. The next day, the samples were washed thrice in BPS and Alexa Fluor® 568 was added for 2 h at RT in dark as secondary antibody. The tissue samples were observed under CSLM (Zeiss).

Statistical analysis

For motion characterization, pairs of speeds at the same frequency (control vs BNNT) subtracted from fitting to motion curves were performed a F-test for two-sample variance. As some of the pairs showed unequal variance, a t-test assuming unequal variances was performed (N = 7-14). Significance was set at p-value < 0.05.

For force characterization, sets of forces of control and BNNT-loaded samples were performed an F-test for two-sample variance. As the variances were not significantly different, a t-test assuming equal variances was performed (N = 6). Significance was set at p-value < 0.05.

References

[1] T. Patino, R. Mestre, and S. Sánchez, *Miniaturized soft bio-hybrid robotics: A step forward into healthcare applications,* Lab on a Chip **16**, 3626 (2016).

[2] M. Cianchetti, C. Laschi, A. Menciassi, and P. Dario, *Biomedical applications of soft robotics,* Nature Reviews Materials **3**, 143 (2018).

[3] L. Ricotti and A. Menciassi, *Bio-hybrid muscle cell-based actuators,* Biomedical Microdevices **14**, 987 (2012).

[4] M. Wehner, R. L. Truby, D. J. Fitzgerald, B. Mosadegh, G. M. Whitesides, J. A. Lewis, and R. J. Wood, *An integrated design and fabrication strategy for entirely soft, autonomous robots,* Nature **536**, 451 (2016).

[5] R. F. Shepherd, F. Ilievski, W. Choi, S. A. Morin, A. A. Stokes, A. D. Mazzeo, X. Chen, M. Wang, and G. M. Whitesides, *Multigait soft robot,* Proceedings of the National Academy of Sciences of the United States of America **108**, 20400 (2011).

[6] M. T. Tolley, R. F. Shepherd, B. Mosadegh, K. C. Galloway, M. Wehner, M. Karpelson, R. J. Wood, and G. M. Whitesides, *A Resilient, Untethered Soft Robot,* Soft Robotics **1**, 213 (2014).

[7] R. V. Martinez, J. L. Branch, C. R. Fish, L. Jin, R. F. Shepherd, R. M. D. Nunes, Z. Suo, and G. M. Whitesides, *Robotic tentacles with three-dimensional mobility based on flexible elastomers,* Advanced Materials **25**, 205 (2013).

[8] F. Ilievski, A. D. Mazzeo, R. F. Shepherd, X. Chen, and G. M. Whitesides, *Soft robotics for chemists,* Angewandte Chemie - International Edition **50**, 1890 (2011).

[9] V. A. Webster-Wood, O. Akkus, U. A. Gurkan, H. J. Chiel, and R. D. Quinn, *Organismal engineering: Toward a robotic taxonomic key for devices using organic materials,* Science Robotics **2**, eaap9281 (2017).

[10] Y. Tanaka, K. Sato, T. Shimizu, M. Yamato, T. Okano, and T. Kitamori, *A micro-spherical heart pump powered by cultured cardiomyocytes,* Lab on a Chip **7**, 207 (2007).

[11] J. Park, J. Ryu, S. K. Choi, E. Seo, J. M. Cha, S. Ryu, J. Kim, B. Kim, and S. H. Lee, *Real-time measurement of the contractile forces of self-organized cardiomyocytes on hybrid biopolymer microcantilevers,* Analytical Chemistry **77**, 6571 (2005).

[12] J. Park, J. Kim, D. Roh, S. Park, B. Kim, and K. Chun, *Fabrication of complex 3D polymer structures for cell-polymer hybrid systems,* Journal of Micromechanics and Microengineering **16**, 1614 (2006).

[13] J. Xi, J. J. Schmidt, and C. D. Montemagno, *Self-assembled microdevices driven by muscle,* Nature Materials **4**, 180 (2005).

[14] J. Kim, J. Park, S. Yang, J. Baek, B. Kim, S. H. Lee, E. S. Yoon, K. Chun, and S. Park, *Establishment of a fabrication method for a long-term actuated hybrid cell robot,* Lab on a Chip **7**, 1504 (2007).

[15] V. Chan, K. Park, M. B. Collens, H. Kong, T. A. Saif, and R. Bashir, *Development of miniaturized walking biological machines.* Scientific Reports **2**, 857 (2012).

[16] A. W. Feinberg, A. Feigel, S. S. Shevkoplyas, S. Sheehy, G. M. Whitesides, and K. K. Parker, *Muscular thin films for building actuators and powering devices,* Science **317**, 1366 (2007).

[17] M. T. Holley, N. Nagarajan, C. Danielson, P. Zorlutuna, and K. Park, *Development and characterization of muscle-based actuators for self-stabilizing swimming biorobots,* Lab on a Chip **16**, 3473 (2016).

[18] R. Takemura, T. Hoshino, Y. Akiyama, and K. Morishima, *Design analysis of self-organized and frameless swimming bio-robots with cardiomyocyte gel,* in *2010 International Symposium on Micro-NanoMechatronics and Human Science: From Micro and Nano Scale Systems to Robotics and Mechatronics Systems, MHS 2010, Micro-Nano GCOE 2010, Bio-Manipulation 2010* (IEEE, 2010) pp. 485–490.

[19] S. J. Park, M. Gazzola, K. S. Park, S. Park, V. Di Santo, E. L. Blevins, J. U. Lind, P. H. Campbell, S. Dauth, A. K. Capulli, F. S. Pasqualini, S. Ahn, A. Cho, H. Yuan, B. M. Maoz, R. Vijaykumar, J. W. Choi, K. Deisseroth, G. V. Lauder, L. Mahadevan, and K. K. Parker, *Phototactic guidance of a tissue-engineered soft-robotic ray,* Science **353**, 158 (2016).

[20] J. C. Nawroth, H. Lee, A. W. Feinberg, C. M. Ripplinger, M. L. McCain, A. Grosberg, J. O. Dabiri, and K. K. Parker, *A tissue-engineered jellyfish with biomimetic propulsion,* Nature Biotechnology **30**, 792 (2012).

[21] M. S. Sakar, D. Neal, T. Boudou, M. A. Borochin, Y. Li, R. Weiss, R. D. Kamm, C. S. Chen, and H. H. Asada, *Formation and optogenetic control of engineered 3D skeletal muscle bioactuators,* Lab on a Chip **12**, 4976 (2012).

[22] M. Das, K. Wilson, and J. J. Hickman, *Differentiation of skeletal muscle and integration of myotubes with silicon microstructures using serum-free medium and a synthetic silane substrate,* Nature Protocols **2**, 1795 (2007).

[23] K. Shimizu, H. Sasaki, H. Hida, H. Fujita, K. Obinata, M. Shikida, and E. Nagamori, *Assembly of skeletal muscle cells on a Si-MEMS device and their generative force measurement,* Biomedical Microdevices **12**, 247 (2010).

[24] T. Boudou, W. R. Legant, A. Mu, M. A. Borochin, N. Thavandiran, M. Radisic, P. W. Zandstra, J. A. Epstein, K. B. Margulies, and C. S. Chen, *A microfabricated platform to measure and manipulate the mechanics of engineered cardiac microtissues,* Tissue Engineering - Part A **18**, 910 (2012).

[25] T. Hoshino and K. Morishima, *Muscle-powered cantilever for microtweezers with an artificial micro skeleton and rat primary myotubes,* Journal of Biomechanical Science and Engineering **5**, 245 (2010).

[26] K. I. Kabumoto, T. Hoshino, Y. Akiyama, and K. Morishima, *Voluntary movement controlled by the surface EMG signal for tissue-engineered skeletal muscle on a gripping tool,* Tissue Engineering - Part A **19**, 1695 (2013).

[27] Y. Morimoto, H. Onoe, and S. Takeuchi, *Biohybrid robot powered by an antagonistic pair of skeletal muscle tissues,* Science Robotics **3**, eaat4440 (2018).

[28] R. Raman, C. Cvetkovic, and R. Bashir, *A modular approach to the design, fabrication, and characterization of muscle-powered biological machines,* Nature Protocols **12**, 519 (2017).

[29] C. Cvetkovic, R. Raman, V. Chan, B. J. Williams, M. Tolish, P. Bajaj, M. S. Sakar, H. H. Asada, M. T. A. Saif, and R. Bashir, *Three-dimensionally printed biological machines powered by skeletal muscle,* Proceedings of the National Academy of Sciences of the United States of America **111**, 10125 (2014).

[30] R. Raman, C. Cvetkovic, S. G. Uzel, R. J. Platt, P. Sengupta, R. D. Kamm, and R. Bashir, *Optogenetic skeletal muscle-powered adaptive biological machines,* Proceedings of the National Academy of Sciences of the United States of America **113**, 3497 (2016).

[31] R. Raman and R. Bashir, *Biomimicry, Biofabrication, and Biohybrid Systems: The Emergence and Evolution of Biological Design,* Advanced Healthcare Materials **6**, 1700496 (2017).

[32] C. Cvetkovic, M. H. Rich, R. Raman, H. Kong, and R. Bashir, *A 3D-printed platform for modular neuromuscular motor units,* Microsystems & Nanoengineering **3**, 17015 (2017).

[33] C. Cvetkovic, M. C. Ferrall-Fairbanks, E. Ko, L. Grant, H. Kong, M. O. Platt, and R. Bashir, *Investigating the Life Expectancy and Proteolytic Degradation of Engineered Skeletal Muscle Biological Machines,* Scientific Reports **7**, 3775 (2017).

[34] L. Grant, R. Raman, C. Cvetkovic, M. C. Ferrall-Fairbanks, G. J. Pagan-Diaz, P. Hadley, E. Ko, M. O. Platt, and R. Bashir, *Long-Term Cryopreservation and Revival of Tissue-Engineered Skeletal Muscle,* Tissue Engineering - Part A **25**, 1023 (2019).

[35] G. J. Pagan-Diaz, X. Zhang, L. Grant, Y. Kim, O. Aydin, C. Cvetkovic, E. Ko, E. Solomon, J. Hollis, H. Kong, T. Saif, M. Gazzola, and R. Bashir, *Simulation and Fabrication of Stronger, Larger, and Faster Walking Biohybrid Machines,* Advanced Functional Materials **28**, 1801145 (2018).

[36] Y. Kim, G. Pagan-Diaz, L. Gapinske, Y. Kim, J. Suh, E. Solomon, J. F. Harris, S. W. Nam, and R. Bashir, *Integration of Graphene Electrodes with 3D Skeletal Muscle Tissue Models,* Advanced Healthcare Materials **9**, 1901137 (2020).

[37] O. Aydin, A. P. Passaro, M. Elhebeary, G. J. Pagan-Diaz, A. Fan, S. Nuethong, R. Bashir, S. L. Stice, and M. T. A. Saif, *Development of 3D neuromuscular bioactuators,* APL Bioengineering **4**, 016107 (2020).

[38] C. D. Kaufman, S. C. Liu, C. Cvetkovic, C. A. Lee, G. Naseri Kouzehgarani, R. Gillette, R. Bashir, and M. U. Gillette, *Emergence of functional neuromuscular junctions in an engineered, multicellular spinal cord-muscle bioactuator,* APL Bioengineering **4**, 026104 (2020).

[39] O. Aydin, X. Zhang, S. Nuethong, G. J. Pagan-Diaz, R. Bashir, M. Gazzola, and M. T. A Saif, *Neuromuscular actuation of biohybrid motile bots,* Proceedings of the National Academy of Sciences of the United States of America **116**, 19841 (2019).

[40] A. Sydney Gladman, E. A. Matsumoto, R. G. Nuzzo, L. Mahadevan, and J. A. Lewis, *Biomimetic 4D printing,* Nature Materials **15**, 413 (2016), arXiv:1011.1669v3 .

[41] Z. X. Khoo, J. E. M. Teoh, Y. Liu, C. K. Chua, S. Yang, J. An, K. F. Leong, and W. Y. Yeong, *3D printing of smart materials: A review on recent progresses in 4D printing,* Virtual and Physical Prototyping **10**, 103 (2015).

[42] A. K. Gaharwar, N. A. Peppas, and A. Khademhosseini, *Nanocomposite hydrogels for biomedical applications,* Biotechnology and Bioengineering **111**, 441 (2014).

[43] T. Dvir, B. P. Timko, M. D. Brigham, S. R. Naik, S. Sandeep, O. Levy, H. Jin, K. K. Parker, R. Langer, and S. Daniel, *Nanowired three dimensional cardiac patches,* Nat Nanotechnol **6**, 720 (2012).

[44] K. Zhu, S. R. Shin, T. van Kempen, Y. C. Li, V. Ponraj, A. Nasajpour, S. Mandla, N. Hu, X. Liu, J. Leijten, Y. D. Lin, M. A. Hussain, Y. S. Zhang, A. Tamayol, and A. Khademhosseini, *Gold Nanocomposite Bioink for Printing 3D Cardiac Constructs,* Advanced Functional Materials **27**, 1605352 (2017).

[45] A. Marino, S. Arai, Y. Hou, A. Degl'Innocenti, V. Cappello, B. Mazzolai, Y. T. Chang, V. Mattoli, M. Suzuki, and G. Ciofani, *Gold Nanoshell-Mediated Remote Myotube Activation,* ACS Nano **11**, 2494 (2017).

[46] S. Ahadian, J. Ramón-Azcón, H. Chang, X. Liang, H. Kaji, H. Shiku, K. Nakajima, M. Ramalingam, H. Wu, T. Matsue, and A. Khademhosseini, *Electrically regulated differentiation of skeletal muscle cells on ultrathin graphene-based films,* RSC Advances **4**, 9534 (2014).

[47] V. Palmieri, F. Sciandra, M. Bozzi, M. De Spirito, and M. Papi, *3D Graphene Scaffolds for Skeletal Muscle Regeneration: Future Perspectives,* Frontiers in Bioengineering and Biotechnology **8**, 383 (2020).

[48] Y. Du, J. Ge, Y. Li, P. X. Ma, and B. Lei, *Biomimetic elastomeric, conductive and biodegradable polycitrate-based nanocomposites for guiding myogenic differentiation and skeletal muscle regeneration,* Biomaterials **157**, 40 (2018).

[49] J. Ciriza, L. Saenz Del Burgo, M. Virumbrales-Muñoz, I. Ochoa, L. J. Fernandez, G. Orive, M. R. Hernandez, and J. L. Pedraz, *Graphene oxide increases the viability of C2C12 myoblasts microencapsulated in alginate,* International Journal of Pharmaceutics **493**, 260 (2015).

[50] C. Vargas-Estevez, A. Blanquer, P. Dulal, R. Pérez del Real, M. Duch, E. Ibáñez, L. Barrios, G. Murillo, N. Torras, C. Nogués, B. J. Stadler, J. A. Plaza, and J. Esteve, *Study of Galfenol direct cytotoxicity and remote microactuation in cells,* Biomaterials **139**, 67 (2017).

[51] C. Vargas-Estevez, A. Blanquer, G. Murillo, M. Duque, L. Barrios, C. Nogués, E. Ibañez, and J. Esteve, *Electrical stimulation of cells through photovoltaic microcell arrays,* Nano Energy **51**, 571 (2018).

[52] G. Murillo, A. Blanquer, C. Vargas-Estevez, L. Barrios, E. Ibáñez, C. Nogués, and J. Esteve, *Electromechanical Nanogenerator–Cell Interaction Modulates Cell Activity,* Advanced Materials **29**, 1605048 (2017).

[53] A. L. Tiano, C. Park, J. W. Lee, H. H. Luong, L. J. Gibbons, S.-H. Chu, S. Applin, P. Gnoffo, S. Lowther, H. J. Kim, P. M. Danehy, J. A. Inman, S. B. Jones, J. H. Kang, G. Sauti, S. A. Thibeault, V. Yamakov, K. E. Wise, J. Su, and C. C. Fay, *Boron nitride nanotube: synthesis and applications,* in *Nanosensors, Biosensors, and Info-Tech Sensors and Systems 2014*, Vol. 9060, edited by V. K. Varadan (International Society for Optics and Photonics, 2014) p. 906006.

[54] S. Pok, F. Vitale, S. L. Eichmann, O. M. Benavides, M. Pasquali, and J. G. Jacot, *Biocompatible carbon nanotube-chitosan scaffold matching the electrical conductivity of the heart,* ACS Nano **8**, 9822 (2014).

[55] S. Sirivisoot and B. S. Harrison, *Skeletal myotube formation enhanced by electrospun polyurethane carbon nanotube scaffolds.* International journal of nanomedicine **6**, 2483 (2011).

[56] S. Ahadian, J. Ramón-Azcón, M. Estili, X. Liang, S. Ostrovidov, H. Shiku, M. Ramalingam, K. Nakajima, Y. Sakka, H. Bae, T. Matsue, and A. Khademhosseini, *Hybrid hydrogels containing vertically aligned carbon nanotubes with anisotropic electrical conductivity for muscle myofiber fabrication,* Scientific Reports **4**, 4271 (2015).

[57] G. Ciofani, L. Ricotti, S. Danti, S. Moscato, C. Nesti, D. D'Alessandro, D. Dinucci, F. Chiellini, A. Pietrabissa, M. Petrini, and A. Menciassi, *Investigation of interactions between poly-l-lysine-coated boron nitride nanotubes and c2c12 cells: Up-take, cytocompatibility, and differentiation,* International Journal of Nanomedicine **5**, 285 (2010).

[58] L. Ricotti, T. Fujie, H. Vazão, G. Ciofani, R. Marotta, R. Brescia, C. Filippeschi, I. Corradini, M. Matteoli, V. Mattoli, L. Ferreira, and A. Menciassi, *Boron Nitride Nanotube-Mediated Stimulation of Cell Co-Culture on Micro-Engineered Hydrogels,* PLoS ONE **8**, e71707 (2013).

[59] I. D. Johnston, D. K. McCluskey, C. K. Tan, and M. C. Tracey, *Mechanical characterization of bulk Sylgard 184 for microfluidics and microengineering,* Journal of Micromechanics and Microengineering **24**, 035017 (2014).

[60] R. Mestre, T. Patiño, X. Barceló, S. Anand, A. Pérez-Jiménez, and S. Sánchez, *Force Modulation and Adaptability of 3D-Bioprinted Biological Actuators Based on Skeletal Muscle Tissue,* Advanced Materials Technologies **4**, 1800631 (2019).

[61] C. A. Powell, B. L. Smiley, J. Mills, and H. H. Vandenburgh, *Mechanical stimulation improves tissue-engineered human skeletal muscle,* American Journal of Physiology - Cell Physiology **283**, 1557 (2002).

[62] D. G. Moon, G. Christ, J. D. Stitzel, A. Atala, and J. J. Yoo, *Cyclic mechanical preconditioning improves engineered muscle contraction,* Tissue Engineering - Part A **14**, 473 (2008).

[63] H. Grabner and H. Bischof, *On-line boosting and vision,* in *Proceedings of the IEEE Computer Society Conference on Computer Vision and Pattern Recognition*, Vol. 1 (IEEE, 2006) pp. 260–267.

[64] U. K. Müller and J. L. Van Leeuwen, *Swimming of larval zebrafish: Ontogeny of body waves and implications for locomotory development,* Journal of Experimental Biology **207**, 853 (2004).

[65] V. Mwaffo, S. Butail, and M. Porfiri, *In-silico experiments of zebrafish behaviour: Modeling swimming in three dimensions,* Scientific Reports 7, 39877 (2017).

[66] A. P. Berke, L. Turner, H. C. Berg, and E. Lauga, *Hydrodynamic attraction of swimming microorganisms by surfaces,* Physical Review Letters **101**, 1 (2008), arXiv:0806.2898 .

[67] J. Simmchen, J. Katuri, W. E. Uspal, M. N. Popescu, M. Tasinkevych, and S. Sánchez, *Topographical pathways guide chemical microswimmers,* Nature Communications **7**, 10598 (2016), arXiv:1602.04094 .

[68] G. Kokot and A. Snezhko, *Manipulation of emergent vortices in swarms of magnetic rollers,* Nature Communications **9**, 2344 (2018).

[69] G. Vizsnyiczai, G. Frangipane, S. Bianchi, F. Saglimbeni, D. Dell'Arciprete, and R. Di Leonardo, *A transition to stable one-dimensional swimming enhances E. coli motility through narrow channels,* Nature Communications **11**, 2340 (2020).

[70] E. M. Purcell, *Life at low Reynolds number,* American Journal of Physics **45**, 3 (1977).

[71] L. Turner, W. S. Ryu, and H. C. Berg, *Real-time imaging of fluorescent flagellar filaments,* Journal of Bacteriology **182**, 2793 (2000).

[72] A. Ghost and P. Fischer, *Controlled propulsion of artificial magnetic nanostructured propellers,* Nano Letters **9**, 2243 (2009).

[73] B. J. Williams, S. V. Anand, J. Rajagopalan, and M. T. A. Saif, *A self-propelled biohybrid swimmer at low Reynolds number,* Nature Communications **5**, 3081 (2014).

[74] S. H. Ku and C. B. Park, *Myoblast differentiation on graphene oxide,* Biomaterials **34**, 2017 (2013).

[75] H. Fujita, T. Nedachi, and M. Kanzaki, *Accelerated de novo sarcomere assembly by electric pulse stimulation in C2C12 myotubes,* Experimental Cell Research **313**, 1853 (2007).

[76] M. Kitsara, A. Blanquer, G. Murillo, V. Humblot, S. De Bragança Vieira, C. Nogués, E. Ibáñez, J. Esteve, and L. Barrios, *Permanently hydrophilic, piezoelectric PVDF nanofibrous scaffolds promoting unaided electromechanical stimulation on osteoblasts,* Nanoscale **11**, 8906 (2019).

[77] D. Golberg, Y. Bando, K. Kurashima, and T. Sato, *Synthesis and characterization of ropes made of BN multiwalled nanotubes,* Scripta Materialia **44**, 1561 (2001).

[78] Y. Xiao, X. H. Yan, J. X. Cao, J. W. Ding, Y. L. Mao, and J. Xiang, *Specific heat and quantized thermal conductance of single-walled boron nitride nanotubes,* Physical Review B - Condensed Matter and Materials Physics **69**, 205415 (2004).

[79] X. Blase, A. Rubio, S. G. Louie, and M. L. Cohen, *Stability and band gap constancy of boron nitride nanotubes,* EPL **28**, 335 (1994).

[80] G. Ciofani, V. Raffa, A. Menciassi, and A. Cuschieri, *Boron nitride nanotubes: An innovative tool for nanomedicine,* Nano Today **4**, 8 (2009).

[81] M. Tolladay, D. Ivanov, N. L. Allan, and F. Scarpa, *Piezoelectric effects in boron nitride nanotubes predicted by the atomistic finite element method and molecular mechanics,* Nanotechnology **28**, 355705 (2017).

[82] Y. Dai, W. Guo, Z. Zhang, B. Zhou, and C. Tang, *Electric-field-induced deformation in boron nitride nanotubes,* Journal of Physics D: Applied Physics **42**, 085403 (2009).

[83] X. Bai, D. Golberg, Y. Bando, C. Zhi, C. Tang, M. Mitome, and K. Kurashima, *Deformation-driven electrical transport of individual boron nitride nanotubes,* Nano Letters **7**, 632 (2007).

[84] G. Ciofani, V. Raffa, A. Menciassi, and A. Cuschieri, *Folate functionalized boron nitride nanotubes and their selective uptake by glioblastoma multiforme cells: Implications for their use as boron carriers in clinical boron neutron capture therapy,* Nanoscale Research Letters **4**, 113 (2009).

VI

Conclusions and final remarks

Conclusions

Hybrid bio-robotics is a discipline that integrates biological entities with synthetic devices with the purpose of improving the performance of man-made robotic systems by incorporating many of the characteristics that biological organisms have optimized through millions of years of evolution. This multidisciplinary integration has led to developments ranging from the nanoscale to the macroscale, putting together fields like nanotechnology, biochemistry, active matter physics, material science or tissue engineering. On the one hand, we can find the creation of nano- and micromotors based on enzymatic reactions that could be the next generation of active drug delivery systems and provide a rather interesting system from the fundamental physics point of view. On the other hand, we have the combination of muscle tissue with artificial materials to compose macroscale actuators that are able to contract, self-heal or adapt to different stimuli.

On the first subject, this thesis addressed several key aspects that were lacking an in-depth analysis in the current literature of enzymatically propelled nano- and micromotors, namely the description and analysis of complex dynamics and their motion in complex media. Firstly, we introduced the topic by studying the motion of a light-powered nanobottle motor and mesoporous silica nanarods propelled by inorganic reactions catalyzed by Pt, Fe_2O_3 nanoparticles or the combination of both. The first case presented non-constant velocity profiles that made difficult their motion analysis by common approaches. Therefore, we focused on the investigation of their directionality and general models of their mean square displacement as alternative metrics to characterize their motion. With this example, we concluded that non-constant velocity profiles would need to be analyzed with extreme care, as the assumptions of the active Brownian particle model require constant speed. A generalization of the formulas in the analysis was necessary and the most characteristic metric of this motion became the scaling exponent of the mean square displacement, instead of the propulsive speed or the diffusion of the motors. In the second case, we followed a statistical approach that divided the total population of nanomotors into two sub-populations with completely different dynamics. We discovered that while one of them needed to be analyzed considering an enhanced diffusion mechanism, the other one was better characterized with a propulsive model. We concluded that differences in the fabrication method (particularly the sputtering of Pt) could result in these distinct sub-populations, highlighting the need of choosing the appropriate metrics to analyze each kind of motion.

After realizing the importance of fulfilling the assumptions of the active Brownian motion when analyzing the results, we focused on a particular example of non-constant dynamics of enzymatically propelled motors. On this regard, we identified the need of developing strategies towards the analysis of motion when the speed decreases exponentially, something that has been shown to occur experimentally but never fully characterized. Based on the characteristics of this system, we developed a new equation describing the time- and ensemble-average mean square displacement that describes the motion of any self-propelled particle with an exponentially decreasing speed. As we noticed the dependence on experimental parameters such as the length of the trajectories recorded by optical microscopy, we investigated the most appropriate experimental approaches to reduce the error associated to the underestimation of motion parameters like the propulsive speed of the particle. This new theoretical framework offers additional analytic tools to discern the motion dynamics of enzymatically propelled nano- and micromotors that move with an exponentially decreasing speed, minimizing the errors associated to the assumptions of classical equations.

Since the most appealing application of these kinds of systems is their use as active drug delivery systems, we studied their motion and interactions with complex matrices, using hyaluronic acid as convenient model of a biological fluid. For this purpose, we used dynamic light scattering as a mea-

surement technique, as it allows to investigate the dynamics of particle diffusion at short times or large frequencies and extract micro-rheological parameters of the material, such as its apparent viscosity or shear moduli. Three types of silica nanoparticles were used to understand the influence of the charge as well as the enzymatic reaction on their subdiffusion through a complex matrix, namely negatively charged nanoparticles, positively charge nanoparticles (through amine functionalization) and urease-powered nanoparticles with an overall negative charge. We concluded that the diffusion of nanoparticles in hyaluronic acid was improved if the charge of the particle was negative, compared to positive, and the presence of urea in the medium further improved the diffusion of urease-powered nanomotors thanks to the activity of the enzymatic reaction.

Moving towards muscle-based bio-robots, we dove into the investigation of biomaterials and the 3D bioprinting technique for the 3D bioengineering of skeletal muscle tissue. This kind of tissue is of particular relevance in the field of bio-hybrid devices due to its inherent three-dimensional organization and its controllability through electrical pulse stimulation. As most biofabrication approaches are based on 2D cultures or mold-casting techniques that might lack scalability, we focused on the potential application of 3D bioprinting as a promising technique for the fabrication of muscle-based bio-actuators. On this topic, we presented the successful bioprinting of a myoblast-laden hydrogel that resulted in functional myotubes, which we assessed by calcium imaging techniques and bright-field microscopy after electrical stimulation. Moreover, we evaluated the alignment of these myotubes through scanning electron microscopy and confocal immunostaining, finding that the shear stress during 3D bioprinting process promotes the alignment of hydrogel chains and therefore that of differentiated myotubes. Thanks to these results, we presented 3D bioprinting as a suitable technique for fast and versatile bioengineering of skeletal muscle tissue for a wide range of applications, ranging from tissue regeneration to bio-actuators or bio-hybrid robots.

Given the main limitation of this technique, namely the lack of control to produce thin and individual fibers that better replicate the organization of native skeletal muscle tissue, we developed a novel co-axial bioprinting approach of universal application to produce controlled fibers with a wide range of materials. This method, based on the confinement of the cell-laden hydrogel around a sheath of pluronic acid, allowed us to control the thickness of the bioprinted fibers, starting from diameters as low as 200 μm. Furthermore, due to the flexibility of this approach, virtually any kind of material could be bioprinted as thin individual fibers, covering the wide range of needs that different cell lines might require in terms of material composition. The largest benefit, however, is found in the 3D bioengineering of skeletal muscle tissue, and we demonstrated its applicability by fabricating functional and organized muscle fibers. This novel co-axial approach based on pluronic shielding, as conclusion, could offer the possibility of obtaining thin, individual and width-controlled fibers of virtually any material or cell type, surpassing the sensibility of current 3D bioprinting approaches based on a single nozzle, having a particularly substantial application in skeletal muscle tissue bioengineering, as we proved the successful fabrication of thin, bundle-like skeletal muscle fibers that were functional and with highly aligned myotubes.

The capabilities of printing multiple materials in the same process was exploited later on to fabricate bio-actuators based on the simultaneous 3D bioprinting of skeletal muscle tissue and soft cantilevers. The self-assembly of the muscle tissue against these posts allowed us to measure the force generated by the contractions due to the deflection of the cantilevers, observed by optical microscopy. We postulated this force measurement platform to be useful for fundamental research in tissue development and drug screening purposes and we demonstrated, as a proof of concept, its applicability by investigating the adaptation of muscle tissue after different kinds of stimulation protocols. We found that, depending on the stimulation frequency and the stiffness of the posts, we could obtain

modulation of the force output, resembling the adaptation of native muscle tissue during exercise. In addition, we studied the possibility of fabricating this bio-actuator with human-derived myoblasts and we adapted our bioengineering protocol for this type of cells. Moreover, after obtaining morphologically and functionally relevant human-derived muscle tissue, we treated the bio-actuators with the cytokine tumor necrosis factor α, mimicking the effects of cellular senescence or tissue aging. We investigated the relevance of these two young and aged skeletal muscle tissue models by using the force measurement platform as a drug testing platform and studying the effects of a cosmetic peptide in development in the contraction kinetics of the muscle. We discovered that this peptide could greatly reduce the relaxation time of high-frequency contractions, almost inhibiting them, in young tissue and, at a lesser extent, in aged tissue. In conclusion, we found that this force measurement platform could be useful not only for studies related to force generation, but also to analyze the dynamics of high-frequency contractions and study the behavior of parameters like the relaxation time. Moreover, we found that human-derived myoblasts could be successfully employed in this platform, opening the door to personalized medicine approaches to investigate the development of myopathies using cells from patients.

Finally, all the developments and acquired knowledge came to an end in the fabrication of two bio-hybrid robots based on skeletal muscle tissue with different motion mechanisms. The first bio-robot consisted of a 3D-printed spring-like skeleton that could swim due to the contractions of the muscle tissue. We fully characterized these bio-robots by finite element simulations in order to optimize the geometry of the skeleton and we analyzed their motion according to symmetric and asymmetric designs. We found that symmetric bio-robots, although numerical simulations suggested the opposite, could attain directional motion after a spontaneous symmetry breaking, yielding a buckling structure. We attributed this type of motion to hydrodynamic couplings between the bottom surface and the flow generated by the contractions, which could not be predicted. Asymmetric bio-robots, on the other hand, always showed fast and consistent motion that matched the expected behavior from numerical simulations. By carefully analyzing the motion dynamics and contraction profiles, we concluded that their movement could be attributed to inertial effects, as the regime of motion was located at a medium Reynolds number. The second type of bio-robot, based on a previously reported design, could move with a crawling mechanism. We demonstrated that the addition of piezoelectric nanocomposites within the muscle tissue could improve the performance of the bio-robot, increasing its speed at high frequencies when compared to control bio-robots. Moreover, we found that their force generation was greatly enhanced, suggesting that the addition of piezoelectric nanocomposites in the tissue during myogenesis can improve the differentiation of the cells due to their spontaneous contractions that can induce local voltage differences in the piezoelectric material to further stimulate the tissue, in a feedback loop. These results open up the possibility of using nanocomposites to enhance the capabilities of bio-hybrid robots, either in the muscle tissue itself or the artificial skeleton.

Future perspectives

Research on hybrid bio-robotics is increasing at a high rate and will continue to do so in the following years and decades. While enzymatically propelled nanomotors are already starting *in vivo* trials with animal models, there is still a lack of understanding of their motion mechanism or their interactions in the crowded environment of cells and tissues. More investigations into this fundamental aspects will be necessary to optimize the fabrication and performance of these devices, but also reduce their side effects. Future research should focus more on the fundamental interactions with biological matrices, following the conclusions drawn from this work, and also in the interaction between several of these nanomotors, which would also offer an interesting system to study in active

matter physics. The effects of other elements, like ionic species, the formation of protein coronae or interactions with the immunitary system are currently being investigated, but more research will be needed once more *in vivo* trials start to be performed.

On 3D bioengineering of skeletal muscle tissue, this work has demonstrated that morphologically and functionally relevant muscle tissue can be fabricated with 3D bioprinting, co-axial bioprinting or mold-casting techniques. Although these results already provide useful information about muscular function or towards drug testing, the complexity of the musculoskeletal system is far from being replicated with this minimal models. The integration with other types of tissues could improve the applicability of these models, such as motor neurons to form neuromuscular junctions, satellite cells to be able to induce self-healing of the tissue when sarcomeres break after exercise, fibroblasts to better emulate the environment of the muscle-tendon unit and finally vasculature to ensure proper delivery of nutrients. 3D bioprinting could be a useful technique for multi-cellular bioengineering but, eventually, the limiting bottleneck could reside in finding appropriate differentiation protocols for these multi-cellular systems. The feasibility of using the presented force measurement platform as a drug testing platform for human muscle tissue opens up the way towards personalized medicine and the study of muscular diseases. Next studies should focus on the optimization of the technique for patient-derived myoblasts, either healthy or diseased, in order to perform extensive drug screenings of new drugs before reaching clinical trials, significantly speeding up the process of drug discovery.

Finally, bio-hybrid robotics based on muscle tissue are already reaching the limit of what can be achieved by simple integration of skeletal muscle tissue with soft skeletons, with bio-swimmers reaching speeds of almost 1 mm/s, as we reported in this thesis. Further research should focus on the integration of several tissues and obtaining more complex, yet useful, ways of actuation that can finally prove the benefits of using native muscle tissue instead of man-made soft actuators. After this, the main challenges reside in ensuring the long-term stability of the constructs, their tolerance to different environments, which might require the fabrication of novel and soft bioreactors to protect the tissue, and the improvement of the control mechanisms, that might require the addition of nanocomposites, as we discussed in the last section. All of these advances will undoubtedly go hand by hand to 3D bioengineering research and communication between both disciplines will be essential.

A word on ethics

The future perspectives of research in bio-hybrid robotics would not be complete without an acknowledgment of the ethical considerations that come into play when dealing with bioengineering or synthetic biology. Top-down approaches based on full tissue explants to power bio-robots face several ethical concerns related to proper animal treatment at scientific facilities and overall ethical procurement of cells or biomolecules from them. Moreover, nano- and micromotors based on enzymatic reactions, if used as drug delivery systems, should be held to the highest health and safety standards even if their biocompatibility issues are improved with the use of enzymes. For this reason, their safety and toxicity should be thoroughly addressed in 2D cultures or 3D cultures before reaching clinical trials or even animal trials.

On this note, 3D bioengineering of tissues becomes a convenient approach to reduce the amount of animal trials in biomedicine or pharmacology research. Furthermore, the use of human-derived cells might also improve the relevance of this type of research by using tissue models that resemble human native tissue the most. However, this bottom-up approach carries more ethical considerations than top-down approaches. On the one hand, the use of human-derived cells carries other ethical

responsibilities, even if they are used for medical purposes. The appropriation of genetic material, together with the use of embryonic stem cells, poses potential harm for public health and privacy, and is already a topic of current controversy with divergent points of view. The use of a patient's own cells for personalized medicine, for instance in drug testing platforms of myopathies or regeneration of damaged muscles with lab-grown tissues, could be revolutionary and improve the health of millions of people worldwide. However, even if considerable efforts are put into ensuring the dignity and anonymity of patients, there are several risks regarding social aspects of the use of this research. This kind of therapies, which could result to be rather expensive, might not be accessible to everyone, increasing the breach of social inequality. If scientists are aiming at creating an equitable and better society, these issues should not remain unaddressed in the near future. Interaction and discussion between society, policy makers and scientists is essential.

On the other hand, one of the most crucial questions resides in whether these fields could be considered to be creating life, replicating it or re-using it for other purposes. This type of language raises fundamental arguments of religious, cultural and political nature that are currently difficult to be settled. Even if an understanding on the meaning of these systems were to be achieved, other controversies arise, such as: where is the limit between an intelligent or unintelligent biological system? What does a sentient being start and when should its dignity be protected? The development of bio-hybrid robotic systems will entail, undoubtedly, an increase in debates of an ethical nature in the near future, especially when more complex devices comprising neural tissue with certain intelligence start to be developed. Sensitivity to all cultural perspectives and potential risks is paramount for ethical research, acknowledging the possibility of precautionary approaches that require stepping down until clear and updated governmental policies are defined to protect society from unethical or corrupt exploitation of this research. The scientific community should not adopt an observing and passive role, but acknowledge and assess both precuationary and proactionary approaches, together with a conscious communication with bioethicists, transparent transmission of research discoveries and participation in risk assessment of the possible dangers.

Articulating the ethical aspects behind any type of research is, therefore, fundamental. During the development of this thesis, the principles and guidelines of ethical research were always kept. The research related to the development of 3D bioengineering approaches for skeletal muscle tissue for bio-actuators and bio-robots was conducted with commercially available murine cell lines, minimizing ethical concerns regarding the isolation of this kind of tissue. Studies with human-derived myoblasts were performed with commercially available cryopreserved myoblasts from a voluntary single donor of which only information about gender, age and BMI was provided. No genetic analysis or other type of study that could result in the identification of the donor were carried out.

We believe that this research offers valuable contributions that could lead to: i) a better understanding of the motion of enzymatically propelled nanomotors and their interactions with biological matrices, which could provide information towards reducing their toxicity and avoiding unnecessary *in vivo* trials; ii) useful insights into fundamental research on muscle development, for instance about its adaptability; iii) the improvement of 3D bioengineering techniques towards muscle regeneration therapies; iv) a step towards reducing the need of animal trials in pharmacological or cosmetic industries and towards personalized medicine to fight against the heterogeneous variety of muscular diseases that could be studied in our drug testing platforms; and v) valuable advances in the biorobotics field that could lead, in the future, to the next generation of more efficient robotic systems. Nonetheless, we acknowledge all the aforementioned ethical considerations and we support and foster collaboration and communication between scientists, engineers, society, bioethicists and policy makers to assess together the risks and ensure transparent and ethical science.